

IDENTIFICATION PAGE

Form Approved
OMB No. 0704-0188

AD-A221 214

Intended to average 1 hour per response, including the time for reviewing instructions, searching existing data sources, gathering the collection of information, and reviewing the collection of information. Send comments regarding this burden estimate or any other aspect of this burden, to Washington Headquarters Services, Directorate for Information Operations and Reports, 1215 Jefferson Davis Highway, Suite 1204, Arlington, VA 22202-4302, and to the Office of Management and Budget, Paperwork Reduction Project (0704-0188), Washington, DC 20503.

REPORT DATE
30 Jan 1990

3. REPORT TYPE AND DATES COVERED
Final Report/1 Jan 86-31 Mar 89

4. TITLE AND SUBTITLE
Light-Millimeter Wave Interactions in Semiconductor Devices

5. FUNDING NUMBERS
61102F/2305/B2

6. AUTHOR(S)
Harold R. Fetterman

(2)

7. PERFORMING ORGANIZATION NAME(S) AND ADDRESS(ES)
UCLA
Dept Electrical Eng
Los Angeles CA 90024

AFOSR-TR-90-0511

8. PERFORMING ORGANIZATION
REPORT NUMBER

9. SPONSORING/MONITORING AGENCY NAME(S) AND ADDRESS(ES)
AFOSR/NP
Bolling AFB DC 20332-6448

DTIC
ELECTE
APR 30 1990

10. SPONSORING/MONITORING
AGENCY REPORT NUMBER
F49620-86-K-0007

11. SUPPLEMENTARY NOTES

S D CG D

12a. DISTRIBUTION/AVAILABILITY STATEMENT
Approved for public release; distribution is unlimited.

12b. DISTRIBUTION CODE

13. ABSTRACT (Maximum 200 words)

The investigation focussed on the nature of optical-millimeterwave interactions in high frequency semiconductor devices. It relied primarily upon optical mixing between frequency locked lasers but also included picosecond studies with a number of different laser systems. Actual devices investigated ranged from FETs to high frequency HEMTs (High Electron Mobility Transistors) and HBTs (Heterojunction Bipolar Transistors.) The actual experiments ranged using optical techniques to obtain fundamental physical information about the nature of these devices at high frequencies to investigating optical control and new application areas. The devices range from special configurations developed at UCLA to advanced, submicron, GaAs alloy devices fabricated in local high technology research laboratories.

ILS

14. SUBJECT TERMS
Light, Millimeter, Wave

15. NUMBER OF PAGES
86

16. PRICE CODE
UL

17. SECURITY CLASSIFICATION
OF REPORT
UNCLASSIFIED

18. SECURITY CLASSIFICATION
OF THIS PAGE
UNCLASSIFIED

19. SECURITY CLASSIFICATION
OF ABSTRACT
UNCLASSIFIED

20. LIMITATION OF ABSTRACT
SAR

FINAL REPORT

Air Force Office of Scientific Research

Award # F49620-86-K-0007

Light-Millimeter Wave Interactions in Semiconductor Devices

from 01/01/86 to 03/31/89

Principal Investigator:

Harold R. Fetterman

Professor

Department of Electrical Engineering

UCLA

Los Angeles, CA 90024

Scientific Program Officer:

Dr. H.R. Schlossberg

Directorate of Electronic and Material Sciences

AFOSR/NE Bldg 410

Bolling AFB

Washington, DC 20332-6448

00 04 27 080

Table of Contents

Introduction	1
Program Description	2
A) Laser Mixing in FETS and HEMTS	3
B) Picosecond Measurement Techniques	7
C) Measurements and Modeling	12
D) Millimeter Radiation Generation	22
Conclusion	26
Appendices	26

Accession For	
NTIS CR&I	<input checked="" type="checkbox"/>
DTIC TAB	<input type="checkbox"/>
Unannounced	<input type="checkbox"/>
Justification	
By	
Distribution /	
Availability Codes	
Dist	Avail and/or Special
A-1	



FINAL REPORT

LIGHT-MILLIMETER WAVE INTERACTIONS IN SEMICONDUCTOR DEVICES

Principal investigator

HAROLD R. FETTERMAN

INTRODUCTION:

This report covers the period from 1/1/86 to 3/31/89 of contract # F49620-86-K-007 and supplement. The investigation focussed on the nature of optical-millimeter wave interactions in high frequency semiconductor devices. It relied primarily upon optical mixing between frequency locked lasers but also included picosecond studies with a number of different laser systems. Actual devices investigated ranged from FETs to high frequency HEMTs (High Electron Mobility Transistors) and HBTs (Heterojunction Bipolar Transistors).

The actual experiments ranged from using optical techniques to obtain fundamental physical information about the nature of these devices at high frequencies to investigating optical control and new application areas. The devices presented in this report range from special configurations developed at UCLA to advanced, submicron, GaAs alloy devices fabricated in local high technology research laboratories.

PROGRAM DISCRIPTION:

The program we have completed will be discussed in four separate areas. The first portion (A) deals with optical mixing using a tunable argon pumped dye laser mixed with a stabilized He-Ne laser. This system was used to injection lock and modulate FET and HEMT based transistor oscillators. It was also employed to examine noise and gain in these systems at relatively high frequencies. This required the development of planar Antenna configurations and suitable circuit elements.

Section (B) of this report deals with the use of picosecond pulses to test and evaluate these experimental high frequency devices. The picosecond techniques utilized both optical switches to generate electronic pulses and direct optical pulse injection into the device of interest. In each case the taking of appropriate Fourier transforms then brought the results into frequency space and provided a direct comparison with the cw measurements.

In the section (C) we discuss the testing and modeling research undertaken as part of this program to understand the devices and Optical response functions. These measurements ranged from observing device characteristics using specially constructed six-port systems to far infrared Shubnikov-de Haas and Cyclotron resonance measurements. A special effort was made to develop an accurate analytic model of the HEMTs to correctly predict the role of optically injected carriers.

Finally, in section (D) we discuss some of the concepts in using these techniques to generate millimeter radiation

using these optical interactions. The cw work, although showing promise, did not yield usable amounts of radiation. However, the picosecond pulsed work using configurations developed along lines discussed in part A was highly successful. Some of the initial spectroscopy done with these systems is included in this section.

A) LASER MIXING IN FETS AND HEMTS

During this contract period optical interaction in three terminal devices has been examined using the techniques of optical mixing. The response to light in these systems has been found to be both extremely strong and fast. This has led to attempts at injection locking and control of high frequency oscillators. Our approach in combining two beams to generate a cw modulated signal is shown in figure 1. When high frequency modulators or diode lasers become available this technique will no longer be required. However, to show feasibility this mixing configuration yielded stable signals which were adjustable from zero to several hundred GHz.

The injection locking of a oscillator at 18 GHz. and the tuning of a 40 GHz. oscillator are shown in figures 2 and 3. The details of these experiments are given in Appendix I papers 1 and 2. These mixing techniques were extended using harmonics of an electrically injected L.O. to over 52 GHz. However, it was clear from these measurements that a more efficient structure would be necessary to bring in millimeter wave signals was required. An integrated planar antenna structure would not only couple the optically controlled device to millimeter waves, it would also provide for a radiative capability.

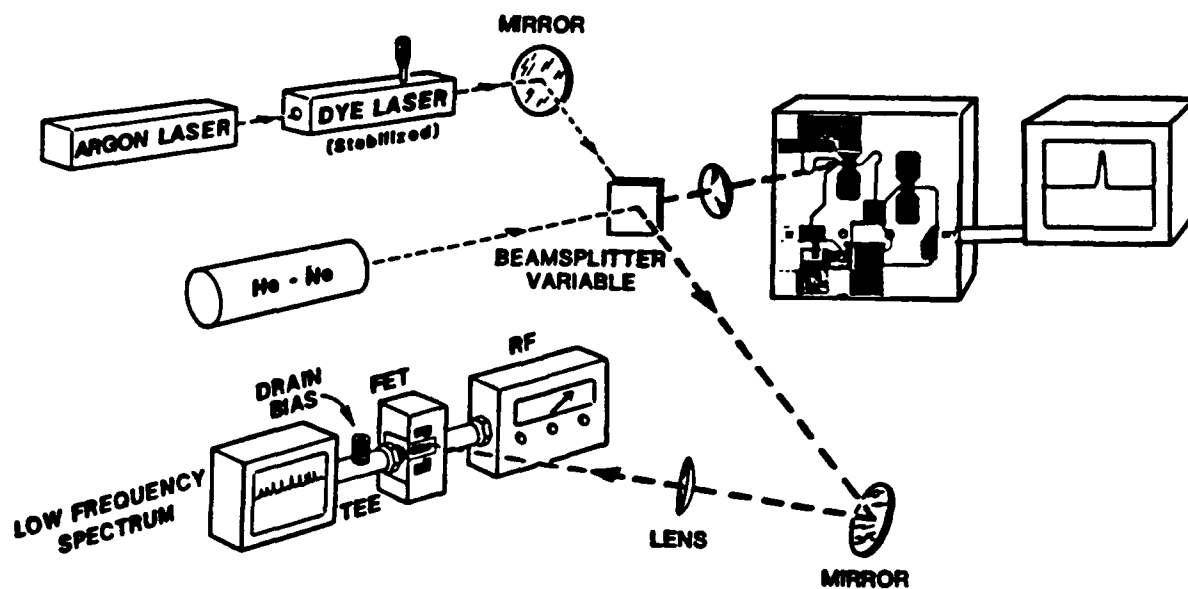


Figure 1. Experimental setup for optical mixing

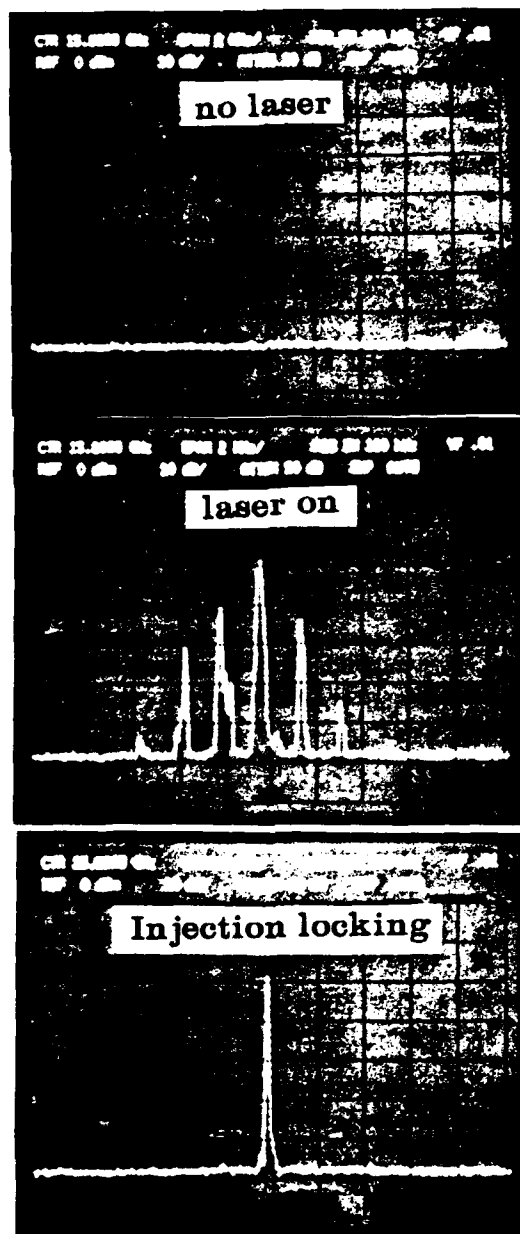


Figure 2.

Signal injection and locking of an oscillator by optical mixing. (a) no laser illumination. (b) laser turns the oscillation on, (c) optical signal locks the signal of oscillator

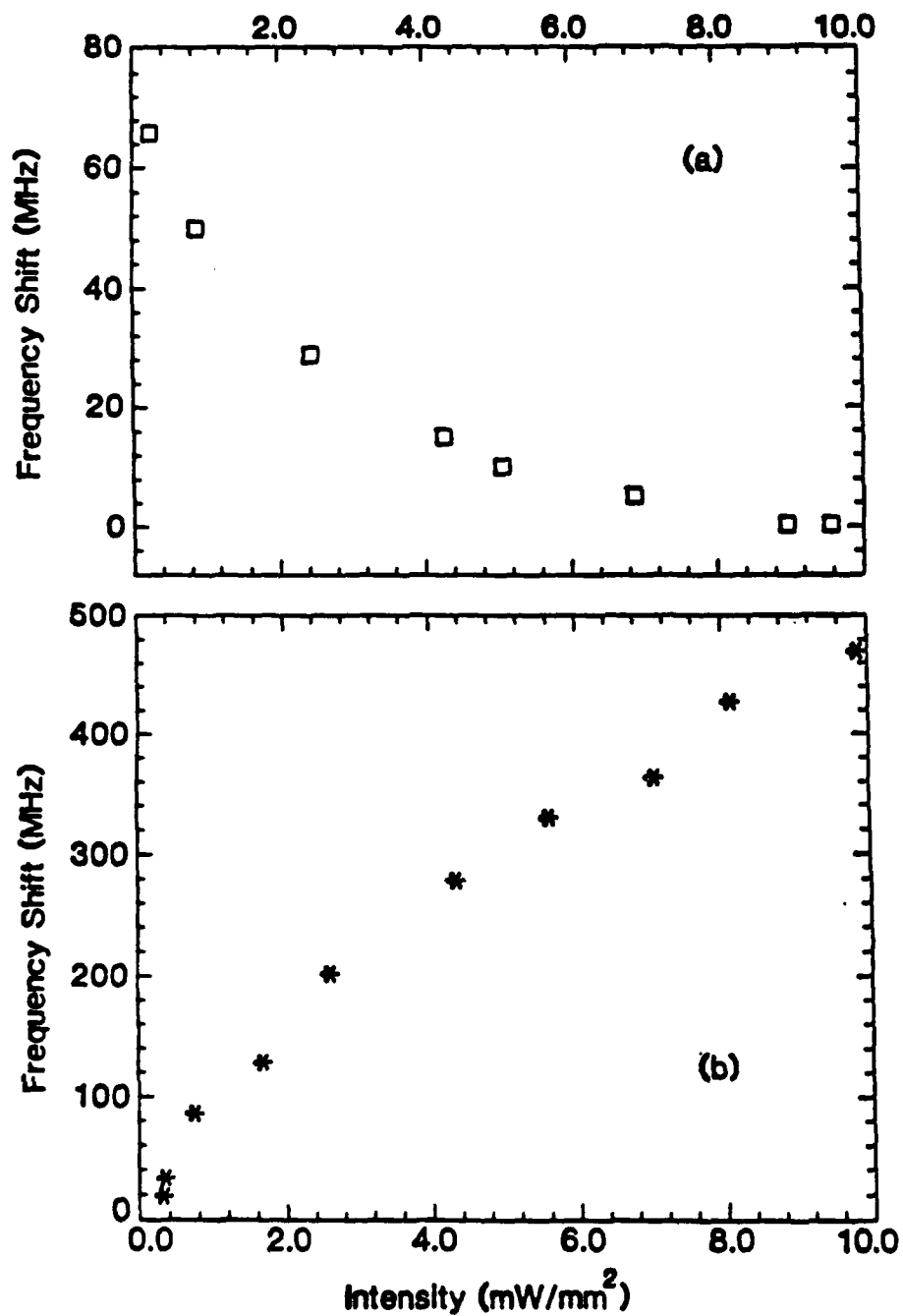


Figure 3 Frequency shifts vs. power of the injection laser of a microwave oscillator in (a) common drain-gate configuration, (b) common source-gate configuration

The development of a printed, planar twin dipole suitable for coupling three terminal devices to millimeter waves is described in paper 3. Shown in figure 4, this antenna is connected across the gate and drain for detection. The connections would be changed to the source and drain in a transmission mode. The basic system that was used is shown in figure 5 and discussed in detail in paper 4 (To be published special issue MTT). The use of a metal mirror with a small optical coupling hole provided an effective means of combining sources for down conversion.

These measurements yielded a significant amount of data about mixer gain and conversion loss. It provided a method to measure noise resulting from hot electron effects. In addition a noise cancellation effect, similar to that observed in a balanced mixer was noted. Figure 6 shows typical curves that were obtained in this study as a function of klystron injected power. Our experiments demonstrated that in addition to having very high non-linear behavior, the three terminal devices we tested had impressive gain at millimeter wave frequencies. Interesting this included some devices which were not really designed for high frequencies. Closer examination revealed that often input parasitics are effectively bypassed when using optical techniques.

(B) PICOSECOND MEASUREMENT TECHNIQUES

The use of picosecond pulse techniques to complete and extend our measurements was a natural outgrowth of these experiments. Again, the major details are given in appendix II, paper 5 (MTT- accepted for publication). Initially we used our mode locked Argon pumping a dye but then went up to a mode locked Nd doubled. The photoconductive switches that were used for electrical measurements were made using the basic design shown in figure 7. Placing this in a microstrip

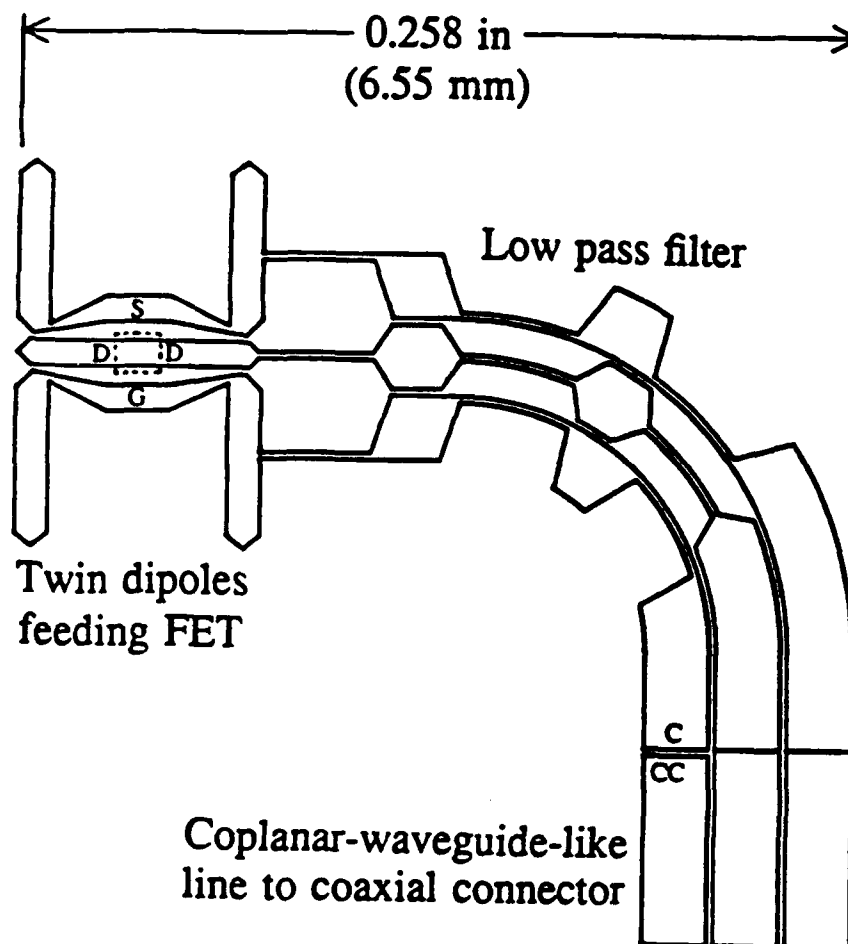


Figure 4. Pattern of the millimeter-wave antenna. FET source, drain, and gate are wire-bonded to points S, D, and G. Gate bias chip capacitor is attached at point CC and wire-bonded to point C

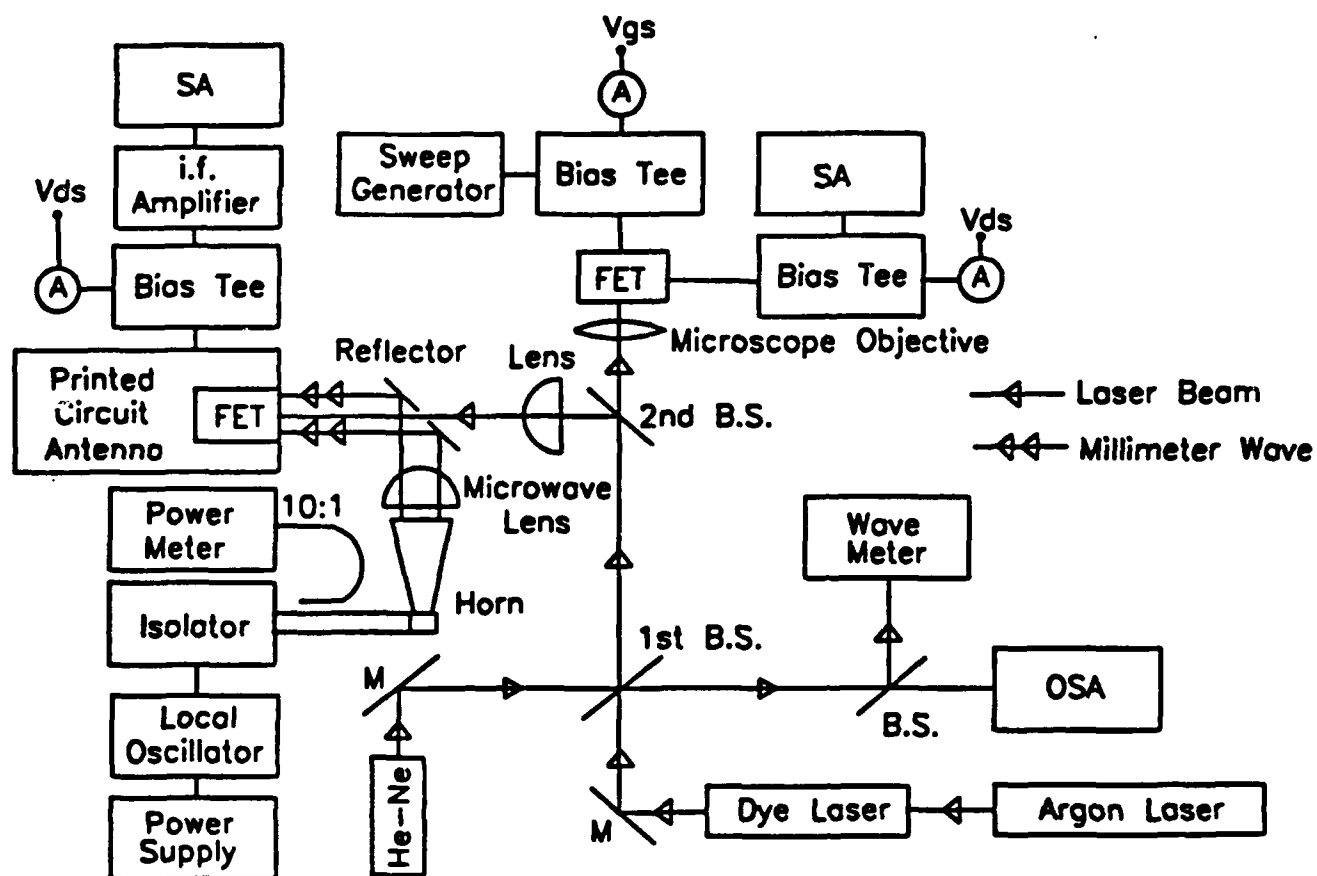


Figure 5. Experimental setup shows the calibrated FET and the FET in the printed antenna circuit.

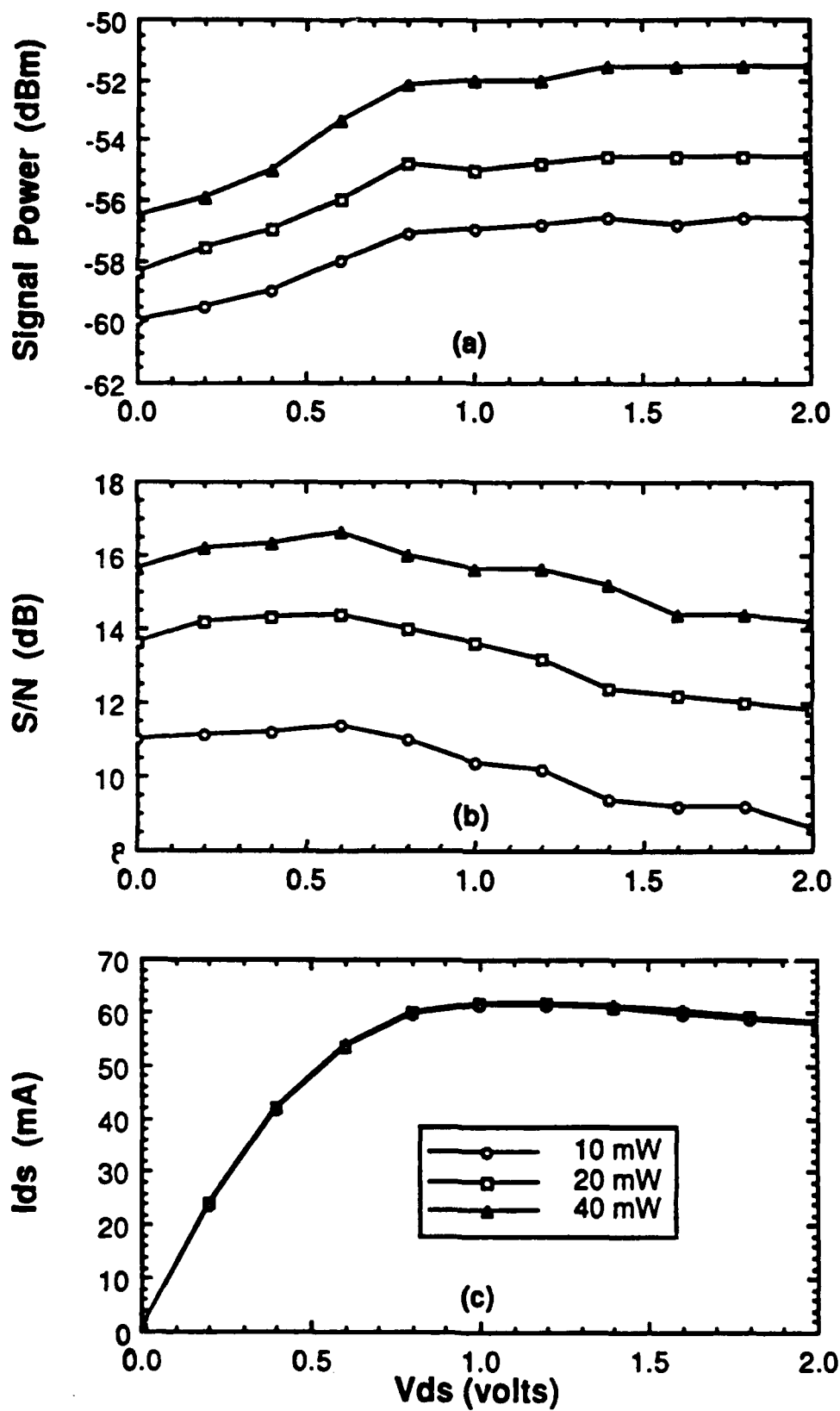
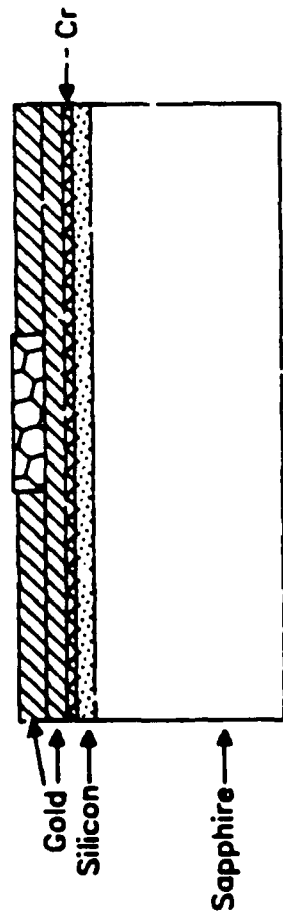
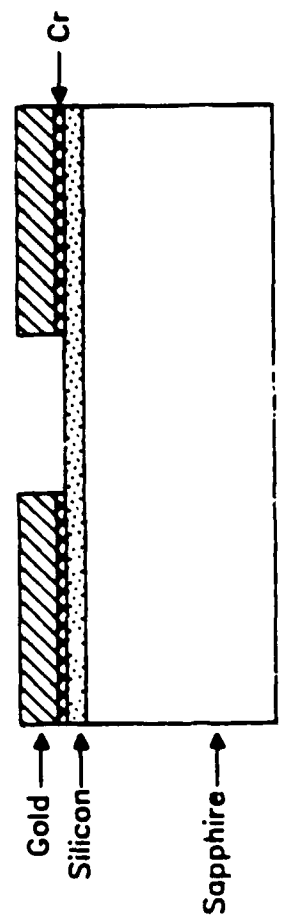


Figure 6. (a) Signal Power, (b) S/N, and (c) I_{ds} of second beat signal versus V_{ds} at 10 mW, 20 mW and 40 mW of klystron power. V_{gs} is at -0.7 V.

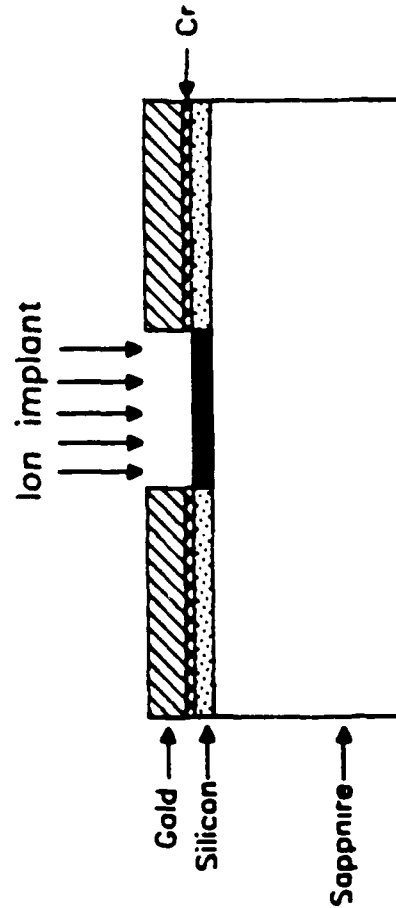
Fabrication of Optical Switches



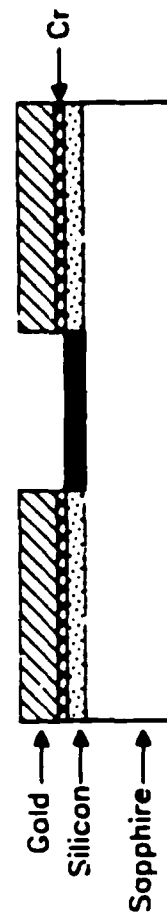
Electroplate gold



Etch the thin Cr-Au layer



Ion implant the wafer



Lap the sapphire wafer

Figure 7.

configuration (figure 8) yielded electrical pulses with a half width on the order of 12 picoseconds. Finally, using a delay system shown in figure 9 created what amounted to a sampling oscilloscope with a frequency response up to about 200 GHz.

Taking the Fourier transform of the time response to the electric pulses yielded a complete set of "S" parameters which completely characterized the linear response of the device. In every case we compared our results with conventional network analyzer measurements and found excellent agreement where they overlapped. Figure 10 shows S_{21} for a HBT with the other parameters shown in paper 5. The work was extended to a broad range of other devices and circuits of interest. These include various types of HEMTs using GaAs and InGaAs alloys and are shown in figures 11 and 12. More complex circuits using MMIC amplifiers (figure 13) were measured and the gain shown in figure 14. Our measurements yielded the entire set of phase and amplitude information with no adjustable parameters. At the highest frequencies the effects of bond wire inductances were readily detected.

The optical response functions of these devices could also be determined by looking directly at these devices and systems as photodetectors. Utilizing the same test system as the electrical measurements but introducing the picosecond laser pulses into the device rather than into the switch yielded the curves in figures 15 and 16. Comparing the observed results with those obtained from the electrical measurements indicates that the base or source resistance is an important factor limiting the high frequency properties of these devices.

(C) MEASUREMENTS AND MODELING

Optoelectronic Test Fixture

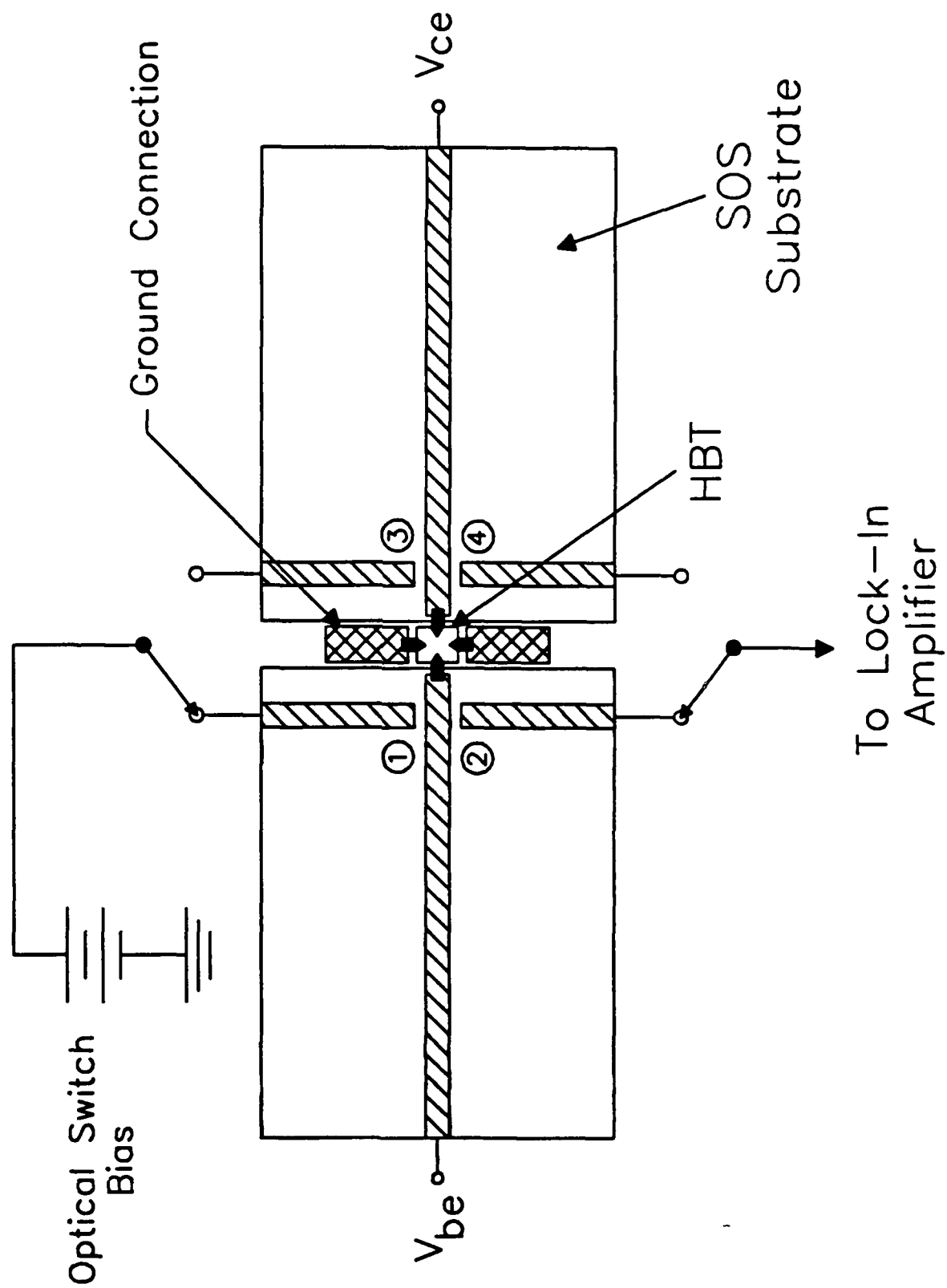


Figure 8.

Optoelectronic Measurement System

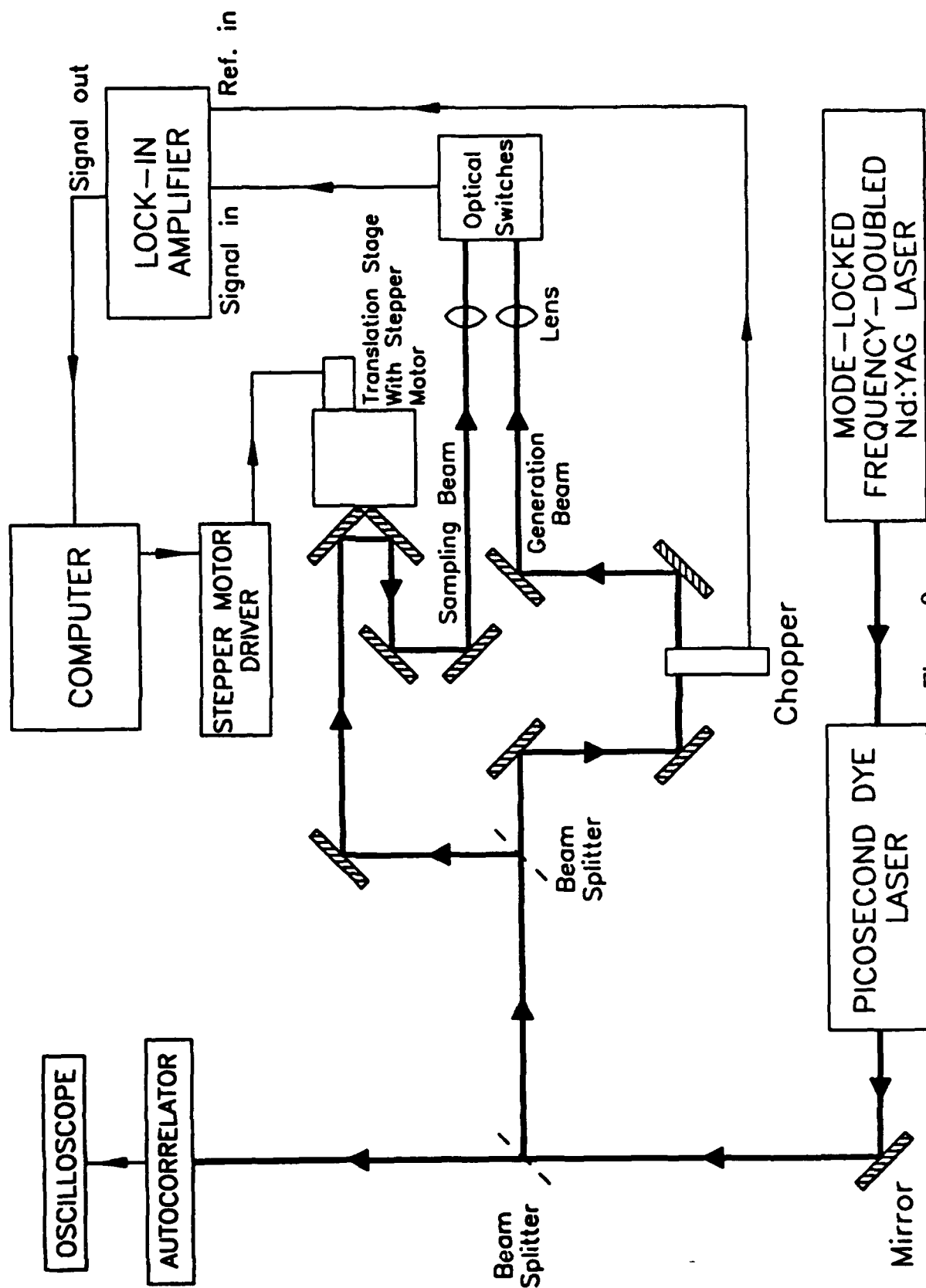


Figure 9.

HBT - S21

Optoelectronic Measurement

Network Analyzer Measurement

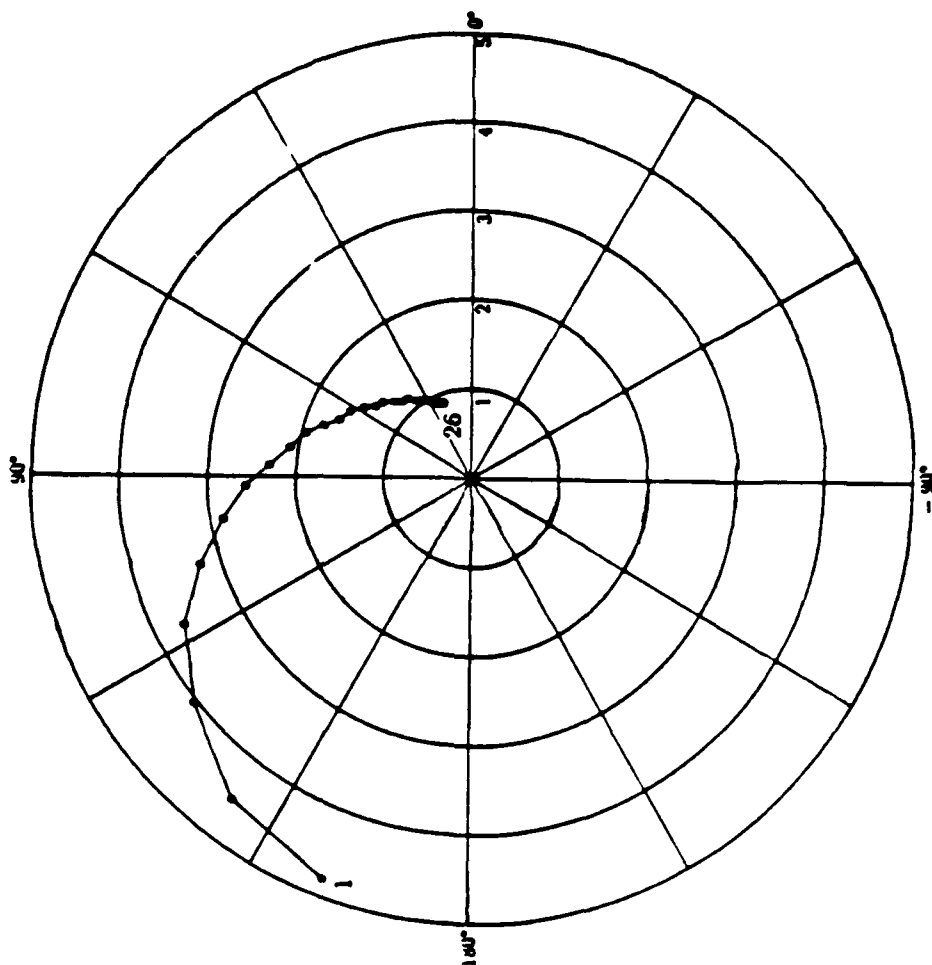
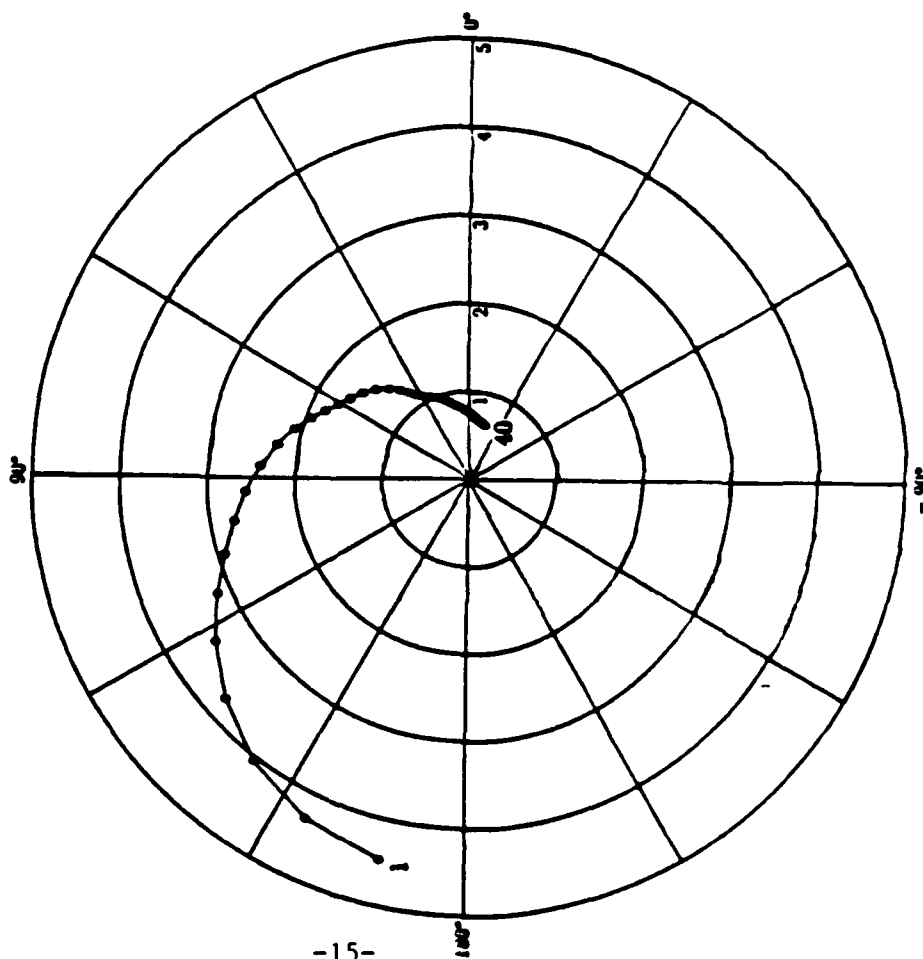


Figure 10.

Power Gain of the AlGaAs/GaAs HEMT

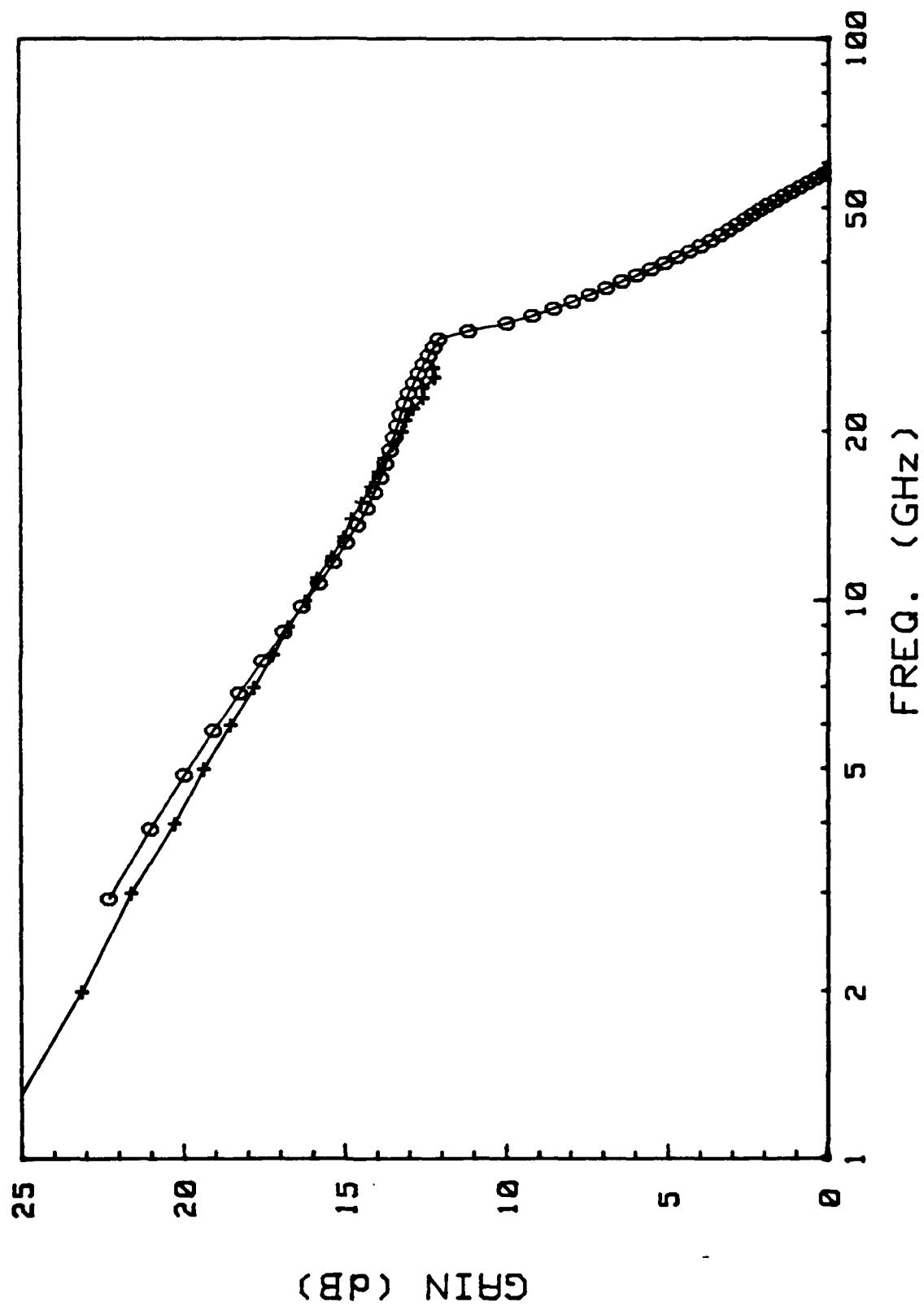


Figure 11.

Power Gain of the AlInAs/GaInAs HEMT

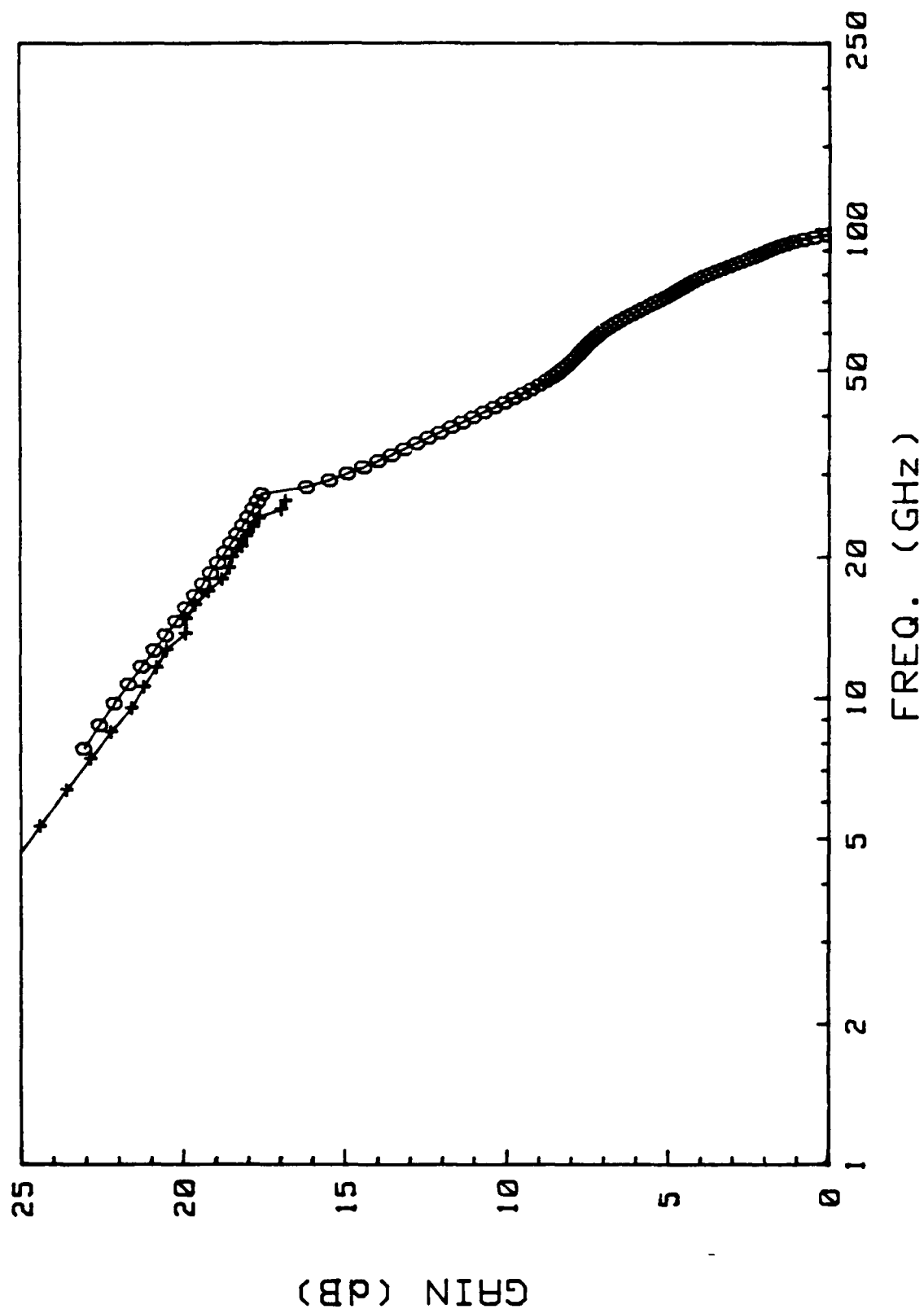


Figure 12

Monolithic Q-band Amplifier

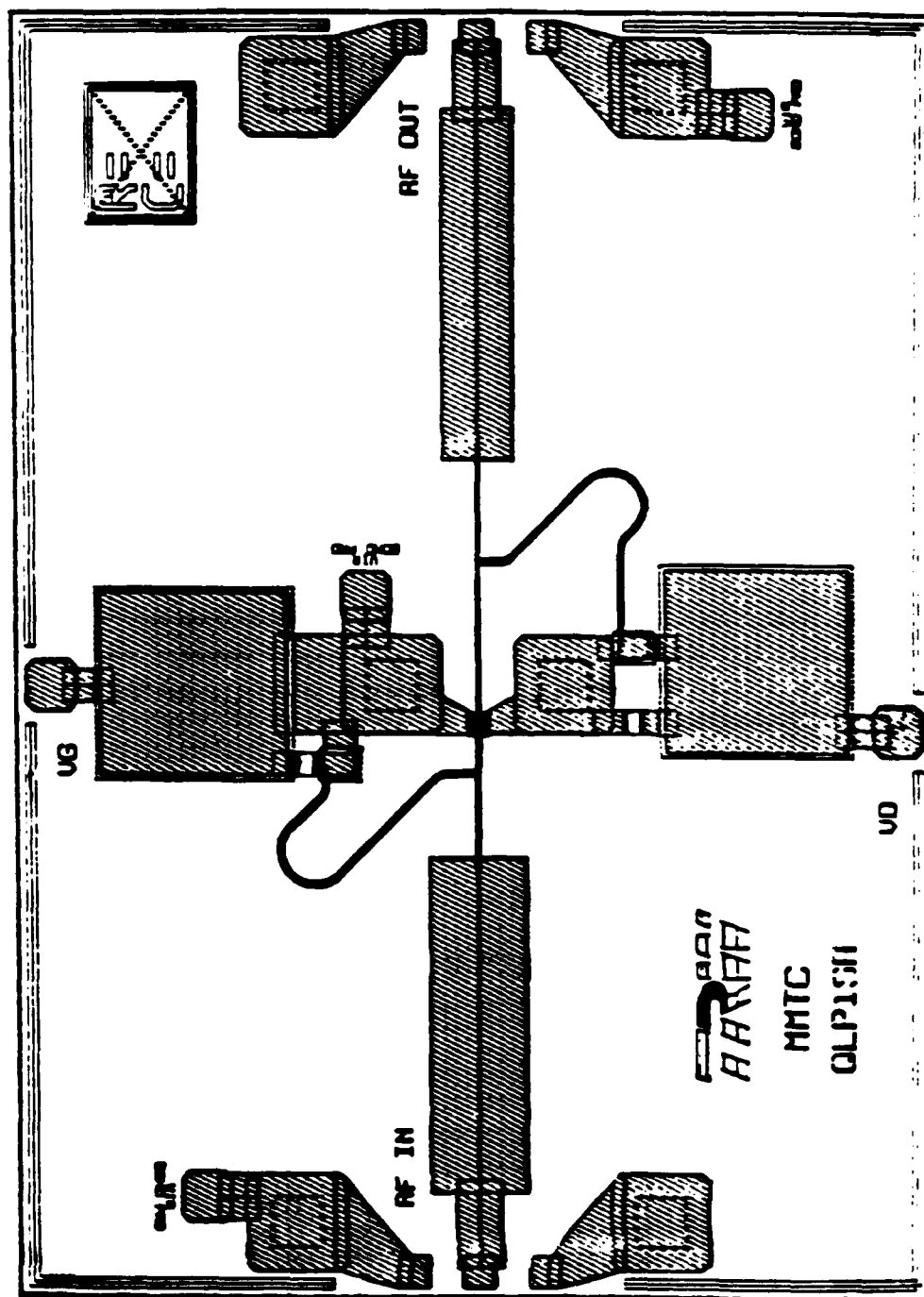


Figure 13.

Gain of the Q-band Amplifier

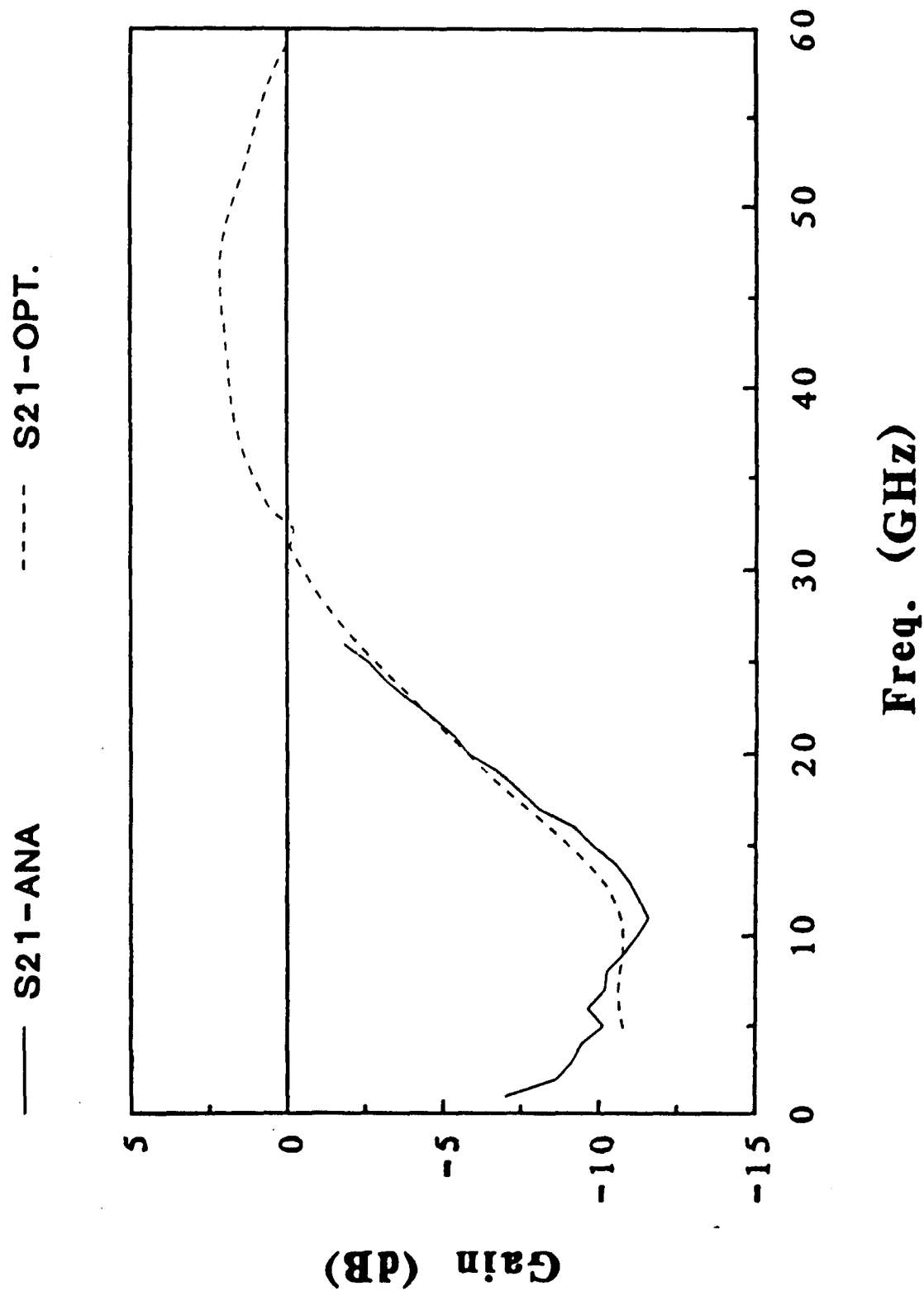
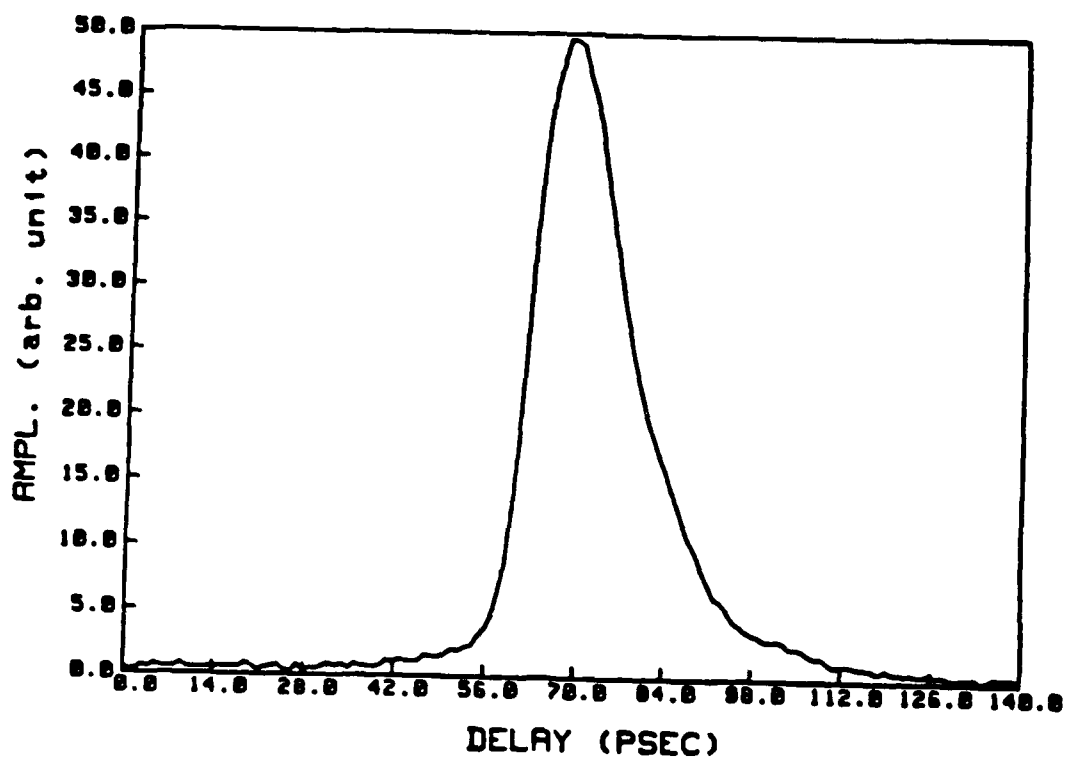
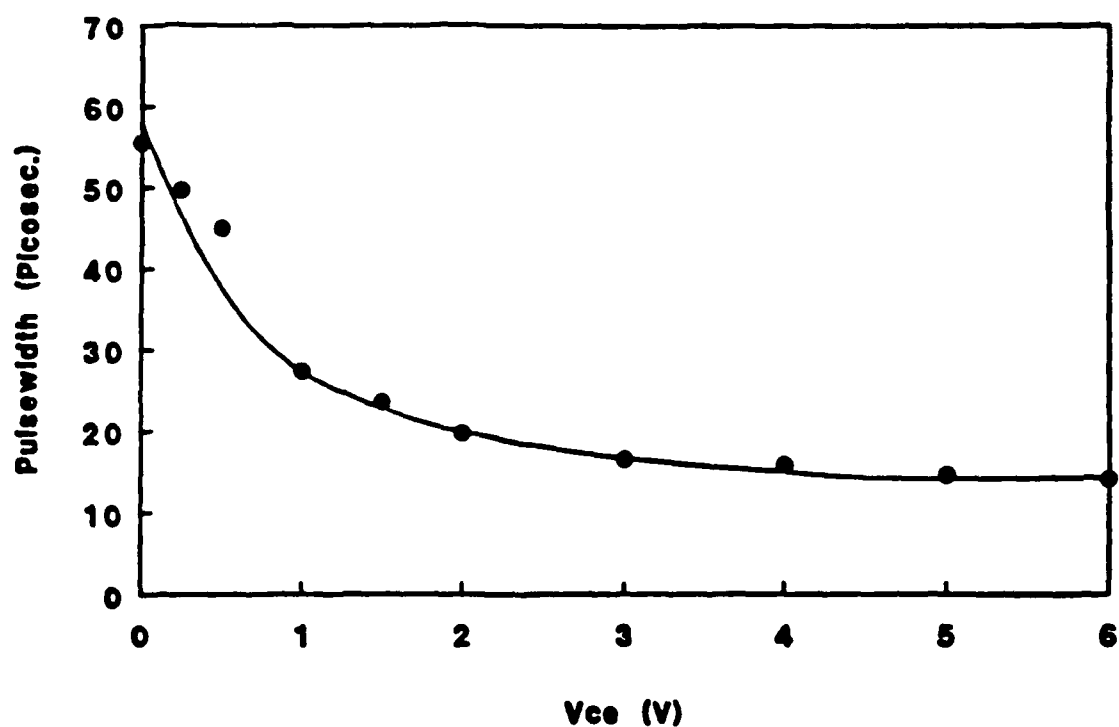


Figure 14.

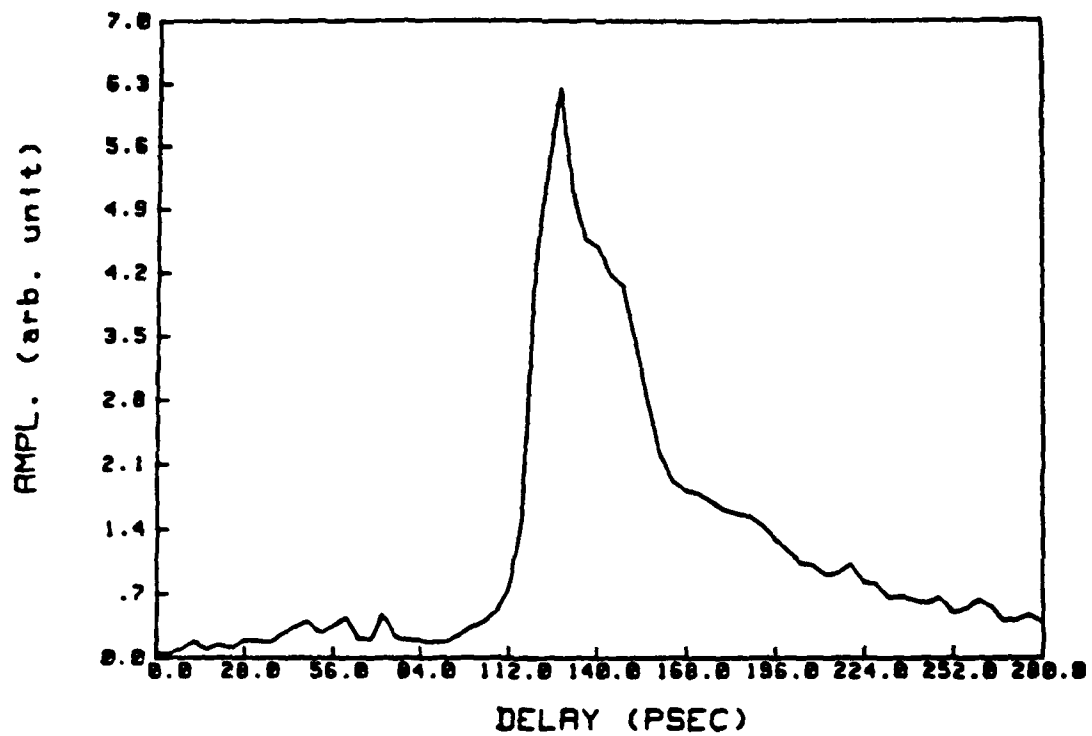


Optical response of the HBT used as a phototransistor for $V_{ce} = 3V$.

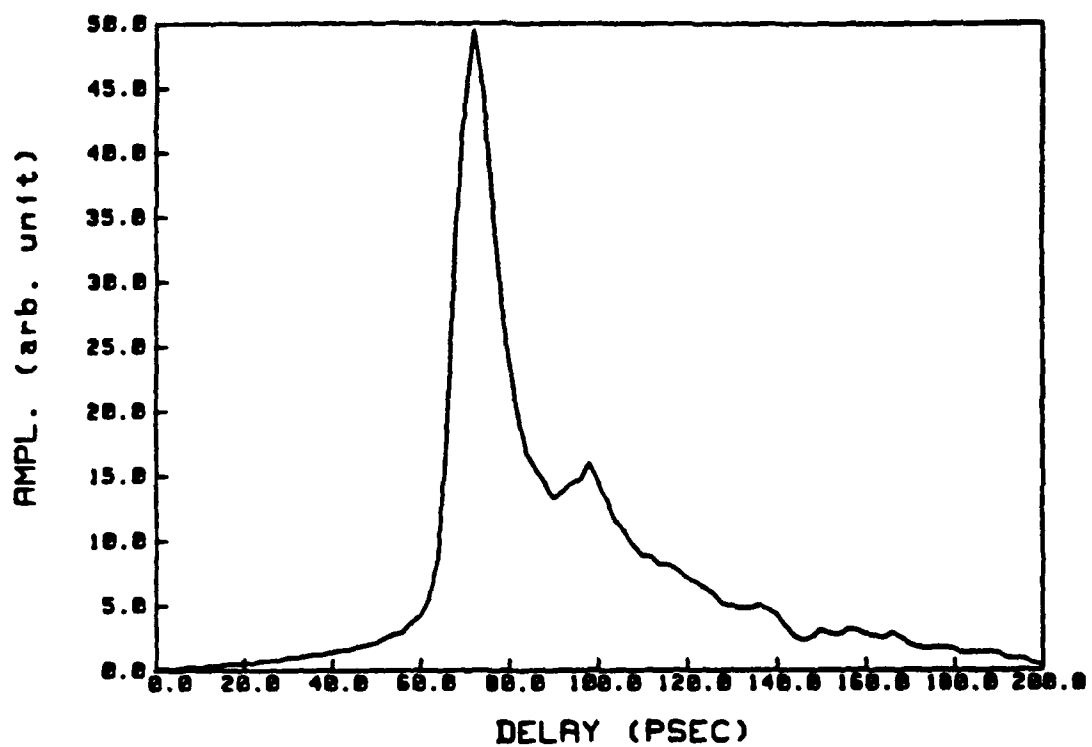


Variation of the optical response pulsewidth as a function of the collector-to-emitter voltage.

Figure 15.



Optical response of the GaAs MESFET for $V_{gs} = -3V$ and $V_{ds} = 3V$.



Optical response of the AlGaAs/GaAs HEMT for $V_{gs} = -2.5V$ and $V_{ds} = 2V$.

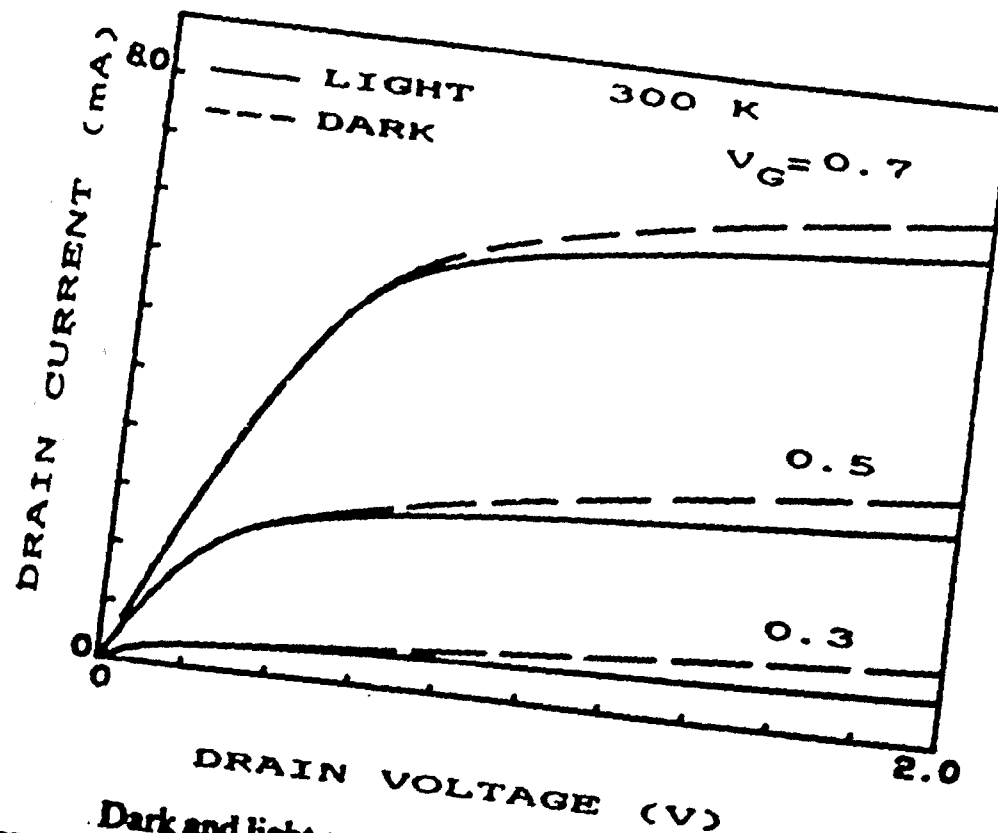
Figure 16.

As part of this program an effort was made to understand the basic elements of the devices being tested. We looked at the theory of these devices and compared it with a number of experimental measurements. The HEMT devices (paper 6) were described analytically and the optical response experimentally found to extend into the infrared (paper 7). We attribute this effect (figure 17) to the transfer of electrons from the 2D electron gas to lower mobility regions of the device (figure 18). Some of this work was extended, using quantum well structures, in combination with the HEMT devices, to wavelengths as long as 10 microns (figure 19 shows the basic spectral response of one structure).

Other measurements of cyclotron resonance (paper 8) using infrared radiation and Shubnikov-de Haas effects (paper 9) inabled us to get fundamental insights into the nature of HEMTs. This is vital to identify the properties of these layered structures which contribute to the optical response function. As part of these efforts a six-port (figure 20) measurement system was also designed (paper 10) and tested and permitted electrical measurements to validate our optical experiments to over 100 GHz (paper 11). These measurements showed additional resonances indicating the limitations of existing test fixtures. This problem was, except for the source inductance associated with bond wires, readily removed in the optical measurements.

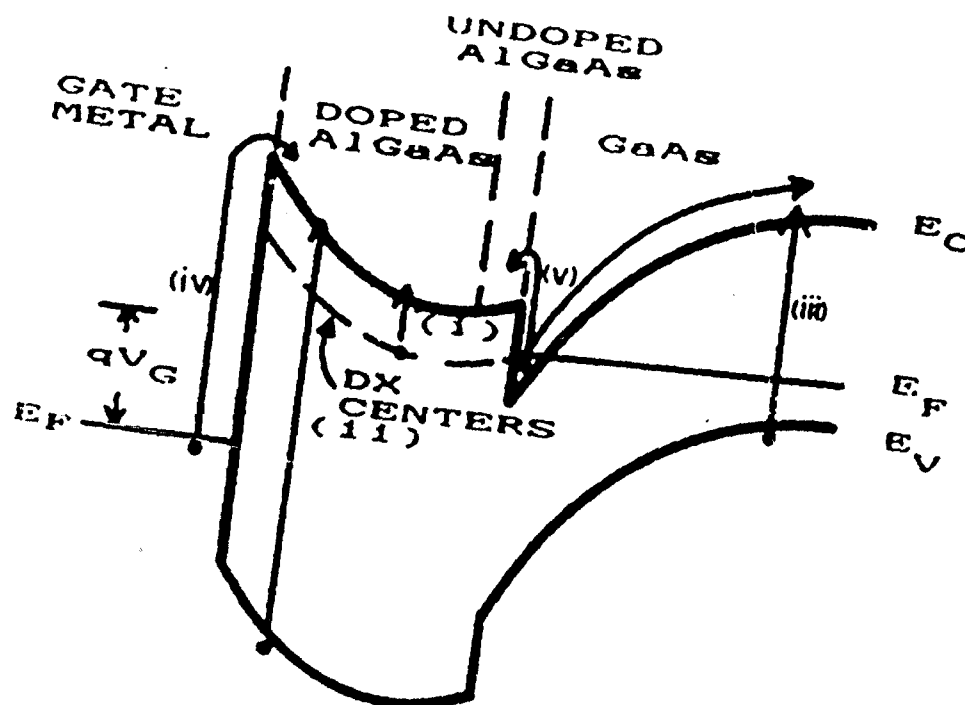
(D) MILLIMETER RADIATION GENERATION

The antenna system previously descibed could be configured into a radiating mode with the source and drain driving the dipoles. Then illuminating the device with either picosecond or cw laser radiation could be used to



Dark and light current-voltage characteristics of the short channel HEMT at room temperature.

Figure 17.



Band diagram of AlGaAs-GaAs heterostructure in the 2DEG control regime by a Schottky gate.

Figure 18.

NICOLET FT-IR

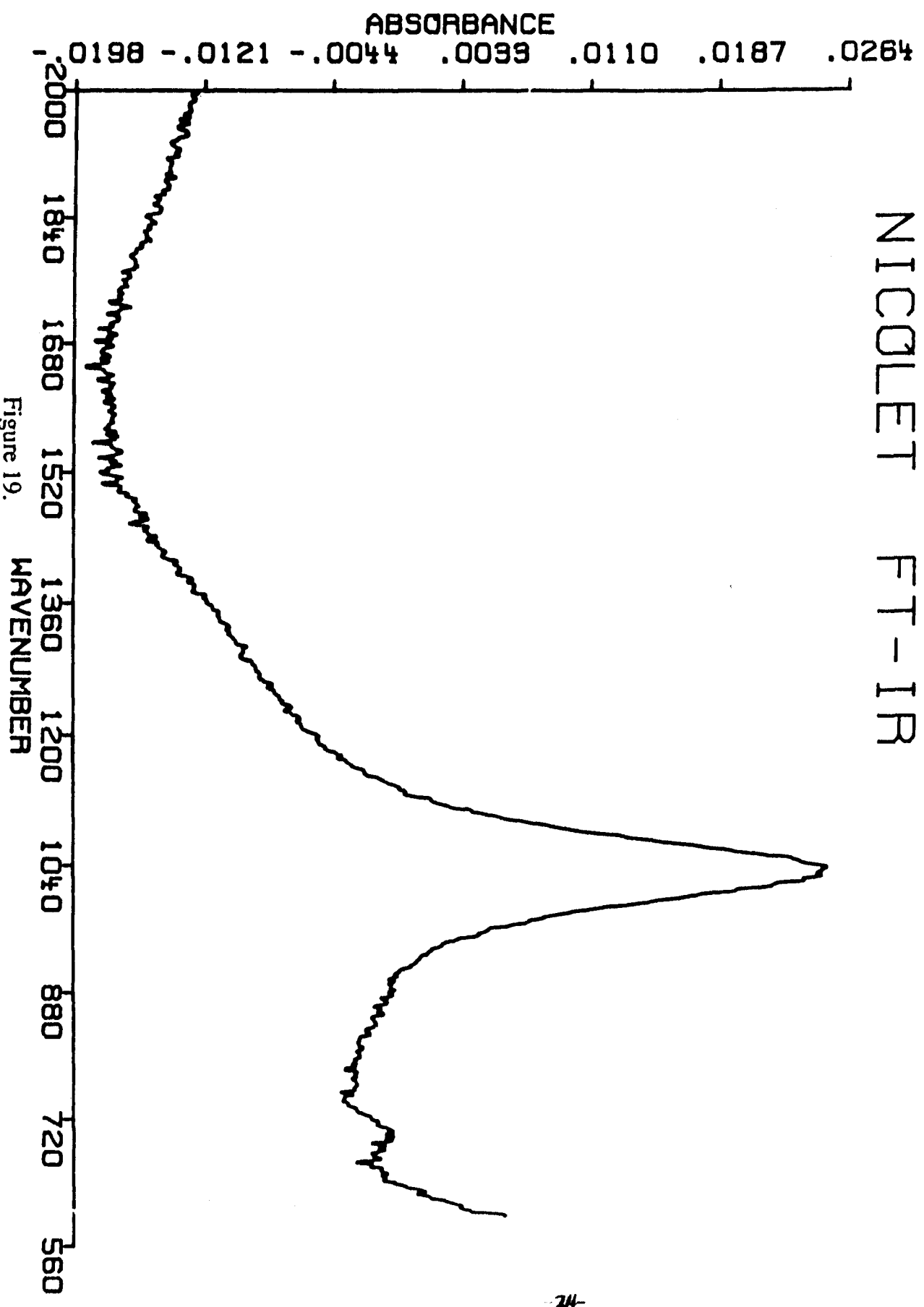


Figure 19.

Six-port Network Analyzer

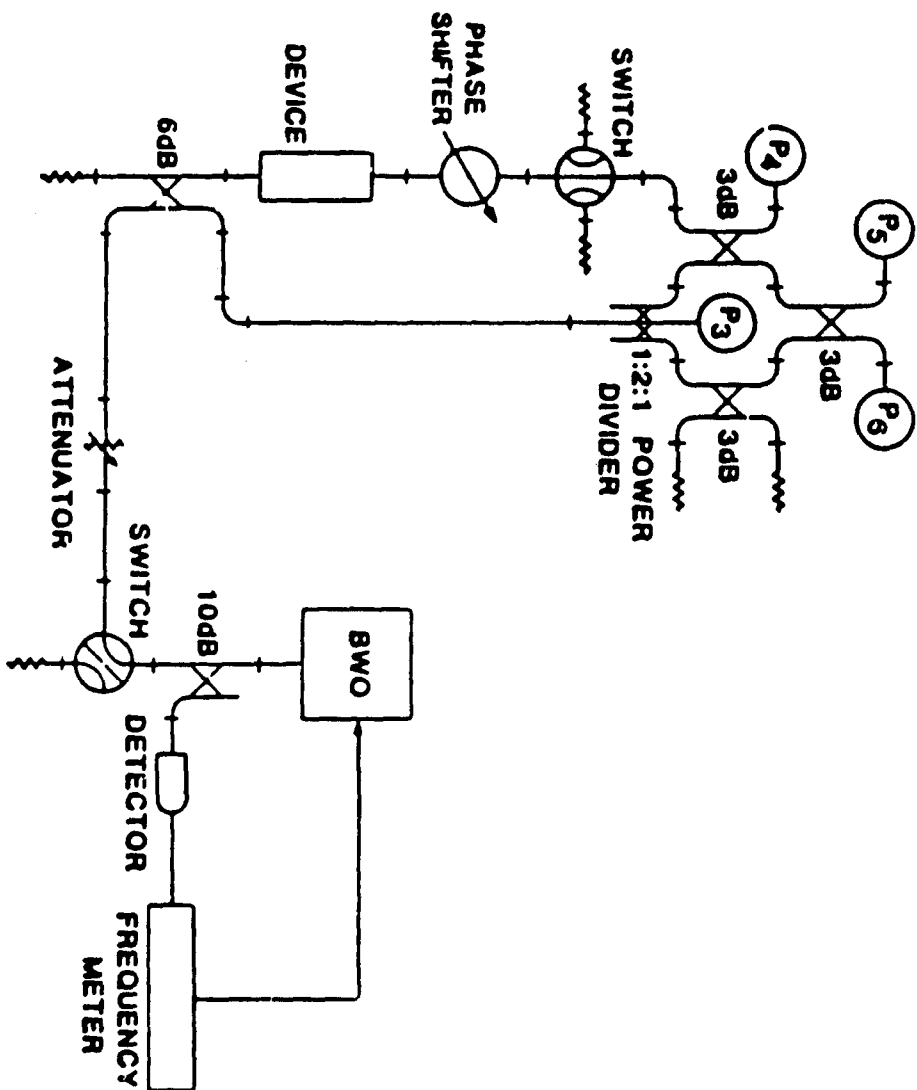


Figure 20.

generate millimeter wave power. The cw work did not generate sufficient levels to be useful and the most fruitful work was accomplished with the picosecond lasers. A klystron used with a second FET - planar antenna system served as a heterodyne receiver at 65 GHz. The system shown in figure 21 seems ideal for real time millimeter wave spectral measurements. A plot of the power dependence of our radiation is shown in figure 22. These results confirm our projections that these optical interactions lend themselves both to the detection and generation of millimeter waves.

CONCLUSION

During this study we have taken the system from simple experimental observations of millimeter - optical interactions into reproducible mixing configurations and now into prototype application areas. We find that this is a very promising synthesis with huge bandwidths and exciting linkages of microwaves and fiberoptical based systems. Given the thrust of millimeter wave systems into large area arrays we project that future systems will be hybrid - optical and millimeterwave combinations all the way up to wafer scale levels.

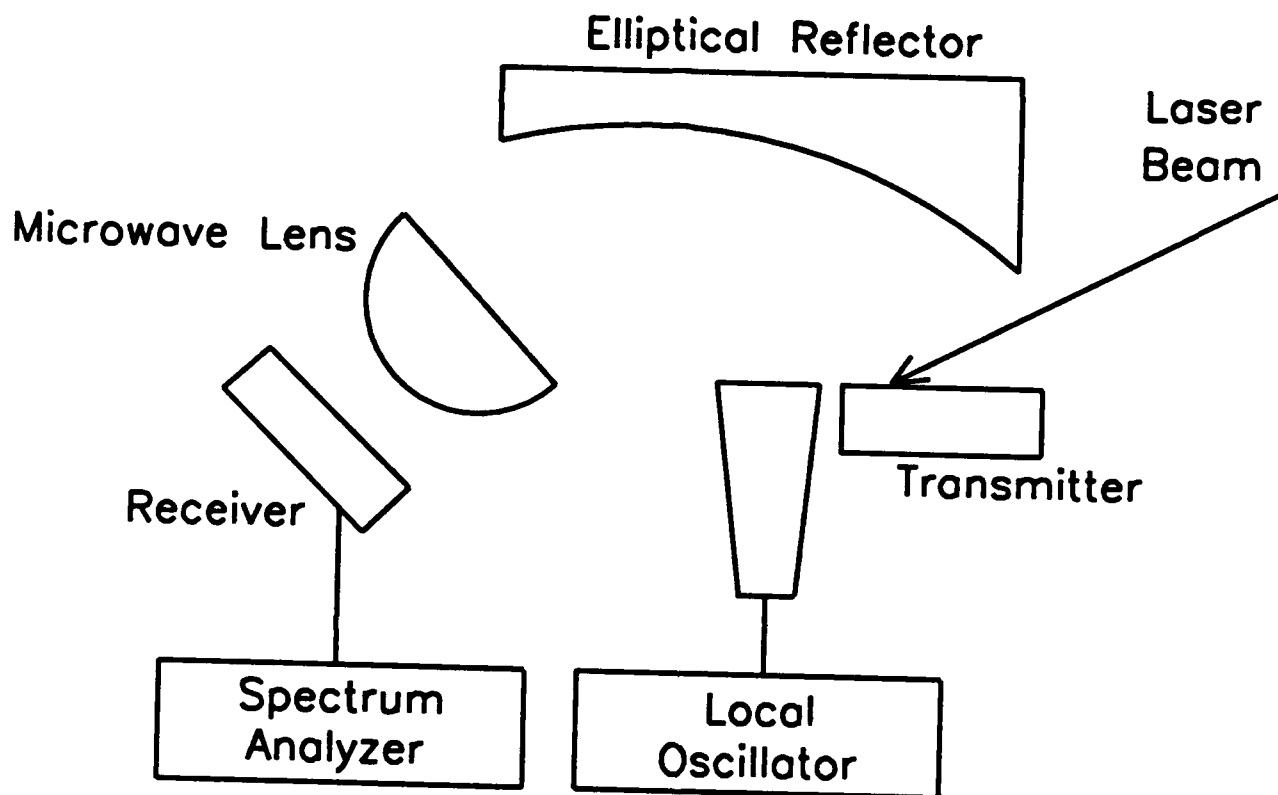


Figure 21. Experimental setup shows millimeter-wave radiation of a microstrip antenna (Transmitter) driven by the signals generated by a picosecond light pulse in a FET connected to the antenna and detection by a second microstrip antenna (Receiver)

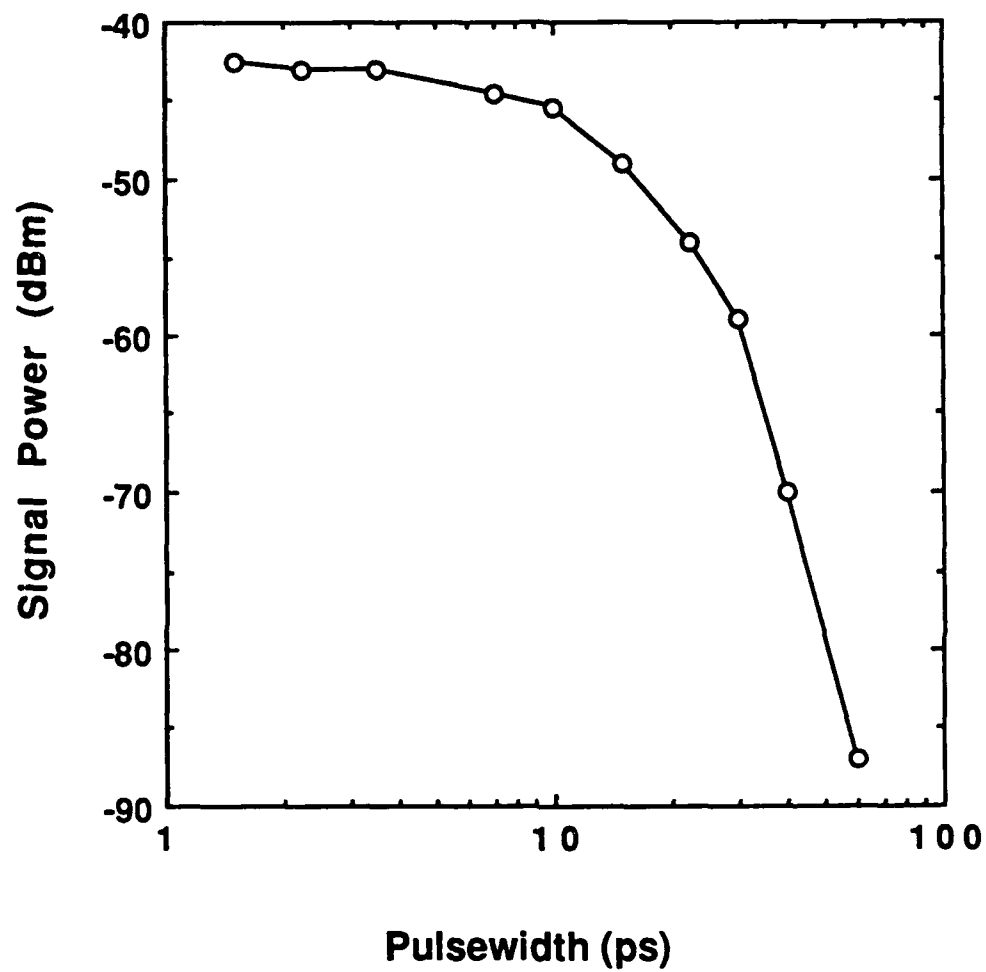


Figure 22. Signal Power of i.f. frequencies vs. Pulsewidth of picosecond laser

APPENDIX I

OPTICAL CONTROL OF MILLIMETER WAVE DEVICES

Harold R. Fetterman, Wei-Yu Wu and David Ni
Department of Electrical Engineering
University of California, Los Angeles
Los Angeles, CA 90024

Abstract

Coherent mixing of optical radiation from a tunable CW ring dye laser and a stabilized HeNe laser was used to inject broadband microwave signals into GaAs MESFETs (FETs), AlGaAs-GaAs HEMTs and monolithic FET amplifiers up to 55 GHz. Using this technique, amplification of an optically injected signal at 32 GHz, direct injection locking of a 17 GHz GaAs oscillator, and frequency tuning of a 40 GHz oscillator by laser intensity modulation were demonstrated. Comparison of the millimeter wave frequency generation mechanism, noise sources and system performance with other techniques used for signal synchronization and distributed control application are discussed.

Introduction

Current interest in optical control of millimeter wave devices can be divided into two areas. Firstly, there is the in device physics area with detailed investigations of mechanisms of photoconductive and photovoltaic response under different conditions [1-5]. Of particular interest are the new device such as HEMTs which use layered structures and extremely short gate FETs with high electric fields. Secondly, in the application areas, considerable attention has been devoted toward dealing with overcoming the frequency constraints of existing devices and performing signal synchronization and distributed control for communication and radar systems [6-8]. Nonlinearities of semiconductor lasers, pin detectors as well as FETs have been utilized extensively to side-band lock [6] or to generate harmonics for multiplication of master oscillation signals [7-8]. In these approaches, reliability and FM noise degradation issues require significant engineering efforts since the devices operating in the nonlinear region are normally under significantly bias stress.

In these study, we explored laser mixing techniques to inject millimeter wave signals in GaAs FETs as well as related devices, such as HEMT [9-10] (High Electron Mobility Transistor). We also examined systems such as monolithic oscillators and amplifiers.

Experiment

A visible CW ring dye laser and stabilized HeNe laser were selected as light sources based on their absorption coefficient for higher carrier generation [11], shallower light penetration for lower backgating and trap effects [4], and lower carrier concentration fluctuation (CW illumination) for lower capacitance effects [12]. The penetration depth of these lasers is about 0.3 μm , which is the same order as the thickness of active region of the FETs (0.2 μm thick n-GaAs on 2 μm thick undoped GaAs buffer layer) and sufficient to illuminate the GaAs and 2D electron gas region of HEMT structures. (0.04 μm thick n-AlGaAs on 1 μm thick undoped GaAs layer). Figure 1 shows the experimental arrangement used in all these measurements. The devices under investigation were illuminated with light obtained by coherent mixing of between two lasers: a frequency stabilized He-Ne laser (632.8 nm) and a Coherent Model 699-21 ring dye laser. The wavelength of the ring dye laser, monitored by a Burleigh WA-20 wavemeter (accurate to 0.001 nm), can be continuously tuned to any value within the dye emission spectrum. For Kiton 620 dye (600 - 640 nm), the tuning range is more than 50 nm around the HeNe line. Consequently the beat frequency (difference of light frequency / optical i.f. signals) of two CW lasers can be easily varied from zero to several hundred GHz. The laser power density on the samples was kept to approximately 10 mW/cm² for the HeNe laser and 1 W/cm² for the dye laser with the linewidth and stability in the sub MHz range.

THE samples were FETs (commercial products from Dexcel, Hughes, NEC etc.) or HEMT'S (from Rockwell, TRW etc.) directly mounted onto a fixture with 50 ohm microstrip lines. The monolithic oscillators and multiple stage amplifiers used in this study were basically composed of GaAs FETs and impedance matching circuits, mounted in appropriated fixtures. HP 8569B and Tektronix 492P spectrum analyzers were used to monitor the outputs. Illuminating the active region of the samples with two coherent CW lasers resulted in the generation of rf electrical signals at the optical beat frequency in these devices. The experiments we examined involve three basic processes: amplification of the injected rf signal, optical injection locking, and frequency tuning by controlling the sample's carrier concentrations.

A. Amplification of the injected rf signals

Although this CW method has considerable advantages over using diode lasers, it makes severe requirements on the lasers. In order to generate optical rf beat frequencies, the wavelength of the dye laser (the resolution of tuning is about the linewidth of laser) must be very close to the wavelength of HeNe laser. To generate a 7.5 GHz optical beat frequency, for example, corresponds to tuning a 0.01 nm wavelength difference between two lasers. Using the FET, we can directly observed the optical beat frequency up to 18 GHz , which was limited by the impedance matching between the device and fixture. Therefore to detect higher frequency optical beat signals, we have superimposed an electrical rf signal on the gate of the FET. As a result of the strong non-linearity of GaAs FET, the electrical signal mixes with the rf signal produced by optical beating, and produces a secondary beat signal. A 30 dB gain rf amplifier (1-3 GHz) was inserted between the FET and spectrum analyzer and HP 8350A sweep generator supplied rf signal power to 40 GHz. Observing the secondary beat signal at 2.6 GHz, therefore permits accurate measurements of the mixing signal up to 42.6 GHz. Beyond this frequency, we used the secondary harmonics of electrical rf signal to obtain optical beat signals up to 52 GHz. Similar mixing techniques have used electrical rf signals to beat optically injected signal from directly modulated semiconductor lasers at lower frequencies [13].

This method provided the means of directly generating rf signals at millimeter frequencies by laser mixing and in addition permitted us to accurately monitor the frequency of our optically generated broadband rf signals. Therefore this system, with a commercial FET, was used in all our measurements giving us a resolution on the order of Kilocycles. As a example of how we used this system to directly observe optical beat signals in Ka band with a monolithic two stage GaAs FET amplifier having 16 dB gain at 32 GHz, fabricated by Hughes Aircraft Company. The active region of the FET at the first stage was illuminated with the mixing light at beat frequency around 32 GHz. The generated rf signal was further amplified through second stage and we observed, as shown in Fig. 2, a -60 dBm (S/N is around 12 - 15 dB) signal. We anticipated better output power with optimized optical access, however, this experiment shows the potential of this technique in distributing power optically to arrays etc. Furthermore, this technique can be used to measure the gain bandwidth of amplifier efficiently.

B. Injection Locking

The device used for injection locking was originally designed to be a monolithic three stage GaAs FET amplifier, by Rockwell, with 20 dB gain between 17 to 21 GHz. By introducing feedback to this common source configuration device, it was made into an broadband oscillator at 17.8 GHz with 15 dbm power output (Q factor was approximately 20). The dc bias levels were as follows: all three stages, drain to source voltage (V_d) were biased at 3.0 V, $V_{g1} = 0$ and $V_{g2} = V_{g3} = -0.5$ V, where V_{gn} represents the gate bias at nth stage. This oscillator can be electrically injection locked by applying a -10 dBm rf signal to the input (first gate) with a locking range was about 40 MHz. To offset the photovoltaic voltage introduced by laser illumination [2], we applied more negative bias to the illuminated gate, $V_{g2} = -2.0$ V, and reduced drain to source voltages $V_{d1} = V_{d2} = 2.3$ V to bias the oscillator below the threshold of oscillation, as shown in Fig. 3 (a). The oscillation was optically turned on, as shown in Fig. 3(b), when the second FET was illuminated. Finally, when the optical beat frequency approached the free run frequency of the oscillator, the signal was locked as shown in Fig. 3(c). The locking range was only about 2 MHz. We attribute the narrow locking range to the optical tuning discussed in the next section. Increasing the power actually tunes the devices and therefore reduce the efficiency of frequency lock.

C. Frequency tuning

Optical frequency tuning using a single laser has been related to capacitance changes, due to optically excited electron-hole pairs. Common-source mode oscillators have found to have an optical-frequency sensitivity approximately 5 times higher than common-drain mode configuration at oscillation frequencies between 4 - 9 GHz [12]. In our experiment, we used a Ka-band (at 40 GHz) GaAs FET oscillator with a common gate configuration. In this configuration, we examined the relative optical sensitivity of frequency tuning of Cgs (with the drain shorted to gate) vs Cds (with the source shorted to gate). A 480 MHz vs 80 MHz (Fig. 4 (a)-(b)) frequency increase was observed with light intensities of about 1 W/cm² (only the dye laser was used with attenuators), which was in agreement with previous result in X band. Using higher illumination density, we have demonstrated 12% optical-frequency tuning in Ka band. Along with the oscillation frequency shift, we have also observed controllable variations in output power.

Result and Discussion

Due to the observation of acoustic noise introduced by light scattering below S band [14] and the difficulty to characterize secondary beating signal (beyond 18 GHz) by current setup, our major characterizations were in S band through Ku band (2 - 18 GHz). Fig. 5 shows the frequency response of optical mixing from 6 GHz to 18 GHz. The response of this 0.25 μ m device is relative flat and indicates by its voltage

dependance that the mechanism is primary photoconductive. From the above observations, we find that under intensive illumination and high photoexcited carrier concentration (photoexcited current was the same magnitude as intrinsic current) the Schottky gate might become unnecessary. This result is in agreement with non-gate high speed photodetectors which responding to picosecond light signals [15,16].

Since the photoconductive mechanism dominates, HEMT structures significantly improve the frequency performance only if properly designed and utilized. The undoped GaAs layer in such devices where the photoexcited carriers are generated reduce the impurity scattering and increase the mobility of carriers. However, the parasitic AlGaAs layer can reduce this advantage , especially if the illumination is absorbed heavily near the surface. The high doping concentration of AlGaAs results in a high trap concentration and low mobility [17]. To take full advantage of HEMT structure, AlGaAs layers with large energy gaps (such as obtained by increasing the Al content) should be fabricated. Then the carriers can be generated in the GaAs near the two dimensional electron gas (2 DEG) channel ("window effect") and shorter electron transit times will be obtained. Preliminary measurements on HEMTs with relatively large gate drain spacings have been relatively encouraging.

Conclusion

By using laser mixing techniques, we have extended direct optical control of FETs, related devices and systems from X band to Ka band. Infrared semiconductor lasers with wavelength stablization and tunability by temperature, cavity and current control) [6] can now be used to replace CW dye and HeNe lasers as light sources for realization of compactness. Specially design structures, such as HEMTs with tailored AlGaAs layers can be incorporated with the optimized lasers to form unique, optically controlled, systems working well into millimeter wave frequency.

Acknowledgement

We acknowledge this work is supported by the Air Force Office of Scientific Research.

References

1. J. P. Noad, E. H. Hara, R. H. Hum, R.I. MacDonald, IEEE Trans. Electron. Devices, ED-29, 1792 (1982).
2. A. A. de Salles, IEEE Trans. Microwave Theory Tech, MTT-31, 812 (1983)
3. J. L. Gautier, D. Pasquet, P. Pouvil, IEEE Trans. Microwave Tech, MTT-33, 819 (1985)
4. G. J. Papaionanou, J. R. Forrest, IEEE Trans. Electron. Devices, ED-33, 373 (1986).
5. R. B. Darling, J. P. Uyemura, IEEE J. Quantum Electron., QE-23, 1160 (1987)
6. L. Goldberg, H. F. Taylor, J. F. Weller, Electorn. Lett. Vol 19, No 13, 491 (1983)
7. A. S. Daryoush, P. R. Herczfled, Z. Turski, P. Wahi, IEEE Trans. Microwave Theory Tech., MTT-34, 1363 (1986)
8. P. Herczfled, A. S. Daryoush, A. Rosen, A. Sharma, V. M. Contarino, IEEE Trans. Microwave Theory Tech., MTT-34, 1371 (1986)
9. C. Y. Chen, A. Y. Cho, C. G. Bethea, P. A. Garbinski, Y. M. Pang, B. F. Levine, K. Ogawa, Appl. Phys. Lett., 42, 1040 (1983)
10. R. N. Simons, K. B. Bhasin, IEEE Trans. Microwave Theory Tech., MTT-34, 1349 (1986)
11. H. Mizuno, IEEE Trans Microwave Theory Tech., MTT-31, 576 (1983)
12. H. J. Sun, R. J. Gutmann, J. M. Borrego, Solid St. Electron., Vol 24, 935 (1981)
13. D. K. W. Lam, R. I. MacDonald, IEEE Trans. Electron. Device, ED-31, 1766 (1984)
14. David Ni, Harold R. Fetterman, submitted for publication
15. S. Y. Wang, D. M. Bloom, Electron. Lett. Vol. 19, No. 14, 554 (1983)
16. S. Y. Wang, D. M. Bloom, D. M. Collins, Appl. Phys. Lett. 42, 190 (1983)
17. A. Kastalsky, J. C. M. Huang, Solid St. Commumnication, Vol 15, No. 5, 317 (1984)

OPTICAL MIXING AT MILLIMETER IF's

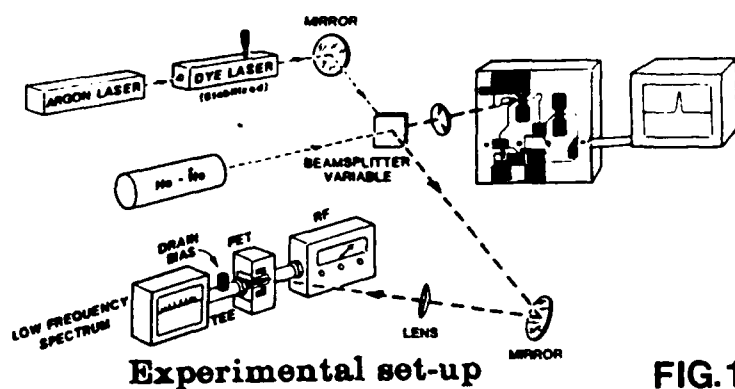


FIG.1

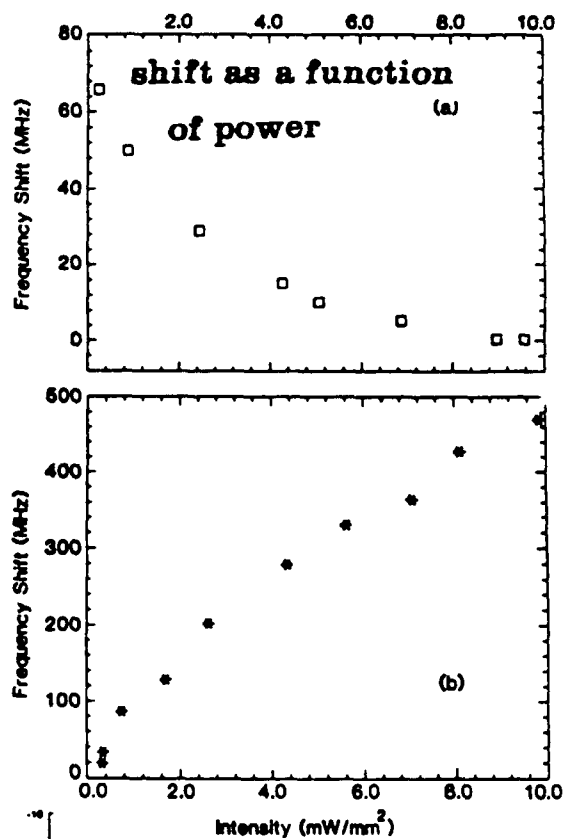


FIG.4

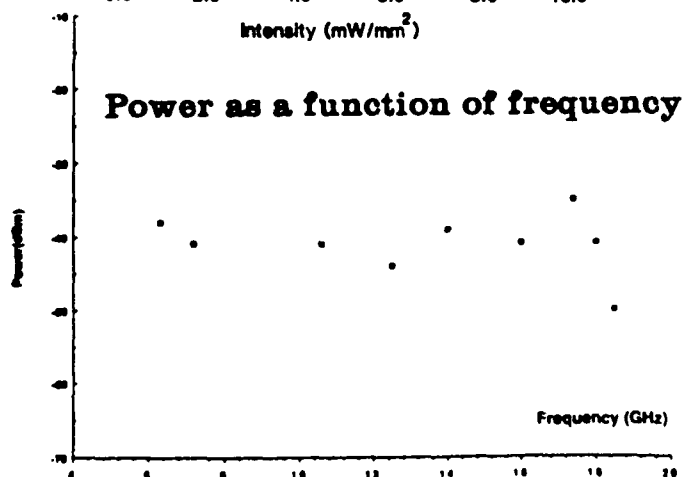


FIG.5

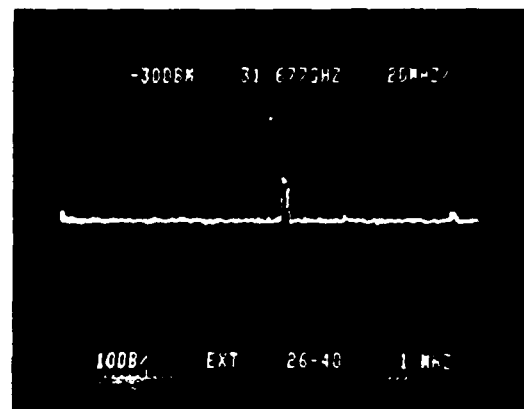


FIG.2

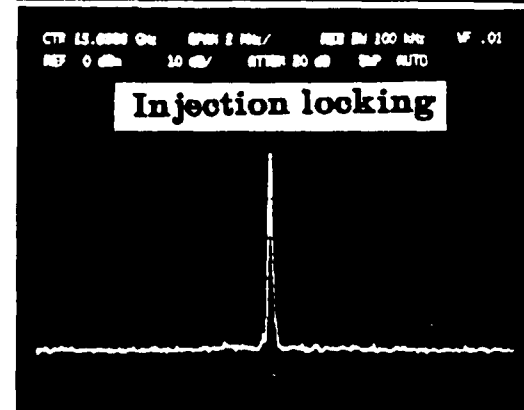
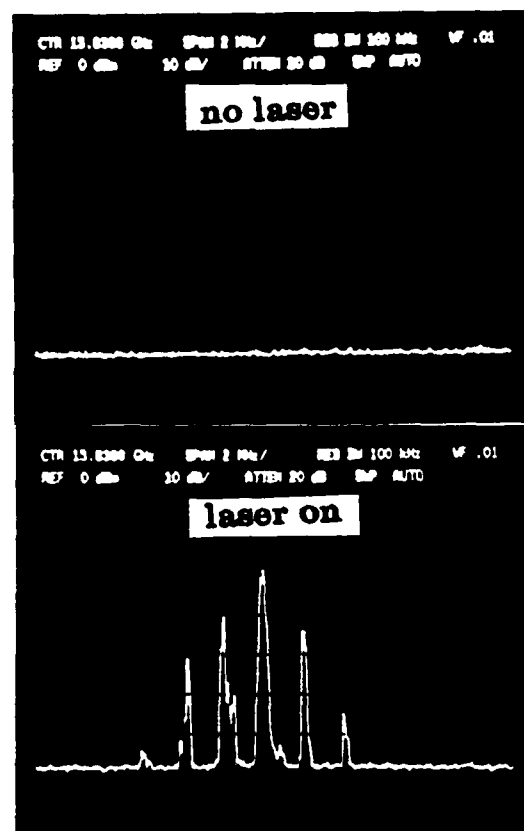


FIG.3

TABLE I Summary of the MESFET Parameters at $V_{gs} = 4.0$ V. V_b is the Potential Barrier. I_d is the Drain Current at $V_g = 0.0$ V. The Small-Signal Parameters, Transconductance (g_m), Gate-to-Source Capacitance (C_{gs}), Drain Conductance (g_d), and the Current-Gain Cutoff Frequency (f_t) are Given at $V_g = -0.25$ V

	N_d (cm^{-3})	V_b (V)	I_d (mA/mm)	g_m (mS/mm)	C_{gs} (pF/mm)	g_d (mS/mm)	f_t (GHz)
MESFET on <i>P</i> -substrate	10^{16}	1.23	221	229.8	0.79	18	46.3
	2.5×10^{16}	1.25	197	232.5	0.785	16	47.1
	5×10^{16}	1.27	74.5	207	0.67	9	49.2
MESFET on thin <i>P</i> -layer	5×10^{16}	0.3	356	206	0.80	14	41.0
	10^{16}	0.55	319.5	221	0.81	14	43.4
	1.5×10^{16}	0.9	280	228.5	0.81	13	44.9

drain current reduction is substantial. Moreover, it should be noted that the electrons can be confined into the active layer using a much smaller potential barrier. This suggests that introducing a thin *P*-layer between the MESFET active layer and the semiinsulating substrate can be very beneficial if the thickness of this layer is chosen so small that the *P*-layer becomes fully depleted. In this case, the height of the potential barrier and the active-layer depletion can be controlled by changing the depth of the *P*-layer or its doping or both.

III. MESFET ON A THIN *P*-LAYER

To examine the effectiveness of the thin *P*-layer approach, three MESFET structures were simulated. All of them have the same active-layer parameters as the previous MESFET on a *P*-substrate. The *P*-layer thickness is chosen such that dopings of 5×10^{15} , 10^{16} , and $1.5 \times 10^{16} \text{ cm}^{-3}$ result in a maximum potential barrier of 0.3, 0.5, and 0.9 V, respectively. The carrier-concentration contour plots for the case $N_a = 10^{16} \text{ cm}^{-3}$ and at $V_g = 0.0$ V, $V_{ds} = 50$ V, are shown in Figure 2(b). It is observed that there is a smaller depletion in the active layer compared to Figure 2(a). The stationary domain extends slightly more inside the *P*-layer. Moreover, the carrier concentration in the channel under the gate is $0.4 < n/N_d < 0.5$ while it is $0.3 < n/N_d < 0.4$ in the MESFET on a *P*-substrate. The *I*-*V* characteristics of the three MESFETs are shown in Figure 3, set B. The drain current shows a dramatic increase compared to the MESFET on a *P*-substrate. In the $N_d = 10^{16} \text{ cm}^{-3}$ case, the device on a thin *P*-layer shows a current increase of about 98 mA/mm over the corresponding device on a *P*-substrate.

A brief comparison of the main small-signal parameters is given in Table I. Before speculating on the behaviour of these parameters, one should notice that increasing the potential barrier between the active layer and the substrate results in two counterbalancing effects simultaneously. First, it increases the carrier's confinement to the active layer; therefore, higher transconductance and lower drain conductance are expected. Second, it reduces the dynamic range of the device, which means that the MESFET becomes closer to pinch-off. Hence, lower transconductance is expected. The drain conductance increases since the device approaches the space-charge limited current mode.

IV. CONCLUSION

Three MESFETs on *P*-substrate of different acceptor dopings are simulated. It is shown that the resulting potential barrier between the active layer and the substrate greatly reduces the carrier injection from the active layer. Increasing the doping of the *P*-substrate leads to a more depletion in the active layer

and, of course, a lower drain current. For MESFET with a thin active layer, it is advised to use a thin *P*-layer between the SI substrate and the *N* active layer. The *P*-layer should be so thin that it becomes fully depleted. The height of the potential barrier should be chosen such that it is capable of producing a good carrier confinement without too much depletion in the active layer. It can be adjusted by controlling either the thickness or the doping of the *P*-layer or both.

ACKNOWLEDGMENT

This work was supported by the U.S. Army Research Office under contract DAAG-29-84-k-0076.

REFERENCES

1. S. El-Ghazaly, T. Itoh, and G. Salmer, "Optimization of the *P* Substrate Doping for the *N* Channel GaAs Submicronic-Gate MESFET," National Radio Science Meeting, Boulder, Colorado, 1988.
2. C. Lee, S. Lee, and B. Welch, "Carrier Injection and Backgating Effects in GaAs MESFETs," *IEEE Trans. ED Letters*, Vol. EDL-3, no. 4, 1982, pp. 97-98.
3. G. Salmer et al., "Substrate Effects in Submicronic Gate Low Noise GaAs MESFETs," *Gallium Arsenide and Related Compounds, Inst. Phys. Conf. Ser. No. 74*, 1984, pp. 503-507.
4. T. Enoki et al., "0.3- μm Advanced SAINT FET's Having Asymmetric n^+ -Layers for Ultra-High-Frequency GaAs MMIC's," *IEEE Trans. ED*, Vol. ED-35, no. 1, 1988, pp. 18-24.
5. S. El-Ghazaly and T. Itoh, "Two Dimensional Numerical Simulation of Short-Gate-Length GaAs MESFET's and Application to Study the Traveling Gunn Domain Phenomenon," *International Journal of Numerical Modeling*, Vol. 1, no. 1, 1988, to be published.

Received 12-18-87

Microwave and Optical Technology Letters, 1/1, 32-34
© 1988 John Wiley & Sons, Inc.
CCC 0895-2477/88/\$4.00

CONTROL OF MILLIMETER WAVE DEVICES BY OPTICAL MIXING

Harold R. Fetterman and David. C. Ni
Department of Electrical Engineering
University of California, Los Angeles
Los Angeles, California 90024

KEY TERMS

Microwave-optical devices, optical mixing, dye lasers, FETs, HEMTs

ABSTRACT

Coherent mixing of optical radiation from a tunable CW dye laser and a stabilized HeNe laser was used to generate broadband microwave signals beyond the Ka band in FETs, HEMTs, and the related devices. Comparing with direct modulation of the light signal, this technique enhances photoconductivity and frequency stability.

I. INTRODUCTION

Optical control of millimeter wave devices has attracted recent attention because of its potential applications in signal synchronization and distributed control of the communication and radar system. Current effort has been devoted toward dealing with overcoming the frequency constraints of both the light sources and detectors. Nonlinearities of semiconductor lasers, optic fibers, pin diodes, and FETs have been utilized extensively to side-band lock or to generate harmonics for multiplication of master oscillation signals [1-3]. In these approaches, reliability and FM noise degradation issues require significant engineering effort since the devices operating in the nonlinear region are normally under significant bias stress. Other effort has been focused on the transport mechanisms of the photoexcited carriers. Several studies on the frequency response of the detectors have indicated the fast photoconductivity mechanism should be used while the slow photovoltaic mechanism should be suppressed or even avoided, and the detectors under higher illumination with conditionally higher bias will result in better transient performance [4-9].

When examining the traditional techniques of modulating semiconductor lasers to optically control FETs, one will realize that the Schottky junction and the interface area between the active and buffer area of FETs react photovoltaically to the light signal because of the capacitance, trap, and backgating effects, and thus inevitably will consider nonlinearities of these devices to overcome the frequency barrier. While using the laser mixing technique as a new approach, we were able to inject millimeter wave signals into several extremely short-gate FETs, heterostructure HEMTs, monolithic amplifiers, and oscillators [10]. We also observed an interesting phenomenon, negative photoconductivity, in HEMTs during the characterization process [11].

In this letter, first we examine the frequency tuning induced by the variation of light intensity and negative photoconductivity induced by the variation of light wavelength. These phenomena have negative impacts on the frequency stability of the optical control of the millimeter wave devices. Second, we characterize the laser mixing technique by examining power dependence of the generated microwave signals on gate bias and frequency to verify that photoconductivity is the dominating mechanism in the devices. Then we demonstrate signal injection and locking up to the Ka band. Third, we discuss the concerned mechanisms of the devices and optimization of a system constructed by HEMTs and controlled by laser mixing techniques.

II. EXPERIMENT

The devices under investigation were illuminated with light (1) from a CW laser or a monochromator with a tungsten bulb as the light source; (2) obtained by coherent mixing between two lasers: a frequency stabilized HeNe laser (632.8 nm) and a Coherent model 699-21 ring dye laser, as shown in Figure 1. These lasers were selected because of (1) generating higher carrier concentration due to shorter wavelengths [12] and suppressing the capacitance effect of the Schottky junction, (2)

penetrating shallower into GaAs for reducing the backgating and trap effects [7], and (3) lowering carrier fluctuation by CW illumination for reducing the capacitance effects [13]. The penetration depth of these lasers is about 0.3 μm , which is the same order as the thickness of the active region of the FETs and sufficient to illuminate the GaAs and two-dimensional electron gas region of HEMT structures.

The wavelength of the ring dye laser, monitored by a Burleigh WA-20 wavemeter (accurate to 0.001 nm) can be continuously tuned to any value within the dye emission spectrum. For Kiton 620 dye (600-640 nm), the tuning range is more than 50 nm around the HeNe line. Consequently the best frequency (difference of light frequency/optical i.f. signals) of two CW lasers can be easily varied from zero to several hundred GHz. The laser power density on the samples was kept to approximately 10 mW/cm² for the HeNe laser and 1 W/cm² for the dye laser with the linewidth and stability in the sub MHz range.

The samples were FETs (commercial products for Dexcel, Hughes, NEC, etc.) or HEMTs (from Rockwell, TRW, etc.) directly mounted onto a fixture with 50 Ω microstrips. The monolithic oscillators and multiple stage amplifiers used in this study were basically composed of GaAs FETs and impedance matching circuits, mounted in appropriate fixtures. Used as the photoconductors, these devices have extremely short gate length (less than 0.3 μm) and drain-source distance, and can be applied to rather high bias voltage.

A. Frequency Tuning and Negative Photoconductivity. Optical frequency tuning using a single laser has been related to capacitance changes, due to optically excited electron-hole pairs. Common-source mode oscillators have been found to have an optical-frequency sensitivity approximately 5 times higher than common-drain mode configurations at oscillation frequencies between 4-9 GHz [13]. In our experiment, we used a Ka-band (at 40 GHz) GaAs FET oscillator with a common-gate configuration. In this configuration, we examined the relative optical sensitivity of frequency tuning of C_g (with the drain shorted to gate) vs. C_{ds} (with the source shorted to gate). A 480 vs. 80 MHz [Figure 2(a), (b)] frequency increase was observed with light intensities of about 1 W/cm² (only the dye laser was used with attenuators), which was in agreement with previous results in the X band. Using higher illumination density, we have observed 12% frequency tuning in the Ka band. This frequency tuning is useful, but it also creates frequency-shift problems when a high-intensity ac light signal, such as from a modulated semiconductor laser, is injected into the devices.

As reported previously [11], negative photoconductivity in HEMTs was initially observed under the illumination of a broadband tungsten bulb. Depending on the bias conditions, the phenomenon was also observed at different wavelengths and was especially sensitive to the light with photon energy just below the energy gap of GaAs. The I - V characteristics and spectral responses are shown in Figure 3(a), (b) [14]. This phenomenon has potential applications but is not desirable when frequency stability turns out more important. To prevent this phenomenon, the devices have to be carefully biased. But if the frequency instability is generated at the light source under high-amplitude modulation, such as the mode hopping of the semiconductor laser, the situation will be complicated.

B. Amplification of the Injected rf Signals and Injection Locking. Although this CW method has considerable advantages

OPTICAL MIXING AT MILLIMETER IF's

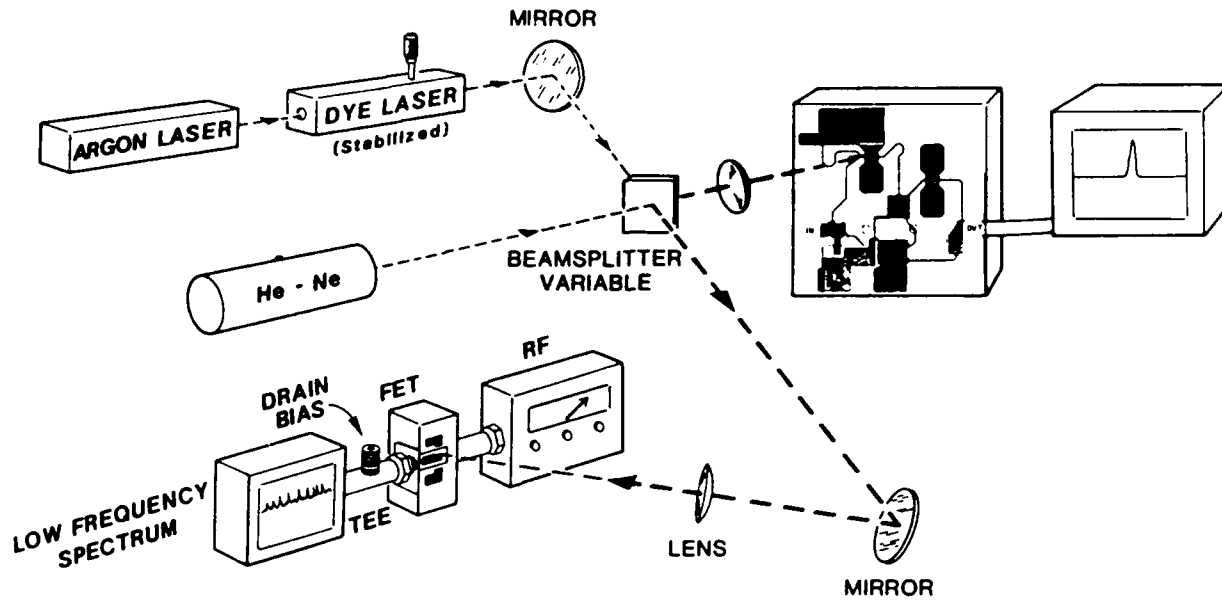


Figure 1 Experimental setup

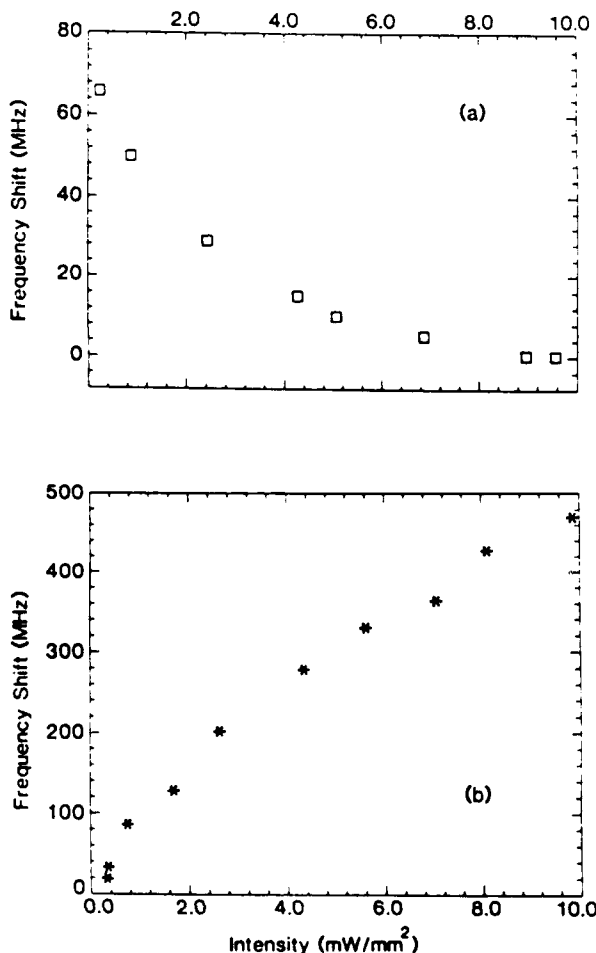


Figure 2 Frequency shift vs. power (a) Common drain gate; (b) common source gate

over using diode lasers based on the preceding discussions, it makes severe requirements on the lasers. In order to generate optical rf beat frequencies, the wavelength of the dye laser (the resolution of tuning is about the linewidth of the laser) must be very close to the wavelength of the HeNe laser. To generate a 7.5-GHz optical beat frequency, for example, corresponds to tuning a 0.01-nm wavelength difference between two lasers. Using the FET, we can directly observe the optical beat frequency up to 18 GHz, which was limited by the impedance matching between the device and the fixture. Therefore, to detect higher-frequency optical beat signals, we have superimposed an electrical rf signal on the gate of the FET. As a result of the strong nonlinearity of the GaAs FET, the electrical signal mixes with the rf signal produced by optical beating and produces a secondary beat signal. A 30-dB gain rf amplifier (1–3 GHz) was inserted between the FET and the spectrum analyzer and an HP 8350A sweep generator supplied rf signal power to 40 GHz. Observing the secondary beat signal at 2.6 GHz, therefore permits accurate measurements of the mixing signal up to 42.6 GHz. Beyond this frequency, we used the secondary harmonics of the electrical rf signal to obtain optical beat signals up to 52 GHz. Similar mixing techniques have used electrical rf signals to beat optically injected signals from directly modulated semiconductor lasers at lower frequencies [15].

This method provided the means of directly generating rf signals at millimeter frequencies by laser mixing and, in addition, permitted us to accurately monitor the frequency of our optically generated broadband rf signals. Therefore, this system, with a commercial FET, was used in all our measurements, giving us a resolution on the order of kilocycles. Direct observation of optical beat signals in the Ku band was also made with a monolithic two stage GaAs FET amplifier having 16-dB gain at 32 GHz, fabricated by Hughes Aircraft Company. The active region of the FET at the first stage was

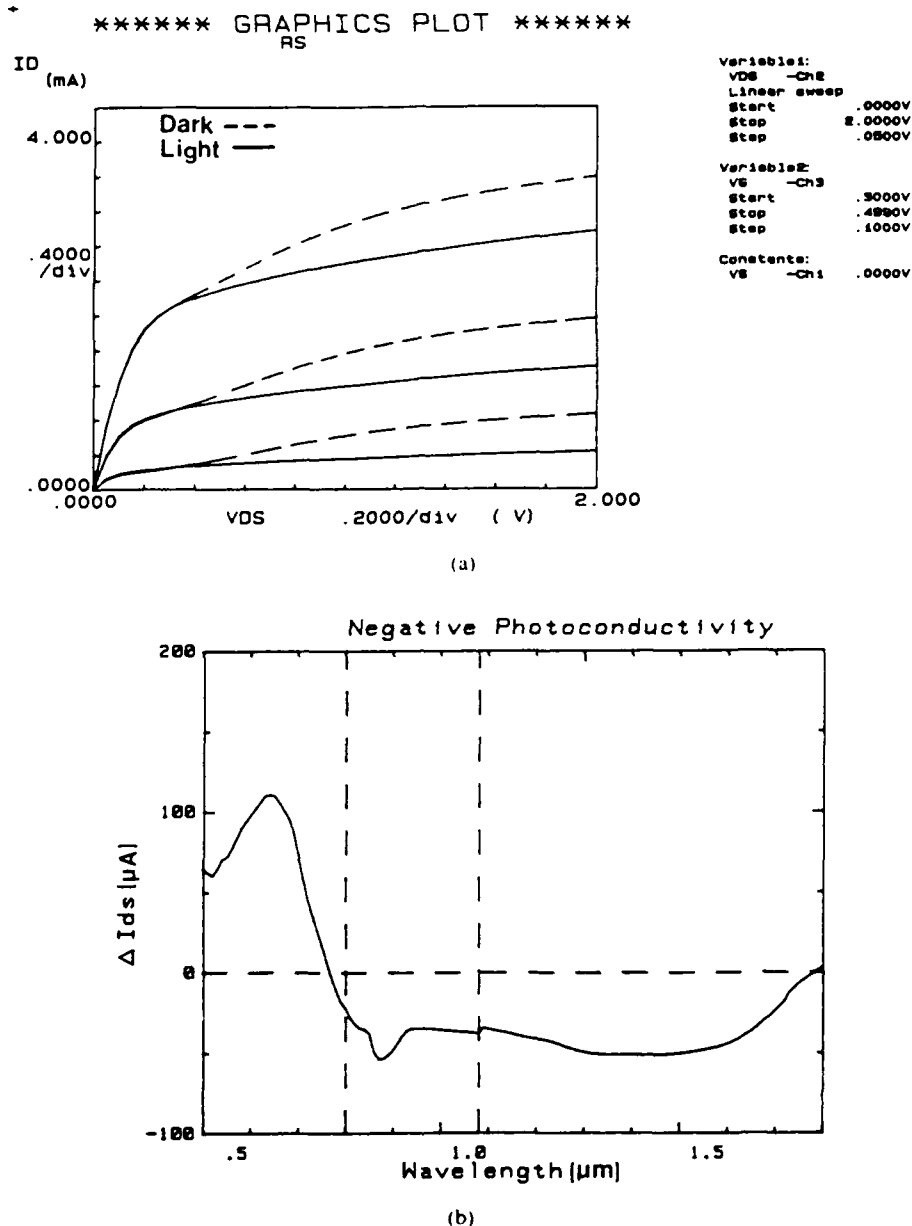


Figure 3 Negative photoconductivity at room temperature. (a) I - V characteristics; (b) spectral response

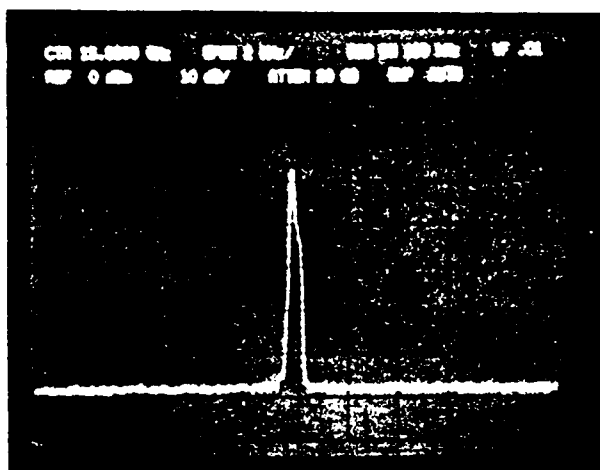
illuminated with the mixing light at a beat frequency around 32 GHz. The generated rf signal was further amplified through a second stage and we observed a -60-dB m (S/N around 12-15 dB) signal. We anticipated better output power with optimized optical access; however, this experiment shows the potential of this technique in distributing power optically to arrays, etc. Furthermore, this technique can be used to measure the gain bandwidth of the amplifier efficiently.

The device used for injection locking was originally designed (by Rockwell) to be a monolithic three stage GaAs FET amplifier with 20-dB gain between 17-21 GHz. By introducing feedback to this common-source configuration device, it was made into a broadband oscillator at 17.8 GHz with 15-dB m power output (Q factor approximately 20). The dc bias levels were as follows: All three stages, drain to source voltage (V_{ds}) was biased at 3.0 V, $V_{g1} = 0$ and $V_{g2} = V_{g3} = -0.5$ V, where V_{gn} represents the gate bias at the n th stage. This oscillator can be electrically injection locked by applying

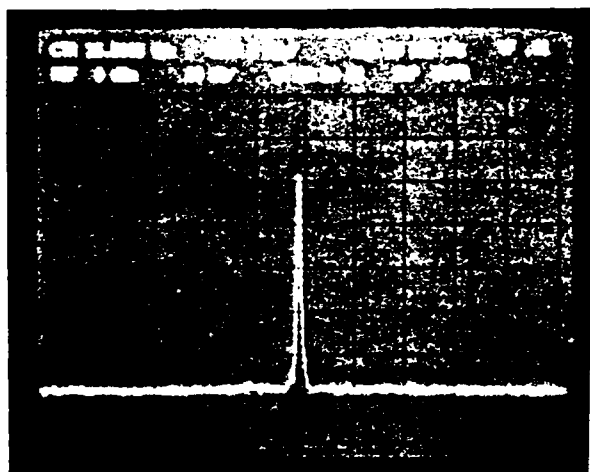
and -10-dB m rf signal to the input (first gate) with a locking range about 40 MHz. To offset the photovoltaic voltage introduced by laser illumination [2], we applied more negative bias to the illuminated gate ($V_{g2} = -2.0$ V) and reduced drain to source voltages $V_{d1} = V_{d2} = 2.3$ V to bias the oscillator below the threshold of oscillation. The oscillation was optically turned on, as shown in Figure 4(a), when the second FET was illuminated. Finally, when the optical beat frequency approached the free run frequency of the oscillator, the signal was locked as shown in Figure 4(b). The locking range was only about 2 MHz. We attribute the narrow locking range to the frequency tuning. Increasing the power actually tunes the devices and therefore reduces the efficiency of frequency lock.

III. RESULT AND DISCUSSION

Due to the observation of acoustic phonons introduced by light scattering below the S band [16] and the difficulty of



a



b

Figure 4 Inject locking. (a) Laser on; (b) locking

characterizing the secondary beating signal beyond 18 GHz by the current setup, our major characterizations were in the *S* through *Ku* band (2–18 GHz). Figure 5 shows the frequency response of optical mixing from 6–18 GHz. The response of this 0.25- μm device is relatively flat and indicates by its voltage dependence that the mechanism is primarily photoconductive. Figure 6 shows the output power vs. gate bias V_g at beat frequency 2.4 GHz. The pinchoff voltage of this particular device was -1.0 V. Under illumination, we observed rather flat output power to $V_g = 2.2$ V. From the preceding observations, the Schottky gate becomes redundant when high photoexcited carrier concentration is generated. The change of built-in voltage ΔV_{bi} of the Schottky barrier is given as

$$\Delta V_{bi} = \frac{KT}{q} \ln \left(1 + \frac{p_i}{p_n} \right) \approx \frac{KT}{q} \ln \frac{p_i}{p_n} \quad \text{when } p_i \gg p_n \quad (1)$$

where p_i and p_n stand for the photoexcited and dark hole concentrations, respectively. By monitoring the photogenerated current and photon flux, we estimate ΔV_{bi} about 1.2 V, which is in agreement with the observed data. This result is encouraging because the extra gate control does not sacrifice the potential usage of this device as a nongate picosecond photodetector [17, 18].

Since the photoconductive mechanism dominates, HEMT structures significantly improve the frequency performance if properly designed and utilized. The optimized gain of a photoconductive device can be written as [8]

$$\text{gain} = \frac{1}{2} \left(1 + \frac{\mu_n}{\mu_p} \right) \quad (2)$$

where μ_n and μ_p stand for the electron and hole mobilities, respectively. The undoped GaAs layer in such devices where the photoexcited carriers are generated reduces the impurity scattering and increases the mobility of carriers. However, the

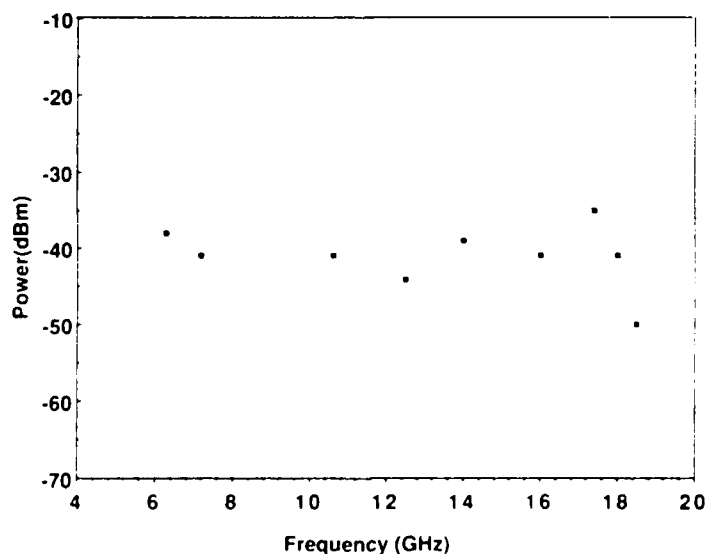


Figure 5 Power as a function of frequency from 6–18 GHz

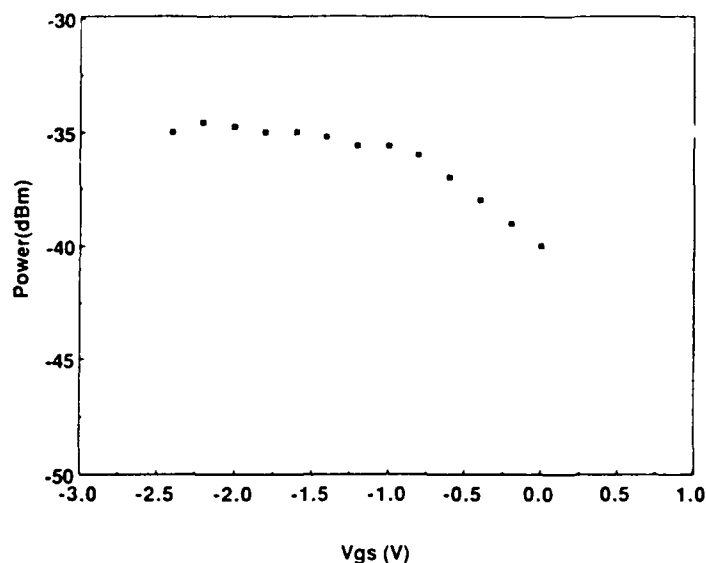


Figure 6 Power vs. V_{gs} at 2.4 GHz

parasitic AlGaAs layer can reduce this advantage, especially if the illumination is absorbed heavily near the surface. The high doping concentration of AlGaAs results in a high trap concentration and low mobility [19]. To take full advantage of HEMT structure, AlGaAs layers with larger energy gaps (such as obtained by increasing the Al content) and lower doping concentration (which is well compensated by the photoexcited carrier) should be fabricated. Thus photoexcited carriers can be generated in the GaAs near the two-dimensional electron gas (2DEG) channel and shorter electron transit times will be obtained. The mobility of the electron is further increased by the lower doping concentration in the AlGaAs layer and gain is increased. The other consideration is to reduce the influence of low-mobility holes by the hole sink configuration [20].

IV. CONCLUSION

Using the photoconductivity-enhanced laser mixing techniques, we have reduced the influence of the drawback effects and extended direct optical control of the devices and systems from the X band to the Ka band. Semiconductor lasers with wavelength stabilization and tunability by temperature, external cavity, and current control [1] can be used to replace CW dye and HeNe lasers as light sources for realization of compactness. Specially designed structures, especially HEMTs with tailored AlGaAs layers and minority-carrier-sink configuration can be incorporated with the optimized lasers to form optically controlled systems working well into the millimeter wave frequency.

ACKNOWLEDGMENT

This work is supported by the Air Force Office of Scientific Research.

REFERENCES

1. L. Goldberg, H. F. Taylor, and J. F. Weller, *Electron. Lett.*, Vol. 19, No. 13, 1983, p. 491.
2. A. S. Daryoush, P. R. Herczfeld, Z. Turski, and P. Wahi, *IEEE Trans. Microwave Theory Tech.*, Vol. MTT-34, 1986, p. 1363.
3. P. Herczfeld, A. S. Daryoush, A. Rosen, A. Sharma, and V. M. Contarino, *IEEE Trans. Microwave Theory Tech.*, Vol. MTT-34, 1986, p. 1371.
4. J. P. Noad, E. H. Hara, R. H. Hum, and R. I. MacDonald, *IEEE Trans. Electron. Devices*, Vol. ED-29, 1982, p. 1792.
5. A. A. de Salles, *IEEE Trans. Microwave Theory Tech.*, Vol. MTT-31, 1983, p. 812.
6. J. L. Gautier, D. Pasquet, and P. Pouvil, *IEEE Trans. Microwave Theory Tech.*, Vol. MTT-33, 1985, p. 819.
7. G. J. Papaionanou and J. R. Forrest, *IEEE Trans. Electron. Devices*, Vol. ED-33, 1986, p. 373.
8. R. B. Darling and J. P. Uyemura, *IEEE J. Quantum Electron.*, Vol. QE-23, 1987, p. 1160.
9. A. E. Iverson and D. L. Smith, *IEEE Trans. Electron. Devices*, Vol. ED-34, 1987, p. 2098.
10. H. R. Fetterman, W. Y. Wu, and D. Ni, *Proc. of SPIE*, Vol. 789, 1987, p. 50.
11. C. S. Chang, H. R. Fetterman, and D. Ni, *Appl. Phys. Lett.* (in press).
12. H. Mizuno, *IEEE Trans. Microwave Theory Tech.*, Vol. MTT-31, 1983, p. 576.
13. H. J. Sun, R. J. Gutmann, and J. M. Borrego, *Solid State Electron.*, Vol. 24, 1981, p. 935.
14. D. Ni, H. R. Fetterman, and C. S. Chang, to be submitted.
15. D. K. W. Lam and R. I. MacDonald, *IEEE Trans. Electron. Devices*, Vol. ED-31, 1984, p. 1766.
16. D. Ni, H. R. Fetterman, and O. M. Stufdudd, submitted to *IEEE J. Quantum Electron.*
17. S. Y. Wang and D. M. Bloom, *Electron. Lett.*, Vol. 19, No. 14, 1983, p. 554.
18. S. Y. Wang, D. M. Bloom, and D. M. Collins, *Appl. Phys. Lett.*, Vol. 42, 1983, p. 190.
19. A. Kastalsky and J. C. M. Huang, *Solid State Communications*, Vol. 15, No. 5, 1984, p. 317.
20. C. Y. Chen, Y. M. Pang, A. Y. Cho, and P. A. Garbinski, *Appl. Phys. Lett.*, Vol. 43, 1983, p. 1115.

Received 12-21-87

Microwave and Optical Technology Letters, 1/1, 35-39
 © 1988 John Wiley & Sons, Inc.
 CCC 0895-2477/88/\$4.00

Printed Circuit Antennas with Integrated FET Detectors for Millimeter-Wave Quasi Optics

WILBERT CHEW AND HAROLD R. FETTERMAN, SENIOR MEMBER, IEEE

Abstract—Planar twin dipole microstrip antennas with integrated FET detectors have been constructed and found to provide antenna patterns suitable for millimeter-wave quasi-optical applications. The circuits are suitable as individual elements of an imaging array. A 63 GHz heterodyne mixer using such a circuit produced a system noise temperature of 7900 K.

I. INTRODUCTION

UTILIZATION of the millimeter-wave region demands the development of economical and practical techniques. Quasi-optical systems using unconfined beam propagation often become more practical than systems using very small waveguide components. Rapid improvements in FET's (field effect transistors) and printed circuit antennas are making them economical and effective components. FET's have demonstrated conversion gain and low noise as heterodyne mixers at lower frequencies [1]. FET detectors can be integrated with printed circuit antennas to take advantage of their qualities in millimeter-wave quasi-optical systems.

An attractive application of these circuits making use of the high resolution of millimeter waves is millimeter-wave imaging. Printed circuit antennas are the most economical way to provide enough antennas for an unscanned imaging array. In an imaging array, in contrast to the more conventional phased array, each array element operates independently and provides the signal for a separate picture element, or pixel. A large reflector or telescope can illuminate an entire quasi-optical array at once. Such an array can image a broad field of view, as optical systems can, without repositioning the telescope for each pixel. Each array element has its own feed antenna. The feed antenna need not have high gain, but should have low side lobes and a fairly symmetrical central lobe which can be efficiently covered by a conventional reflector.

A simple twin dipole antenna design inspired by previous millimeter-wave twin slot [2] and twin microstrip dipole [3], [4] designs can provide performance suitable for imaging and other quasi-optical systems. The antenna is printed

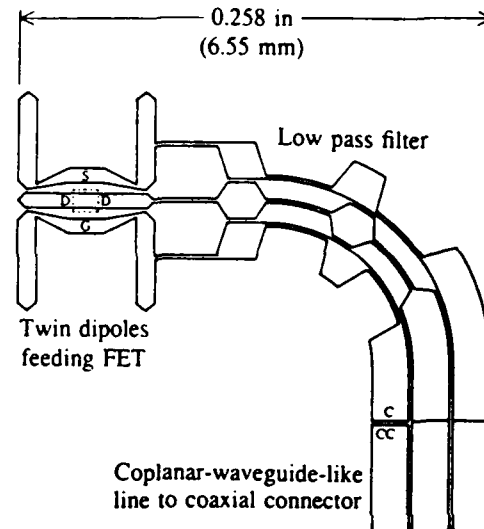


Fig. 1. Quasi-optical FET mixer/detector microstrip circuit for 0.011 in. (0.28 mm) thick PTFE/glass substrate. FET source, drain, and gate are wire-bonded to points S, D, and G. Gate bias chip capacitor is attached at point CC and wire-bonded to point C.

on one side of the substrate, along with IF (intermediate frequency) and bias lines in a single patterning step (e.g. Fig. 1). The detector FET is mounted on the surface between the twin full-wave dipoles. The FET will normally be used as a heterodyne mixer for sensitive detection. In this study, they also operated as video detectors for easily testing the antenna patterns. The essential nonlinearity used for either video detection or heterodyne mixing in a FET is the nonlinear drain current versus gate voltage characteristic, the slope of which is the gate-voltage-dependent transconductance. The FET mixer/detector is biased near the turn-on point, where the nonlinearity is greatest, unlike a FET amplifier. In either case, the lines away from the antenna need carry only dc bias voltages and IF or video signals, avoiding the difficulties of providing a low-loss millimeter-wave transmission line.

II. DESIGN

The microstrip circuit of Fig. 1 was designed as a FET gate mixer on a 0.011 in. (0.28 mm) thick glass-filled PTFE (polytetrafluoroethylene) substrate. Both RF (radio frequency) signal and LO (local oscillator) inputs are sent

Manuscript received May 27, 1988; revised October 3, 1988. This work was supported by TRW and the University of California through the University of California MICRO program and by the Air Force Office of Scientific Research.

The authors are with the Department of Electrical Engineering, University of California at Los Angeles, Los Angeles, CA 90024.

IEEE Log Number 8825391.

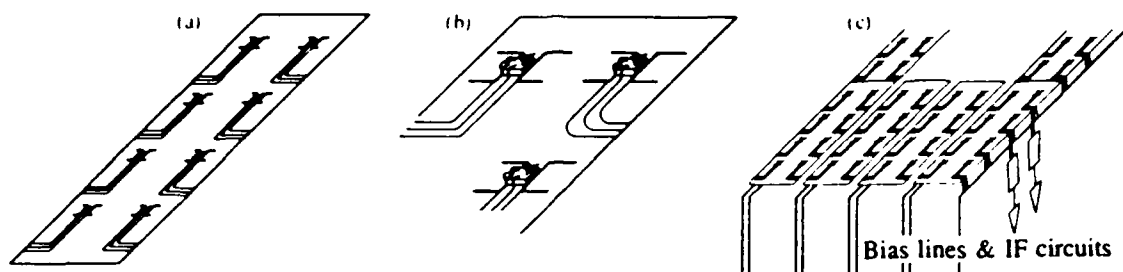


Fig. 2. Projected construction of a large two-dimensional imaging array using tested circuits. (a) Fabricate printed circuits. (b) Cement FETs to substrate and wire-bond FETs to circuits. (c) Assemble substrates to form focal-plane array and make connections to IF circuits.

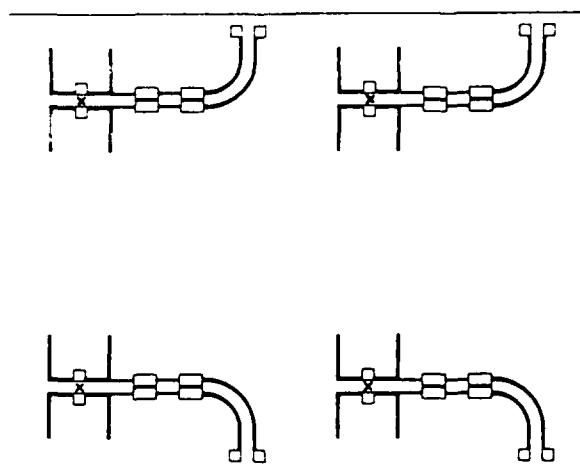


Fig. 3. Four-element building block for large imaging array. Microstrip circuits for beam-lead Schottky diodes. Diodes are placed at points marked X. Lines indicating edges of substrate are 0.400 in. (10.16 mm) apart. Substrate is 0.009 in. (0.23 mm) thick fused quartz.

through the antenna to the FET gate-source input. The FET is used to convert from the balanced dipole RF feed at its input to an unbalanced IF transmission line at the drain output. The IF transmission line is intended to work as coplanar waveguide backed by a lower ground plane [5], [6], with the lines used to bias the FET gate and source serving as the coplanar ground conductors and the line from the drain used as the center line of the coplanar waveguide. The IF/bias lines consist of cascaded quarter-wave sections for RF forming low-pass filters which present a low impedance for RF and LO at the FET output as desired for a gate mixer, but present high impedances to the dipoles to avoid disturbing the antenna performance. Effects of the IF at the FET input are minimized by operating the IF line in the coplanar waveguide mode and suppressing the balanced IF mode. The undesired balanced IF mode [6], in which the coplanar ground conductors take on opposing mode voltages instead of being at the same potential, would allow spurious low-frequency responses and IF noise. The IF ground conductor used to bias the FET gate is connected to the other ground conductors via a 100 pF chip capacitor.

Many ingenious and efficient quasi-optical mixers use too much area for a reasonably dense two-dimensional imaging array. The circuits here are compact enough to place detectors two free-space wavelengths apart in an

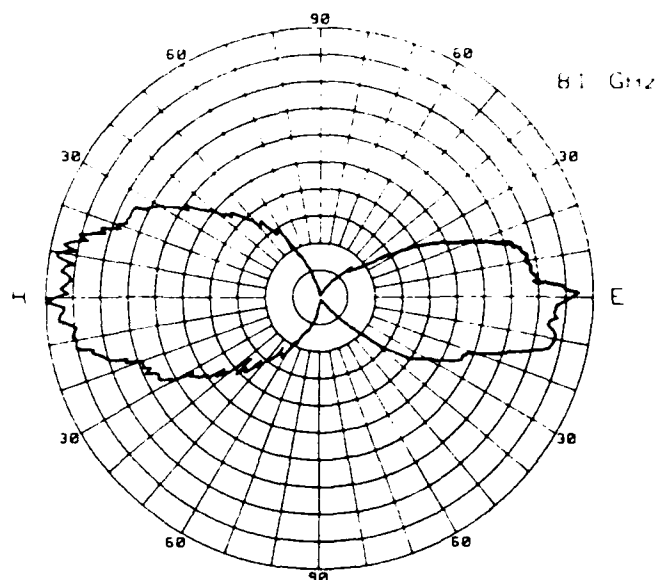


Fig. 4. Antenna pattern of twin microstrip dipoles with diodes. Video response at 81 GHz (linear voltage scale, arbitrary normalization) versus position angle. Left side: *H*-plane cut. Right side: *E*-plane cut.

arbitrary large array, as in Fig. 2. The practicality of such an array design was tested using beam-lead diode detectors in the circuits of Fig. 3. The diodes are similar to those described by Calviello *et al.* [7]. The measured video response versus angle for one of them at 81 GHz is shown in Fig. 4. Pattern cuts taken in the *E* plane and the *H* plane are shown on opposite sides of the same plot. The pattern is respectable despite the proximity of neighboring elements and the substrate edge.

Although diode mixers are presently better developed than FET mixers at millimeter-wave frequencies, FET mixers offer the possibility of conversion gain, at ever-increasing frequencies [8]. Also, FETs are three-terminal devices which allow some separation of input and output. For example, the diode circuits of Fig. 3 require baluns when operated as mixers with coaxial output; the FET circuit of Fig. 1 does not, because the FET separates the balanced dipole RF input from the unbalanced IF output.

III. ANTENNA PATTERNS WITH INTEGRATED FET'S

To study antenna problems without the problems caused by using FETs beyond their usual operating frequencies, we tested *X*-band (8–12 GHz) antenna models with pack-

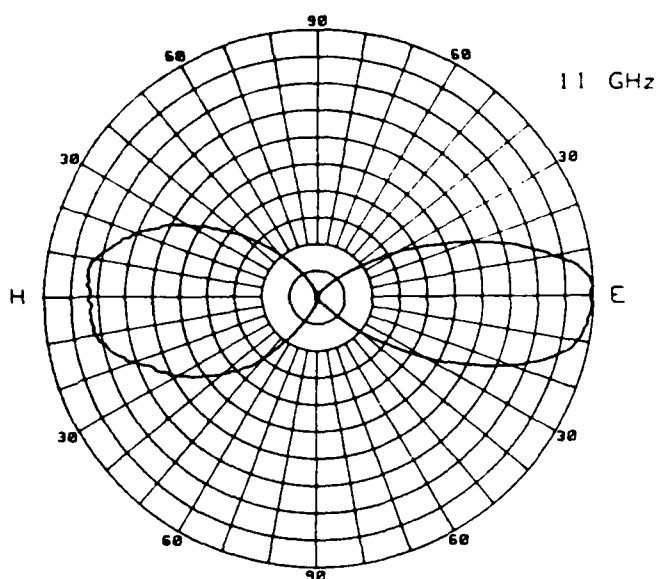


Fig. 5. Antenna pattern of X-band fused quartz superstrate antenna with FET. Video response at 11 GHz (linear voltage scale, arbitrary normalization) versus position angle. Left side: *H*-plane cut. Right side: *E*-plane cut.

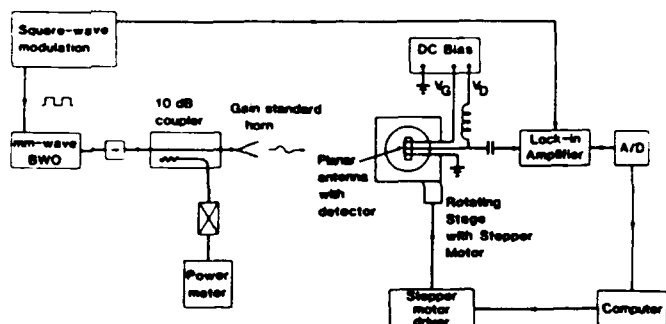


Fig. 6. Microcomputer-controlled bench-top antenna pattern measurement setup. Video response of the integrated detector is recorded as the antenna is rotated.

aged FET's (NEC NE70083) before trying millimeter-wave circuits. X-band copper foil microstrip antennas on fused quartz and glass-filled PTFE (3M CuClad with permittivity of 2.3) substrates, and an inverted microstrip antenna on a fused quartz superstrate, were fabricated and tested.

The inverted microstrip antenna is a practical modification of a superstrate structure in which a microstrip antenna on a low-permittivity substrate is covered by a high-permittivity superstrate. Such a superstrate structure was suggested by Alexopoulos and Jackson [9] to prevent losses to substrate or surface modes. In the inverted microstrip structure, an air gap replaces the low-permittivity substrate. Air gap thickness was experimentally adjusted to 0.11 in. (2.8 mm) with a 0.050 in. (1.27 mm) thick fused quartz superstrate to obtain the antenna pattern of Fig. 5. The pattern is easily ruined if the air gap is too wide.

We measured antenna patterns using the apparatus of Fig. 6. On all three microstrip types, twin dipole antennas (with circuit patterns similar to Fig. 1) gave acceptable antenna patterns. All acceptable antenna patterns were essentially similar; the representative pattern of Fig. 5

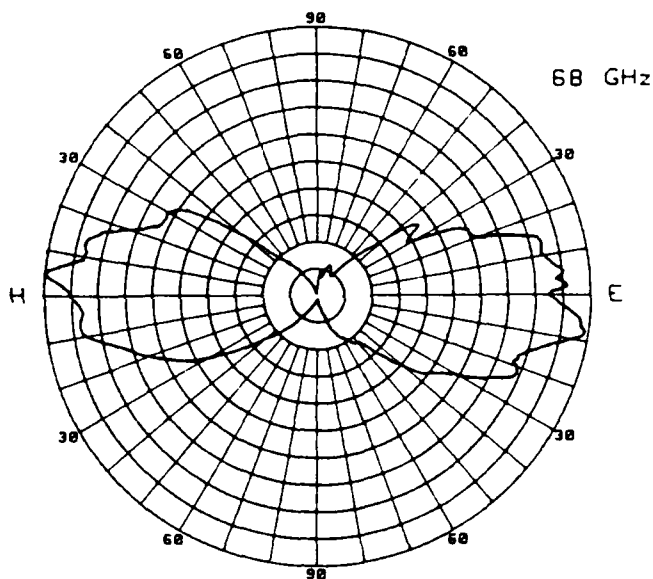


Fig. 7. Antenna pattern of millimeter-wave fused quartz microstrip antenna with FET. Video response at 68 GHz (linear voltage scale, arbitrary normalization) versus position angle. Left side: *H*-plane cut. Right side: *E*-plane cut.

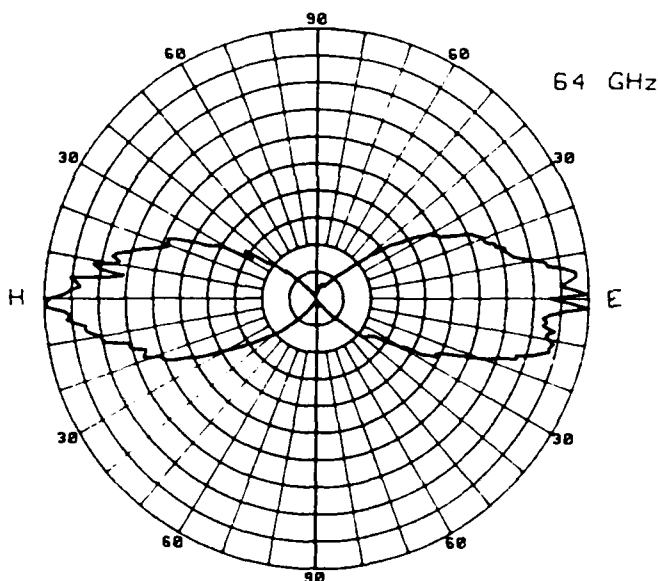


Fig. 8. Antenna pattern of millimeter-wave PTFE-glass microstrip antenna with FET. Video response at 64 GHz (linear voltage scale, arbitrary normalization) versus position angle. Left side: *H*-plane cut. Right side: *E*-plane cut.

came from the inverted microstrip structure. Video response from the FET is shown versus orientation (0° represents the direction perpendicular to the substrate surface).

Since all three X-band models gave acceptable patterns with FET's, we constructed 60 or 70 GHz versions of each. The inverted microstrip (superstrate) antenna proved difficult to fabricate without disturbing bond wires to the FET while fitting them within an air gap as narrow as desired for 70 GHz. The nominal FET chip thickness of $140 \mu\text{m}$ is an appreciable fraction of the desired gap of less than $400 \mu\text{m}$. Using a wider air gap did not produce an acceptable

antenna pattern. Monolithic construction could be more practical.

The other two structures gave better results. The video response antenna pattern at 68 GHz of a quartz microstrip circuit wire-bonded with an NEC NE71000 FET chip is shown in Fig. 7. The video response antenna pattern at 64 GHz of a similar PTFE-glass microstrip circuit is shown in Fig. 8. Both are suitable patterns for quasi-optical applications with conventional mirrors and lenses, having well-shaped main lobes directed perpendicular to the substrate surface, and small side lobes (on a linear scale).

IV. MIXER RESULTS

The microstrip circuit of Fig. 1, which gave the antenna pattern of Fig. 8, was constructed on RT/Duroid 5880 (Rogers Corp., permittivity 2.2) using an NEC NE71000 FET (a widely used 0.3 μm gate length GaAs FET). The coplanar IF line was soldered to an SMA coaxial connector at the substrate edge. It was operated as a gate mixer with the gate dc bias near the turn-on point at -0.8 V and the drain bias at 0.7 V, both with respect to the grounded source.

The maximum conversion gain of a gate mixer and the LO power requirement for maximum gain can be estimated using Maas's [1], [8] simple modifications of the expressions of Pucel *et al.* [10]. Maximum conversion gain is approximately

$$G_c \approx \frac{g_1^2 R_L}{\omega_{RF}^2 C^2 R_{in}}$$

and the required local oscillator power for maximum gain is approximately

$$P_{LO} \approx (\omega_{LO} C V_{LO})^2 R_{in} / 2$$

where g_1 is the magnitude of the fundamental component of the time-varying transconductance, ω_{RF} is the RF signal radian frequency, C is the time-averaged gate-source capacitance, R_L is the IF load impedance at the drain, R_{in} is the input resistance (including gate, source, and intrinsic resistances), ω_{LO} is the LO radian frequency, and V_{LO} is the LO voltage amplitude for maximum gain. Using $g_1 \approx G_{Mmax}/4$, where G_{Mmax} is the maximum value of the dc transconductance, using V_{LO} as the voltage swing between the turn-on point and the point of maximum dc transconductance, and using typical values of $G_{Mmax} \approx 68 \times 10^{-3}$ S, $C \approx 0.28 \times 10^{-12}$ F, $R_L \approx 55 \Omega$, $R_{in} \approx 5.1 \Omega$, $V_{LO} \approx 1$ V, and the values $\omega_{RF} = 2\pi \times 63 \times 10^9$ Hz and $\omega_{LO} = 2\pi \times 62 \times 10^9$ Hz, we obtain an estimated maximum conversion gain of 0.25 or a conversion loss of 6 dB, with an LO requirement of 30 mW. The orders of magnitude match the measured values, indicating that at these millimeter-wave frequencies, the basic microwave gate mixer mechanisms still apply and the quasi-optical input has reasonable efficiency.

To operate it as a mixer, LO and RF inputs were combined using a quasi-optical diplexer [11] in the quasi-optical noise measurement system of Fig. 9. This produced

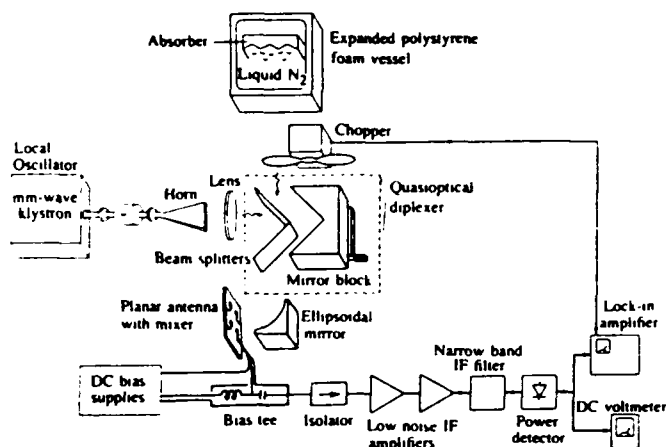


Fig. 9. Quasi-optical noise measurement system. LO (from klystron) and RF (from blackbody) are combined using a quasi-optical diplexer. System noise and system response to hot and cold blackbody radiation are measured using the mixer under test.

a directly measured system noise temperature of 7900 K with a conversion loss of 9.5 dB at an IF of 1.25 GHz and an LO of 35 mW at 62 GHz. This was a double sideband measurement made at room temperature (298 K). Since the circuit is most sensitive near 64 GHz and is much less sensitive to the lower sideband near 61 GHz, the single sideband noise figure should be nearly as low as this double sideband noise figure measurement, while the single sideband conversion loss should be almost half of this double sideband measurement. The system noise temperature includes any noise from the klystron LO, the losses from optics, diffraction, obscuration, and coupling inefficiencies, IF isolator loss, and the noise of the IF chain, in addition to the noise of the mixer circuit. Noise from the klystron LO is expected to be low, and is filtered by the quasi-optical interferometer diplexer [11]. The IF isolator and amplifier chain had a measured noise temperature of 113 K. The mixer conversion loss includes all losses and gains between the hot/cold blackbody radiator (chopper or absorber) and the input of the IF isolator. The integrated structure makes separate losses difficult to evaluate accurately without more detailed measurements. The LO power level was optimized for noise figure, and at a saturation level for conversion efficiency. Both conversion loss and noise were higher when LO power was increased to 50 mW. Though the mixer produced conversion loss rather than conversion gain, and the LO requirement is relatively high, our results show a promising noise figure. The noise measurement system constitutes a practical Dicke [12] radiometry system, so these measurements represent realistic system performance.

V. CONCLUSIONS

These results show that a FET mixer integrated with a simple printed circuit antenna can provide useful performance at 63 GHz. The circuits are suitable for imaging and other quasi-optical applications. The results were obtained using a popular commercial FET wire-bonded to the circuit. Further advances in performance may be ex-

pected with custom optics, refinements in circuit design, beam-lead devices or monolithic approaches, and relentless advances in available FET's.

ACKNOWLEDGMENT

The authors wish to thank J. A. Calviello of the AIL Division of Eaton Corporation for providing beam-lead diodes and W. W. Ho of Rockwell International Science Center for providing a low-noise millimeter-wave local oscillator for noise measurements.

REFERENCES

- [1] S. A. Maas, *Microwave Mixers*. Dedham, MA: Artech House, 1986.
- [2] A. R. Kerr, P. H. Siegel, and R. J. Matlack, "A simple quasi-optical mixer for 100–120 GHz," in *1977 IEEE MTT-S Int. Microwave Symp. Dig.*, pp. 96–98.
- [3] P. T. Parrish *et al.*, "Printed dipole-Schottky diode millimeter wave antenna array," *SPIE Proc. Millimeter Wave Technology*, vol. 337, pp. 49–52, 1982.
- [4] H. R. Fetterman *et al.*, "Printed dipole millimeter wave antenna for imaging array applications," *Electromagnetics*, vol. 3, pp. 209–215, 1983.
- [5] C. P. Wen, "Coplanar waveguide: A surface strip transmission line suitable for nonreciprocal gyromagnetic device applications," *IEEE Trans. Microwave Theory Tech.*, vol. MTT-17, pp. 1087–1090, Dec. 1969.
- [6] M. Riazat, I. J. Feng, R. Majidi-Ahy, and B. A. Auld, "Single-mode operation of coplanar waveguides," *Electron. Lett.*, vol. 23, pp. 1281–1283, 19 Nov. 1987.
- [7] J. A. Calviello, J. L. Wallace, and P. R. Bie, "High-performance GaAs beam-lead mixer diodes for millimetre and submillimetre applications," *Electron. Lett.*, vol. 15, pp. 509–510, 16 Aug. 1979.
- [8] S. A. Maas, "Design and performance of a 45-GHz HEMT mixer," *IEEE Trans. Microwave Theory Tech.*, vol. MTT-34, pp. 799–803, July 1986.
- [9] N. G. Alexopoulos and D. R. Jackson, "Fundamental superstrate (cover) effects on printed circuit antennas," *IEEE Trans. Antennas Propagat.*, vol. AP-32, pp. 807–816, Aug. 1984.
- [10] R. A. Pucel, D. Masse, and R. Bera, "Performance of GaAs MESFET mixers at X band," *IEEE Trans. Microwave Theory Tech.*, vol. MTT-24, pp. 351–360, June 1976.
- [11] J. M. Payne and M. R. Wordeman, "Quasi-optical diplexer for millimeter wavelengths," *Rev. Sci. Instrum.*, vol. 49, pp. 1741–1743, Dec. 1978.
- [12] R. H. Dicke, "The measurement of thermal radiation at microwave frequencies," *Rev. Sci. Instrum.*, vol. 17, pp. 268–275, July 1946.

✱



Wilbert Chew received the B.S. degree in applied physics from the California Institute of Technology in 1978 and the M.S.E.E. degree in electrical engineering from the University of Washington in 1980.

From 1981 to 1983 he analyzed infrared imaging systems at Hughes Aircraft Company. He is currently a research assistant and Ph.D. student in electrical engineering at the University of California, Los Angeles, studying solid-state electronics and millimeter-wave systems and components.

✱

Harold R. Fetterman (SM'81) received the Ph.D. degree from Cornell University in 1967.

He is currently a Professor in the Department of Electrical Engineering and Associate Dean of the School of Engineering and Applied Science at the University of California, Los Angeles. He joined UCLA after 14 years at the MIT Lincoln Laboratory, where he was Project Leader of the submillimeter/millimeter-wave detector and source programs. He successfully directed the development of heterodyne receivers and solid-state sources with applications in plasma diagnostics, remote sensing, and imaging radars. Since coming to UCLA, he has been active in the development of millimeter-wave FET devices and large-area arrays, and established the new UCLA High Frequency Electronics Center.

MILLIMETER-WAVE GENERATION AND CHARACTERIZATION OF A GaAs FET BY OPTICAL MIXING

D. Ni, W. Chew and H. R. Fetterman

Department of Electrical Engineering
University of California, Los Angeles
Los Angeles, CA 90024

ABSTRACT

Coherent mixing of optical radiation from a tunable CW dye laser and a stabilized He-Ne laser was used to generate millimeter-wave signals in GaAs FETs attached to printed circuit millimeter-wave antennas. The generated signal was further down-converted to a 2 GHz i.f. by an antenna-coupled millimeter LO at 62 GHz. Detail characterization of power and S/N under different bias conditions have been performed. This technique is expected to allow signal generation and frequency-response evaluation of millimeter-wave devices at frequencies as high as 100 GHz.

I. Introduction

Optical control of millimeter-wave devices has attracted recent attention because of its potential applications, such as in enhancement of device performance, signal switching, signal synchronization and distributed control of communications and radar systems [1-8]. Recently we demonstrated coherent mixing of optical radiation to generate stable broadband-microwave signals beyond Ka band in FETs and related three-terminal devices [9-10]. In this paper we describe the use of this optical-mixing technique to generate a 64 GHz signal in a GaAs FET with an integrated printed-circuit antenna designed for quasioptical millimeter-wave applications [11]. This configuration permits the direct coupling of a millimeter-wave local oscillator (LO) through the antenna to the illuminated gate terminal of the GaAs FET. We obtain i.f. (1 - 2 GHz) beat signals between the optical beat signal and the millimeter-wave LO (klystron, Impatt diode or Gunn diode), which can then be characterized for power and gain.

Using intensity-stabilized and optically tunable lasers together with millimeter-wave sources will allow the generation of signals and characterization of millimeter-wave devices at frequencies as high as 100 GHz relatively free from the limitations imposed by the mounting fixtures and the related parasitics associated with these devices. In addition to testing, this approach has potential for generation and heterodyne detection of millimeter waves.

II. Experiment

The experimental setup is shown in Fig. 1. A stabilized He-Ne laser (Model 200 / Coherent) and a CW ring dye laser (Model 699-21 / Coherent), optically pumped by an Ar⁺ laser, were used to illuminate the GaAs FETs. The penetration depth of these lasers into GaAs is about 0.3 μm , which is the same order as the thickness of the active region of the FETs. The wavelength of the ring dye laser, monitored by a Burleigh optical wavemeter can be continuously tuned to any value within the dye emission spectrum. For the Kiton 620 dye (600 - 640 nm), the tuning range is more than 40 nm around the He-Ne line. Consequently the beat frequency of the two CW lasers can be easily varied from zero to several hundred

GHz while the intensities of the lasers are kept constant.

In order to generate optical millimeter-wave beat frequencies, the wavelength of the dye laser must be very close to the wavelength of the He-Ne laser. To generate a 7.5 GHz optical beat frequency, for example, corresponds to tuning a 0.01 μm wavelength difference between two lasers. Therefore an extremely accurate measurement of the frequency difference between the lasers is required to make this technique practical. The laser powers are approximatedly 0.5 mW for the He-Ne laser and 400 mW for the dye laser. The linewidth and stability of both lasers were typically less than one MHz.

The commercially available FETs (NEC/NE71000), which have gate length about 0.3 μm and drain-source distance of 2 μm , were integrated on a printed circuit RT/duroid microstrip antenna (dash-lined area in Fig. 2). This microstrip circuit was designed as a FET gate mixer on a RT/ duroid substrate with permittivity of 2.2 (from Rogers Corp.). The FET is used to convert from the balanced dipole r.f. feed (signal and LO) at its input to an unbalanced i.f. transmission line at the drain terminal of the FET. The i.f. transmission line is intended to work as coplanar waveguide backed by a lower ground plane. These i.f. lines, which also carry the DC biases, consist of cascaded quarter-wave (at r. f.) sections forming low pass filters which approximately present an effective short circuit for r.f. at the FET output without disturbing the antenna feed. Effects of the i.f. at the input are minimized by operating the i.f. line in the coplanar waveguide mode without exciting the balanced i.f. mode. A 100 pF capacitor grounds the FET gate line at the i.f. (Some data in Appendix A and more information in Ref. 11).

The above configuration prevents the direct application of microwave signals to the FET in the antenna circuit via the i.f. and bias lines. Therefore we used a second FET of the same type mounted and connected to 50 Ω microstrip lines on alumina substrate at the gate and the drain for calibration and normalization [9]. This calibration FET, marked "FET" in Figure 1, was used to evaluate optical conversion loss, loss in the printed-circuit-antenna circuit and noise figures at i.f. frequencies.

To detect the millimeter-waves generated by optical beating, an LO can be introduced to the gate of the FET either by an external generator [9] or by the FET itself, configured with a feedback loop, to serve as an oscillator [12]. As a result of the nonlinearity of the GaAs FET's transconductance, the electrical r.f. signal mixes with the r.f. signal produced by optical beating, and produces an i.f. beat signal. In the past, millimeter-wave signals generated in this manner have been measured using harmonic mixing with Ka-band sources [9]. However, the power output of the different harmonics had been observed to be highly nonlinear in the FETs. For example, depending on the input power, the output power of the third harmonic can be higher than of the second harmonic at microwave frequencies [12-13]. Although these harmonics can be used for frequency measurements, they are generally not sufficient to serve as LO. In order to characterize the device performance more precisely, we used a fundamental millimeter-wave LO from either a reflex klystron (Varian VC-1112 with Harris 819 power supply), a Gunn diode (Hughes 47224H) or an Impatt solid state source (Hughes 47174H) quasioptically coupled to the antenna to generate the i.f. beat signal.

To couple simultaneously the optical and millimeter-wave signals to the FET , a flat brass reflector with a central hole (1 mm diameter) was used. A 25 dB directivity horn and a polyethylene lens with focal length (f.l.) of 25.4 mm effectively coupled the LO to the antenna. A f.l. 50 mm lens was inserted between the reflector and beam splitter to focus the laser beam into a spot of 4.5 μm in diameter (original beam size 0.75 mm in diameter). A DC current meter was used to monitor indirectly the power of the optical and millimeter-wave signals. Since the power of the stabilized He-Ne laser is about two orders lower than that of the dye laser, the first variable beam splitter was adjusted to transmit less than 10 % of the total dye-laser power to the second beam splitter. On the other arm of the second beam splitter, the microstrip-line-mounted FET on alumina substrate with the gate connected to a sweep generator and the drain connected to a spectrum analyzer directly, was illuminated by the focused lasers through a microscope objective (f.l. 16 mm). The optical power density on the calibration FET were approximately 5 KW/cm² for He-Ne laser and 40 KW/cm² for dye

laser, respectively.

In our experiment, we first calibrated the r.f. power gain of the optical-input/electrical-output against that of an electrical input/output and evaluated the conversion loss with the FET on alumina substrate at i.f. (1-2 GHz). The noise figure of this FET is specified to be 0.6 dB at 1-4 GHz. Instead of S-parameter measurements, the increases of the power and of the S/N between the biased and the unbiased conditions, i.e. $V_{ds} = V_{gs} = 0$ V, were measured. In most measurements at i.f. frequencies, the S/N increases will be presented. Since the noise figures of the FET are almost constant at these frequencies, the S/N increases were approximately equal to the power increases in our measurements. At millimeter-wave frequencies, however, the noise figure of the FET changes and therefore the power and the S/N are presented together. The adoption of this approach will be discussed later.

The S/N increase of the optical-mixing signal between the biased and the unbiased conditions was 27 dB. This was within 5 % of the S/N increase measured with an electrical signal applied to the gate from a sweep generator under the same DC biases (V_{ds} and I_{ds}) and unbiased conditions while the FET was not illuminated. Therefore we consider the S/N increase of the optical-input/electrical-output as that of the electrical input/output of a matched network. To evaluate the conversion loss at the i.f., we applied a 0 dBm electrical signal at 4 GHz from the sweep generator to the gate of the FET on alumina substrate to mix the optical beat signal (S/N was 37 dB) at 2 GHz. The resulting i.f. beat signal was found to have S/N of 30 dB near 2 GHz (Fig. 3(a)). A conversion loss of 7 dB was therefore obtained, which was close to that of a GaAs Schottky diode (about 6 dB). Power versus V_{gs} , for both optical-mixing signals and electrical signals without illumination, was also measured (Fig. 4). With an adequate LO power, the conversion loss of 64 GHz mixing is expected to be of the same order of magnitude as this measurement since the mixing mechanism is the same. This prediction is based on the similar data for the conversion loss of the GaAs Schottky diodes at these frequencies [14].

Next looking at the antenna-coupled FET, we found that the power of an optical beat signal of this FET at 2 GHz was substantially lower than that of the FET on alumina substrate at 2 GHz. This difference is attributed to the gate-grounding configuration at i.f. as well as the low permittivity substrate of the antenna circuit. Because the detectable power at i.f. was substantially lower for the antenna circuit, a 1-2 GHz, 37-dB-gain i.f. amplifier with noise figure of 1.0 dB was inserted between the FET of the antenna circuit and the spectrum analyzer.

Using this system the evaluation of the performance of the FET at 64 GHz was obtained when the optical beat signal was tuned to millimeter-wave frequencies. A 50 mW klystron LO was mixed with the optical beat signal and an i.f. at 2 GHz with a S/N of 25 dB was generated (Fig. 3(b)). The conversion loss of i.f. beat signal is assumed to be 7 dB as determined previously. With a Gunn diode as LO at 20 mW, the S/N was about 15 dB and with a noisier 50 mW Impatt diode as LO, the S/N was only 7 dB. No sidebands had been observed for all three different LO's. By tuning the wavelength of the dye laser, we performed optical scanning over the bandwidth of i.f. amplifier. Although this technique could in principle be used to determine the bandwidth of the antenna structure, we found the frequency response to be limited by the i.f. amplifier.

Saturation phenomena were observed when the power of the klystron (Fig. 5) or the dye laser was higher than a critical value. This effect indicates a compression of signal resulting from the nonlinear response to klystron power and the saturation of electron-hole-pair generation in the active area of the FET with the dye laser power. For the FET's, the compression of fundamental output power occurred when the input power exceeds about -5 dBm [13]. And the saturation of carrier generation depends on the effective density of states (N_c) in conduction band ($4.7 \times 10^{17} \text{ cm}^{-3}$ for GaAs). Fig. 5 also shows the S/N is more sensitive to V_{ds} than to V_{gs} . In these experiments, the optical intensities were adjusted to the saturation region to prevent the influence of small intensity fluctuation of the lasers. Intensity of dye laser was adjusted such that I_{ds} and output power of beat signals remained the

same when there was even a 10% reduction of it. Under the above conditions, the power, S/N and I_{ds} versus V_{ds} curves were obtained, as shown in Figures 6(a)-(c).

III. Discussion

One of the current efforts of optical control of millimeter wave devices has been focused on the transport mechanism of the photoexcited carriers. For the bulk-type devices of the high purity semiconducting materials, such as optical switches and delay lines, or diode-type devices, such as pin diodes and avalanche diodes, several authors had discussed the related mechanisms in detail (for examples in Ref. 3 and 5). For the FET's, however, the plasma frequencies of injected carriers are normally higher than the operating frequencies (active region is doped to $10^{17}/cm^3$). Additionally, two applied electrical fields, V_{ds} and V_{gs} complicate the theoretical analysis. Several experimental studies on the frequency response of these devices have indicated the fast photoconductivity mechanism should be implemented while the slow photovoltaic mechanism should be suppressed [15-17]. As discussed previously, using optical mixing technique, we suppressed some of undesirable effects such as capacitance, trap and backgating effects to obtain higher frequency response [10].

Fig. 4 shows the output power versus gate bias, V_{gs} , at 2 GHz. The pinchoff voltage of this particular FET is -0.8 V. Electrical signals applied to the gate of the FET without illumination. The output signals show no gain when V_{gs} is less than -0.8 V. Under illumination, the output power of beat signal increases to a maximum value around $V_{gs} = -1.0$ V, then declines slowly even beyond the pinchoff voltage. For the latter case, the change of built-in voltage, ΔV_{bi} , of the Schottky barrier between the gate electrode and GaAs active area under illumination is given as [4]

$$\Delta V_{bi} = \frac{KT}{q} \ln \left(1 + \frac{p_l}{p_o} \right) \approx \frac{KT}{q} \ln \frac{p_l}{p_o} \quad \text{When } p_l \gg p_o \quad (1)$$

where p_l and p_o stand for the photoexcited and dark hole (lifetime about 50 ns) concentrations, respectively. By comparing the photogenerated currents (in order of 10 mA when V_{gs} biased

at pinchoff voltage) from two CW lasers with the currents of no illumination, we estimate p_i in the order of $10^{17}/\text{cm}^3$ and obtain ΔV_{bi} about 1.0 V which indicates the space-charge region under the gate electrode was suppressed by the photogenerated carriers. For the steady state under illumination and without biases, the fluctuation of carrier concentration is expected in the limit of dielectric relaxation time (sub-picoseconds). The FET can be thought as a photoconductive device under this circumstance since the related input capacitances are either suppressed or not related to the optical mixing signals. To obtain a peak output power is equivalent to have maximum modulation depth which occurs when the original carriers are depleted by the applied V_{gs} . The injected holes suppress the space-charge region while the injected electrons modulated by the beat frequency to a maximum depth. More discussions on photoconductivity mechanism of optical mixing can be found in Ref. 10.

The nonlinearity of FET's has been observed when FET's were used as mixers with two electric signals applied to the gate of FET (for example in Ref. 11). In this case, only unipolar carriers (electrons) are dominant. In the optical mixing case when both electrons and holes are generated in the form of plasma. In both cases, the FET's can be used as the square-law detectors [18]. To account for the phase delay as a function of complex dielectric constant, the nonlinearity of plasma can be under consideration [2,5].

Rigorously, power gain analysis should be modified to adjusted for the light input as an additional terminal either by converting the two port circuit to a three port network or represent the beat signal as an input to a modified equivalent circuit model of FET. Additionally, nonlinear circuit model should be also considered. From the other viewpoint, if the experimental data can be analyzed in the relative basis against a calibration FET, some relevant information can also be obtained. The latter approach is adopted in the current paper.

The power increase is equivalent to the ratio between $|S_{21}|^2$ with bias and $|S_{21}|^2$ without bias. For a passive and matched circuit, $|S_{21}|^2$ is equal to unity, the power increase can be considered as $|S_{21}|^2$ with bias. In our approach, the matched condition is not difficult to obtain since the characterization is performed at i.f. frequencies. Even if the circuit is not

matched, the S parameters are still easy to measure at these frequencies. Under these circumstances, the unbiased $|S_{21}|^2$ can be measured and used as a proportionality constant between the power increase and the biased $|S_{21}|^2$.

On the other aspect, the optical beat signal generated by two CW lasers can be technically considered as no electrical input and therefore no reflected signal, i.e., $S_{11} = 0$. Since power gain can be defined as follows:

$$\text{Power Gain} = \frac{|S_{21}|^2(1-\Gamma_L)}{(1-|S_{11}|^2) + \Gamma_L^2(|S_{22}|^2 - D^2) - 2 \operatorname{Re}(\Gamma_L N)} \quad (2)$$

where

$$\Gamma_L = \frac{Z_L - Z_0}{Z_L + Z_0}$$

$$D = S_{11}S_{22} - S_{12}S_{21}$$

$$N = S_{22} - DS_{11}^*$$

We assume the impedance is matched for our concerned circuit, i.e., $Z_L = Z_0$, the power gain is then equal to $|S_{21}|^2$. Therefore the power increase can be considered to be the r.f. power gain for optically generated signal.

The power conversion efficiency from optical signal to electrical signal can be evaluated as follows. The GaAs FETs are passivated by a mixture layer of Si_3N_4 and Si_2N_2 , with index of refraction 1.46 and 2.05, respectively. The original purpose of this passivation layer is to prevent contamination from foreign materials and to condition surface stress. In our experiments, this layer also served as an Anti-Reflecting (AR) coating between air and GaAs (relative dielectric constant $\epsilon_r = 12.90$). Actually this layer has been used on semiconductor lasers as AR coating for years. By adjusting the thickness of this layer we can theoretically obtain 100 % coupling efficiency. The optical mixing efficiency can attain 50 % at maximum if the a square-law detector is used and the intensities of two input lasers are adjusted equal [18]. Therefore we expect to obtain a better power output if the power of He-Ne laser can be

increased.

The phase angles of the optical beat signals can be related to an experimental observation. When the signal from the LO was applied to the FET, the noise floor was raised at i.f. frequencies. For example, when the noisy Impatt diode was used as LO, a raise of more than 5 dB of the noise floor had been observed. If only one laser illuminated the FET with the LO applied, the noise floor raised more but in negligible fractions of 1 dB. But when FETs were illuminated by both lasers, the noise induced by LO's was significantly suppressed. This interesting phenomenon can be explained as follows. At 64 GHz, the phase angle of S_{21} of the r.f. signal from the LO is assumed to be 180 degrees. The optical beat signals, on the other hand, were generated at both gate-source and gate-drain terminals simultaneously, namely the phase angle is 0 degree. This configuration is similar to of a 180-degree hybrid microwave mixer and therefore the LO noise is suppressed [19]. The observation of the LO excess-noise suppression by the similar configuration, in which a double-detector system with a 180-degrees phase shifter connected to one of the detectors, had also been reported in optical regime [20]. The concept of local oscillator noise suppression can also be explained in terms of well known DPSK (Differential Phase Shift Keying) receiver systems [21].

Under the condition of $V_{gs} = 0$ V and $V_{ds} = 0$ V, which is similar to a Schottky diode without bias, the i.f. beat signal was still observed (Fig. 4). In Fig. 5(a), a power increase of 3.8 dB was observed when $V_{ds} = 1.0$ V in comparison with the power at $V_{ds} = 0$ V. But the best S/N increase, about 1 dB, was obtained when $V_{ds} = 0.6$ V (Fig. 5(b)). The noise-temperature parameters of the GaAs FETs are turned out lower but still reasonable in agreement with the previous observations (detailed is explained in see Appendix B). When V_{ds} was greater than 0.8 V, both S/N and I_{ds} declined and power saturated (Fig. 5(a)-(c)). The decreasing S/N and I_{ds} was observed only when both optical signals and LO signal were applied simultaneously and V_{ds} exceeded the saturation voltage (or electrical field).

For further comparison, the S/N of the i.f. beat signal versus V_{ds} was measured in the FET on alumina substrate. This i.f. beat signal was generated by the same method for

evaluating the conversion loss as described previously, i.e., by a 2 GHz optical beat and a 4 GHz electrical signal introduced to the gate from a sweep generator. A similar decline of S/N, when V_{ds} exceeded 0.8 V, was observed. This degradation of performance of both S/N and I_{ds} can be explained by the electron heating and intervalley scattering effect in the GaAs FET. The increase of the scattering noise degrades the S/N while the lower mobility of electrons in the upper valley degrades I_{ds} [22]. Fig. 5(b) indicates that for obtaining the optimal noise figure, the device should be biased at V_{ds} just below the saturation voltage.

In summary, either optical or millimeter-wave mixing occurred in the FETs without requiring biases. Adjusting both V_{ds} and V_{gs} will improve the beat signals with V_{ds} having a greater effect. At 64 GHz, adjusting V_{ds} can add a few dB to the S/N for the FET. Using this setup, we demonstrated an efficient method to down-convert the millimeter-wave signal to i.f. with minimum parasitics associated with the mounting fixture as well as the devices. The characterization of the power and gain at i.f. is therefore equivalent to their evaluation using the millimeter-wave signal.

The performance of related devices, such as High Electron Mobility Transistor (HEMT), Heterostructure Bipolar Transistor (HBT) and monolithic HEMT amplifiers, is currently being investigated.

IV. Conclusion

This paper reports the generation and detection of a millimeter-wave signal at 64 GHz in a GaAs FET integrated with a millimeter-wave antenna by optical mixing. The interesting noise-suppression phenomenon in the process of signal generation not only reveals rich physical content but also suggests potential applications. The demonstrated technique also shows the capability of the measurement of a r.f.-isolated three-terminal millimeter-wave device. Performance of the devices, such as power, gain and bandwidth can be measured.

These advantages come from the optical mixing of the lasers, which supply a stable source to generate millimeter-wave signals in these devices relatively free from the parasitics

and the limitations associated with the devices as well as the mounting features. With minor modifications, the technique is ready to be extended as high as 100 GHz. Future work will include improvement in the antenna design and the extension of the bandwidth of i.f. amplifier to enable the measurement of the frequency response of the candidate millimeter-wave devices by direct optical-scan.

V. Appendices

Appendix A : Some data for the printed circuit antenna

The estimated directivity of the printed circuit antenna is about 11 dB. The measured conversion loss of quasioptical mixer using the FET circuit at 63 GHz was 9.5 dB double sideband, i.e., a conversion gain of 0.112. The integrated structure makes other separate parameters difficult to extract. A figure of merit often used for other quasioptical mixer is the isotropic conversion gain, G_{iso} , given by [23]

$$G_{iso} = G_c G_{ant} \quad (3)$$

where G_c is the mixer conversion gain not including antenna losses, and G_{ant} is the antenna gain. In this case, since the measured conversion loss includes antenna losses,

$$G_{iso} = G_m D \approx (0.112) (12) \approx 1.4 \quad (4)$$

where G_m is the measured mixer conversion gain, and D is the antenna directivity.

Appendix B. Evaluation of Noise Figure

To treat the noises of GaAs FETs, van der Ziel included the induced gate noise mechanism [24]. Baechtold introduced the hot-electron effect [22]. Pucel *et al.* presented the mechanism of high-field diffusion noise due to dipole layer drifting through the saturated velocity portion of the channel [25]. Fukui, on the other hand, gave empirical equations which are based upon fitting noise data of GaAs FETs at 1.8 GHz [26] which were not favored at

higher frequencies [27].

In our particular case, we firstly consider three major extrinsic elements related to noise parameter calculation : Gate metallization-resistance, source resistance and pad resistance [22]. The optical-injection signals actually bypass the gate-metallization and pad resistance. The generated electron-hole pairs between source and gate region reduce significantly the source resistance by suppressing space-charge region as well as increasing the density of conducting carriers. Secondly the saturation-velocity region, which described by Pucel *etal.* is not easily to be defined since the space-charge region is suppressed. When the signal from LO applied to the gate of the FETs, we can visualize the Schottky gate simply a zero biased or even a forward biased Schottky diode. Under above considerations, we can simply start from

$$\frac{T_n}{290} = 1 + \gamma \left(\frac{E}{E_{sat}} \right)^3 \quad (5)$$

Where T_n , E , and E_{sat} are noise temperature, applied electric field and saturation electric field, respectively. And γ is the concerned fitting parameter. This empirical equation is effective when $E \leq E_{sat}$ [22]. The noise temperature in eqn (5) includes the noises related to GaAs FET as a mixer as well as an amplifier at i.f. and r.f. frequencies. The rigorous treatment can be found in [28].

Using a technique similar to the well-known Y-factor method although we are dealing with a nonlinear case, the calculation can be proceeded as follows. The noise figure, NF, can be written in terms of noise temperature as

$$NF \text{ (dB)} = 10 \log_{10} \left[1 + \frac{T_n}{290} \right] \quad (6)$$

Substituting eqn (6) directly into (5) with two different data points

$$NF_1 = 10 \log_{10} \left[2 + \gamma \left(\frac{E_1}{E_{sat}} \right)^3 \right] \quad (7)$$

$$NF_2 = 10 \log_{10} \left[2 + \gamma \left(\frac{E_2}{E_{sat}} \right)^3 \right] \quad (8)$$

Subtracting eqn (7) from eqn (8) results in

$$\Delta NF = 10 \log_{10} \left[\frac{2 + \gamma \left(\frac{E_2}{E_{sat}} \right)^3}{2 + \gamma \left(\frac{E_1}{E_{sat}} \right)^3} \right] \quad (9)$$

To define the noise figure in terms of the S/N, we have

$$NF = 10 \log_{10} \left[\frac{\left(\frac{S_i}{N_i} \right)}{\left(\frac{S_o}{N_o} \right)} \right] \quad (10)$$

Using similar procedure for two data points as eqn (4) through eqn (6) to obtain

$$NF_1 - NF_2 = 10 \left[\log_{10} \left(\frac{S_i}{N_i} \right) - \log_{10} \left(\frac{S_{o1}}{N_{o1}} \right) - \log_{10} \left(\frac{S_i}{N_i} \right) + \log_{10} \left(\frac{S_{o2}}{N_{o2}} \right) \right] \quad (11)$$

Therefore

$$\Delta NF = - 10 \left[\log_{10} \left(\frac{S_{o1}}{N_{o1}} \right) - \log_{10} \left(\frac{S_{o2}}{N_{o2}} \right) \right] = - \Delta S/N \quad (12)$$

Since $E \leq E_{sat}$, we can assume

$$\frac{E_{1,2}}{E_{sat}} \approx \frac{V_{ds1,2}}{V_{sat}} \quad (13)$$

Selecting $V_{ds1} = 0.0$ V, $V_{ds2} = 0.6$ V and $V_{sat} = 0.8$ V, we can obtain S/N difference ($\Delta S/N$), about 0.8 dB, between S/N's at V_{ds1} and V_{ds2} from Figure 6(b) (krystron power at 20 mW), then substitute these values into eqn (9) to obtain $\gamma \approx 1.0$. This value is in agreement with the previous results : the values of γ were in the range of 0.6 to 6.0 [29].

ACKNOWLEDGEMENT

This work was supported by the Air Force Office of Scientific Research.

REFERENCES

1. H. W. Yen, M. K. Barnoski, R. G. Hunsperger and R. T. Melville, " Switching of GaAs IMPATT diode oscillator by optical illumination," *Appl. Phys. Lett.*, vol. 31, pp. 120-122, 1977.
2. C. H. Lee, Paul S. Mak and A. P. DeFonzo, " Optical Control of Millimeter-Wave Propagation in Dielectric Waveguides," *IEEE J. Quantum Electron.* vol. QE-16, pp. 277-288, 1980.
3. R. A. Kiehl and D. M. Drury, " Performance of optically coupled microwave switching devices," *IEEE MTT-S*, vol. MTT-29, pp. 1004-1010, 1981.
4. A. A. A. De Salles, " Optical Control of GaAs MESFET's," *IEEE Trans. Microwave Theory Tech.*, vol. MTT-31, pp. 812-820, 1983.
5. A. M. Yurek, C. D. Striffler and C. H. Lee, " Optoelectronic devices for millimeter-waves," in *Infrared and Millimeter-Wave*, vol. 14, K. J. Button edited, Academic Press, pp. 249-290, 1985.
6. L. Goldberg, A. M. Yurek, H. F. Taylor, and J. F. Weller, " 35 GHz Microwave Signal Generation with an Injection-Locked Diodes," *Electron. Lett.* vol. 21, pp. 491-493, 1985.
7. R. N. Simons and K. B. Bhasin, " Analysis of optically controlled microwave/millimeter-wave device structures," *IEEE Trans. Microwave Theory Tech.*, vol. MTT-34, pp. 1349-1355, 1986.
8. A. S. Daryoush, P. R. Herczfeld, and Z. Turski, P. Wahi, " Comparison of Indirect Optical Injection-Locking Techniques of Multiple X-Band Oscillators," *IEEE Trans. Microwave Theory Tech.*, vol. MTT-34, pp. 1363-1369, 1986.
9. H. R. Fetterman, W. Y. Wu, and D. Ni, " Optical Control of Millimeter Wave Devices," *Proc. of SPIE*, vol. 789, pp. 50-53, 1987.
10. H. R. Fetterman and D. Ni, " Control of Millimeter Wave Devices by Optical Mixing," *Microwave Opt. Tech. Lett.*, vol. MOTL-1, pp. 34-39, 1988.

11. W. ~~Chen~~ and H. R. Fetterman, "Printed circuit antennas with integrated FET detectors for Millimeter-Wave Quasioptics," IEEE Trans. Microwave Theory Tech., vol. 37, pp. 593-597, 1989.
12. C. ~~Rauscher~~, L. Goldberg, and A. M. Yurek, "GaAs FET Demodulator and Down-Converter for Optical-Microwave Links," Electron. Lett. vol. 22, pp. 705-706, 1986.
13. W. R. ~~Cumace~~ and M. Ettenberg, "A Nonlinear GaAs FET Model for Use in the Design of Output Circuits for Power Amplifiers," IEEE Trans. Microwave Theory Tech., vol. MTT-33, pp. 1383-1394, 1985.
14. D. N. ~~Heune~~ and A. R. Kerr, "Conversion Loss and Noise of Microwave and Millimeter-Wave Mixers. Part 2 - Experiment," IEEE Trans. Microwave Theory Tech., vol. MTT-26, pp. 55-61, 1978.
15. J. P. ~~Nolan~~, E. H. Hara, R. H. Hum and R. I. MacDonald, "FET Photodetectors: A Combined Study Using Optical and Electron-Beam Stimulation," IEEE Trans. Electron. Devices, vol. ED-29, pp. 1792-1797, 1982.
16. G. J. ~~Fotomianou~~ and J. R. Forrest, "On the Photoresponse of GaAs MESFET's: Back-gating and Deep Traps Effect," IEEE Trans. Electron. Devices, vol. ED-33, pp. 373-378, 1986.
17. R. B. ~~Dunning~~ and J. P. Uyemura, "Optical Gain and Large-Signal Characteristics of Illuminated GaAs MESFET's," IEEE J. Quantum Electron., vol. QE-23, pp. 1160-1171, 1987.
18. R. H. ~~Engstrom~~, *Detection of Optical and Infrared Radiation*, Springer, Berlin, 1978, Chapter 3.
19. S. A. ~~Mias~~, *Microwave Mixer*, Artech House, Inc., pp. 232-236, 1986.
20. G. L. ~~Ashley~~, V. W. S. Chan, and T. K. Yee, "Local-oscillator excess-noise suppression for homodyne and heterodyne detection," Opt. Lett., vol. 8, pp. 419-421, 1983.
21. S. ~~Benec~~, E. Biglieri and V. Castellri, "Digital Transmission Theory," pp. 211-220, Addison-Wesley, 1987.

FIGURE CAPTIONS

Fig. 1 Experimental setup shows the calibrated FET and the FET in the printed antenna circuit

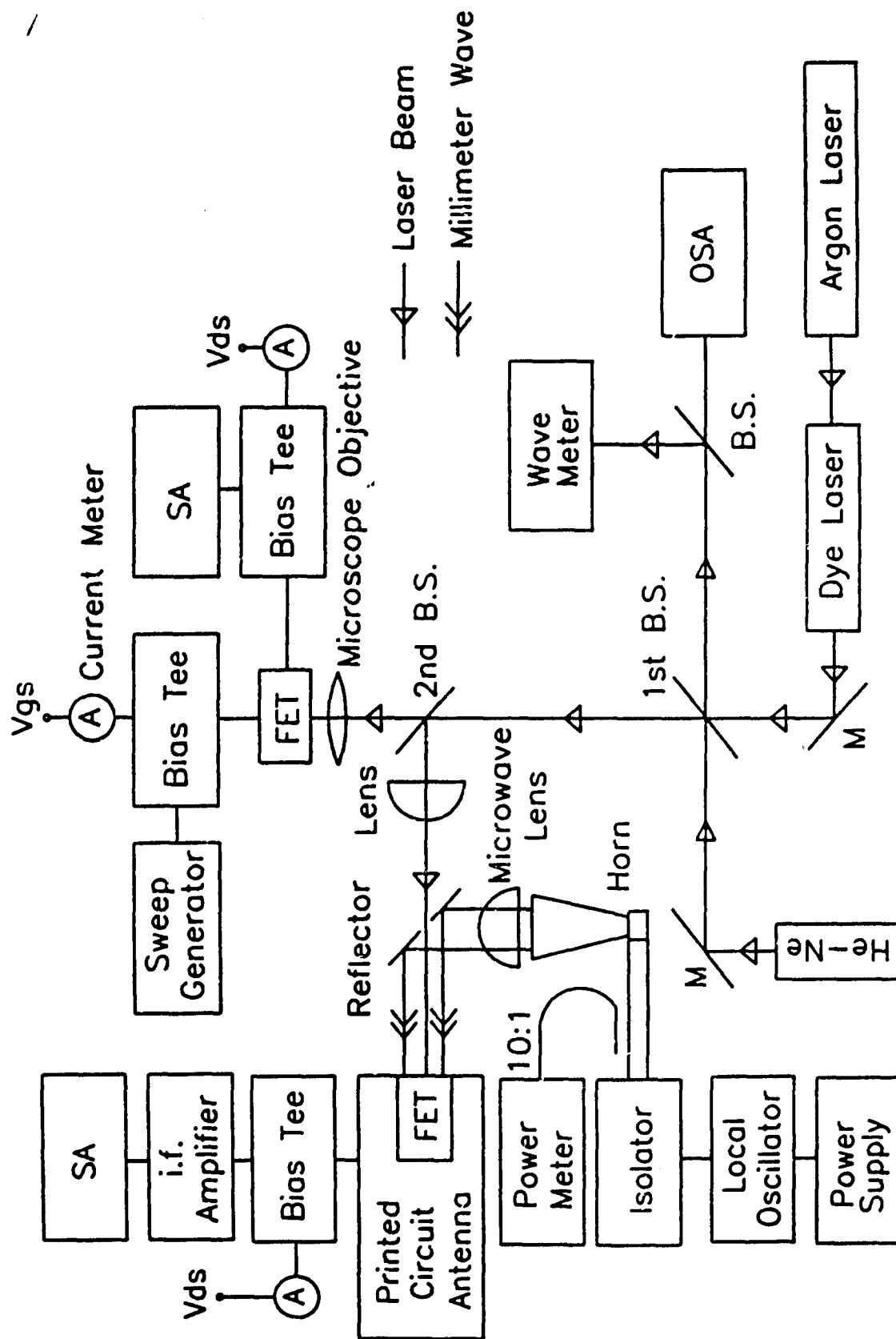
Fig. 2 Pattern of the millimeter-wave antenna. FET source, drain, and gate re wire-bonded to points S, D, and G. Gate bias chip capacitor is attached at point CC and wire-bonded to point C [Ref. 11].

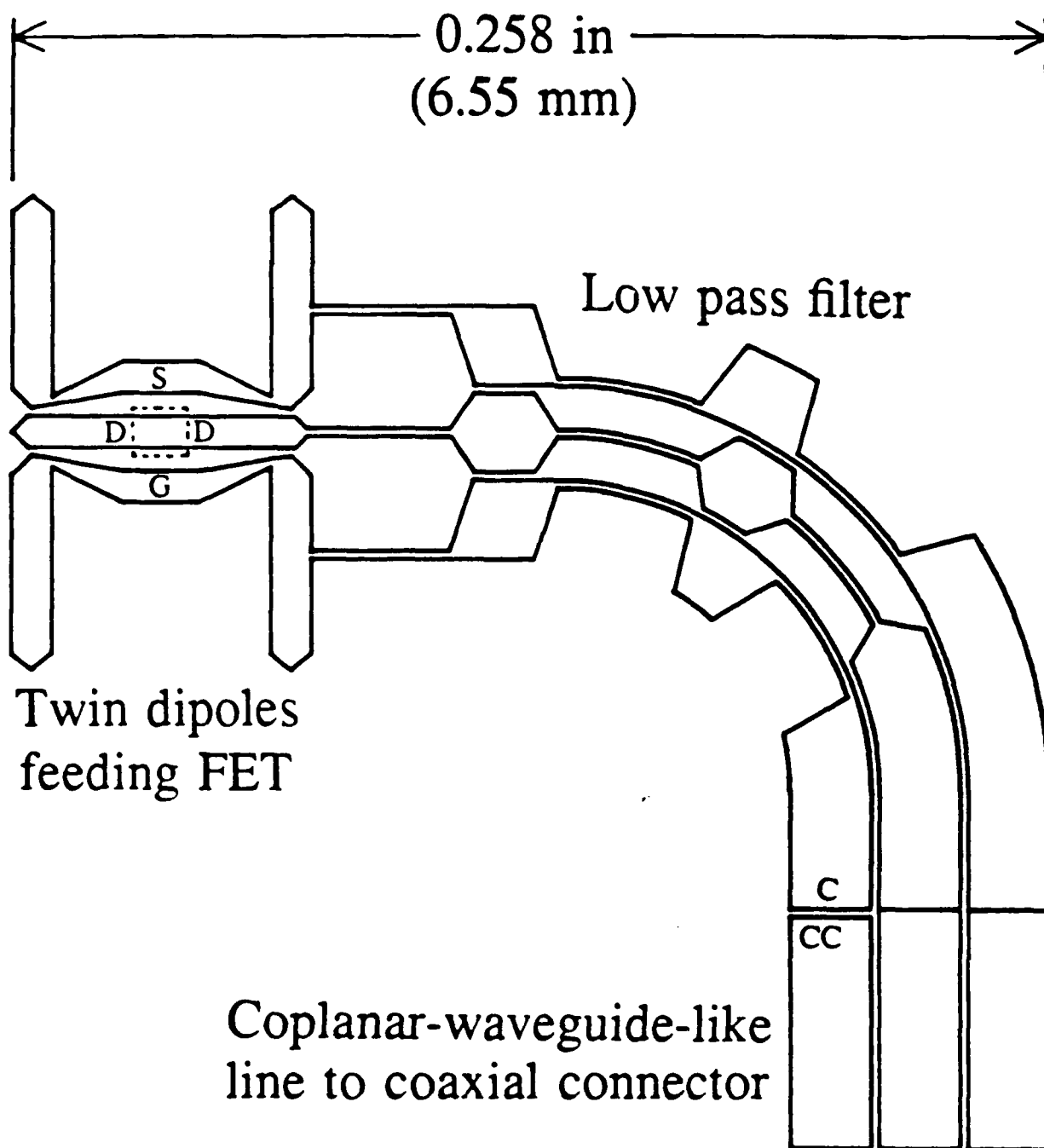
Fig. 3(a) A -39 dBm optical beat signal with 37 dB S/N at 2.056 GHz and a -45 dBm second beat signal at 2.016 GHz (between electrical and optical beat signal). A 7 dB conversion loss is shown. 3(b) A S/N 25 dB second-beat i.f. between klystron signal and optical-beat signal.

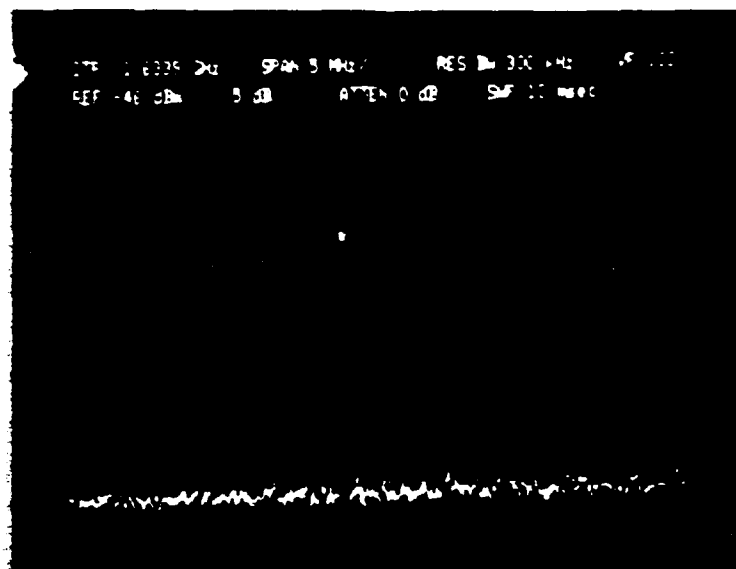
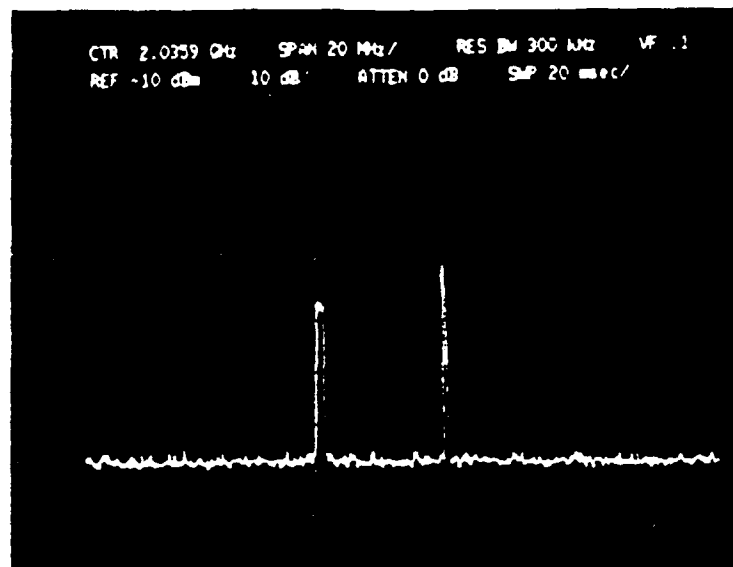
Fig. 4 Output power vs. V_{gs} of optical beat signal and electrical signal without illumination at 2 GHz. Both output signal are adjusted to -35 dBm at $V_{gs} = 0$ V.

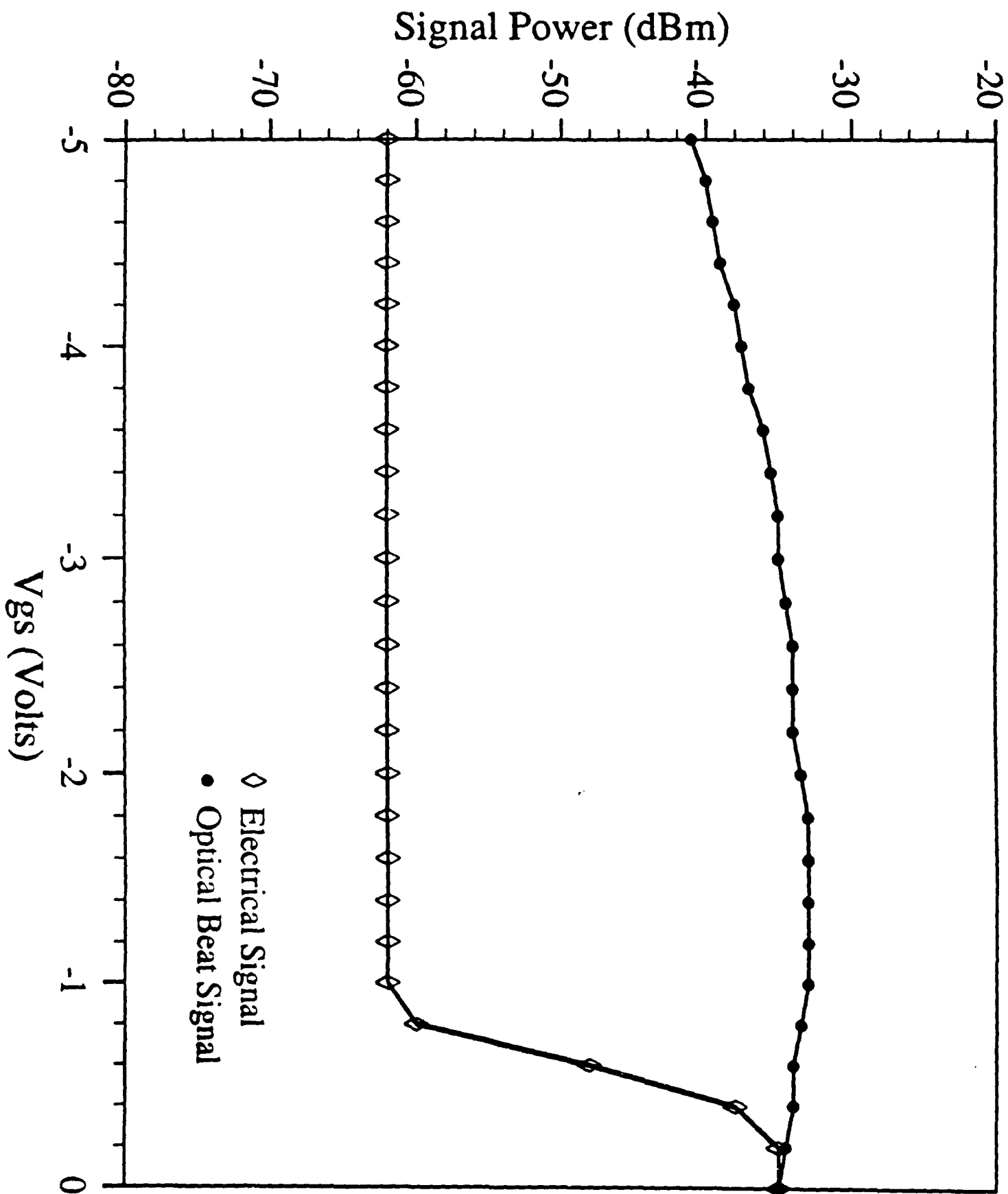
Fig. 5 S/N of second beat signal versus klystron power at different biases of V_{gs} and V_{ds}

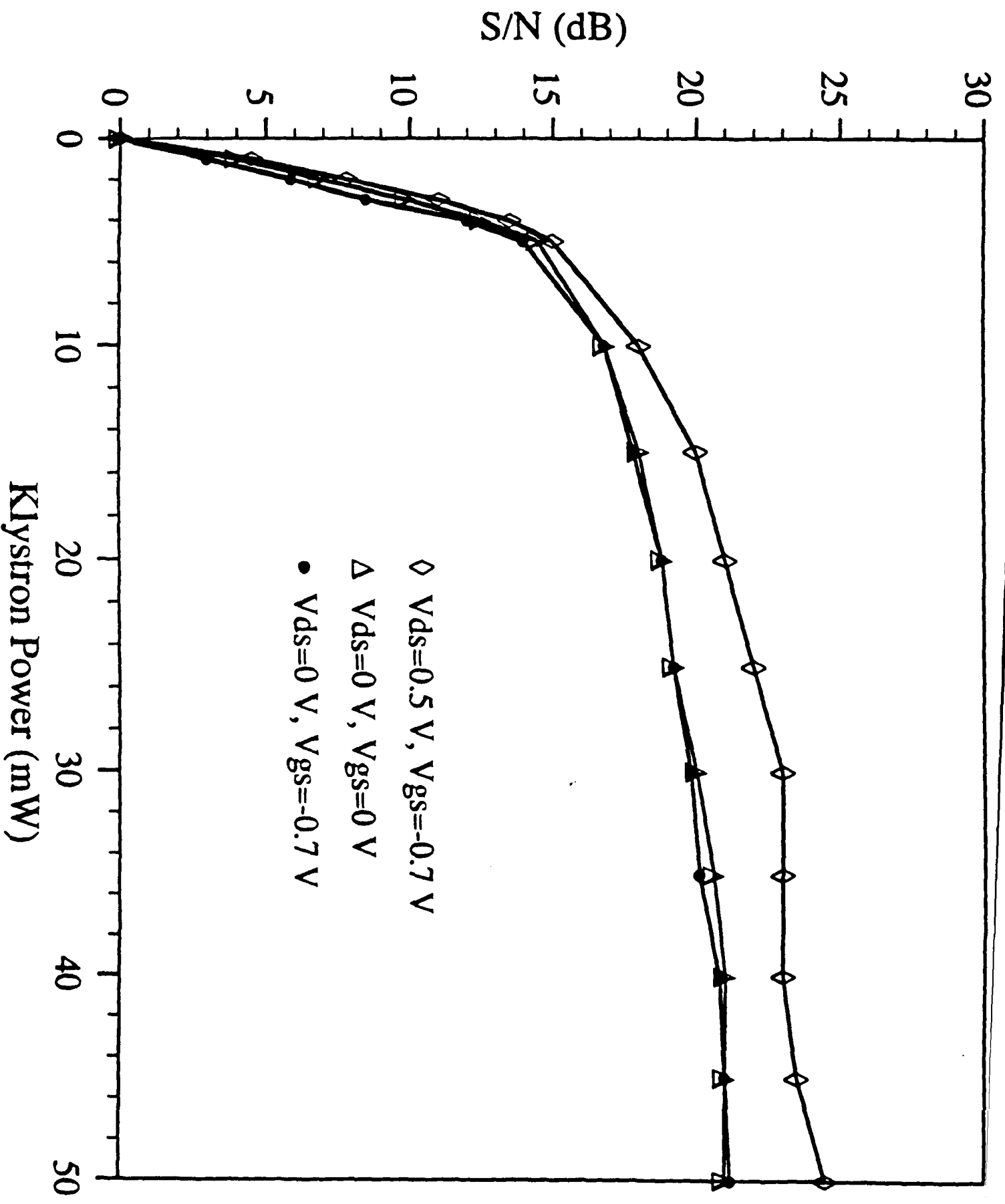
Fig. 6(a) Signal Power, (b) S/N, and (c) I_{ds} of second beat signal versus V_{ds} at 10 mW, 20 mW and 40 mW of klystron power. V_{gs} is at - 0.7 V.

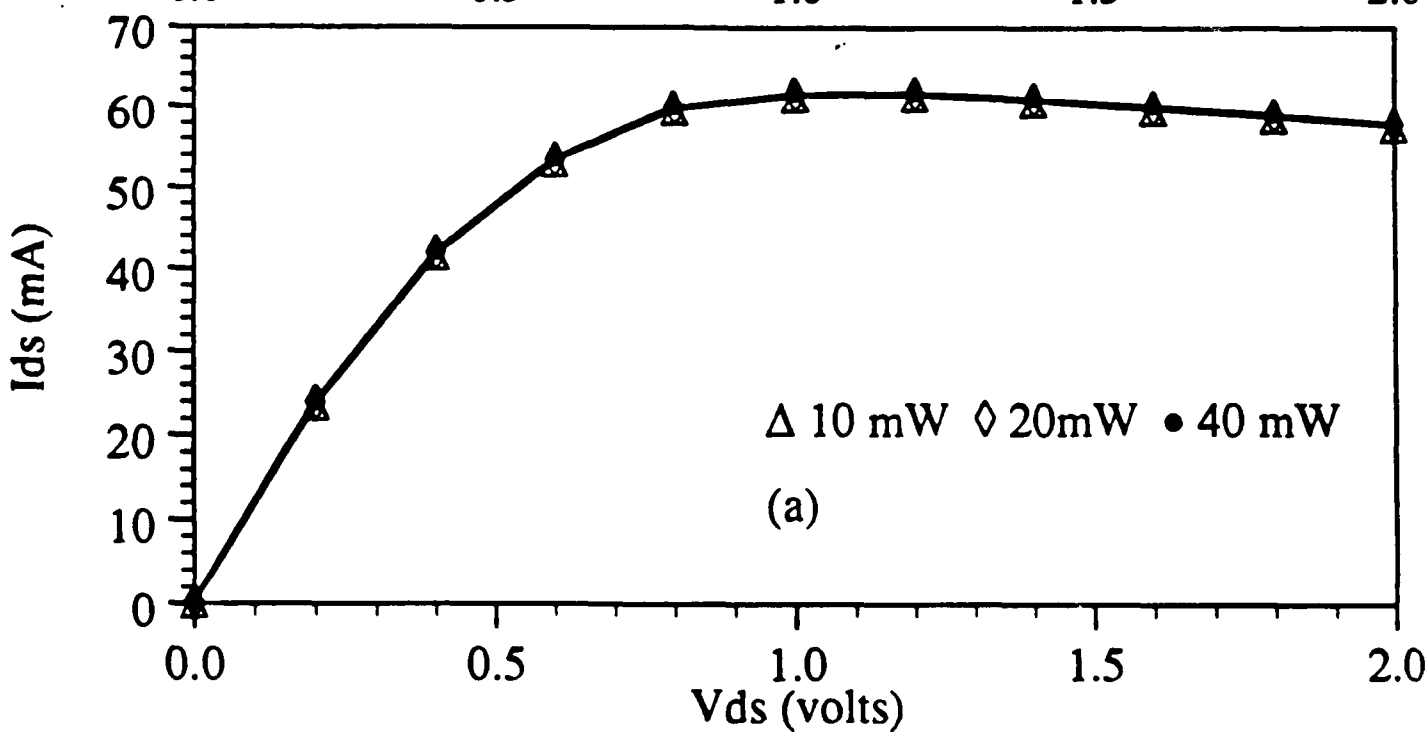
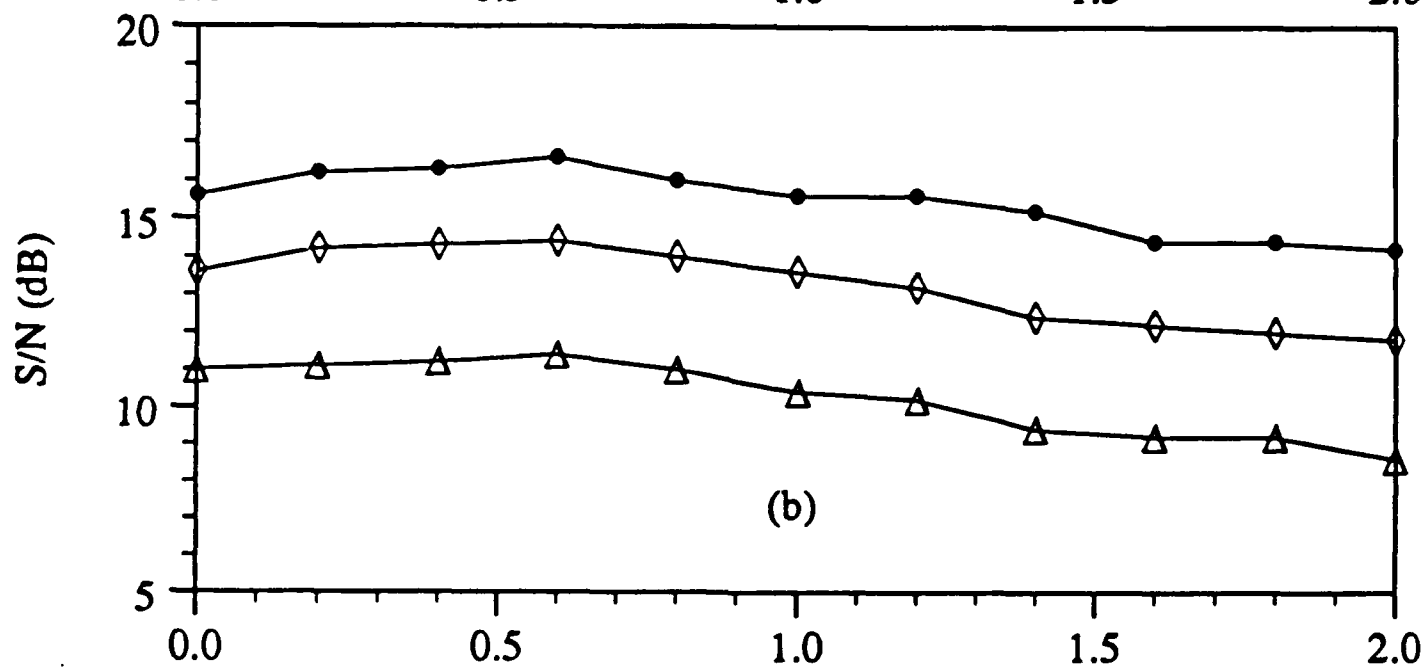
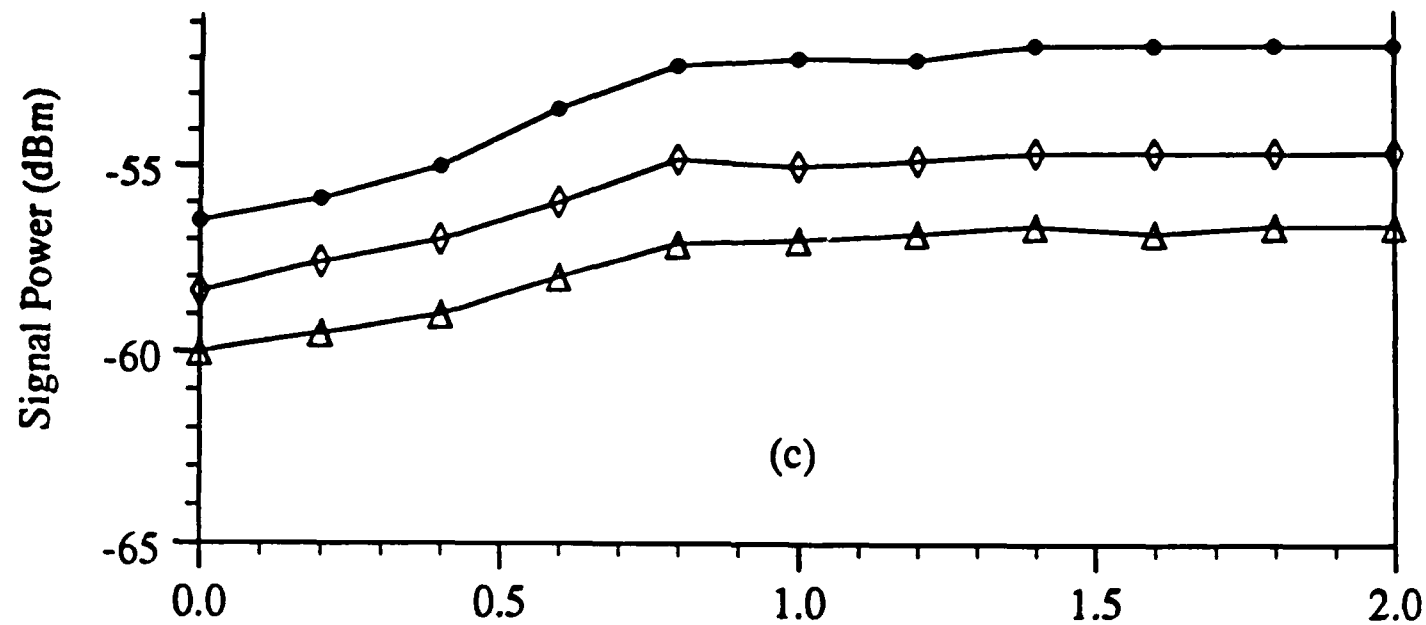












APPENDIX II

PICOSECOND OPTOELECTRONIC MEASUREMENT OF S-PARAMETERS AND OPTICAL RESPONSE OF AN AlGaAs/GaAs HBT

M. Matloubian*, H. Fetterman*, M. Kim†, A. Oki†, J. Camou†, S. Moss‡, and D. Smith‡

* Department of Electrical Engineering, University of California, Los Angeles, CA 90024

† TRW, Electronic Systems Group, Redondo Beach, CA 90278

‡ The Aerospace Corporation, The Chemistry and Physics Laboratory, LA, CA 90009

ABSTRACT

The S-parameters of an AlGaAs/GaAs heterojunction bipolar transistor (HBT) was measured using a picosecond optoelectronic system. The measured S-parameters show good agreement with those obtained using a conventional vector network analyzer. The optical response of the HBT was also measured using this system by directly illuminating the base-collector region. Used as a phototransistor the HBT showed pulsewidths with FWHM on the order of 15 picoseconds.

I. INTRODUCTION

In recent years there has been steady progress in the development of high frequency semiconductor devices and millimeter wave integrated circuits. Current high frequency transistors have cutoff frequencies well beyond the bandwidth that can be measured conveniently using conventional network analyzers. As a result the millimeter wave S-parameters of devices are commonly calculated from the extrapolation of small signal models of the transistor based on the microwave measurements. This extrapolation method has not been proven to be reliable in predicting behavior of devices at frequencies much higher than the measured frequency. By using external mixers the current bandwidth of network analyzers has been extended to about 110 GHz. But several difficulties arise in characterization of devices in the millimeter wave region. At high frequencies the transistors have to be mounted in test fixtures with waveguide-to-microstrip transitions. It is difficult to design wide bandwidth and low loss waveguide-to-microstrip transitions. The actual S-parameters of the device have to be de-embedded from the test fixture and with transitions having a high insertion loss erroneous results can be obtained. Another technique for characterization of high frequency transistors relies upon using six-port network analyzers [1]. Although this method does not require mixers, transitions and a complicated de-embedding procedure are still necessary to obtain the actual S-parameters of the device.

Use of time-domain techniques for characterization of devices offer advantages over frequency-domain techniques used by most network analyzers. By measuring the response of the device in the time-domain and taking the Fourier transform of the data the frequency performance of the device

can be calculated. The response of the device can be "windowed" in the time-domain and separated from reflections from transitions and other unwanted signals before it is analyzed. This will simplify de-embedding of the S-parameters of devices. But the use of TDNA for device characterization has been very limited due to a lack of availability of fast electrical pulse generators and oscilloscopes.

In order to improve and optimize performance of millimeter wave transistors it is important to have a simple technique for direct characterization of devices at very high frequencies. Picosecond optoelectronic techniques offer a new method for generation and sampling of ultrafast electrical pulses [2-4]. These electrical pulses can be used to test the response of high speed semiconductor devices [5] and integrated circuits [6,7]. Using photoconductive switches, picosecond electrical pulses can be generated and sampled at a very short distance from a device. Therefore, the high frequency signals do not have to travel through long sections of transmission lines and waveguide transitions, making this technique superior to conventional network analyzers. In this study S-parameters and optical response of AlGaAs/GaAs heterojunction bipolar transistors (HBTs) which are very promising devices for applications in microwave and millimeter wave integrated circuits [8] were characterized using the picosecond optoelectronic technique.

II. MEASUREMENT

An AlGaAs/GaAs HBT was mounted in an optoelectronic test fixture as shown in figure 1. The HBT tested had $3 \times 10 \mu m^2$ emitter and self-aligned base ohmic metal. The structure and fabrication of this device was previously reported in detail [9]. The microstrip lines were fabricated using

gold on silicon on sapphire (SOS) substrates. A thin layer of chromium was used to improve adhesion between the gold and the silicon surface. The sapphire substrates were about $125\ \mu\text{m}$ thick and the microstrip lines were designed to have a $50\ \Omega$ impedance. The silicon epi-layer was about $0.5\ \mu\text{m}$ thick and was heavily implanted with four different energies of silicon ions to shorten the carrier lifetime to subpicosecond levels.

On each side of the device there are two photoconductive switches which consist of $25\ \mu\text{m}$ gaps in the side microstrip lines. By applying a DC bias to a photoconductive switch and focusing a picosecond laser beam on the gap fast electrical pulses are generated that propagate on the center transmission line. A second photoconductive switch is used for sampling of the electrical pulses. The center microstrip lines, in addition to being used for launching the fast electrical pulses, are also used to supply the DC biases to the transistor. This will allow the characterization of the device at any bias point. The center microstrip lines are made long enough such that the reflections from the bias lines arrive at the sampling switch outside the "time-window" necessary to measure the response of the device.

Figure 2 shows the schematic of the picosecond optoelectronic system used to measure the S-parameters of the HBT. The pump source for the dye laser is an actively modelocked frequency doubled Nd:YAG laser putting out 70 ps pulses at a wavelength of 532 nm and repetition rate of 14 ns. The dye laser uses Rhodamine 6G (R6G) dye and has a cavity dumper which allows the repetition rate of the pulses to be varied. The dye laser is operated at a wavelength of 600 nm with repetition rate of 140 ns and average power of 70 mW. The optical pulses have a pulsewidth of 1.2 ps measured using an optical autocorrelator. The train of picosecond laser pulses from the

dye laser is split into two beams. The first beam passes through an optical chopper and is focused onto one of the pulse generating switches on the optoelectronic test fixture. The second beam travels a path with a variable length and is focused onto one of the sampling switches. The length of this path can be varied very precisely by movement of a computer controlled translation stage. The pathlength of the second beam can be varied such that it arrives at the sampling switch, before, during, or after the arrival of the optical pulse at the generation switch. The output from the sampling switch is fed into the input of the lock-in amplifier. Depending on which one of the four optical switches is used as the generator and which one as the sampler the HBT can be characterized completely in the time-domain. By taking the Fourier transform of the reflected and transmitted signals and normalizing it to the Fourier transform of the appropriate input signal the S-parameters of the device can be determined [5].

III. RESULTS

Figure 3 shows the time-domain response of the HBT measured by the picosecond optoelectronic system. In figure 3(a) the input reflection of the device was measured by using switch 1 as the pulse generator and sampling switch 2. The first peak in the figure corresponds to the electrical autocorrelation of the input pulse to the device. As the delay of the sampling pulse was varied the reflection from the bond wires and then the reflection from the device was obtained. To analyze the data the autocorrelation signal was separated from the bond wires and device reflections. Then the reflection of the bond wires was also "windowed out". Since a small section of microstrip transmission line separates the device from the sampling point

the reference plane of the measurement has to be moved to account for the phase change. This can be done very simply in the time-domain by time shifting the reflected signal. Then by taking the ratio of the Fourier transform of the reflected signal to the autocorrelation signal the input reflection coefficient (S_{11}) of the HBT can be determined.

To measure the input gain of the transistor (S_{21}) switch 1 was used as the pulse generator and switch 4 as the sampler. The result shown in figure 3(c) shows the electrical pulse that has been broadened to about 35 ps by passing through the transistor. Again this pulse has to be time-shifted to account for the short length of microstrips on both side of the device. S_{21} of the HBT can be determined by taking the Fourier transform of this pulse and normalizing it to the effective input signal to the transistor. A similar procedure was also used to measure the reverse transmission and output reflection of the HBT (figures 3(b) and 3(d)) and then S_{12} and S_{22} were determined from these measurements.

The optically measured S-parameters of the HBT are shown in figure 4 for the frequency range of 1-40 GHz. For comparison S-parameters of a similar HBT was measured using on-wafer RF probes and a conventional vector network analyzer (HP 8510). The network analyzer measurements for the range of 1-26 GHz are also shown in figure 4. Except for some discrepancies the two measurement techniques are relatively in good agreement. The discrepancies are believed to be due to the effect of the bond wires on the optically measured S-parameters and slight differences between the two HBTs tested.

IV. OPTICAL RESPONSE

HBTs are also important in applications such as high speed optical detectors for optical communication [10], and for optical control of MMICs [11]. As a result, it is important to measure the speed of the HBT as a photodetector. Using picosecond optoelectronic techniques the speed of photodetectors can be measured [12]. The same optoelectronic test fixture used in the S-parameter measurements was used to measure the speed of the HBT as an optical detector. In this case the optical generation pulse was focused onto the HBT and the output signal was sampled at switch 4. In these measurements the base of the HBT was floating and the device was tested as a phototransistor. Since this device has a self-aligned base metal the separation between the base fingers and the emitter edge is only about $0.15\text{ }\mu\text{m}$ [9]. As a result the laser pulse penetrates the device only between the base and the collector fingers. For a wavelength of 600 nm the penetration depth in GaAs is about $3000\text{ }\text{\AA}$ [13]. With base and collector thicknesses of $1500\text{ }\text{\AA}$ and $5000\text{ }\text{\AA}$ respectively most of the light absorption will occur within these two layers.

The optical response of the HBT for a collector-to-emitter voltage of 3 volts is shown in figure 5. The pulse has a FWHM of about 15 ps which is very fast considering the device does not have a built in field in the base region. The pulsewidth of the optical response of the HBT vs. the collector-to-emitter voltage is shown in figure 6. As can be seen from this figure the pulsewidth decreases from about 55 ps at 0 V to 15 ps at 3 V and remains constant for higher voltages. Comparing figure 5 with figure 3(c) it is observed that a much faster response time was obtained by directly injecting an optical signal into the HBT (bypassing the base input). This demon-

strates that this device is intrinsically fast and the electrical performance is limited by the base resistance.

V. CONCLUSION

S-parameters of an HBT were measured up to 40 GHz using a picosecond optoelectronic technique. The results show good agreement with measurements of a similar HBT using on-wafer RF probes and a conventional vector network analyzer over the bandwidth of the network analyzer (26 GHz). The optoelectronically measured S-parameters of the device were limited by the cutoff frequency of the device. The system itself has a bandwidth greater than 150 GHz. New HBTs with higher cutoff frequencies are currently being characterized. The optical response of the HBT was also measured using this system. HBTs appear to be very promising as high speed optical detector. Although in this study the optical switches were fabricated on a different substrate from the device, it is possible to integrate optical switches with devices on the same wafer and remove the effect of the bond wires on the measurements. This will allow on-wafer measurement of S-parameters over a wide bandwidth. But since the switches occupy a large area of the wafer, the number of test patterns will be limited. Other techniques for on wafer measurement of S-parameters are currently being investigated.

ACKNOWLEDGEMENT

The UCLA portion of this work was supported by TRW under the California MICRO and by the Air Force Office of Scientific Research.

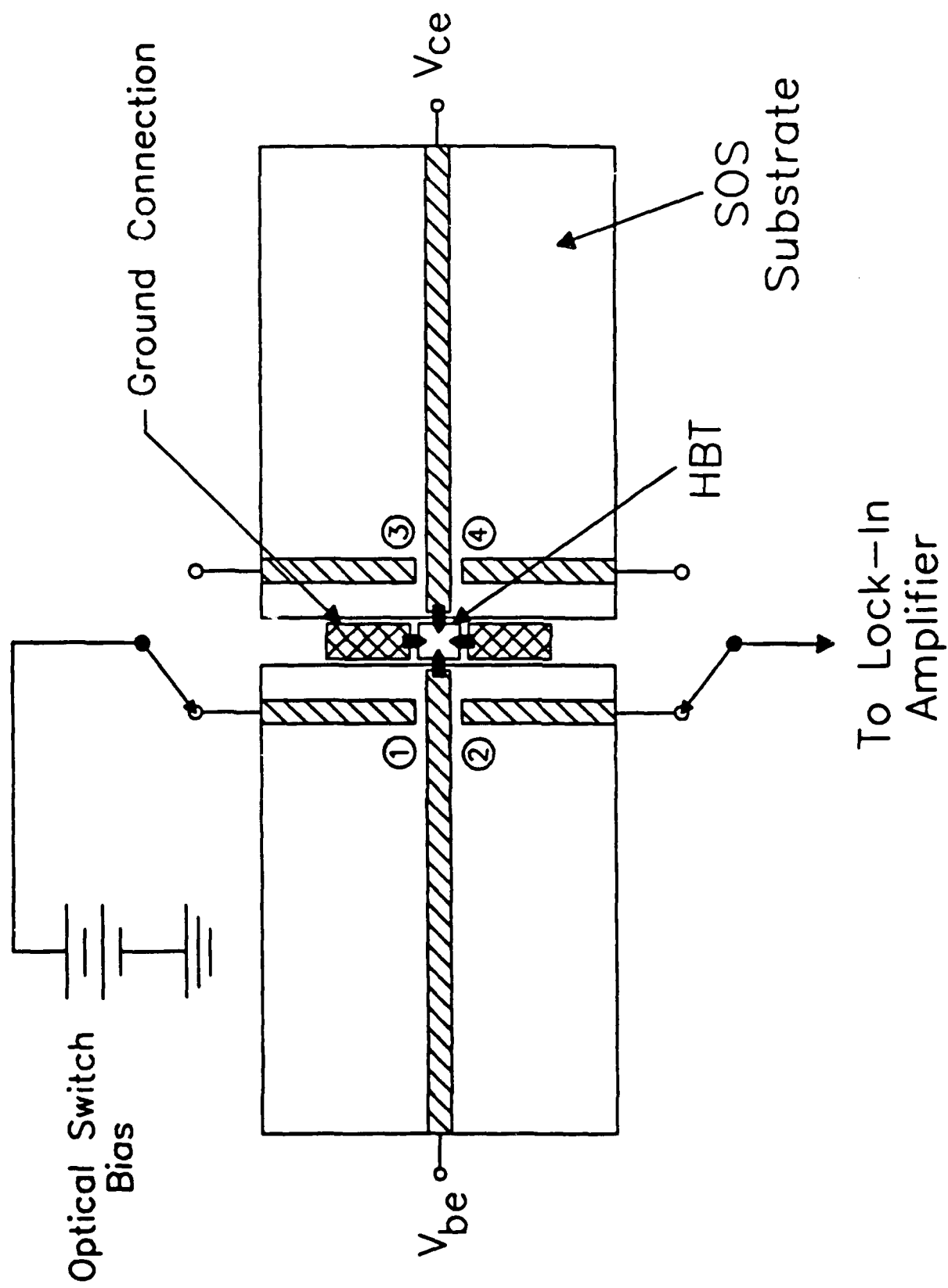
REFERENCES

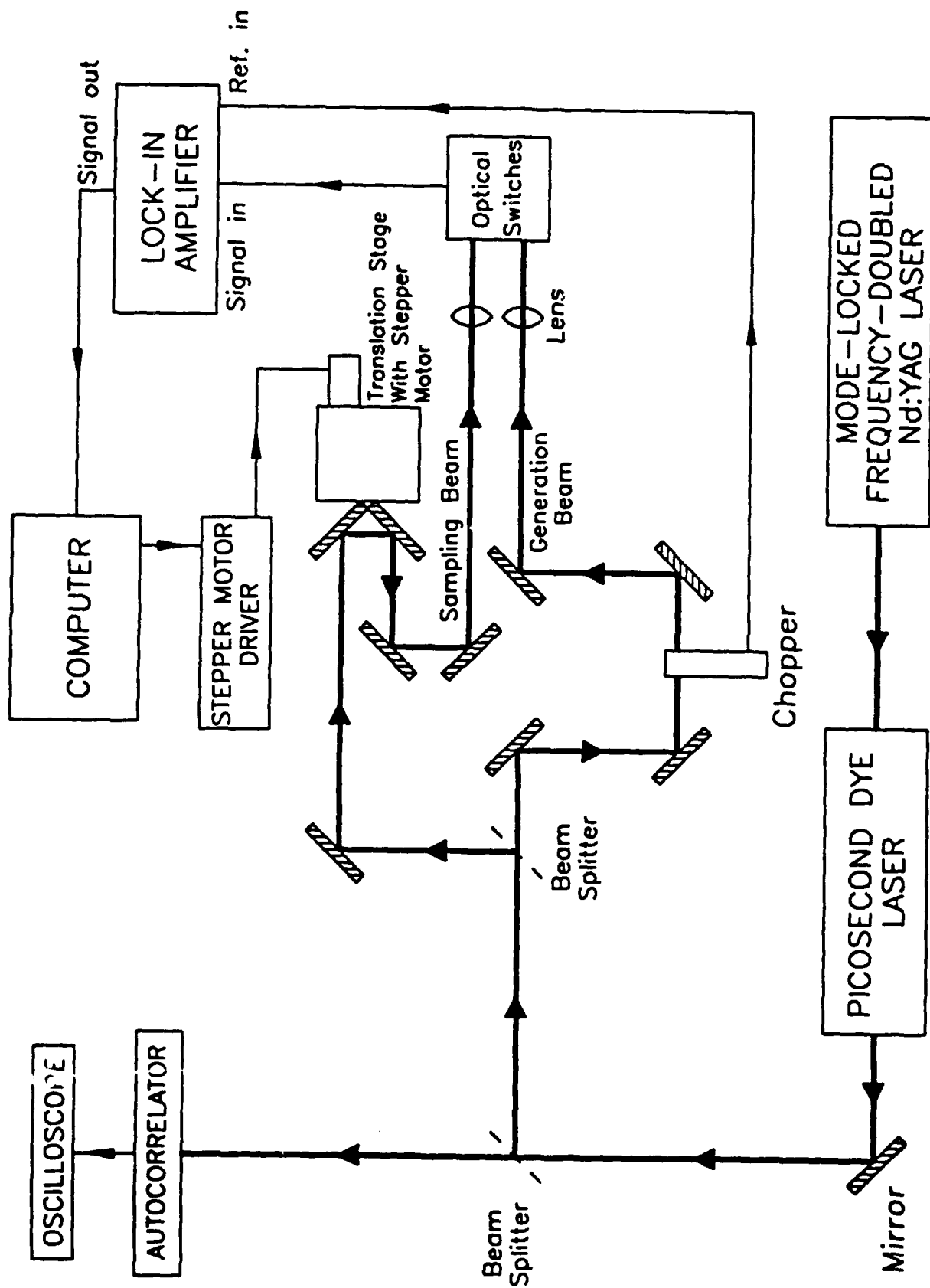
- [1] J. Schaffner, F. Oshita, H. Fetterman, J. Berenz, K. Nakano, and H. C. Yen, "Two-port s-parameter characterization of high electron mobility transistors at millimeterwave and microwave frequencies," *IEEE MTT-S Int. Microwave Symp. Digest*, 1988, pp. 233-236.
- [2] D. H. Auston, "Impulse response of photoconductors in transmission lines," *IEEE J. Quantum Electron.*, vol. QE-19, pp. 639-648, April 1983.
- [3] K. J. Weingarten, M. J. W. Rodwell, and D. M. Bloom, "Picosecond optical sampling of GaAs integrated circuits," *IEEE J. Quantum Electron.*, vol. QE-24, pp. 198-220, Feb. 1988.
- [4] J. A. Valdmanis, and G. Mourou, "Subpicosecond electrooptic sampling: Principles and applications," *IEEE J. Quantum Electron.*, vol. QE-22, pp. 69-78, Jan. 1986.
- [5] D. E. Cooper and S. C. Moss, "Picosecond optoelectronic measurement of high frequency scattering parameters of a GaAs FET," *IEEE J. Quantum Electron.*, vol. QE-22, pp. 94-100, Jan. 1986.
- [6] P. Polak-Dingles, H-L. Hung, T. Smith, H. Huang, K. Webb, and C. H. Lee, "On wafer characterization of monolithic millimeter-wave integrated circuits by picosecond optical electronic technique," *IEEE MTT-S Int. Microwave Symp. Digest*, 1988, pp. 237-240.
- [7] R. K. Jain, D. E. Snyder, and K. Stenersen, "A new technique for the measurement of speeds of Gigahertz digital IC's," *IEEE Electr. Dev. Lett.*, vol. EDL-5, pp. 371-373, Sept. 1984.

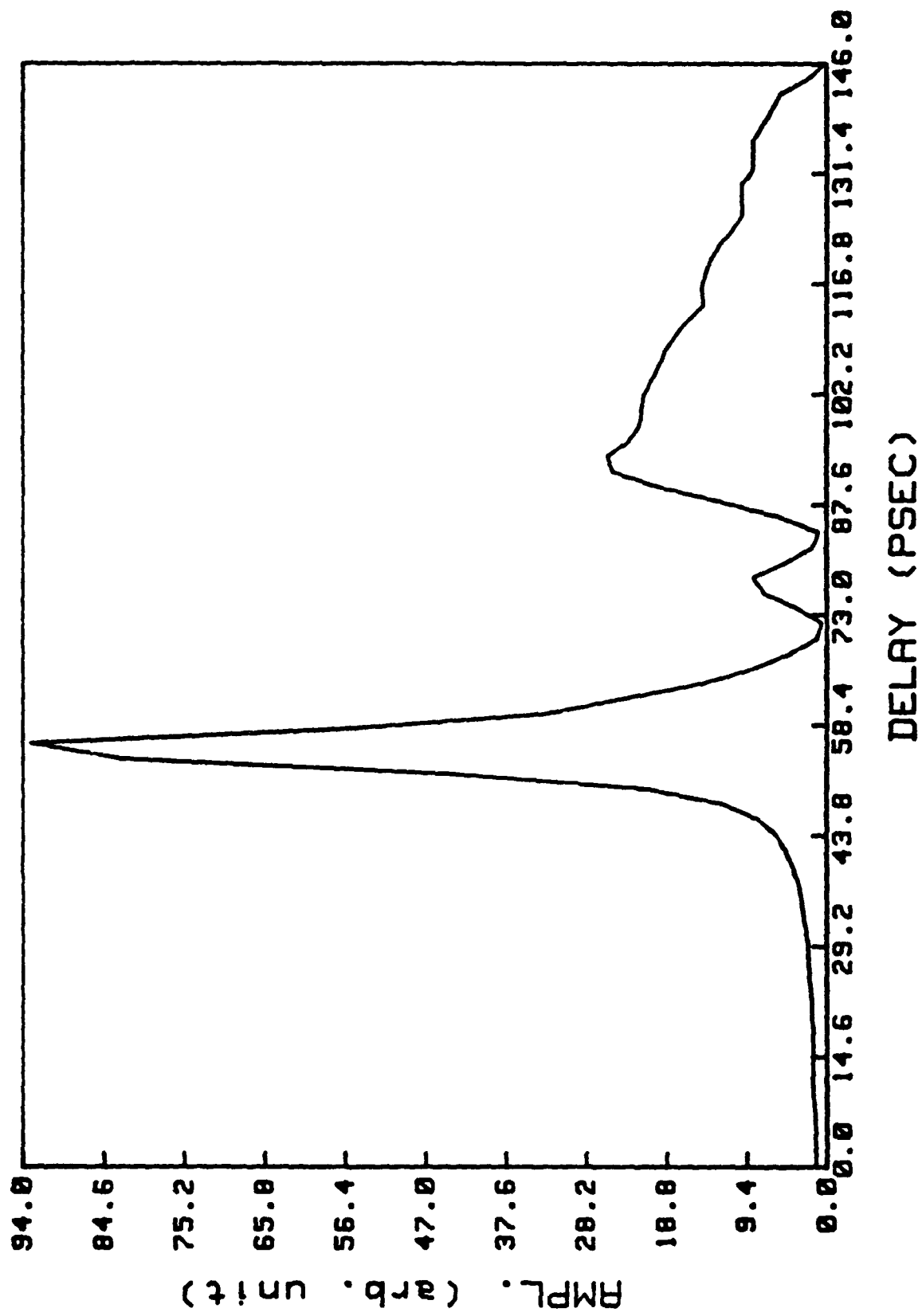
- [8] P. M. Asbeck, M. F. Chang, K. C. Wang, D. L. Miller, G. J. Sullivan, N. H. Sheng, E. Sovero, and J. A. Higgins, "Heterojunction bipolar transistors for microwave and millimeter-wave integrated circuits," *IEEE Trans. Microwave Theory Tech.*, vol. MTT-35, pp. 1462-1470, Dec. 1987.
- [9] A. K. Oki, M. E. Kim, G. M. Gorman, and J. B. Camou, "High-performance GaAs heterojunction bipolar transistor logarithmic IF amplifier," *IEEE Trans. Microwave Theory Tech.*, vol. MTT-36, pp. 1958-1965, Dec. 1988.
- [10] F. Capasso, W. T. Tsang, C. G. Bethea, A. L. Hutchinson, and B. F. Levine, "New graded band-gap picosecond phototransistor," *Appl. Phys. Lett.*, vol. 42, pp. 93-95, Jan. 1983.
- [11] R. N. Simons, "Microwave performance of an optically controlled Al-GaAs/GaAs high electron mobility transistor and GaAs MESFET," *IEEE Trans. Microwave Theory Tech.*, vol. MTT-35, pp. 1444-1455, Dec. 1987.
- [12] D. H. Auston and P. R. Smith, "Picosecond optical electronic sampling: Characterization of high-speed photodetectors," *Appl. Phys. Lett.*, vol. 41, pp. 599-601, Oct. 1982.
- [13] S. M. Sze, "Physics of Semiconductor Devices," 2nd. Edn., Wiley-InterScience, 1981.

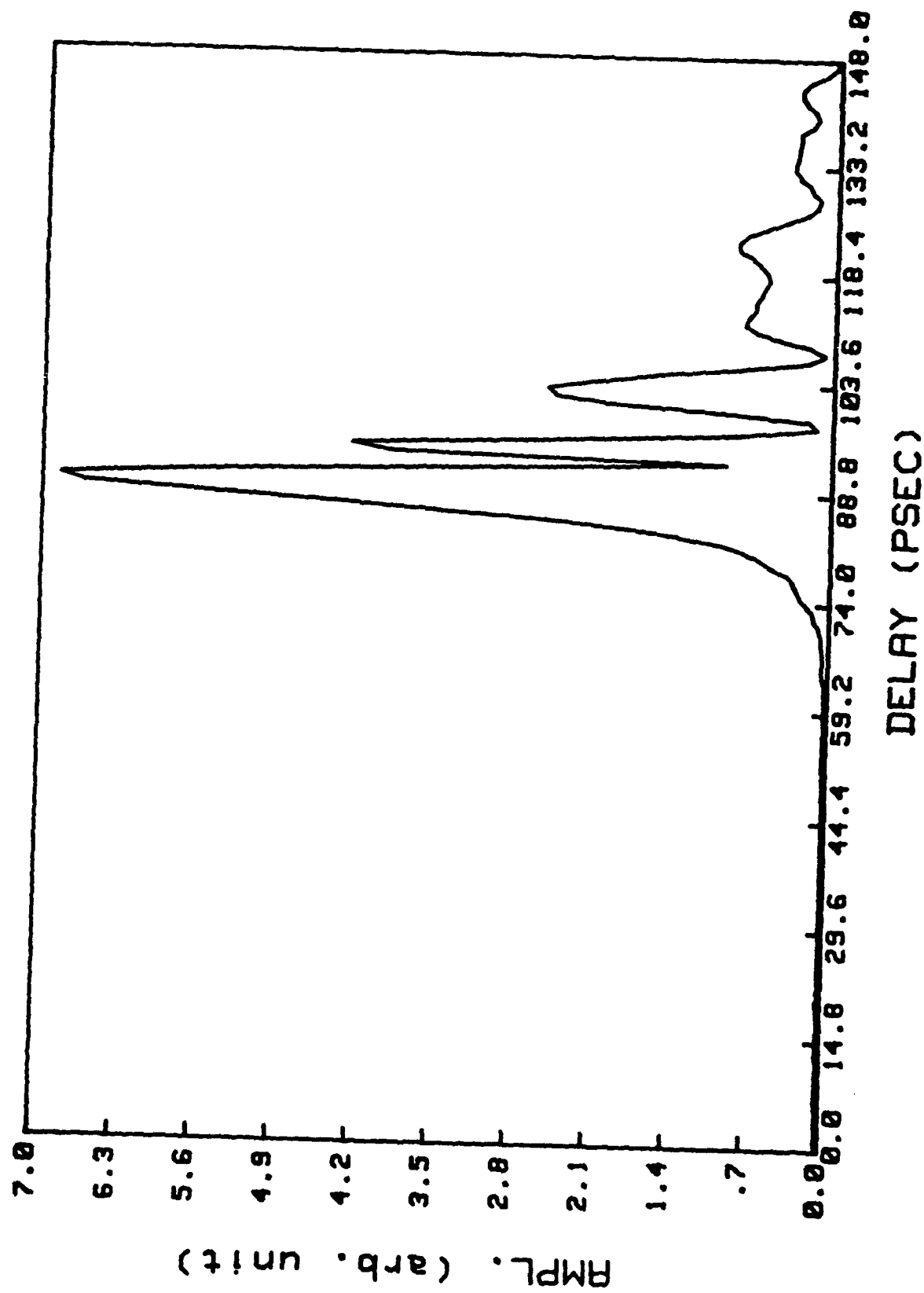
LIST OF FIGURES

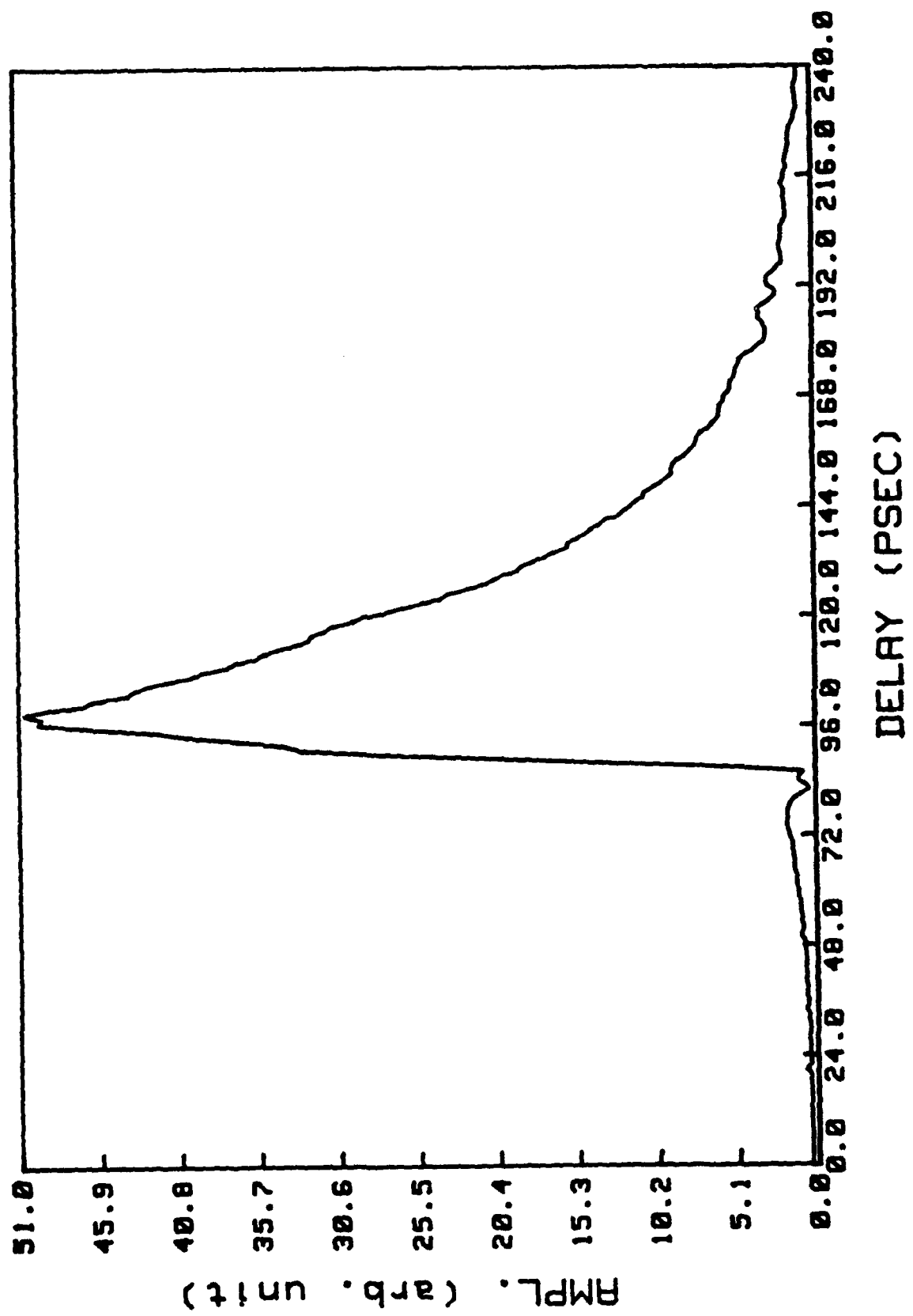
- Fig. 1 Picosecond optoelectronic test fixture with an HBT attached to the center microstrip lines.
- Fig. 2 Experimental setup for generation and sampling of fast electrical pulses using a computer controlled optical time delay.
- Fig. 3 (a) Input reflection measurement of the HBT using switch 1 as the pulse generator and sampling switch 2. (b) Reverse transmission measurement using switch 3 as the pulse generator and sampling switch 2. (c) Forward transmission measurement using switch 1 as the pulse generator and sampling switch 4. (d) Output reflection measurement using switch 3 as the pulse generator and sampling switch 4.
- Fig. 4 Comparison between optically measured S-parameters of the HBT (left figures) and network analyzer measurements (a) S_{11} (b) S_{12} (c) S_{21} (d) S_{22} .
- Fig. 5 Optical response of the HBT used as a phototransistor for $V_{ce} = 3V$.
- Fig. 6 Variation of the optical response pulsewidth as a function of the collector-to-emitter voltage.

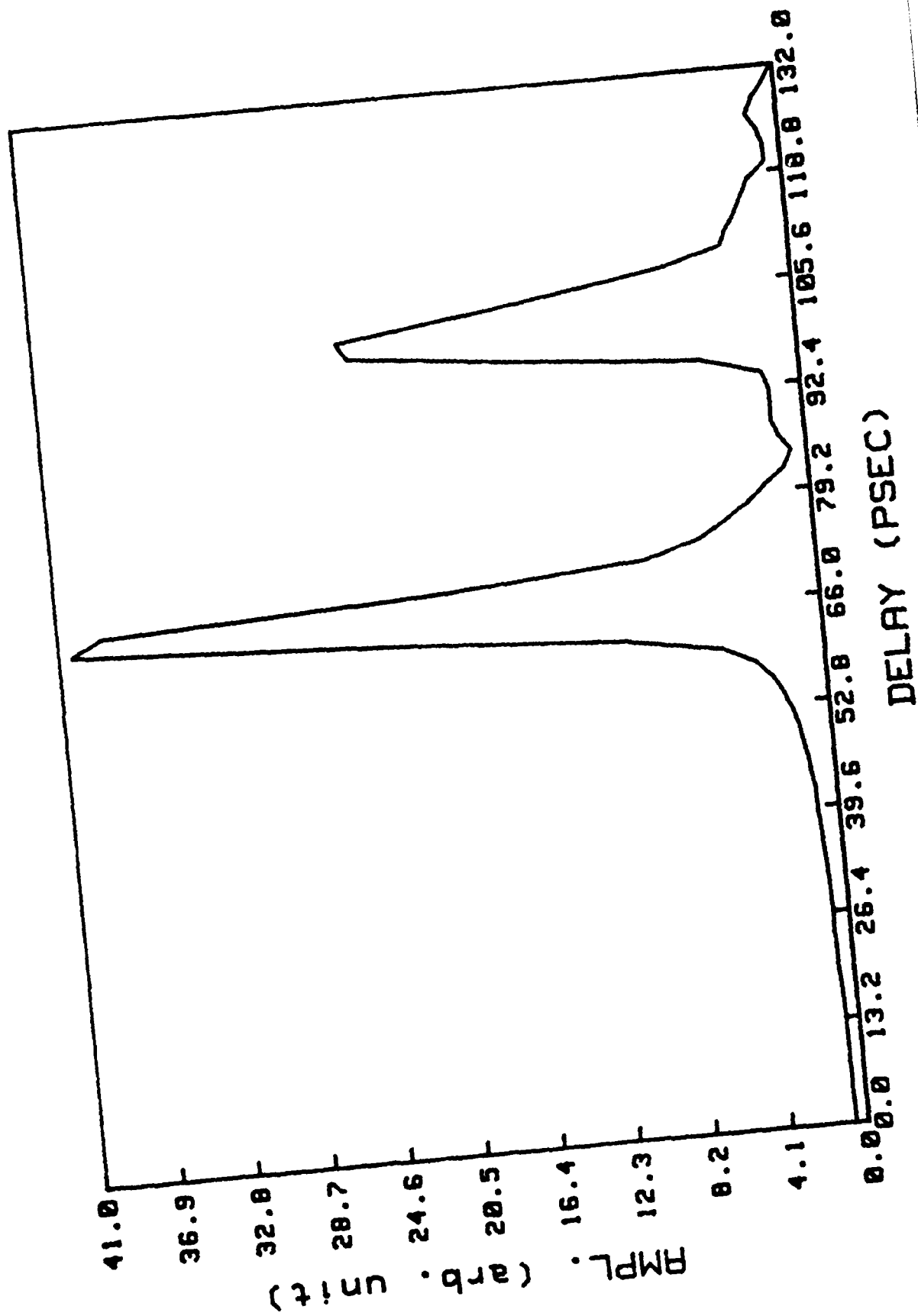




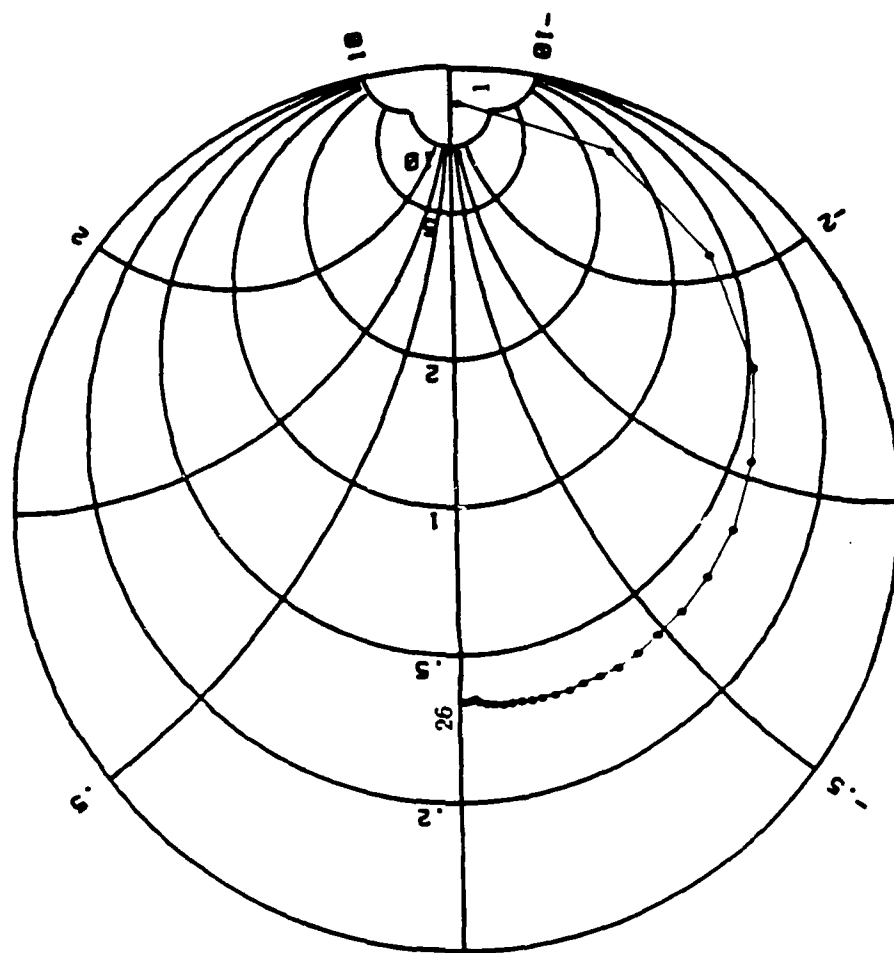




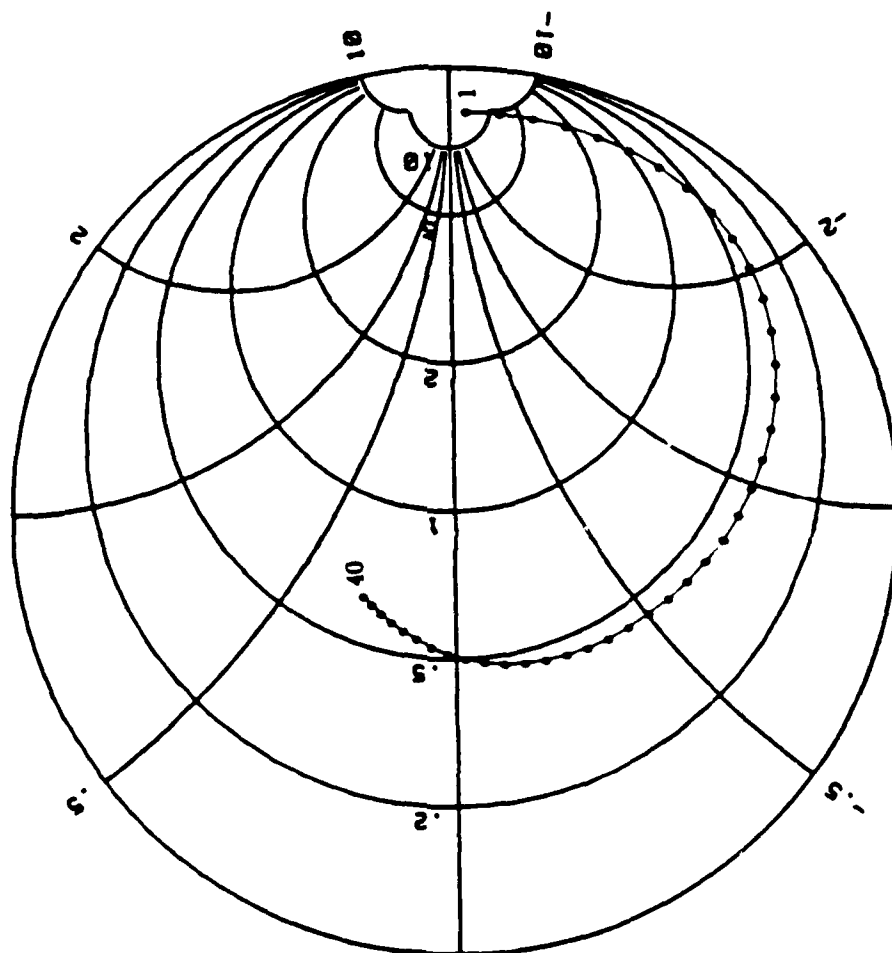




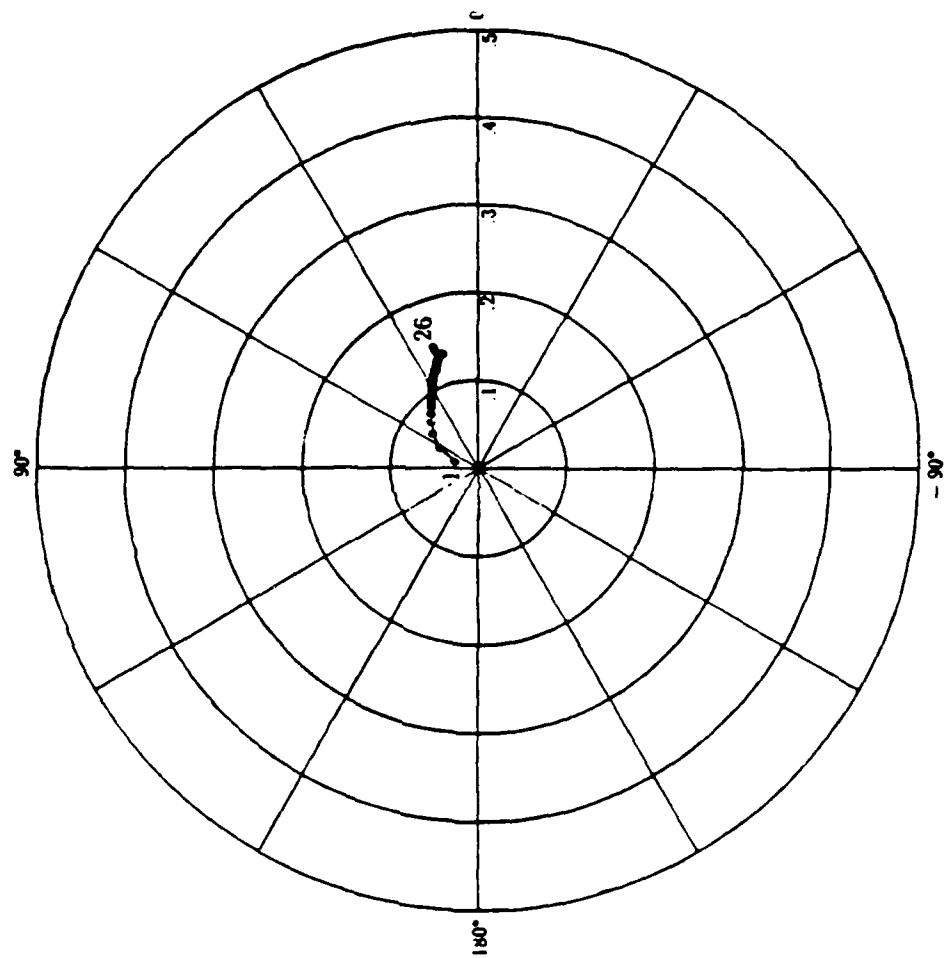
Network Analyzer Measurement



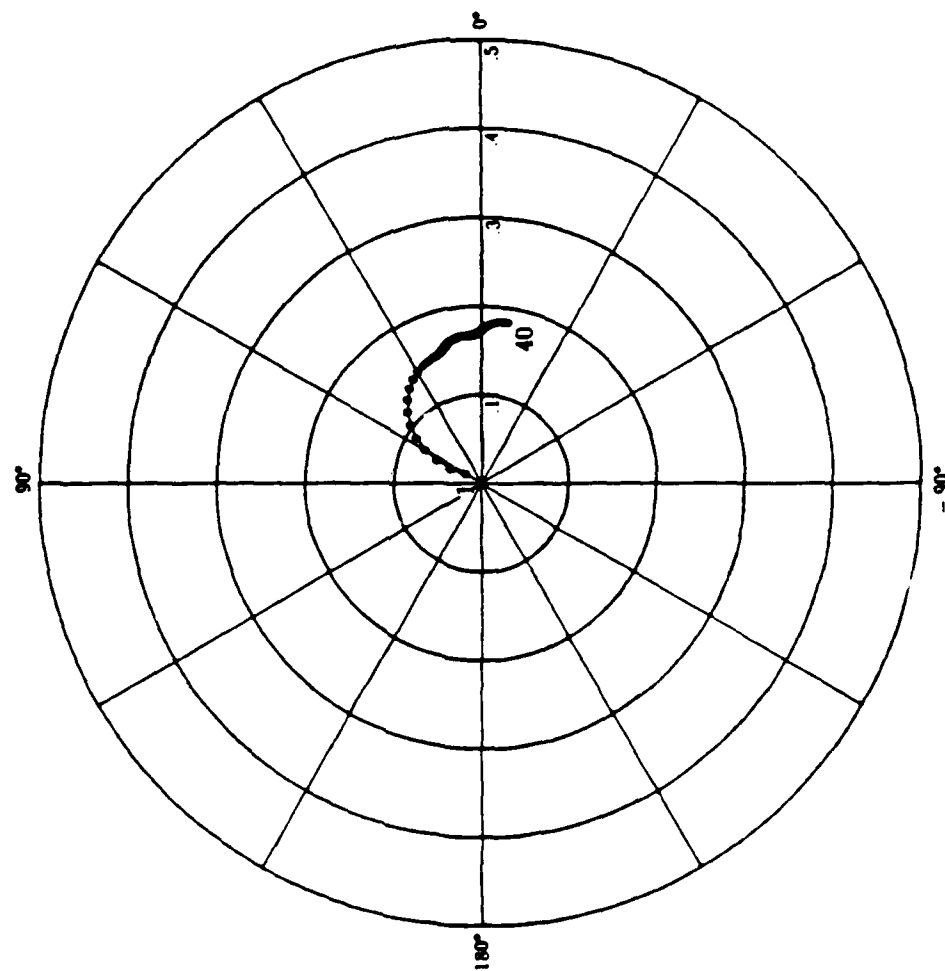
Optoelectronic Measurement



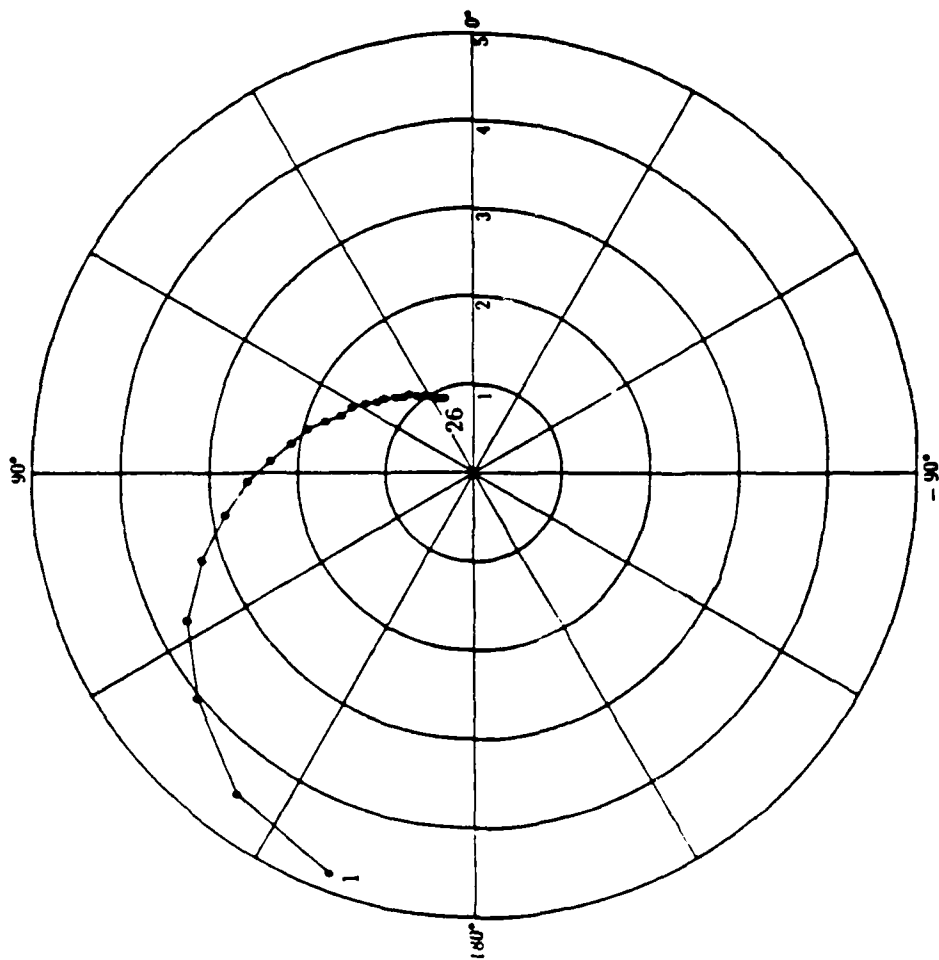
Network Analyzer Measurement



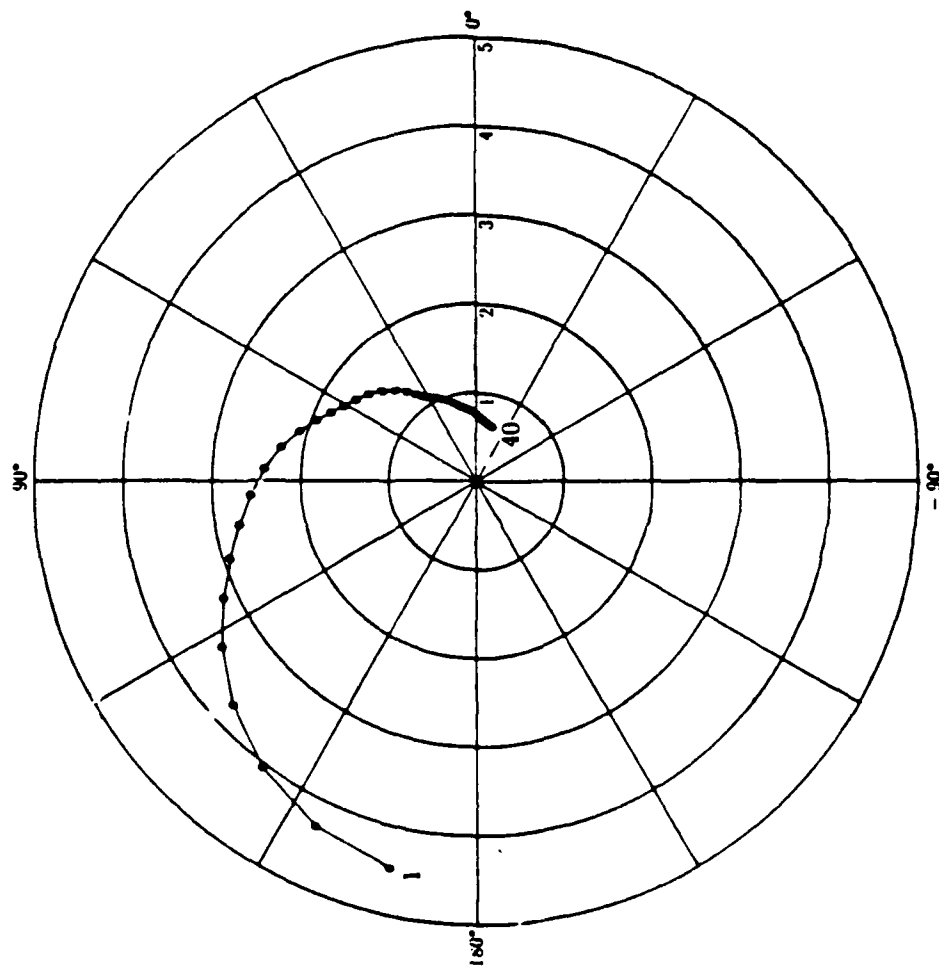
Optoelectronic Measurement



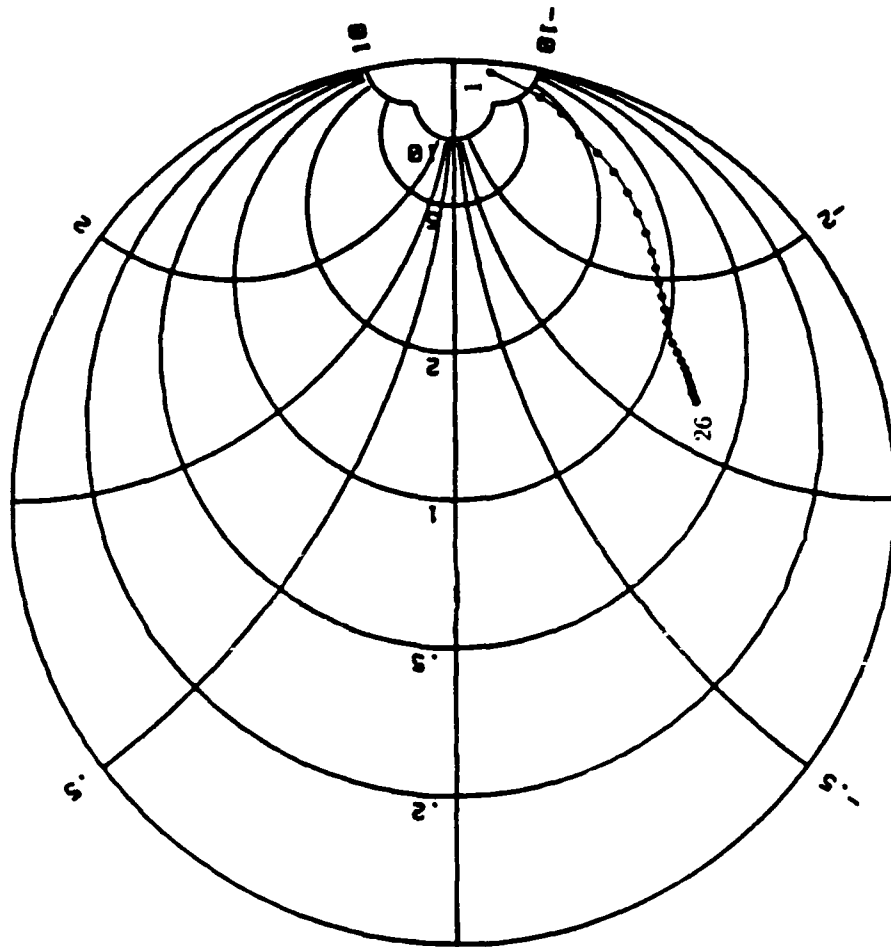
Network Analyzer Measurement



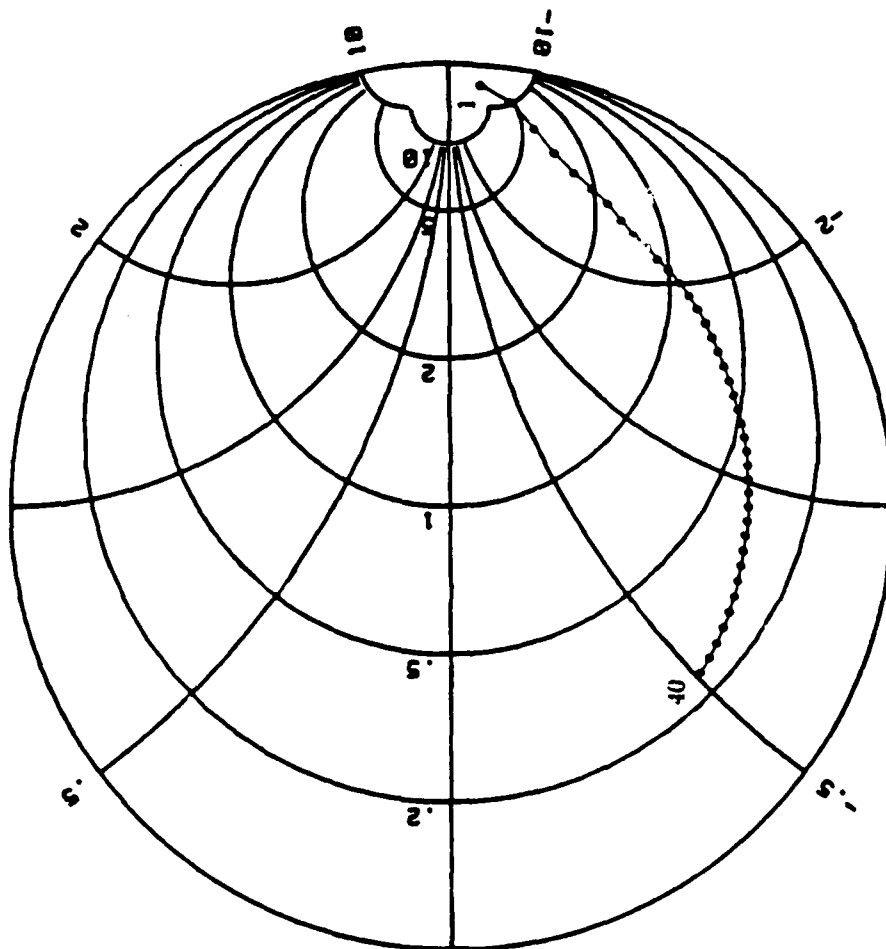
Optoelectronic Measurement

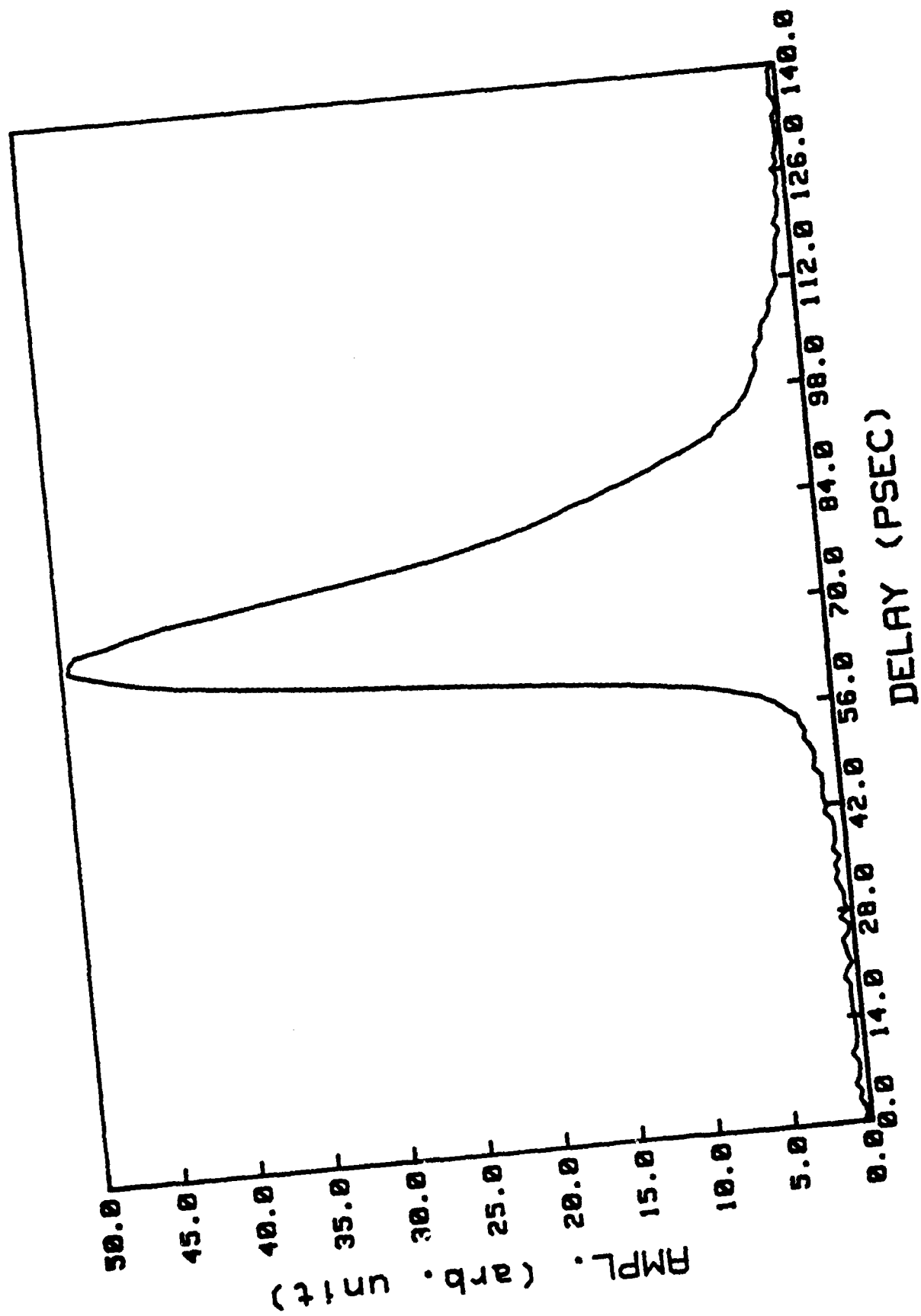


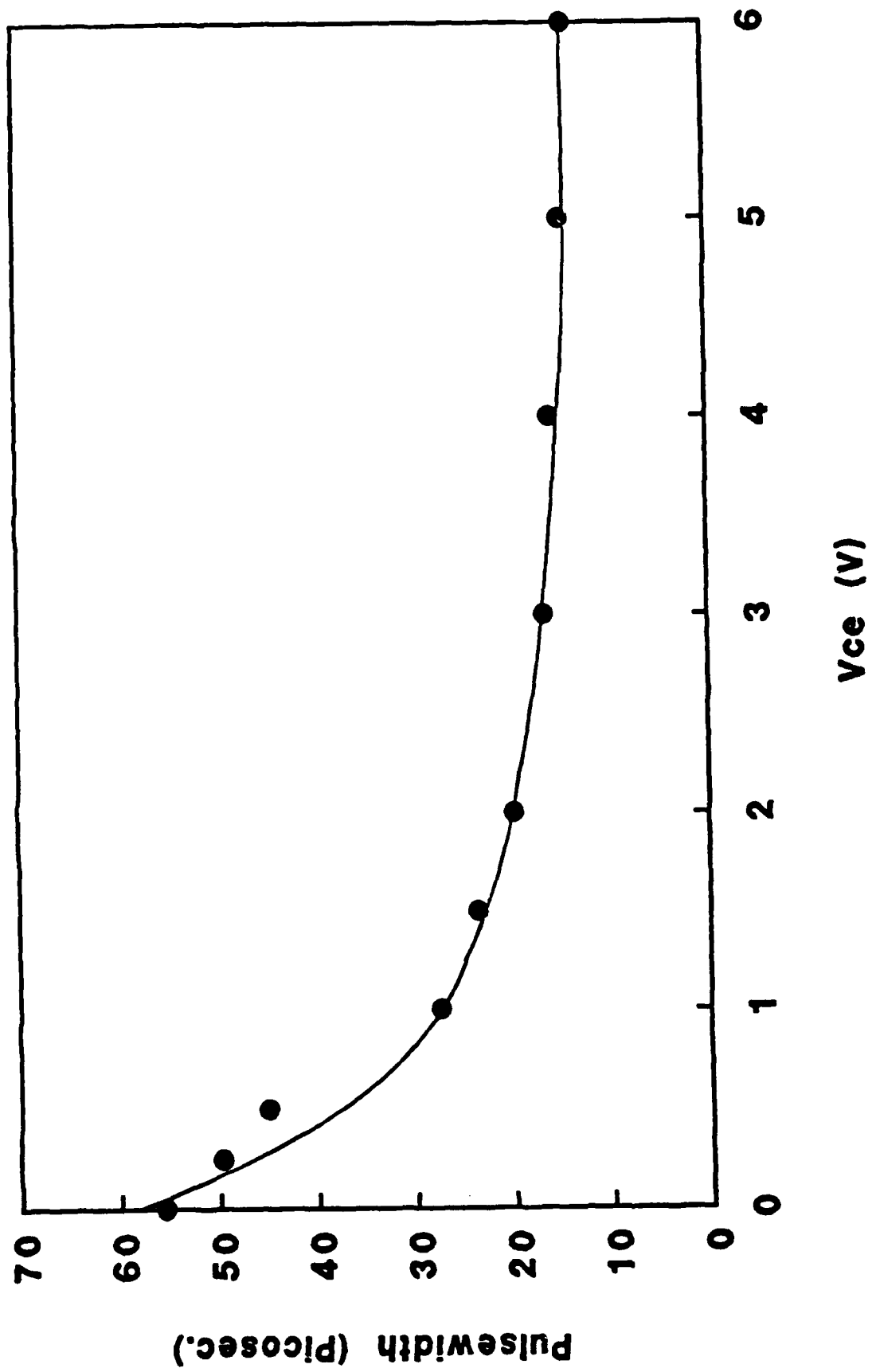
Network Analyzer Measurement



Optoelectronic Measurement







An Analytic Model for HEMT's Using New Velocity-Field Dependence 6

CHIAN-SERN CHANG AND HAROLD R. FETTERMAN, SENIOR MEMBER, IEEE

Abstract—An analytic model is developed for the output current-voltage characteristics and microwave-signal parameters of high electron mobility transistors (HEMT's). In this model, the GSW equation is used to approach the behavior of electron drift velocity versus electric field. The resulting I - V curves are in excellent agreement with experimental data. In order to predict the microwave performance of these devices, this model is then used to derive the small-signal parameters, transconductance, channel conductance, and gate capacitance.

I. INTRODUCTION

THE HIGH electron mobility transistor (HEMT) has been the focus of research on high-speed and high-frequency semiconductor devices since it was introduced [1] in 1980. A reliable analytic model is needed for fast and economical design of semiconductor components and integrated circuits.

Recently, many researchers [2]–[5] have modeled HEMT I - V characteristics by using Trofimenkoff's velocity-field dependence and adjusting parameters to fit experimental data. We have reported [6] that the velocity-field dependence given by Giblin *et al.* [7] (GSW equation) fits the experimental data better than that given by Trofimenkoff. And we have used the GSW equation to describe the electron behavior of the velocity versus electric field in HEMT and to derive the I - V characteristics. In this paper, we extend this model to include the channel conductance in the saturation region by solving the two-dimensional Poisson equation and the parasitic resistance due to the undoped GaAs buffer layer. This extended model is then used to derive the small-signal parameters, transconductance, gate capacitance, and channel conductance for microwave performance. Without adjusting the parameters, the theoretical calculations are in excellent agreement with the experimental data measured by Drummond *et al.* [8].

II. REVIEW OF THE MODEL

Fig. 1 shows a band diagram of a heterostructure under the influence of a Schottky gate in contact with the larger gap semiconductor. The AlGaAs layer in a HEMT is fully depleted under normal operating conditions and the electrons are confined to the heterointerface. The two-dimen-

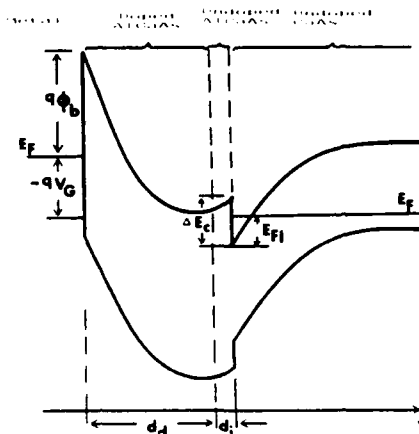


Fig. 1. The band diagram of AlGaAs/GaAs heterostructures in the 2DEG control regime by a Schottky gate.

sional electron gas (2DEG) density depends on the gate voltage V_G and the potential $V(x)$ in the 2DEG channel according to the following equation [6]:

$$n_s(x) = \frac{q\epsilon_2}{q^2d + \epsilon_2a} (V_G - V(x) - T_{TO}) \quad (1)$$

where ϵ_2 is the permittivity of AlGaAs, d the total thickness of AlGaAs layer, $a = 0.125 \times 10^{-12} \text{ eV} \cdot \text{cm}^2$, and

$$V_{TO} = \phi_b - \frac{\Delta E_c}{q} + \frac{\Delta E_{F1}}{q} - \frac{qN_D d_d^2}{2\epsilon_2} \quad (2)$$

In (2), ϕ_b represents the Schottky-barrier height between the gate metal and the AlGaAs, ΔE_c the conduction band energy discontinuity, $\Delta E_{F1} = 0$ at 300 K and $\Delta E_{F1} = 0.025 \text{ eV}$ at 77 K and below, N_D the doping density of the doped AlGaAs layer, and d_d the thickness of the doped AlGaAs layer.

The drain current is given by

$$I_D = qn_s(x) Zv(x) \quad (3)$$

where Z is the gate width and $v(x)$ the electron drift velocity.

The GSW equation for velocity-field dependence is

$$v = v_s(1 - e^{-\xi/\xi_c}) \quad (4)$$

where v_s is the saturation drift velocity, $\xi_c = v_s/\mu$, and μ the low-field mobility.

Using $\xi = dV/dx$ and substituting (4) into (3) yields

Manuscript received September 16, 1986; revised February 26, 1987. This work was partially supported by the Department of the Navy, Office of Naval Research, under Contract N00014-84-K-0430.

The authors are with the Department of Electrical Engineering, University of California, Los Angeles, CA 90066.

IEEE Log Number 8714642.

$$\frac{dV(x)}{dx} = -\xi_c \ln \left(1 - \frac{I_D}{G_0(V_G - V_{TO} - V(x))} \right) \quad (5)$$

where

$$G_0 = \frac{q^2 \epsilon_2 Z v_s}{q^2 d + \epsilon_2 a} \quad (6)$$

Integrating (5) from $x = 0$ to $x = L$ and using the variable transformation

$$t(x) = \frac{I_D}{G_0(V_G - V_{TO} - V(x))} \quad (7)$$

one obtains

$$I_D \int_0^L \frac{dt}{t^2 \ln(1-t)} = -\xi_c L G_0 \quad (8)$$

where

$$t_0 = \frac{I_D}{G_0(V_G - V_{TO} - I_D R_S)} \quad (9a)$$

and

$$t_L = \frac{I_D}{G_0(V_G - V_{TO} - V_D + I_D R_D)} \quad (9b)$$

in which R_S is the source resistance due to the contact resistance and the resistance from the source to channel, and R_D is the drain resistance. Equation (8) describes the output I - V characteristics of HEMT's before saturation.

To obtain saturation current and voltage, calculating $g_D = \partial I_D / \partial V_D$ and setting $g_D = 0$ at saturation yields [6]

$$t_{L, \text{sat}} = \frac{I_{DS}}{G_0(V_G - V_{TO} - V_{DS} + I_{DS} R_D)} = 1 \quad (10)$$

where I_{DS} and V_{DS} are the saturation current and voltage, respectively, for a given gate voltage.

Substituting (10) into (8) yields

$$C_2(t_{os}) = \frac{\xi_c L G_0}{I_{DS}} \quad (11)$$

where

$$t_{os} = \frac{I_{DS}}{G_0(V_G - V_{TO} - I_{DS} R_S)} \quad (12)$$

and C_2 is a function defined as

$$C_2(z) = \int_1^z \frac{dt}{t^2 \ln(1-t)} \quad (13)$$

The function $C_2(z)$ is plotted in Fig. 2.

Equation (11) is used for calculating I_{DS} for a given V_G . Once I_{DS} is determined, V_{DS} is calculated from (10). Usually, we need the I_{DS} - V_G curve to determine the basic device characteristics. Equation (11) allows us to quickly work out the I_{DS} - V_G curve. First, we start from a given value of I_{DS} , get $C_2(t_{os})$ by (11), then find t_{os} from Fig. 2, and finally, obtain V_G by (12). Using this procedure,

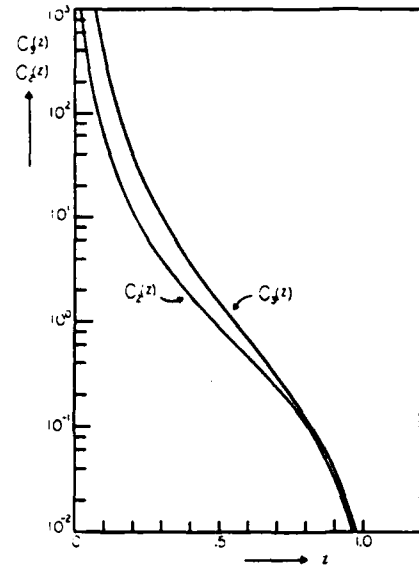


Fig. 2. The function $C_2(z)$ and $C_3(z)$.

we can get many points of (V_G, I_{DS}) to obtain the whole I_{DS} - V_G curve.

For determining microwave performance, the transconductance and gate capacitance in the saturation region are very important. Taking the derivative of (11), the saturation transconductance is given by

$$g_{ms} = \frac{\partial I_{DS}}{\partial V_G} = \frac{I_{DS}}{V_G - V_{TO} + \xi_c L \ln(1-t_{os})} \quad (14)$$

The gate capacitance in the saturation region is defined by

$$C_G = \frac{\partial Q_s}{\partial V_G} \quad (15)$$

where Q_s is the saturation channel charge and is given by

$$Q_s = qZ \int_0^L n_s(x) dx \quad (16)$$

After manipulation, one obtains

$$C_G = g_{ms} \frac{L}{v_s} \left(2 \frac{C_3(t_{os})}{C_2(t_{os})} - \frac{1}{t_{os}} \right) \quad (17)$$

where C_3 is an integral function defined as

$$C_3(z) = \int_1^z \frac{dt}{t^3 \ln(1-t)} \quad (18)$$

The function C_3 is also shown in Fig. 2.

III. THE EXTENDED MODEL

In the above model, we only consider the current in the 2DEG channel and assume that the current remains constant after saturation, for $V_D > V_{DS}$. However, the true drain current is not constant. To explain this behavior, we will consider the channel conductance in the saturation region by solving the two-dimensional Poisson equation

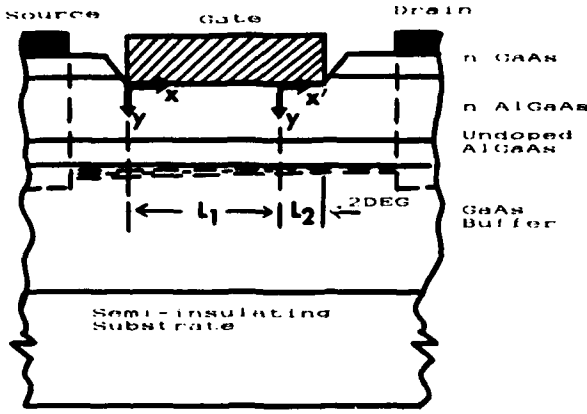


Fig. 3. The HEMT structure.

and the parasitic resistance due to the undoped GaAs buffer layer.

Divide the 2DEG channel into two regions: low-field region $0 \leq x \leq L_1$, and the high-field region, $L_1 \leq x \leq L$, as shown in Fig. 3. At $x = L_1$, $t(L_1) = 1$, the electric field is infinite by (5), and the electron drift velocity is v_s by (4). From (7), the potential at $x = L_1$ is

$$V_{L1} = V_G - V_{TO} - \frac{I_c}{G_0} \quad (19)$$

where I_c is the current in the 2DEG channel.

Because we only consider the 2DEG channel current in the above section, in all of the equations and the definitions of $t(x)$, t_0 , t_L , t_{os} and $t_{L,sat}$ in Section II, I_D must be replaced by I_c in this section. The channel current-voltage relation in the low field region, according to (11), is then given by

$$L_1 = \frac{I_c C_2(t_0)}{\xi_c G_0} \quad (20)$$

where t_0 is defined in (9a) with I_D replaced by I_c .

Define $x' = x - L_1$. In the high-field region, $0 \leq x' \leq L_2$, we need to solve the two-dimensional Poisson equation

$$\frac{\partial^2 V(x', y)}{\partial x'^2} + \frac{\partial^2 V(x', y)}{\partial y^2} = -\frac{qN_D(y)}{\epsilon_2} \quad (21)$$

subject to the following boundary conditions:

$$(a) \quad V(0, y) = V_G + \frac{q}{\epsilon_2} \left(\int_0^d N_D(y) dy - \frac{I_c}{qZv_s} \right) \cdot y - \frac{q}{\epsilon_2} \int_0^y \int_0^y N_D(y) dy dy$$

$$(b) \quad \frac{\partial V}{\partial x'}(0, d) = \xi_0$$

$$(c) \quad V(x', 0) = V_G$$

$$(d) \quad \frac{\partial V}{\partial y}(x', d) = -\frac{I_c}{\epsilon_2 Zv_s}$$

Boundary condition (a) ensures the continuity of the potential across the interface of the two regions. In the low-

field region, $x \leq L_1$, we assume that in the depletion region the x component of the electric field is a slow-varying function and hence $\partial^2 V / \partial x^2 \approx 0$, and get condition (a) (see Appendix A). In condition (b), we assume $\xi = \xi_0$ at $x' = 0$ in the 2DEG channel. Because we use the condition $t(L_1) = 1$ to determine the interface of the low-field and high-field regions, the electron drift velocity at $x' = 0$ is v_s and ξ_0 is infinite, which is physically impossible. In the calculation in Section IV we make an assumption that ξ_0 is the electric field at which the electron velocity v reaches the value $0.99v_s$. Actually, any choice for field ξ_0 at which $v = \gamma v_s$ is acceptable if $C_2(\gamma)$ is much smaller than $C_2(t_{os})$. In order to be more consistent with the physical condition, $v = v_s$ in the high-field region, we made the choice $v(\xi = \xi_0) = 0.99v_s$. With this choice, (19) and (20) are still very good approximations because $C_2(0.99) \approx 0$. Condition (c) treats the metal gate as an equipotential plane. Condition (d) is the condition that the y component of the electric field is discontinuous at the hetero-interface due to 2DEG (see Appendix A).

Grebene and Ghandhi [9] have solved this kind of two-dimensional Poisson equation using a self-consistent approach. Here we will introduce a simple and direct method to solve (21) subject to boundary conditions (a), (b), (c), and (d). Using the variable transformation

$$W(x', y) = V(x', y) + \frac{q}{\epsilon_2} \int_0^y \int_0^y N_D(y) dy dy \quad (22)$$

one has

$$\frac{\partial^2 W(x', y)}{\partial x'^2} + \frac{\partial^2 W(x', y)}{\partial y^2} = 0. \quad (23)$$

The boundary conditions for (23) are then given by

$$(e) \quad W(0, y) = V_G + \frac{q}{\epsilon_2} \left(\int_0^d N_D(y) dy - \frac{I_c}{qZv_s} \right) \cdot y$$

$$(f) \quad \frac{\partial W}{\partial x'}(0, d) = \xi_0$$

$$(g) \quad W(x', 0) = V_G$$

$$(h) \quad \frac{\partial W}{\partial y}(x', d) = \frac{q}{\epsilon_2} \left(\int_0^d N_D(y) dy - \frac{I_c}{qZv_s} \right).$$

Using the method of separation of variables to solve (23), $W(x', y)$ has the following form:

$$(A_1 e^{kx'} + B_1 e^{-kx'}) (C_1 \cos ky + D_1 \sin ky).$$

Examining (23), one can see that the following form is also a solution:

$$A_2 x'y + B_2 x' + C_2 y + D_2.$$

Hence we choose the following function form to match boundary conditions:

$$W(x', y) = (A_1 e^{kx'} + B_1 e^{-kx'}) (C_1 \cos ky + D_1 \sin ky) + A_2 x'y + B_2 x' + C_2 y + D_2. \quad (24)$$

Through boundary conditions (e), (g), (h), and (f), one can easily obtain the solution.

$$W(x', y) = \frac{2d\xi_0}{\pi} \sinh \frac{\pi x'}{2d} \sin \frac{\pi y}{2d} + V_G + \frac{q}{\epsilon_2} \left(\int_0^d N_D(y) dy - \frac{I_c}{qZv_s} \right) y \quad (25)$$

or

$$g_m = \frac{I_c \left(1 + \frac{\xi_c \ln(1-t_0)}{\xi_0 \sqrt{\lambda^2 + 1}} \right)}{V_G - V_{TO} + \xi_c \left(L - \frac{2d}{\pi} \sinh^{-1} \lambda \right) \ln(1-t_0) + I_c(R_0 - R_D) \frac{\xi_c \ln(1-t_0)}{\xi_0 \sqrt{\lambda^2 + 1}}} \quad (33)$$

and

$$g_D = \frac{-I_c \frac{\xi_c \ln(1-t_0)}{\xi_0 \sqrt{\lambda^2 + 1}}}{V_G - V_{TO} + \xi_c \left(L - \frac{2d}{\pi} \sinh^{-1} \lambda \right) \ln(1-t_0) + I_c(R_0 - R_D) \frac{\xi_c \ln(1-t_0)}{\xi_0 \sqrt{\lambda^2 + 1}}} + \frac{1}{R_p} \quad (34)$$

$$V(x', y) = \frac{2d\xi_0}{\pi} \sinh \frac{\pi x'}{2d} \sin \frac{\pi y}{2d} + V_G + \frac{q}{\epsilon_2} \left(\int_0^d N_D(y) dy - \frac{I_c}{qZv_s} \right) y - \frac{q}{\epsilon_2} \int_0^y \int_0^y N_D(y) dy dy. \quad (26)$$

In the 2DEG channel, $y = d$, the voltage across the high-field region, $L_1 \leq x \leq L$, therefore is given by

$$V_L - V_{L1} = \frac{2d\xi_0}{\pi} \sinh \frac{\pi L_2}{2d} \quad (27)$$

where V_L is the potential at $x = L$.

Substituting (19) into (27) yields

$$L_2 = \frac{2d}{\pi} \sinh^{-1} \lambda \quad (28)$$

where

$$\lambda = \frac{\pi(V_D - V_G + V_{TO} + I_c(R_0 - R_D))}{2d\xi_0} \quad (29)$$

and

$$R_0 = \frac{1}{G_0} \quad (30)$$

Combining (20) with (28) and using $L = L_1 + L_2$, we get the channel current-voltage characteristics after saturation.

$$L = \frac{I_c C_2(t_0)}{\xi_c G_0} + \frac{2d}{\pi} \sinh^{-1} \lambda. \quad (31)$$

Including the current due to the parasitic resistance of the undoped GaAs buffer layer R_p , the total drain current is

$$I_D = I_c + \frac{V_D}{R_p}. \quad (32)$$

The channel currents I_c after saturation and before saturation are determined by (31) and (8), respectively, with I_D replaced by I_c in (8) in the definitions of t_0 and t_L .

For microwave performance, we need to know the transconductance, channel conductance, and gate capacitance in the saturation region. The transconductance and channel conductance are obtained by taking the derivatives of (32) and (31). (See Appendix B.)

From (16), the channel charge in the saturation region is given by

$$Q = qZ \int_0^{L_1} n_s(x) dx + qZ \int_{L_1}^L n_s(x) dx. \quad (35)$$

In the low-field region, $0 < x \leq L_1$, $n_s(x)$ is given by (1), and in the high-field region, $L_1 < x < L$, $n_s = I_c/qZv_s$. Hence the channel charge is

$$Q = \frac{G_0}{v_s} \int_0^{L_1} (V_G - V_{TO} - V(x)) dx + \frac{I_c L_2}{v_s}. \quad (36)$$

Taking the derivative of Q with respect to V_G , we can get the gate capacitance. (See Appendix C.)

$$C_G = \frac{g_m}{v_s \xi_c} \left(\xi_c L + 2I_c R_0 (C_3(t_0) - C_2(t_0)) + \left(V_G - V_{TO} - \frac{I_c}{g_m} \right) \cdot \frac{1 - t_0}{t_0 \ln(1 - t_0)} \right). \quad (37)$$

In this model, we obtain current-voltage characteristics based on the normal operating condition, i.e., the AlGaAs layer is fully depleted. For a gate voltage exceeding a critical value [4], [10], the AlGaAs layer is not fully depleted by the Schottky gate and the heterojunction, one must consider the conducting current in the AlGaAs layer, which causes the transconductance to be suppressed. There are two other possible causes for transconductance degradation [11]: 1) the series resistance increases as gate voltage increases, or 2) the gate to channel capacitance decreases as gate voltage increases. In this paper, we assume that the drain resistance is constant in the whole region. Actually, in the saturation region, there is a higher field region near the gate end, which causes the drain re-

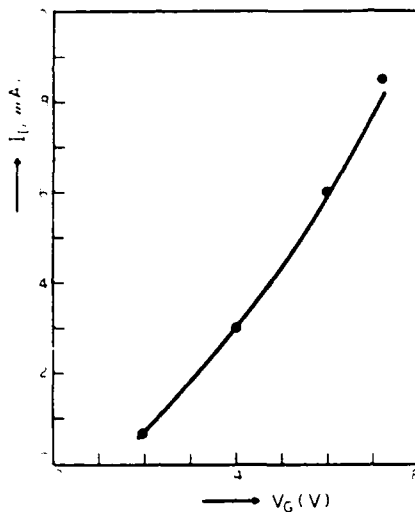


Fig. 4. The calculated and experimental drain current in the saturation region as a function of the gate voltage ($V_D = 1$ V).

sistance to increase. However, the voltage across the high-field region in (27) is exaggerated [11] since the field strength is already in the negative differential mobility regime. This allows us to neglect the increased voltage drop between the gate end and drain and to assume that the drain resistance is a constant.

IV. COMPARISON WITH EXPERIMENT

Theoretical I - V curves are compared to experimental curves measured by Drummond *et al.* [8]. Fig. 4 shows the calculated and experimental drain current in the saturation region at room temperature as a function of gate voltage. In Fig. 5, we compare the calculated output current-voltage characteristics using the extended model and the simple model described in Section II to the experimental data. The circles (\cdots) are the experimental data. The solid lines (---) and the dashed lines (---) represent the calculated curves using the extended model and the simple model, respectively. As we can see from this figure, the curves using the extended model are in excellent agreement with the experimental data.

The parameters used for calculating the theoretical curves in Figs. 4 and 5 are listed in Table I. N_D , μ , d_d , d , L , Z , and R_s are the stated parameters of Drummond *et al.* They fabricated the HEMT using an $\text{Al}_{0.3}\text{Ga}_{0.7}\text{As}/\text{GaAs}$ heterostructure. $R_D = 25 \Omega$ is used for the best fit in the linear region. $R_p = 4 \text{ K}$ is chosen for the fit in the saturation region. v_s is the electron drift velocity in GaAs [12]. ξ_0 is the electric field as the electron velocity reaches $0.99 v_s$. ϵ_2 and ΔE_c in $\text{Al}_x\text{Ga}_{1-x}\text{As}$, according to Mailhot *et al.* [13], are determined by x as follows:

$$\epsilon_2 \approx (12.1 - 3x)\epsilon_0 = 12.2\epsilon_0 \quad (38)$$

$$\Delta E_c \approx 1.06x = 0.32 \text{ eV}. \quad (39)$$

ϕ_b in a $\text{Au-Al}_x\text{Ga}_{1-x}\text{As}$ system is approximated by [14]

$$\phi_b \approx 0.92 + 0.62x = 1.106 \text{ V}. \quad (40)$$

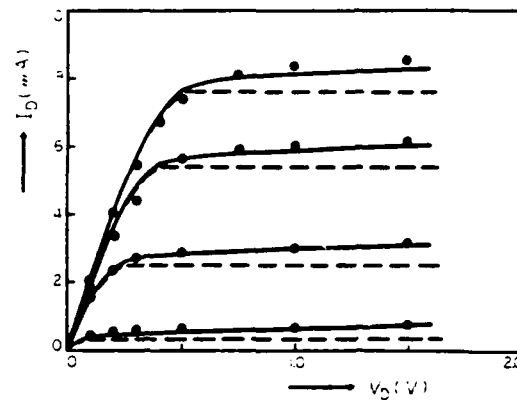


Fig. 5. Output I - V characteristics. (---) the calculated curves using the extended model. (---) the calculating curves using the simple model. (\cdots) the experimental data after Drummond *et al.* [8].

TABLE I
THE PARAMETERS USED FOR CALCULATING THE THEORETICAL CURVES IN FIGS. 4 AND 5

$N_D = 10^{18} \text{ cm}^{-3}$	$R_D = 25 \Omega$
$\mu = 4300 \text{ cm}^2/\text{V}\cdot\text{sec}$	$R_p = 4000 \Omega$
$d_d = 300 \text{ \AA}$	$\epsilon_2 = 12.2 \epsilon_0$
$d = 400 \text{ \AA}$	$\Delta E_c = 0.32 \text{ eV}$
$L = 1 \mu\text{m}$	$\phi_b = 1.106 \text{ V}$
$Z = 145 \mu\text{m}$	$v_s = 8 \times 10^6 \text{ cm/sec}$
$R_s = 12 \Omega$	$\xi_0 = 4.6 \xi_c$

In the theoretical calculations using the simple model in [6], ϕ_b was adjusted to 1.08 V for the best fit in the saturation region. Therefore, we had a bad fit with experimental data in the knee region. In Fig. 5, the calculated curves using the extended model show excellent agreement with the experimental data in the whole region.

V. CONCLUSION

An analytic model is developed for the output current-voltage characteristics and the microwave-signal parameters of HEMT's. We use the GSW equation to describe the electron drift velocity versus electric field in HEMT's, solve the two-dimensional Poisson equation to explain the channel conductance in the saturation region, and consider the current due to the parasitic resistance of the undoped GaAs buffer layer. The proposed analytic model for HEMT I - V characteristics shows excellent agreement with experimental data.

APPENDIX A BOUNDARY CONDITIONS

Assume that the x component of the electric field is a slow-varying function in the low-field region, $0 \leq x \leq L_1$, and hence $\partial^2 V / \partial x^2 \approx 0$. The Poisson equation becomes

$$\frac{\partial^2 V}{\partial y^2} = -\frac{qN_D(y)}{\epsilon_2}. \quad (\text{A1})$$

Integrating (A1) and using boundary condition $\xi_y(y=d) = (-\partial V / \partial y)_{y=d} = qn_s(x) / \epsilon_2$, we have

$$\frac{\partial V}{\partial y} = -\frac{q}{\epsilon_2} \int_0^y N_D(y) dy + \frac{q}{\epsilon_2} \left(\int_0^d N_D(y) dy - n_s(x) \right). \quad (A2)$$

For $L_1 \leq x \leq L$, $n_s(x) = I_c/qZv_s$, and therefore we have boundary condition (d). Integrating (A2) and using the condition $V(x, 0) = V_G$, we have

$$V(x, y) = V_G + \frac{q}{\epsilon_2} \left(\int_0^d N_D(y) dy - n_s(x) \right) y - \frac{q}{\epsilon_2} \int_0^y \int_0^y N_D(y) dy dy \quad (A3)$$

which is boundary condition (a) with $n_s(0) = I_c/qZv_s$.

APPENDIX B

TRANSCONDUCTANCE AND CHANNEL CONDUCTANCE

From (31), we can define

$$F(I_c, V_D, V_G) = I_c \int_{t_0}^1 \frac{dt}{t^2 \ln(1-t)} - \frac{2d\xi_c G_0}{\pi} \sinh^{-1} \lambda + \xi_c G_0 L = 0. \quad (B1)$$

Therefore,

$$g_m = \frac{\partial I_D}{\partial V_G} = \frac{\partial I_c}{\partial V_G} = -\frac{\frac{\partial F}{\partial V_G}}{\frac{\partial F}{\partial I_c}} \quad (B2)$$

and

$$g_D = \frac{\partial I_c}{\partial V_D} + \frac{1}{R_p} = -\frac{\frac{\partial F}{\partial V_D}}{\frac{\partial F}{\partial I_c}} + \frac{1}{R_p}. \quad (B3)$$

From (B1), one easily obtains

$$\frac{\partial F}{\partial V_G} = \frac{G_0}{\ln(1-t_0)} + \frac{G_0 \xi_c}{\xi_0} \cdot \frac{1}{\sqrt{\lambda^2 + 1}} \quad (B4)$$

$$\frac{\partial F}{\partial V_D} = -\frac{G_0 \xi_c}{\xi_0} \cdot \frac{1}{\sqrt{\lambda^2 + 1}} \quad (B5)$$

and

$$\frac{\partial F}{\partial I_c} = -\frac{G_0(V_G - V_{T0})}{I_c \ln(1-t_0)} - \frac{G_0 \xi_c}{\xi_0} \cdot \frac{R_0 - R_D}{\sqrt{\lambda^2 + 1}} + \frac{2dG_0 \xi_c}{\pi I_c} \sinh^{-1} \lambda - \frac{G_0 \xi_c L}{I_c}. \quad (B6)$$

Hence, we have the final results in (33) and (34).

APPENDIX C

GATE CAPACITANCE

From (36), we have

$$Q = \frac{G_0(V_G - V_{T0})L_1}{v_s} - \frac{G_0}{v_s} \int_0^{L_1} V(x) dx + \frac{I_c L_2}{v_s}. \quad (C1)$$

Using (5) and replacing I_D by I_c , we get

$$\int_0^{L_1} V(x) dx = \frac{I_c(V_G - V_{T0})}{G_0 \xi_c} \int_0^{t_0} \frac{dt}{t^2 \ln(1-t)} + \frac{I_c^2}{G_0^2 \xi_c} \int_{t_0}^1 \frac{dt}{t^3 \ln(1-t)}. \quad (C2)$$

Recalling $t_{L1} = 1$ and substituting (20) into (C2) yields

$$\int_0^{L_1} V(x) dx = (V_G - V_{T0})L_1 - \frac{I_c^2}{G_0^2 \xi_c} \int_{t_0}^1 \frac{dt}{t^3 \ln(1-t)}. \quad (C3)$$

Substituting (C3) into (C1), we have

$$Q = -\frac{I_c^2}{v_s \xi_c G_0} \int_{t_0}^1 \frac{dt}{t^3 \ln(1-t)} + \frac{I_c L_2}{v_s}. \quad (C4)$$

Taking the derivative of Q with respect to V_G

$$\frac{\partial Q}{\partial V_G} = \frac{I_c}{v_s} \frac{\partial L_2}{\partial V_G} + \frac{g_m L_2}{v_s} - \frac{I_c^2}{v_s \xi_c G_0} \frac{\partial}{\partial V_G} \left(\int_{t_0}^1 \frac{dt}{t^3 \ln(1-t)} \right) - \frac{2g_m I_c}{v_s \xi_c G_0} \int_{t_0}^1 \frac{dt}{t^3 \ln(1-t)}. \quad (C5)$$

Using (28), (33), and (31), after manipulation, one can get the final result, (37).

ACKNOWLEDGMENT

The authors would like to thank W. Chew for proof-reading.

REFERENCES

- [1] T. Mimura, S. Hiyaizumi, T. Fujii, and K. Nanbu, "A new field-effect transistor with selectively doped GaAs/n-Al_{0.3}Ga_{0.7}As heterojunctions," *Japan. J. Appl. Phys.*, vol. 19, no. 5, pp. L225-L227, May 1980.
- [2] M. H. Weiler and Y. Ayashi, "DC and microwave models for Al_{0.3}Ga_{0.7}As/GaAs high electron mobility transistors," *IEEE Trans. Electron Devices*, vol. ED-31, no. 12, pp. 1854-1861, Dec. 1984.
- [3] C. Z. Cil and S. Tansal, "A new model for modulation-doped FET's," *IEEE Electron Device Lett.*, vol. EDL-6, no. 8, pp. 434-436, Aug. 1985.
- [4] G. W. Wang and W. H. Ku, "An analytic computer-aided model for the AlGaAs/GaAs high electron mobility transistor," *IEEE Trans. Electron Devices*, vol. ED-33, no. 5, pp. 657-663, May 1986.
- [5] K. Park and K. D. Kwack, "A model for the current-voltage char-

acteristics of MODFET's," *IEEE Trans. Electron Devices*, vol. ED-33, no. 5, pp. 673-676, May 1986.

- [6] C.-S. Chang and H. R. Fetterman, "An analytic model for high electron mobility transistors," *Solid-State Electron.*, vol. 30, no. 5, May 1987.
- [7] R. A. Giblin, E. F. Scherer, and R. L. Wierich, "Computer simulation of instability and noise in high-power avalanche devices," *IEEE Trans. Electron Devices*, vol. ED-20, pp. 404-418, Apr. 1973.
- [8] T. J. Drummond, H. Morkoç, K. Lee, and M. S. Shur, "Model for modulation-doped field effect transistors," *IEEE Electron Device Lett.*, vol. EDL-3, pp. 338-341, Nov. 1982.
- [9] A. B. Grebene and S. K. Ghandhi, "General theory for pinched operation of the junction-gate FET," *Solid-State Electron.*, vol. 12, pp. 573-589, 1969.
- [10] D. Delagebeaudeuf and N. T. Linh, "Metal-(n)AlGaAs-GaAs two-dimensional gas FET," *IEEE Trans. Electron Devices*, vol. ED-29, pp. 955-960, June 1982.
- [11] J. Y.-H. Tang, "Two-dimensional simulation of MODFET and GaAs gate heterojunction FET's," *IEEE Trans. Electron Devices*, vol. ED-32, no. 9, Sept. 1985.
- [12] C.-S. Chang and H. R. Fetterman, "Electron drift velocity versus electric field in GaAs," *Solid-State Electron.*, vol. 29, no. 12, pp. 1295-1296, Dec. 1986.
- [13] C. Mailhot, Y. C. Chang, and T. C. McGill, "Energy spectra of donors in GaAs-Ga_{1-x}Al_xAs quantum well structures," *Surface Sci.*, vol. 113, pp. 161-164, 1982.
- [14] A. J. Best, "The Schottky-barrier height of Au on n-Ga_{1-x}Al_xAs as a function of AlAs Content," *Appl. Phys. Lett.*, vol. 34, pp. 522-524, 1979.



Chian-Sern Chang was born in Tainan County, Taiwan, Republic of China, on November 25, 1955. He received the B.S. and M.S. degrees in electrical engineering from National Chen Kung University, Taiwan, in 1978 and 1980, respectively. He is currently working toward the Ph.D. degree in the Department of Electrical Engineering at the University of California, Los Angeles.

After receiving the M.S. degree, he served for two years in the military. In 1983, he joined the Far East Engineering College and was an Instructor and Chairman of the Electrical Engineering Department.

*



Harold R. Fetterman (SM'81) received the Ph.D. degree from Cornell University in 1967.

He is currently a Professor in the Department of Electrical Engineering at the University of California, Los Angeles. He joined UCLA after 14 years at the MIT Lincoln Laboratory. At MIT, he was Project Leader of the submillimeter/millimeter-wave detector and source programs. He successfully directed the development of heterodyne receivers and solid-state sources with applications in plasma diagnostics, remote sensing, and

imaging radars. Since coming to UCLA, he has been active in the development of millimeter-wave FET devices and large-area arrays. He is presently the director of the new UCLA High-Frequency Electronics Center.

Negative photoconductivity in high electron mobility transistors

C. S. Chang, H. R. Fetterman, and D. Ni

Department of Electrical Engineering, University of California, Los Angeles, California 90024

E. Sovero, B. Mathur, and W. J. Ho

Rockwell International Science Center, Thousand Oaks, California 91360

(Received 21 July 1987; accepted for publication 29 October 1987)

High electron mobility transistors are sensitive to light since illumination ionizes deep donor centers and increases the drain current. In this letter the first observation of negative photoconductivity, i.e., drain current decreasing with light, will be reported. The current-voltage characteristics were enhanced by shining white light onto the devices showing negative photoconductivity.

In this letter we report an interesting phenomenon in high electron mobility transistors. Negative photoconductivity due to white light illumination has been observed. In addition to possible device applications, this yields important information on the electronic confinement in these devices. GaAs-Al_xGa_{1-x}As structures have been of intense interest recently because of their high electron mobilities.^{1,2} In this structure only the larger band gap Al_xGa_{1-x}As is doped with a donor, and the GaAs layer is left undoped. Electrons in the Al_xGa_{1-x}As, having a larger energy than they would in the GaAs, diffuse into GaAs and form a two-dimensional electron gas (2DEG). Since the electrons and donors are spatially separated, ionized impurity scattering is avoided, and extremely high electron mobilities can be obtained. Field-effect transistors using the novel properties of the 2DEG were first demonstrated in 1980 by Mimura *et al.*³ who called this device the high electron mobility transistor (HEMT). Since then, the HEMT has been the focus of research on high-speed and high-frequency semiconductor devices.

HEMT's are sensitive to light over a broad spectral region. It has been reported that at low temperature under white light illumination, channel carrier concentration increases. After this illumination is removed, the photogenerated carrier concentration decays to a level that is still higher than that at dark operating condition.⁴⁻⁶ This effect is called persistent photoconductivity (PPC). Under dark operating condition, the low-temperature current-voltage characteristics suffer from two forms of degradation^{7,8}: (1) threshold shifts and (2) collapse of the family of curves near the origin (a strong sublinearity at low drain voltage). It is proposed that these effects are mainly caused by deep donor centers in the Al_xGa_{1-x}As layers. These are referred to as DX centers^{9,10} which may in fact be the Si donor itself. At $x = 0.3$, the Si donor energy level is about 50 meV below the conduction-band edge.¹¹ Therefore, in the highly doped AlGaAs, this level should be occupied with significant electrons, even at room temperature.

Besides (i) the photogenerated carriers due to the DX centers, there are four other possible mechanisms with illumination (refer Fig. 1): (ii) band-to-band electron-hole generation in the AlGaAs layer, (iii) band-to-band electron-hole generation in the bulk GaAs, (iv) pumping of electrons from gate metal into the AlGaAs layer, and (v) pumping of

electrons from 2DEG channel into the AlGaAs layer or bulk GaAs. All of the mechanisms except (v) make the conductivity increase. In this letter we report the first observation of negative photoconductivity in HEMT's due to light, which is suggested to be due to mechanism (v).

The devices used in this work are the enhancement-type HEMT's. The heterostructures are grown on a semi-insulating GaAs substrate by molecular beam epitaxy. The layer sequence of the modulation-doped structures includes an undoped 1- μm -thick p^- -GaAs buffer layer, an undoped Al_{0.3}Ga_{0.7}As spacer of thickness 40 Å, a Si-doped 400-Å-thick Al_{0.3}Ga_{0.7}As layer with a doping concentration $2 \times 10^{18} \text{ cm}^{-3}$, and an undoped GaAs cap layer with thickness of 400 Å. The heterostructures are then fabricated into the normal-off field-effect transistors. Illumination is provided by 1 W wheat grain light bulbs located about 1 cm from the devices. Light and dark current-voltage characteristics are measured. The devices that we measured do not have PPC effect.

Figure 2(a) shows the dark and light current-voltage characteristics with gate length 100 μm and width 200 μm (FAT HEMT) at temperature 77 K. At low drain voltages, the drain current with the light on is smaller than the dark current at the same bias. This is contrary to the predicted current behavior caused by the DX centers. As the drain voltage increases high enough, the light response of the drain currents returns to that usually expected; the light currents

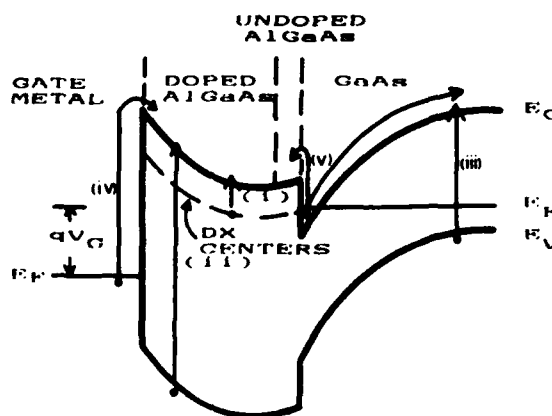


FIG. 1. Band diagram of AlGaAs-GaAs heterostructure in the 2DEG control regime by a Schottky gate.

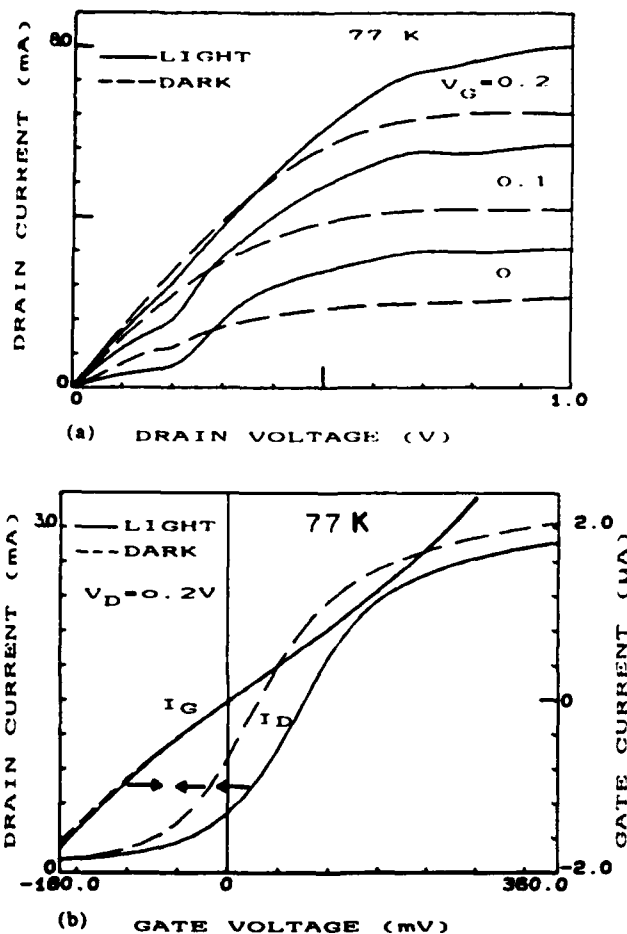


FIG. 2. (a) Dark and light current-voltage characteristics of the long channel HEMT at 77 K. (b) Dark and light drain current I_D and gate current I_G as a function of the gate voltage V_G at drain voltage $V_D = 0.2$ V.

are larger than the dark currents. Figure 2(b) shows the dark and light drain current I_D and gate current I_G as a function of gate voltage V_G at drain voltage $V_D = 0.2$ V. The explanation for this negative photoconductivity is suggested as follows.

$\text{Al}_x\text{Ga}_{1-x}\text{As}$ is transparent for the photons with energy below the energy gap of the $\text{Al}_x\text{Ga}_{1-x}\text{As}$, which is 1.8 eV for $x = 0.3$. Some of the electrons in the 2DEG channel can obtain enough energy from these photons and jump into the AlGaAs layer, which has relatively low mobility, or into the bulk GaAs, where the electric field is relatively low. This effect causes the electron concentration in the 2DEG channel to decrease. If the decrease of the electron concentration caused by this effect is more than the increase of the electron concentration caused by the DX centers (the major mechanism causes 2DEG density to increase), the negative photoconductivities will be observed. Hence, in order to have the negative photoconductivity, the device cannot have too many DX centers in the AlGaAs layer.

As the drain voltage increases further, the electric field in the 2DEG channel between gate and drain is higher. Most of the higher energy electrons (due to the light absorption) still stay in the 2DEG channel and are swept to the drain to be recorded as a current. Hence the light current is larger than the dark current.

The negative photoconductivity is also observed in short channel HEMT's. Figure 3 shows the dark and light current-voltage characteristics of a device with gate length $0.5 \mu\text{m}$ at room temperature. In this device the negative photoconductivities are observed for both low and high drain voltages. The channel conductances in the saturation region with light on are smaller than that with light off. This means that the current-voltage characteristics are improved by providing light. The devices showing this kind of negative photoconductivity are expected to operate at higher frequency when illumination is available. The improved channel conductance can be explained with the following model: Some of the high field electrons under the gate at the drain end get sufficient energy and are promoted into the AlGaAs layer or bulk GaAs, preventing that region from accumulating more electrons to build a higher electric field. The electric field under the gate end at the drain end is thus kept around threshold value,¹² and hence the drain current is almost constant in the saturation region. In the case of long channel HEMT's, only a small part of the 2DEG channel under the gate is exposed to light. For short channel HEMT's, all of the 2DEG channel under the gate is illuminated because of light diffraction. Therefore, we do not see the increasing drain current at high drain voltage due to light as that observed in the long channel devices.

To help establish the mechanisms for the negative photoconductivity of HEMT's, we have performed a number of optical spectral measurements. When the devices were illuminated through silicon filters, which have energy gap of 1.12 eV at room temperature, the negative photoconductivity was still observed. We also used argon (wavelength 5145 Å), tunable dye (5900–6200 Å), He-Ne (6238 Å), and GaAs diode lasers to illuminate the devices. The negative photoconductivity was not observed in these measurements. For the argon, dye, and He-Ne lasers, the photon energy is larger than both the energy gap of $\text{Al}_{0.3}\text{Ga}_{0.7}\text{As}$ and GaAs, and therefore creates electron-hole pairs. For the GaAs diode laser, the photon energy is almost the same as the energy gap of GaAs, and hence the effect due to the band-to-band electron-hole generation in the bulk GaAs is also very strong. A monochromator with a tungsten lamp was also used to measure photoconductivity. Negative photoconduc-

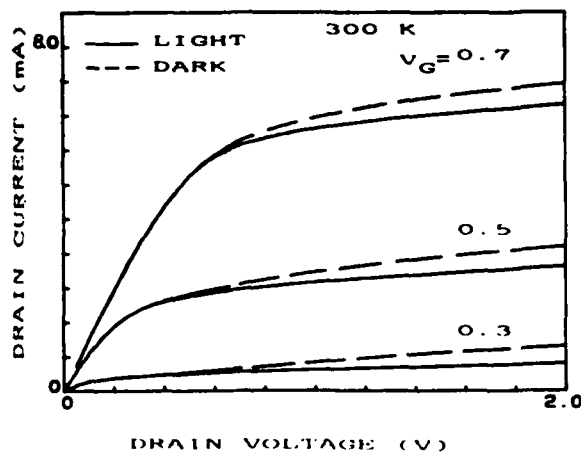


FIG. 3. Dark and light current-voltage characteristics of the short channel HEMT at room temperature.

tivity was only observed at photon energies below 1.6 eV. Additional spectral analysis as well as response time measurements is now in progress to further identify the mechanism of negative photoconductivity.

In conclusion, negative photoconductivities have been observed in high electron mobility transistors. To observe this effect, the amount of DX centers in the AlGaAs layer must be significantly small. The complete explanation to the light response of the electrons must take this effect into account besides the effects due to the DX centers. The channel conductance and frequency response can be improved upon by shining light onto the devices showing this kind of negative photoconductivity. In addition, this effect provides a useful criterion to determine the quality of HEMT's.

The authors would like to thank Jimmin Chang for revising and proofreading the manuscript. This work is partially supported by the Office of Naval Research and by the Air Force Office of Scientific Research.

- ¹R. Dingle, H. L. Stormer, A. C. Gossard, and W. Wiegmann, *Appl. Phys. Lett.* **33**, 665 (1978).
- ²T. J. Drummond, W. Kopp, H. Morkoç, and M. Keever, *Appl. Phys. Lett.* **41**, 277 (1982).
- ³T. Mimura, S. Hiyamizu, T. Fujii, and K. Nanbu, *Jpn. J. Appl. Phys.* **19**, L225 (1980).
- ⁴H. L. Stormer, R. Dingle, A. C. Gossard, W. Wiegman, and M. A. Sturge, *Solid State Commun.* **29**, 705 (1980).
- ⁵E. F. Schubert and K. Ploog, *Phys. Rev. B* **29**, 4562 (1984).
- ⁶H. Kunzel, K. Ploog, K. Wunstel, and B. L. Zhou, *J. Electron. Mater.* **13**, 281 (1984).
- ⁷A. Kastalsky and R. A. Kiehl, *IEEE Trans. Electron Devices* **33**, 414 (1986).
- ⁸R. Fisher, T. J. Drummond, J. Klen, W. Kopp, T. Henderson, D. Perrachione, and H. Morkoç, *IEEE Trans. Electron Devices* **31**, 1028 (1984).
- ⁹M. I. Nathan, P. M. Mooney, P. M. Solomon, and S. L. Wright, *Appl. Phys. Lett.* **47**, 628 (1985).
- ¹⁰D. V. Lang, R. A. Logan, and M. Joros, *Phys. Rev. B* **19**, 1015 (1979).
- ¹¹N. Chand, T. Henderson, W. T. Masselink, R. Fisher, Y. C. Chang, and H. Morkoç, *Phys. Rev. B* **30**, 4481 (1984).
- ¹²C. S. Chang and H. R. Fetterman, *IEEE Trans. Electron Devices* **34**, 1456 (1987).

Cyclotron resonance measurements of the high electron mobility transistor

Chian-Sern Chang and Harold R. Fetterman

Department of Electrical Engineering, University of California, Los Angeles, California 90024

Arold Green

Semiconductor and Surface Science Branch, Naval Weapons Center, China Lake, California 93555

(Received 2 June 1989; accepted for publication 23 October 1989)

The photoconductivity cyclotron resonance measurement is used to determine the effective masses of the high electron mobility transistor. The experimental data show that the effective mass is a function of the gate voltage.

GaAs-Al_xGa_{1-x}As structures have been of intense interest because of their high electron mobilities.^{1,2} In these structures only the larger band-gap AlGaAs is doped with a donor and the GaAs layer is left undoped. Electrons in the AlGaAs having a larger energy than they would in the GaAs diffuse into GaAs and form a two-dimensional electron gas (2DEG). Since the electrons and donors are spatially separated, ionized impurity scattering is avoided and extremely high electron mobilities can be obtained. Field-effect transistors using the novel properties of the two-dimensional electron gas were first demonstrated in 1980 by Mimura *et al.*,³ who called this device the high electron mobility transistors (HEMT). Since then the HEMT has been the focus of research on high-speed and high-frequency semiconductor devices.

The electron effective mass is an important parameter in understanding the physical properties of electrons in the 2DEG channel. The cyclotron resonance (CR) measurement is a technique widely applied to obtain the effective mass. Both the far-infrared transmission⁴⁻⁶ and photoconductivity^{7,8} can, in principle, be used for the CR measurement. It is impractical to use the transmission measurement for a HEMT since the gate metal is not transparent to photons. Hence, we measure the photoconductivity of a HEMT to obtain the cyclotron resonance.

In bulk materials the measurement of the photoconductivity via the magnetic field is an easy and sensitive way to study the cyclotron resonance.^{9,10} However, in the two-dimensional systems the cyclotron resonance induced signal is usually distorted or obscured by a strong magnetic field dependent signal, which is due to Shubnikov-de Haas oscillations (SdH). The Shubnikov-de Haas oscillations are the dominant features and the cyclotron resonance signal only appears as a small modulation of the oscillation amplitude.¹¹ Maan *et al.*⁷ were the first to report a clear signal due to the cyclotron resonance in the measurement of photoconductivity of a modulation-doped GaAs-AlGaAs heterostructure. To reduce the SdH signal, they used a sample with low 2DEG concentration, $n_s = 3.4 \times 10^{11} \text{ cm}^{-2}$. Nevertheless, the 2DEG density and the effective mass are fixed for a given modulation-doped GaAs-AlGaAs heterostructure. The channel concentration of a HEMT can be varied by applying a gate voltage. Of course, it is of interest to study the effective masses of a HEMT subject to the influence of a gate bias.

The heterostructure is grown on a semi-insulating GaAs substrate by the molecular beam epitaxy. The typical layer sequence of the modulation-doped structures includes an

undoped 1- μm -thick p^- -GaAs buffer layer, an undoped Al_{0.3}Ga_{0.7}As spacer of thickness 40 Å, a Si-doped 400-Å-thick Al_{0.3}Ga_{0.7}As with a doping concentration 10^{18} cm^{-3} , and an undoped GaAs cap layer with thickness 200 Å. The source and drain ohmic contact material is Ni/88% Au/12% Ge. The Ni-Au-Ge is evaporized using a vacuum evaporator. The contacts are then sintered at a temperature of 450 °C for 4 min with a continuous flow of nitrogen. The GaAs cap layer is etched off using NH₄OH-H₂O₂ solution with pH = 7 for 20 s. Au is then evaporated for the gate Schottky contact. For increasing the optical signal and reducing the series effect of the source and drain resistances, the devices used in this work are the long-channel HEMT (FAT HEMT). Far-infrared laser beams are introduced to illuminate the back of the devices. Because the GaAs semi-insulating substrate and buffer layer are transparent to far infrared (FIR), we can observe the photoresponse of the 2DEG to the laser beams and measure the cyclotron resonance. All of the measurements are performed at liquid-helium temperature, 4.2 K, and taken in the linear region of the current-voltage characteristics.

Figure 1 shows the output current-voltage characteristics of a FAT HEMT, with the ratio of the gate length to gate width 2. The gate voltage dependence of the 2DEG density, which is deduced from Shubnikov-de Haas measurements,¹² is shown in Fig. 2. There is a sharp turning point at $V_G = 0.1 \text{ V}$. This is due to the incompletely depleted AlGaAs layer,^{12,13} and hence reduces the charge control ability of the gate voltage. Figure 3 shows the photoconductivity as a function of magnetic field for the gate voltage $V_G = 0.4 \text{ V}$ at the laser wavelength 118.8 μm . A clear optical

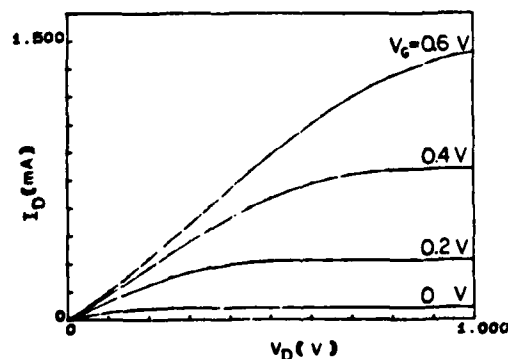


FIG. 1. Output current-voltage characteristics of a long-channel high electron mobility transistor at 4.2 K.

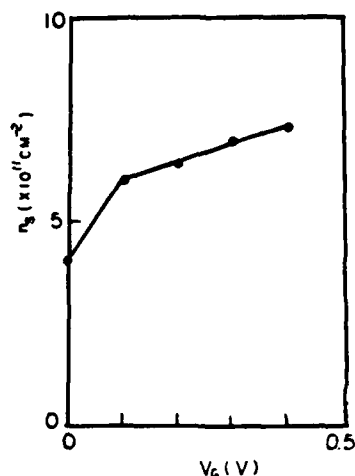


FIG. 2. Two-dimensional electron density as a function of the gate voltage.

signal due to the cyclotron resonance has been observed. For the CR measurements under other gate voltages, we observed the peaks due to Shubnikov-de Haas oscillation, which were still much smaller compared to the peak due to the cyclotron resonance. Figure 4 shows the CR measurements for different gate voltages $V_G = 0.2, 0.4$, and 0.6 V. The CR measurements for a bulk GaAs and a modulation-doped GaAs/AlGaAs structure (no gate metal) are also shown in this figure for comparison. The resonance field is a function of the gate voltage, as shown in Fig. 5.

The electron effective mass is enhanced by applying a magnetic field. Two major mechanisms cause the effective mass to increase: (i) the band nonparabolicity and (ii) the polaron effect. It has been reported^{5,14} that the enhancement of the effective mass due to the polaron effect for the two-dimensional electrons at the GaAs-AlGaAs interface is very small. For the magnetic field $B < 10$ T, the enhancement of the effective mass almost can be predicted by the band nonparabolicity. Hence we estimate the zero-field effective mass by the following equation,¹⁵ which is corrected by the band nonparabolicity:

$$m^*(0) = m^*(B) (1 + \sqrt{1 - 8\hbar\omega/E_g})/2,$$

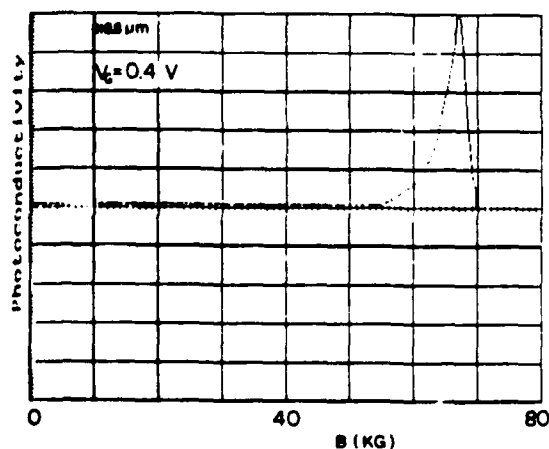


FIG. 3. Photoconductivity as a function of magnetic field at the gate voltage $V_G = 0.4$ V. The unit for photoconductivity is an arbitrary unit.

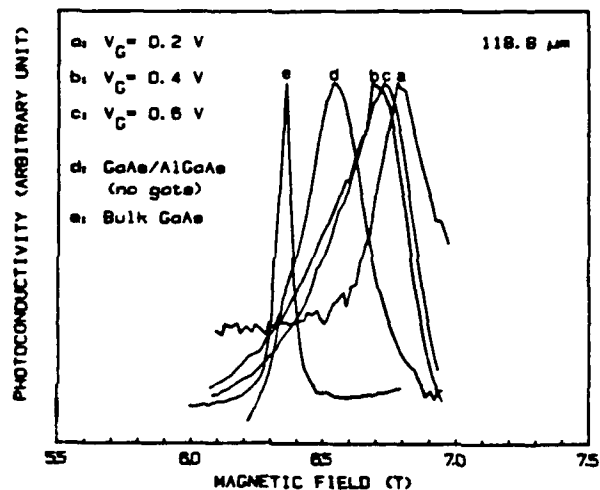


FIG. 4. Cyclotron resonance measurements for a high electron mobility transistor under different gate voltages, a bulk GaAs, and a modulation-doped GaAs-AlGaAs structure.

where $m^*(B) = qB/\omega$ is the effective mass at the magnetic field B , q is the electron charge, ω is the laser angular frequency, \hbar is the Planck's constant, $\hbar = h/2\pi$, and E_g is the energy gap (1.52 eV for GaAs at 0 K).

Figure 5 also shows the zero-field effective mass as a function of the gate voltage by using the correction of band nonparabolicity. m_0 is the free-electron mass. The effective mass has a higher value at low gate voltage; it attains a minimum at the gate voltage $V_G = 0.4$ V and increases as the gate voltage increases further. A possible physical explanation for causing the change of the effective mass with the gate voltage is suggested as follows.

At a low gate voltage, the AlGaAs layer is fully depleted and the 2DEG density is low. The electrons in the 2DEG channel are scattered by a Coulomb force due to remote ionized donors in the AlGaAs layer. A perturbation term due to a heavily doped AlGaAs layer should be added into the Hamiltonian. This results in a higher effective mass. As the gate voltage increases, the 2DEG density increases and the AlGaAs layer is not fully depleted. A bulk electron layer exists in the AlGaAs. The Coulomb scattering is weakened

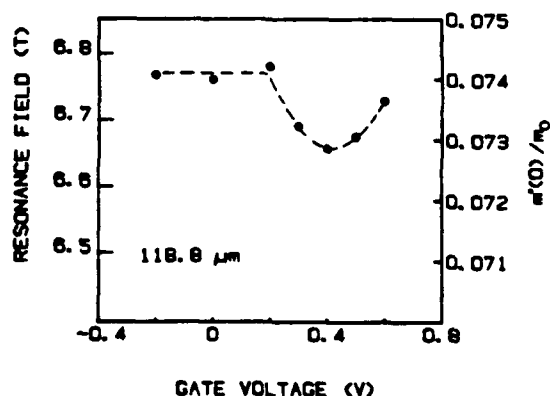


FIG. 5. Resonance field and the effective mass as a function of the gate voltage.

by the high 2DEG density and the bulk electrons in the AlGaAs. Hence the 2DEG has a light effective mass. As the gate voltage increases further, the 2DEG density becomes higher. The quantized energy levels of the 2DEG increase with the density $E_j (j = 0, 1, \dots) = r_j (n_s)^{2/3}$,¹⁶ where n_s is the 2DEG density and r_j the proportional constant. As a result, E_j is higher for a higher gate voltage. Therefore, according to the theory of the band nonparabolicity, the two-dimensional electrons have a higher effective mass.

Note that the Landau level filling factor also has an effect on the resonance field of the 2DEG.¹⁷ The resonance field shifts to a lower value as the filling factor is reduced to be less than 1. However, this effect is not applicable to the data in Fig. 5 because the filling factors obtained from Fig. 2 are larger than 2.

We also measured the cyclotron resonances using other wavelengths: 184.3, 393.6, and 432.6 μm . These cyclotron resonance induced signals are smaller compared to the signals due to Shubnikov-de Haas oscillations. The Shubnikov-de Haas oscillations are the dominant features in these measurements.

In conclusion, we have succeeded in measuring the cyclotron resonance of the high electron mobility transistor. The effective mass is a function of the gate voltage.

This work was partially supported by the Office of Naval Research and by the Air Force of Scientific Research.

- ¹D. Dingle, H. L. Stormer, A. C. Gossard, and W. Wiegmann, *Appl. Phys. Lett.* **33**, 665 (1978).
- ²T. J. Drummond, W. Kopp, H. Morkoç, and M. Keever, *Appl. Phys. Lett.* **41**, 277 (1982).
- ³T. J. Mimura, S. Hiyamizu, T. Fujuu, and K. Nanbu, *Jpn. J. Appl. Phys.* **19**, L225 (1980).
- ⁴K. Muro, S. Narita, S. Hiyamizu, K. Nanbu, and H. Hashimoto, *Surf. Sci.* **113**, 321 (1982).
- ⁵H. Sigg, P. Wyder, and J. Perenboom, *Phys. Rev. B* **31**, 5253 (1985).
- ⁶G. A. Rodriguez, R. M. Hart, A. J. Sievers, F. Keilmann, Z. Schlesinger, S. L. Wright, and W. I. Wang, *Appl. Phys. Lett.* **49**, 458 (1986).
- ⁷J. C. Maan, T. Englert, D. C. Tsui, and A. C. Gossard, *Appl. Phys. Lett.* **40**, 609 (1982).
- ⁸R. E. Horstman, E. Broek, J. Wolter, R. Heijden, G. Rikken, H. Sigg, P. M. Frijlink, J. Maluenda, and J. Hallais, *Solid State Commun.* **50**, 753 (1984).
- ⁹H. R. Fetterman, D. M. Larson, G. E. Stillman, P. E. Tannenwald, and J. Waldman, *Phys. Rev. Lett.* **26**, 975 (1971).
- ¹⁰H. J. A. Bluyssen, J. C. Maan, L. J. van Ruyven, F. Williams, and P. Wyder, *Solid State Commun.* **25**, 895 (1978).
- ¹¹C. F. Lavine, R. J. Wagner, and D. C. Tsui, *Surf. Sci.* **113**, 112 (1981).
- ¹²C.-S. Chang, H. R. Fetterman, and C. R. Viswanathan, *J. Appl. Phys.* **66**, 928 (1989).
- ¹³D. Delagebeaudeuf and N. T. Linh, *IEEE Trans. Electron Devices* **29**, 995 (1982).
- ¹⁴W. Seidenbusch, G. Lindemann, R. Lassnig, J. Edlinger, and G. Gornik, *Surf. Sci.* **142**, 375 (1984).
- ¹⁵J. Waldman, Ph.D. dissertation, Dept. of Phys., Massachusetts Institute of Technology, 1970.
- ¹⁶W. Zawadzki, in *Springer Series in Solid-State Science*, edited by G. Bauer, F. Kuchar, and H. Heinrich (Springer, Berlin, 1984), Vol. 53, p. 2.
- ¹⁷Z. Schlesinger, W. I. Wang, and A. H. MacDonald, *Phys. Rev. Lett.* **58**, 73, 1987.

The characterization of high electron mobility transistors using Shubnikov-de Haas oscillations and geometrical magnetoresistance measurements

Chian-Sern Chang, Harold R. Fetterman, and Chand R. Viswanathan
Department of Electrical Engineering, University of California, Los Angeles, California 90024

9

(Received 28 November 1988; accepted for publication 31 March 1989)

Shubnikov-de Haas oscillations and geometrical magnetoresistance measurements are used to determine the two most important parameters, channel concentration and mobility, respectively, for high electron mobility transistors. To deduce useful data from measurements, the theory of the Shubnikov-de Haas oscillation for the two-dimensional electrons is derived and discussed in detail. The experimental data for the channel concentration as a function of gate voltage is used to check the accuracy of the charge-control law. We also derive a simple formula of the geometrical magnetoresistance to calculate the mobility for any aspect ratio. The concentration and mobility deduced from the Shubnikov-de Haas and geometrical magnetoresistance measurements give us insight on the nature and properties of the devices. The experimental data shows that the impurity scattering is the dominant mechanism for the low channel concentration. The maximum transconductance occurs at a compromise between the charge-control ability of the gate voltage and the channel mobility. Near the cutoff region the decrease of the conductivity is due to the decrease of both the channel concentration and the mobility.

I. INTRODUCTION

GaAs-Al_xGa_{1-x}As modulation-doped structures have been of intense interest because of their high electron mobilities.^{1,2} In these structures only the larger band gap Al_xGa_{1-x}As is doped with a donor and the GaAs layer is left undoped. Electrons in the Al_xGa_{1-x}As having a larger energy than they would in the GaAs diffuse into GaAs and form a two-dimensional electron gas (2DEG). Since the electrons and donors are spatially separated, ionized impurity scattering is avoided and extremely high electron mobilities can be obtained. Field-effect transistors using the novel properties of the two-dimensional electron gas were first demonstrated in 1980 by Mimura *et al.*³ who called this device the high electron mobility transistor (HEMT). Since then the HEMT has been the focus of research on high-speed and high-frequency semiconductor devices.

For design purposes and insight on the nature of device operation or structure, characterization is an important and integral part of the study of semiconductor devices. The carrier concentration and mobility are the two most important factors determining the device performance. They are usually measured by the Hall-effect technique together with gated van der Pauw structures.⁴⁻⁶ However, this approach is complicated by requiring special test patterns. It is, of course, desirable to measure these quantities on the device itself rather than on a special test structure. The Shubnikov-de Haas (SdH) oscillation of magnetoresistance⁷⁻¹⁰ together with geometrical magnetoresistance (GMR)¹¹⁻¹⁴ are ideally suited for measuring carrier concentration and mobility. No special test pattern is necessary in these measurements.

The SdH oscillations have been widely applied to measure the two-dimensional electron concentration of modulation-doped AlGaAs/GaAs heterostructures.^{7,8} Chou, Antoniadis, and Smith¹⁰ are the first to use SdH oscillations to

measure 2DEG channel concentration as a function of gate voltage for HEMTs. They used the theory developed for the bulk electrons (three-dimensional electrons) to calculate the two-dimensional electron concentration. The charge-control law,¹⁵ shown as the following equation, is assumed to be an accurate formula to derive the gate-to-channel capacitance:

$$n_s = (C/q)(V_G - V_T), \quad (1)$$

where n_s is the 2DEG density, C the gate-to-channel capacitance, V_G the gate voltage, and V_T the threshold voltage. However, the properties of the two-dimensional electrons are quite different from that of three-dimensional electrons. The two-dimensional electrons are confined at the GaAs-AlGaAs heterointerface and are quantized due to the potential well. The charge-control law (1) is derived with assumptions,¹⁶⁻¹⁸ and hence it is only an approximate relation. To deduce useful data from the SdH measurement, it is necessary to understand the basic theory of the SdH oscillation for the two-dimensional electrons. Our experimental data show that SdH oscillations consist of two oscillating periods, which correspond to the electron concentration at the two lowest subbands. The electron concentration due to the second subband cannot be neglected. The charge-control law (1) is only an approximate formula.

Beside the electron concentration, the electron mobility is the other important parameter for determining the device performance. To deduce mobility from $C-V$ ¹⁹ or van der Pauw^{5,6} measurements we need to know the electron concentration or related parameters. The GMR measurement to calculate the electron mobility has the merit that it is independent of the electron concentration. We do not need to know the concentration to determine the mobility. The SdH measurement combined with the GMR measurement can

provide the characterization of HEMTs and insight on the nature of the devices because these two measurements do not depend on each other.

The basic theory for the GMR measurement has been developed by Lippmann and Kuhrt.^{20,21} They derived a simple formula of the GMR for the aspect ratio less than 0.3 or larger than 1. However, there is no simple formula available for the aspect ratio between 0.3 and 1, which is an important range in fabricating a long channel device for characterization. We will follow the theory developed in Refs. 20 and 21 to derive a simple formula for any aspect ratio, especially for the ratio between 0.3 and 1. We obtain the drift mobility and GMR mobility versus the gate voltage from the SdH and GMR measurements, respectively. This enables us to understand the scattering mechanisms. Combining the SdH and GMR measurements also gives us insight into the device physics and performance. It is generally accepted that the maximum transconductance occurs at the gate voltage to turning on the AlGaAs layer to conduct. The experimental data show that the maximum transconductance occurs at a higher gate voltage due to the screening effect of electrons in the AlGaAs. In addition, the data also make the mechanism clear for the operating point at near the cutoff region.

In this paper, we will first use a simple method to derive the basic theory and formula of the SdH oscillation for the two-dimensional electron gas. Next, we derive a simple formula of the GMR for any aspect ratio. Finally, we show and discuss the experimental data. Because the SdH oscillation must be measured at low temperature, both the SdH and GMR measurements were done at liquid-helium temperature, which is 4.2 K, for comparison. All of the measurements are taken in the linear region of the output current-voltage characteristics. For reducing the series effect of the source and drain resistances, the devices used in this work are long channel HEMTs (FAT HEMT).

II. SHUBNIKOV-de HAAS OSCILLATIONS

Figure 1 shows the band diagram of the heterostructure submitted to the influence of a Schottky gate in contact with the larger gap semiconductor. The two-dimensional electrons are confined at the heterointerface of AlGaAs and GaAs. The electron energies are quantized along the z direction, which is perpendicular to the heterointerface, due to the potential well at the heterointerface:

$$E = E_j + (\hbar^2/2m^*)(k_x^2 + k_y^2), \quad j = 0, 1, 2, \dots \quad (2)$$

where $\hbar = h/2\pi$, h the Planck constant, m^* the effective mass, k_x and k_y the x and y components of the wave vector, respectively, and E_j the quantized energy along the z direction. Using the triangular-potential-well approximation and solving the Schrödinger equation, E_j is approximated by²²

$$E_j = \left(\frac{\hbar^2}{8m^*} \right)^{1/3} \left[\frac{3}{2} \frac{q^2}{\epsilon_1} \left(j + \frac{3}{4} \right) \right] n_i^{2/3}, \quad j = 0, 1, 2, \dots \quad (3)$$

The energy-band structure is shown in Fig. 2. The energy along the z direction is quantized.

When a magnetic field B is applied normal to the electron conduction plane of a HEMT, the electron energy is

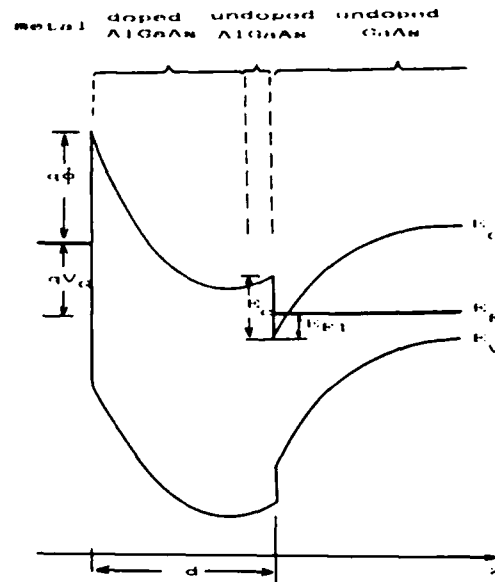


FIG. 1. Band diagram of the AlGaAs-GaAs heterostructure submitted to the influence of a Schottky gate in contact with the larger gap semiconductor.

completely quantized. Neglecting the spin effect the quantized energy is²²

$$E_{jp} = E_j + E_p, \quad (4)$$

where

$$E_p = (p + \frac{1}{2})\hbar\omega_c, \quad p = 0, 1, 2, \dots \quad (5a)$$

and

$$\omega_c = qB/m^*. \quad (5b)$$

The quantized energy E_p is due to magnetic field quantization and is called Landau quantization. The quantized energy levels due to magnetic field are called Landau levels. ω_c is called the cyclotron frequency.

In Landau quantization, the density of states of electrons confined to a two-dimensional plane is no longer constant with energy. The density of states for the j th subband is given by²²

$$D_j(E) = \frac{2qB}{h} \sum_{jp} \delta(E - E_{jp}), \quad (6)$$

where δ denotes the Dirac delta function, and the factor 2 is

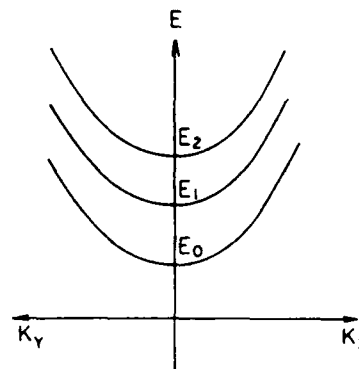


FIG. 2. Energy-band structure for the two-dimensional electron gas. The energy is quantized along the z direction.

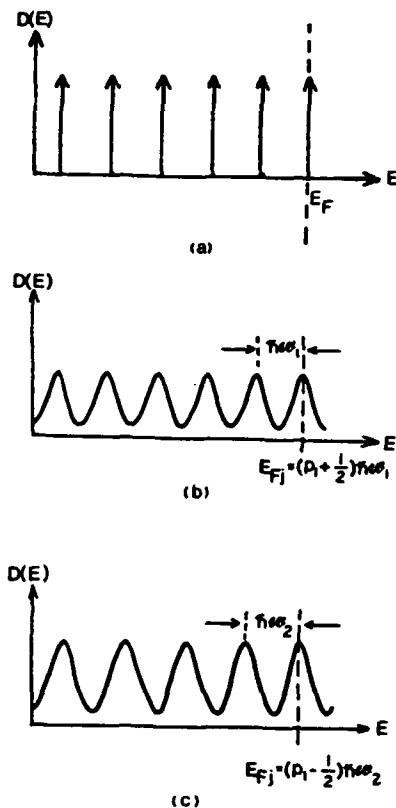


FIG. 3. Density of states for Landau quantization. (a) Delta-like singularities. (b) Damped and broadened density of states due to scattering. Assume that at magnetic field B_1 the $(p_1 + 1)$ -th Landau level is lined up with the Fermi level. (c) B_2 is the next higher magnetic field such that P_1 -th Landau level is lined up with the Fermi level.

due to spin consideration. The density of state is therefore characterized by periodic and delta-like singularities, as shown in Fig. 3(a). However, in real systems the density of states is not singular. Due to scattering, the singularities are damped and broadened, as depicted in Fig. 3(b).

Because of the periodic character of the density of states, the channel conductance versus magnetic field has an oscillation. This is because the conductivity depends on the number of available states nearby in energy that electrons can scatter into. The conductance has a maximum as the Fermi level and a Landau level are lined up because the density of states has a maximum at each Landau level and hence the whole system energy has a maximum. Correspondingly, the conductance dips when the Fermi level is between two adjacent Landau levels.

Define the j th subband Fermi energy E_{Fj} as follows:

$$n_j = \int_{E_j}^{\infty} D_j(E) f(E) dE, \quad (7)$$

where n_j is the concentration of electrons belonging to the j th subband, and $f(E)$ is the Fermi-Dirac distribution function:

$$f(E) = 1/[1 + \exp(E - E_{Fj})/kT]. \quad (8)$$

At low temperature, for example, liquid-helium temperature, $kT \approx 0$, the Fermi-Dirac function $f(E) = 1$ if $E < E_{Fj}$, $f(E) = 1/2$ if $E = E_{Fj}$, and $f(E) = 0$ if $E > E_{Fj}$. Note that E_{Fj} is different from the Fermi energy of the whole system, E_F . E_{Fj} defined in (7) and (8) is the j th subband Fermi energy. The Fermi energy E_{Fj} is independent of magnetic field. To derive an expression for E_{Fj} , for convenience we can assume that the Fermi level E_{Fj} is lined up with a Landau level, as shown in Fig. 3(a). Using E_j as a reference energy,

i.e., $E_j = 0$, it is easy to obtain the following equation by Fig. 3(a):

$$E_{Fj} = (p + \frac{1}{2}) \hbar \omega_c. \quad (9)$$

Substituting (6) and (8) into (7) yields

$$n_j = (2qB/h)(p + \frac{1}{2}), \quad (10)$$

where the factor $1/2$ is due to $f(E_{Fj}) = 1/2$. Recalling $\omega_c = qB/m^*$ and substituting (10) into (9) yields

$$E_{Fj} = n_j \hbar^2 / 4\pi m^*. \quad (11)$$

As seen from (11), the Fermi energy E_{Fj} is independent of magnetic field B .

To derive the concentration versus oscillation period, referring to Figs. 3(b) and 3(c), assume that at magnetic field B_1 the $(p_1 + 1)$ -th Landau level is lined up with the Fermi level E_{Fj} .

$$E_{Fj} = (p_1 + \frac{1}{2}) \hbar \omega_1, \quad (12)$$

where $\omega_1 = qB_1/m^*$. Suppose that B_2 is the next higher magnetic field such that its p_1 -th Landau level is lined up with the Fermi level E_{Fj} again. Hence

$$E_{Fj} = (p_1 - \frac{1}{2}) \hbar \omega_2, \quad (13)$$

where $\omega_2 = qB_2/m^*$.

Combining (11), (12), and (13), we obtain the oscillation period

$$\Delta \left(\frac{1}{B} \right) = \frac{1}{B_1} - \frac{1}{B_2} = \frac{2q}{n_j \hbar}. \quad (14)$$

The concentration n_j is therefore

$$n_j = (2q/h) [1/\Delta(1/B)] \\ = 4.836 \times 10^{10} (\text{T}^{-1} \text{cm}^{-2}) [1/\Delta(1/B)], \quad (15)$$

where T (tesla) is the unit of the magnetic field B . The period $\Delta(1/B)$ is determined by the oscillation period of the resistance versus $1/B$. Equation (15) is used for calculating the electron concentration in Shubnikov-de Haas measurements. Because the lowest two subbands are dominant for electrons, two oscillation periods corresponding to these two subbands are possibly observed.

Besides the channel conductance, the transconductance or drain current can be made to oscillate with respect to gate voltage with constant drain voltage under fixed magnetic field. Because the Landau level spacing is constant, the drain current or transconductance can be made to oscillate by varying the gate voltage to move the Fermi level to pass the discrete Landau levels.¹⁰ The number of states per unit area in each Landau level, according to (6), is $2qB/h$. At low temperature, for levels below Fermi energy E_{Fj} the occupied probability is 1. Hence the number of electrons per unit area, n_{jp} , in a Landau level which is below the Fermi level E_{Fj} is

$$n_{jp} = 2qB/h. \quad (16)$$

For a constant magnetic field, the Landau level spacing is fixed. Assume that at gate voltage V_{G1} the Fermi level E_{Fj} is lined up with a Landau level, and at the next higher gate voltage V_{G2} the Fermi level moves up to line up with the next higher Landau level. From (16), the increase of the concentration, Δn_j , due to the increase of the gate voltage, $\Delta V_G = V_{G2} - V_{G1}$, is

$$\Delta n_j = 2qB/h. \quad (17)$$

For useful application, we need to know the relationship between ΔV_G and Δn_j . For convenience, rewrite the charge-control law (1) as follows:

$$n_s = (C/q)(V_G - V_T), \quad (18)$$

where V_T is the threshold voltage, $C = q_2 \epsilon_2 / (q^2 d + \epsilon_2 a)$, ϵ_2 the permittivity of the AlGaAs, d the total thickness of the AlGaAs layer, and $a = 0.125 \times 10^{-12} \text{ eV cm}^2$.¹⁸

The concentration of the lowest subband, n_0 , is the most sensitive to the gate voltage V_G . Neglecting the contribution due to the higher subband and combining (17) and (18), one obtains

$$\begin{aligned} C &= (2q^2/h)(B/\Delta V_G) \\ &= 7.75 \times 10^{-9} (\text{F V cm}^{-2} \text{ T}^{-1})(B/\Delta V_G). \end{aligned} \quad (19)$$

Therefore, SdH measurements can be applied to estimate the capacitance C and the thickness of AlGaAs layer d .

Unfortunately, this is not an accurate formula for the following two reasons: first, the electrons in the higher subband have been neglected in deriving (19); second, the channel carrier density expressed by (18) is derived with assumptions, and hence it is only an approximate formula. We have measured the oscillations of the resistance versus magnetic field to determine the electron concentration as a function of gate voltage. The experimental data will be shown in Sec. IV. The data show that we cannot neglect the concentration in the second lowest subband n_1 and n_0 vs V_G is not linear dependent. The charge-control law is only an approximate relation. Hence, it may cause a serious error if we use (19) to determine the gate capacitance C and the thickness of the AlGaAs layer d .

III. GEOMETRICAL MAGNETORESISTANCE

Shown in Fig. 4(a) is a long and thin rectangular bar, the conventional Hall plate, with an applied transverse magnetic field. If the electronic conduction process is due to a single band of carrier and is isotropic, and if the scattering is independent of energy, then the Lorentz force on the carriers is exactly balanced by the Hall electric field developed across the bar. In this case, the current flows directly down the length of the bar and the electric field is oriented at the Hall angle θ_H relative to this direction, as shown in Fig. 4(a). The resistivity $\rho(B)$ measured in the presence of the magnetic field B will be the same as the resistivity $\rho(0)$ measured with no magnetic field applied. Thus, for this ideal case, the Hall plate will show no magnetoresistance.

In practice, however, $\rho(B)$ is different from $\rho(0)$, usually larger. This increased resistivity in the presence of the magnetic has been called physical magnetoresistance (PMR) and occurs if the conduction processes are anisotropic, the conduction involves more than one type of carrier, or the scattering is energy dependent. PMR arises because the Hall field can only compensate the average Lorentz force of the carriers. So in a real semiconductor many carriers will be over or under compensated resulting in an increase in the observed resistivity.

If, instead of a long bar, we have a thin plate with metal-

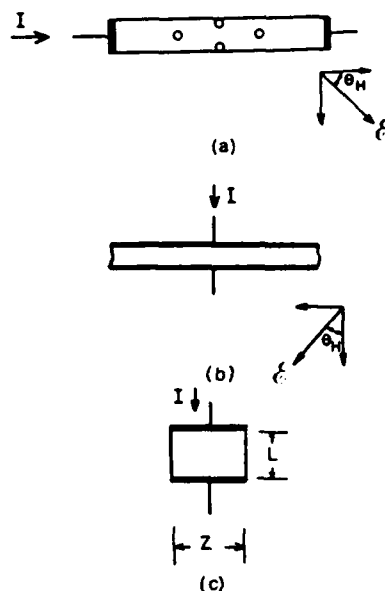


FIG. 4. Sample geometries. (a) Long and thin rectangular bar. (b) Short and infinitely wide diode. (c) Finite diode.

lic contacts on the large faces as shown in Fig. 4(b), the Hall field set up by the transverse field B is shorted out by the contacts. The Lorentz force acting on the carriers is no longer compensated. The average carriers move at a Hall angle with respect to the applied electric field. The electric field is directed across the sample, and the resulting current thus flows at the Hall angle as shown in Fig. 4(b). In this case, a magnetoresistance will be observed even if the material exhibits no PMR. This effect is called geometrical magnetoresistance (GMR). Its existence is due to solely the boundary conditions of the problem. Of course, if physical magnetoresistance is present, the total observed magnetoresistance will be a combination of the physical and geometrical effects. In many cases, however, the PMR is much smaller effect than the GMR. In GaAs, for example, at room temperature, and in a magnetic field of 1 T, the PMR is about 2% and the GMR about 50%.

The theory for GMR has been developed in the text book.²³ The resistance for a thin plate, shown in Fig 4(b), with an applied magnetic field B is given by

$$R(B) = R(0)(1 + \alpha^2 \mu_H^2 B^2), \quad (20)$$

where $R(0)$ is the sample resistance with no magnetic field applied, μ_H the Hall mobility, and α a parameter which depends on the details of the scattering mechanisms.

Since α is the quantity which relates the Hall mobility to the magnetoresistance, it is essential that this constant be determined. Calculations of α for several idealized types of scattering show the following results:

$$\alpha = \begin{cases} 1.00, & \text{constant relaxation time approximation} \\ 1.13, & \text{lattice scattering} \\ 1.25, & \text{ionized impurity scattering.} \end{cases} \quad (21)$$

Define the GMR mobility as follows:

$$\mu_G = \alpha \mu_H. \quad (22)$$

The resistance as a function of magnetic field becomes

$$R(B) = R(0)(1 + \mu_G^2 B^2). \quad (23)$$

This equation is good for an infinitely wide diode only. For a finite diode, Fig. 4(c), the transverse current must be collected by the contacts and so will influence the measured

$$R(B) = \begin{cases} R(0) \frac{1 + \mu_G^2 B^2 [1.7052/K(t')]}{(1 - \frac{1}{2} \mu_G^2 B^2) \{1 + \mu_G^2 B^2 [\pi/4K(t)]\}} \\ R(0) \frac{1 + \mu_G^2 B^2 [\pi/4K(t')]}{(1 - \frac{1}{2} \mu_G^2 B^2) \{1 + \mu_G^2 B^2 [0.4263/K(t)]\}} \end{cases}$$

where L is the sample length, Z the sample width, and $K(t)$ is an elliptic integral defined as²⁴

$$K(t) = \int_0^1 \frac{d\lambda}{\sqrt{(1-\lambda^2)(1-t^2\lambda^2)}} \\ = \frac{\pi}{2} \left[1 + \left(\frac{1}{2}\right)^2 t^2 + \left(\frac{1}{2} \frac{3}{4}\right)^2 t^4 + \left(\frac{1}{2} \frac{3}{4} \frac{5}{6}\right)^2 t^6 + \dots \right]. \quad (25)$$

In (24), t and t' are the parameters determined by the aspect ratio L/Z ,

$$L/Z = K(t')/2K(t) \quad (26)$$

and

$$t^2 + t'^2 = 1. \quad (27)$$

Using the Taylor expansion, $1/(1+x) \approx 1-x$, and neglecting the high-order terms, (24) becomes

$$R(B) = \begin{cases} R(0) \left[1 + \left(\frac{1}{2} - \frac{\pi}{4K(t)} + \frac{0.4263}{K(t')}\right) \mu_G^2 B^2 \right] & \text{for } L/Z > 1, \\ R(0) \left[1 + \left(\frac{1}{2} + \frac{\pi}{4K(t')} - \frac{0.4263}{K(t)}\right) \mu_G^2 B^2 \right] & \text{for } L/Z < 1. \end{cases} \quad (28)$$

For $L/Z > 1$, $K(t) \approx \pi/2$. Using (26), we have

$$R(B) = R(0) [1 + 0.543(L/Z) \mu_G^2 B^2] \quad \text{for } L/Z > 1. \quad (29)$$

If $L/Z < 0.3$, $K(t') \approx \pi/2$ (see Table I). Substituting (26) into (29) yields

TABLE I. t , $K(t)$, $K(t')$, and l_z as a function of the aspect ratio.

L/Z	t	$K(t)$	$K(t')$	l_z
0.2	0.997	3.933	1.573	0.891
0.3	0.958	2.674	1.604	0.830
0.4	0.854	2.121	1.697	0.762
0.5	0.707	1.854	1.854	0.694
0.6	0.556	1.719	2.063	0.633
0.7	0.423	1.649	2.309	0.582
0.8	0.316	1.612	2.580	0.540
0.9	0.233	1.593	2.867	0.506

resistance. Lippmann and Kuhrt^{20,21} have calculated this kind of resistance. Neglecting physical magnetoresistance which is a very small effect in the two-dimensional system, for a small applied field B such that $\tan(\mu_G B) \approx \mu_G B$, the resistance as a function of magnetic field is

$$\begin{aligned} &\text{for } \frac{L}{Z} > 1, \\ &\text{for } \frac{L}{Z} < 1, \end{aligned} \quad (24)$$

$$R(B) = R(0) \{1 + [1 - 0.543(L/Z)] \mu_G^2 B^2\}$$

$$\text{for } L/Z < 0.3. \quad (30)$$

For aspect ratio L/Z between 0.3 and 1.0, there is no simple formula available. Table I shows the t , t' , $K(t)$, and $K(t')$ as a function of the aspect ratio L/Z . We can use this table to calculate $R(B)$. Summarizing (28), (29), and (30), we have the following formula for calculating the GMR mobility μ_G :

$$r(B) = \begin{cases} 0.543(L/Z) \mu_G^2 B^2, & L/Z > 1, \\ l_z \mu_G^2 B^2, & 0.3 < L/Z < 1 \text{ (using Table I)}, \\ [1 - (0.543(L/Z))] \mu_G^2 B^2, & L/Z < 0.3, \end{cases} \quad (31)$$

where

$$r(B) = [R(B)/R(0)] - 1 \quad (32)$$

is the normalized magnetoresistance, and

$$l_z = \frac{1}{2} + \frac{\pi}{4K(t')} - \frac{0.4263}{K(t)} \quad (33)$$

is a constant determined by the aspect ratio L/Z . l_z as a function of the aspect ratio L/Z is also listed in Table I. We can determine μ_G from the slope of r vs B^2 and the zero-field resistance $R(0)$.

The geometrical magnetoresistance measurement to determine the mobility has the merit that it is independent of the electron concentration. We do not need to know the concentration to determine the mobility. The GMR mobility μ_G is very close to the Hall mobility. GMR measurements combined with SdH measurements can provide the characterization of HEMTs and insight on the nature of the devices because these two measurements do not depend on each other.

On the other hand, if we know the electron concentration from SdH measurements, we can obtain the drift mobility μ_D instead of the GMR mobility μ_G or the Hall mobility μ_H by measuring the zero-field resistance $R(0)$. Hence, we can compare the parameters μ_D and μ_G , or calculate the ratio μ_G/μ_D to determine which scattering mechanism is dominant.

The drain current for a HEMT in the linear region of the output current-voltage characteristics is given by¹⁵

$$I_D = qn_s Z \mu_D \xi, \quad (33)$$

where ξ is the electric field. Using $\xi = dV/dx$, integrating (33) from $x = 0$ to $x = L$ and neglecting the series source and drain resistances, one obtains

$$\mu_D = (L/Z)(1/qn_s R), \quad (34)$$

where $R = V_D/I_D$, V_D the drain voltage, and I_D the drain current. Using this equation, we can determine the drift mobility if the electron concentration is known, for example, from Shubnikov-de Haas measurements. We will compare the drift mobility μ_D to the GMR mobility μ_G to determine the scattering mechanisms.

IV. EXPERIMENTS AND DISCUSSION

Figure 5(a) shows the typical resistance as a function of magnetic field for a modulation-doped AlGaAs/GaAs heterostructure, sample No. S1. As predicted from the theory of the Shubnikov-de Haas oscillation, we can see the resistance oscillates as the magnetic field changes. From the oscillation peaks, we can calculate the oscillation period $\Delta(1/B)$, which is then used for estimating the electron concentration by (15). However, this R - B curve only provides the information for the lowest subband. To observe the second oscillation period, one must take the first or second derivative of R with respect to B , as shown in Figs. 5(b) and 5(c), respectively. It is obvious that d^2R/dB^2 vs B in Fig. 5(c) has two

oscillation periods. One is the same period as that of Fig. 5(a); the other, which is marked by the dashed line in Fig. 5(c), is due to the electrons in the second low subband, E_1 . To add an understanding of the periodic property of the SdH oscillation, we replot the d^2R/dB^2 as a function of $1/B$ in Fig. 5(d). The two oscillation periods in Figs. 5(c) or 5(d), $\Delta(1/B)$, are 0.0442 T^{-1} and 0.37 T^{-1} , respectively. Therefore, according to (15), the concentration of the 2DEG in the lowest subband is $n_0 = 1.09 \times 10^{12} \text{ cm}^{-2}$ and the concentration in the second lowest subband is $n_1 = 1.3 \times 10^{11} \text{ cm}^{-2}$. The total concentration of the 2DEG is $n_s \approx n_0 + n_1 = 1.22 \times 10^{12} \text{ cm}^{-2}$.

For the measurement of a HEMT, we need to know the channel concentration as a function of gate voltage. Figure 6 shows the output current-voltage characteristics of a HEMT, sample No. D1, with gate length $100 \mu\text{m}$ and width $200 \mu\text{m}$ at temperature 4.2 K . Figures 7(a) and 7(b) show the dR/dB vs B at different gate voltage $V_G = 0$ and 0.2 V , respectively. It is shown that with different gate voltages we observe the different oscillation periods corresponding to the channel concentration. We can see a second oscillation period corresponding to the concentration belonging to the sec-

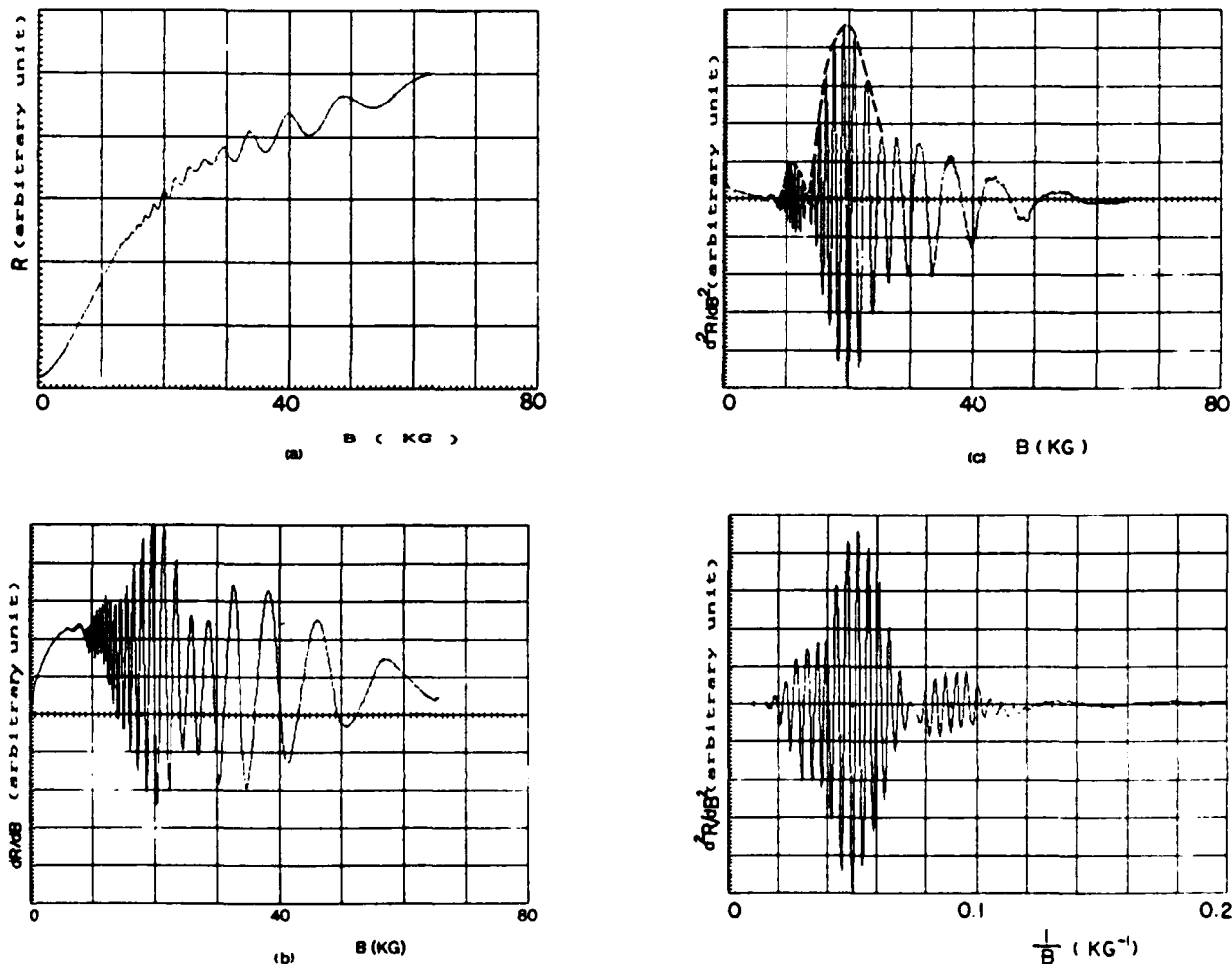


FIG. 5. Shubnikov-de Haas oscillation for an AlGaAs-GaAs modulation-doped heterostructure. ($1 \text{ T} = 10 \text{ kG}$.) (a) Resistance vs magnetic field. (b) First derivative of resistance with respect to magnetic field. (c) Second derivative of resistance with respect to magnetic field. (d) Second derivative of resistance with respect to $1/B$.

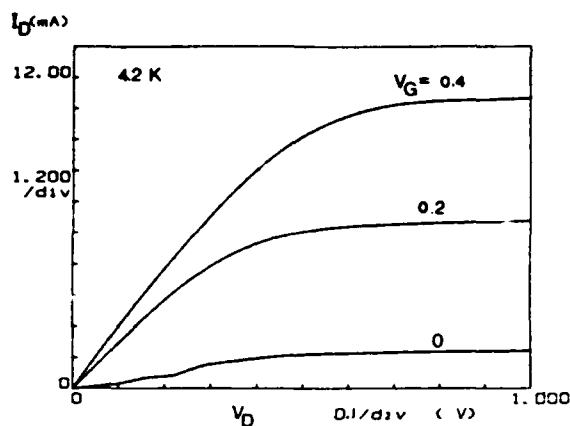


FIG. 6. Output current-voltage characteristics of a long channel HEMT at temperature 4.2 K.

and lowest subband at gate voltage $V_G = 0.2$ V. However, for the low gate voltage $V_G = 0$, the second oscillation period is not observed. To observe a second oscillation period corresponding to the concentration of the second lowest subband requires a reasonably high electron concentration. Figure 8 shows the concentration of the 2DEG as a function of gate voltage, which is obtained from Shubnikov-de Haas

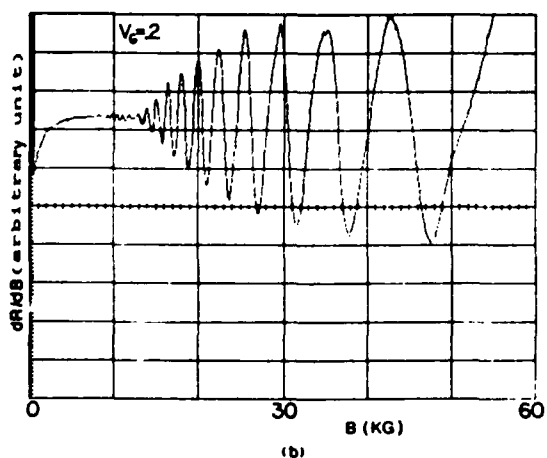
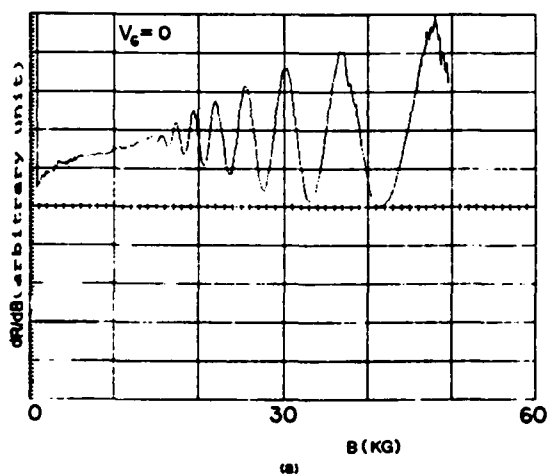


FIG. 7. Shubnikov-de Haas measurements for a HEMT with different gate biases. (a) Gate voltage 0 V. (b) Gate voltage 0.2 V.

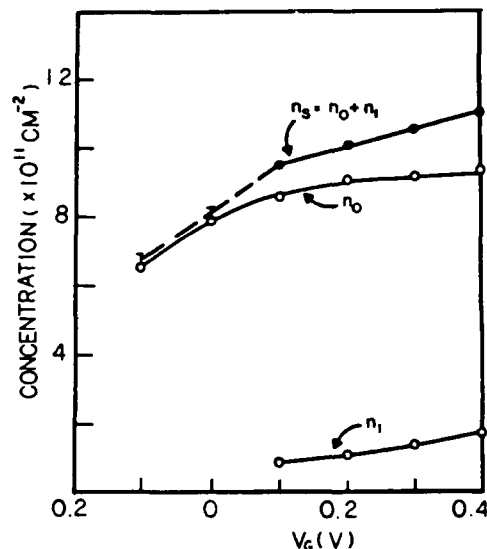


FIG. 8. Concentration of the two-dimensional electron gas as a function of gate voltage.

measurements. n_0 is the concentration of the lowest subband, n_1 is the concentration of the second low subband, and $n_s = n_0 + n_1$ is the total channel electron concentration. For the gate voltage $V_G > 0.1$ V, the second oscillation period corresponding to n_1 is observed. For the gate voltage $V_G < 0.1$ V, the second oscillation period is not observable in the measurements.

However, we cannot arbitrarily say that n_1 is 0 for gate voltage $V_G < 0.1$ V. Figure 8 shows the uncertainty errors at the gate voltage $V_G = 0$ and -0.1 V due to unobservable n_1 . Because of the uncertainty in the range between voltage $V_G = -0.1$ V and $V_G = 0.1$ V, the n_s - V_G curve is marked by a dashed line in this region.

It is obvious that the n_s - V_G curve has a turning point at $V_G = 0.1$ V. This is due to the incompletely depleted AlGaAs layer,^{16,25} and hence reduces the charge control ability of this gate voltage. Figure 9 shows the n_s - V_G characteristics of a long-channel HEMT with $L/Z = 2$, sample No. D2. It also shows that there is a sharp turning point at

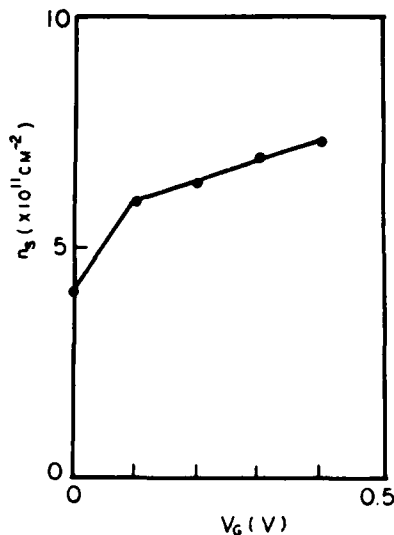


FIG. 9. Concentration vs gate voltage for a HEMT.

$V_G = 0.1$ V. However, in this device the second oscillation period due to the second lowest subband are not observed. Observing the second oscillation period requires high channel concentration, as shown in Figs. 5 and 8. From the data in Fig. 8, $n_0 > 8.5 \times 10^{11} \text{ cm}^{-2}$ is required to observe the second oscillation period.

As shown in Fig. 8, n_0 vs V_G is not linear. Besides, as mentioned in Sec. II, the charge-control law [(1) or (18)] is derived with approximate assumptions. Therefore, it will cause a serious error if we use (19) to calculate the gate-to-channel capacitance C .

Comparing Fig. 8 to Fig. 6, it is interesting to note that even near the cutoff region there is still an appreciable concentration, which is contrary to the prediction of the charge-control law [(1) or (18)]. Therefore, the small current in the cutoff region is not completely due to the decrease of channel concentration only. It may be also due to the rapid decrease of the electron mobility as the gate voltage decreases, as will be discussed in the following.

Figure 10 shows a plot of normalized magnetoresistance r vs B^2 for a HEMT, sample No. D1, with different gate voltages. It can be seen that r vs B^2 is linear. The deduced GMR mobility μ_G as a function of gate voltage is shown in Fig. 11. The current-voltage characteristics and the gate voltage dependence of the concentration of the two-dimensional electron gas of this device have been shown in Figs. 6 and 8, respectively.

As shown in Fig. 11, we can see that the mobility is not a constant as the gate voltage changes. The mobility has a low value near the cutoff region, and increases as the gate voltage increases. This may be due to the following reasons. At low gate voltage, which gives a low 2DEG concentration in the channel, the interface field is smaller, and hence the confinement of electrons in the potential well is not very strong. Also, at low temperature the scattering of electrons due to remote ionized donors in the AlGaAs layer, through the Coulomb force, is the dominant mechanism.²⁶ The screening effect for this Coulomb force is weak for the low 2DEG concentration. Hence, the electron mobility has a lower value at low gate voltage.

The ionized-impurity scattering and lattice scattering are the two major mechanisms affecting the carrier transport. $\mu_H/\mu_D = 315\pi/512$ if the impurity scattering is the dominant effect, and $\mu_H/\mu_D = 3\pi/8$ if the lattice scattering

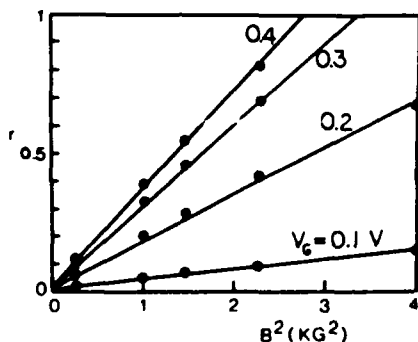


FIG. 10. Normalized magnetoresistance r vs B for a HEMT with different gate voltages.

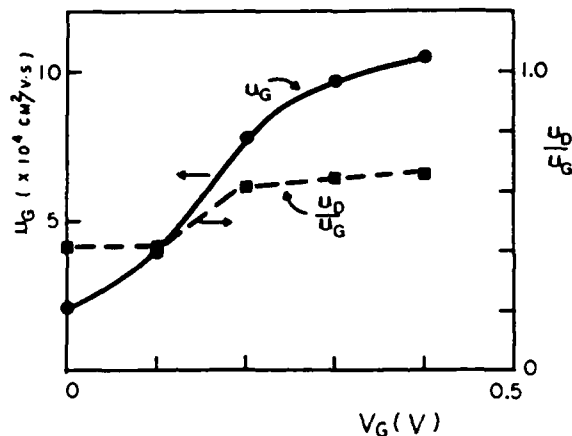


FIG. 11. The GMR mobility and the ratio of the drift mobility to GMR mobility vs the gate voltage.

is dominant. Therefore, according to (21), μ_D/μ_G is 0.41 for the impurity scattering and 0.75 for the lattice scattering. To verify the scattering mechanisms, Fig. 11 also shows the ratio of the drift mobility to the GMR mobility, μ_D/μ_G , as a function of gate voltage V_G . For the gate voltage, $V_G < 0.1$ V, with the low concentration, $\mu_G/\mu_D \approx 0.41$. This is the same value as that predicted by the impurity scattering. Therefore, the impurity scattering is the dominant mechanism for the low 2DEG concentration. As the gate voltage increases to 0.2 V, the ratio of μ_D to μ_G increases sharply up to 0.61, which is between the theoretical values predicted by the impurity scattering, 0.41, and by the lattice scattering, 0.75. The scattering of electrons due to impurity ions becomes weak for the gate voltage $V_G > 0.2$ V. As shown in Fig. 8, the AlGaAs layer is not completely depleted for $V_G > 0.1$ V. The weakening impurity scattering may be due to the strong screening effect by the incompletely depleted AlGaAs layer and high 2DEG concentration. It is important to note that although the charge-control ability of the gate voltage is weakened by the incompletely depleted AlGaAs layer for $V_G > 0.1$ V, the maximum transconductance occurs around $V_G = 0.2$ V due to the increasing mobility with the increasing gate voltage.

As mentioned in the above, from Shubnikov-de Haas measurement, near the cutoff region we still see an appreciable 2DEG concentration. From Figs. 6, 8, and 11, we could conclude that near the cutoff region the decrease of the conductivity is due to both the decrease of the channel concentration and the rapid decrease of the electron mobility.

V. CONCLUSION

For the characterization of high electron mobility transistors, the Shubnikov-de Haas oscillation and geometrical magnetoresistance are used to determine the two most important parameters, channel concentration and mobility, respectively. To deduce useful data from SdH measurements, the theory of the Shubnikov-de Haas oscillation for two-dimensional electrons has been derived and discussed in detail. The experimental data shows two oscillation periods corresponding to the two lowest subbands. The experimental data for the channel concentration as a function of the

gate voltage is used to characterize the devices and to check the accuracy of the charge-control law.

A series of formulas for the geometrical magnetoresistance is provided to calculate the GMR mobility for any aspect ratio. We need not know the channel concentration to determine the mobility. Hence the GMR together with SdH measurements provide for the characterization of HEMTs and insight into the nature of the devices because these two measurements do not depend upon each other.

The experimental data show that the mobility is a function of gate voltage. The impurity scattering is the dominant mechanism for the low two-dimensional electron concentration. The maximum transconductance occurs at a compromise between the charge control ability of the gate voltage and the channel mobility. Near the cutoff region, the decrease of the conductivity is due to both the decrease of the channel concentration and the rapid decrease of the electron mobility.

ACKNOWLEDGMENTS

The authors would like to thank A. Green at Naval Weapon Center, China Lake, for providing the AlGaAs-GaAs heterostructures, and E. Sovero, B. Mathur, and W. J. Ho at Rockwell Science Center for providing the FAT HEMTs. This work is partially supported by the Office of Naval Research and by the Air Force of Scientific Research.

¹D. Dingle, H. L. Stormer, A. C. Gossard, and W. Wiegmann, *Appl. Phys. Lett.* **33**, 665 (1978).

- ²T. J. Drummond, W. Kopp, H. Morkoç, and M. Keever, *Appl. Phys. Lett.* **41**, 277 (1982).
- ³T. Mimura, S. Hiyamizu, T. Fujii, and K. Nanbu, *Jpn. J. Appl. Phys.* **19**, L225 (1980).
- ⁴L. J. van der Pauw, *Philips Res. Rep.* **13**, 1 (1958).
- ⁵M. G. Buehler, *Appl. Phys. Lett.* **31**, 848 (1977).
- ⁶M. G. Buehler, *J. Electrochem. Soc.* **127**, 701 (1980).
- ⁷M. L. Stormer, R. Dingle, A. C. Gossard, W. Wiegmann, and M. D. Sturge, *J. Vac. Sci. Technol.* **16**, 1517 (1979).
- ⁸D. C. Tsui, H. L. Stormer, A. C. Gossard, and W. Wiegmann, *Phys. Rev. B* **21**, 1589 (1980).
- ⁹S. Luryi and Kastalsky, *Appl. Phys. Lett.* **45**, 164 (1984).
- ¹⁰S. Y. Chou, D. A. Antoniadis, and H. I. Smith, *IEEE Trans. Electron Devices* **ED-34**, 883 (1987).
- ¹¹T. R. Jervis and E. F. Johnson, *Solid-State Electron.* **13**, 181 (1970).
- ¹²J. R. Sites and H. H. Wieder, *IEEE Trans. Electron Devices* **ED-27**, 2277 (1980).
- ¹³P. R. Jay and R. H. Walls, *IEEE Electron Dev. Lett.* **EDL-2**, 265 (1981).
- ¹⁴D. C. Look, G. B. Norris, W. Kopp, T. Henderson, and H. Morkoç, *Appl. Phys. Lett.*, **47**, 267 (1985).
- ¹⁵C.-S. Chang and H. R. Fetterman, *IEEE Trans. Electron Devices* **ED-34**, 1456 (1987).
- ¹⁶D. Delagebeaudeuf and N. T. Linh, *IEEE Trans. Electron Devices* **ED-29**, 995 (1982).
- ¹⁷T. J. Drummond, H. Morkoç, K. Lee, and M. S. Shur, *IEEE Electron Device Lett.* **EDL-3**, 338 (1982).
- ¹⁸C.-S. Chang and H. R. Fetterman, *Solid-State Electron.* **30**, 485 (1987).
- ¹⁹R. A. Pucel and C. F. Krumm, *Electron. Lett.* **12**, 240 (1976).
- ²⁰H. J. Lippmann and F. Kuhrt, *Z. Naturforsch.* **13a**, 462 (1958).
- ²¹H. J. Lippmann and F. Kuhrt, *Z. Naturforsch.* **13a**, 474 (1958).
- ²²W. Zawadzki, in *Springer Series in Solid-State Science*, edited by G. Bauer, F. Kuchar, and H. Heinrich (Springer, Berlin, 1984), Vol. 53, pp. 2-11.
- ²³R. A. Smith, *Semiconductors*, 2nd ed. (Cambridge University Press, Cambridge, 1978) pp. 114-116.
- ²⁴See, for example, S. M. Selby, Ed., *Standard Mathematical Tables*, 21st ed. (Chemical Rubber Co., Cleveland, OH, 1975), pp. 529-541.
- ²⁵G. W. Wang and W. H. Ku, *IEEE Trans. Electron Devices* **ED-33**, 657 (1986).
- ²⁶B. J. Lin, D. C. Tsui, M. A. Paalanen, and A. C. Gossard, *Appl. Phys. Lett.* **45**, 695 (1984).

W-band six-port network analyzer for two-port characterization of millimeter wave transistors

10

Karl J. Moeller,^{a)} James H. Schaffner,^{b)} and Harold R. Fetterman

Department of Electrical Engineering, University of California, Los Angeles, California 90024

(Received 18 August 1988; accepted for publication 7 November 1988)

A W-band (75–100 GHz) six-port network analyzer was constructed from discrete WR-10 waveguide components for the two-port S -parameter characterization of state-of-the-art submicron gate length high electron mobility transistors. The six-port was capable of measuring the phase of a circuit's reflection or transmission coefficient to within a 6° and the magnitude to within 1.5% for large reflections and to within 10% for small reflections (return loss of 20 dB). A comparison between the six-port and a down-converter-type frequency extender for a conventional network analyzer revealed the superior performance of the six-port. To demonstrate the applicability of the six-port network analyzer to device characterization, the S -parameters of 0.1- μm gate length HEMTs were measured and then used to calculate the maximum available gain achievable with these transistors at W-band frequencies. These measurements indicate the important role the six-port network analyzer will play in the future development of millimeter wave transistors.

INTRODUCTION

Transistor technology has reached a point where amplifiers and oscillators, utilizing either GaAs FETs,¹ or $\text{Al}_x\text{Ga}_{1-x}\text{As}$ high electron mobility transistors (HEMTs)² have been fabricated to operate at W-band frequencies (75–110 GHz). The typical design procedure for these circuits begins with the determination of the two-port scattering parameters of the transistor (S parameters) at microwave frequencies up to 26 GHz. The measured S parameters are then used in a microwave circuit analysis program (such as TouchstoneTM or SupercompactTM) to generate a small-signal lumped element model of the transistor, which is then extrapolated up to the millimeter wave frequency where the circuit is to be designed. This procedure works reasonably well when the extrapolation is not too severe, such as at Ka band,³ but at higher frequencies actual device performance deviates substantially from the model. A better approach to precise and efficient high frequency circuit design is to measure the transistors' S parameters directly at the frequency of intended circuit operation.

In the past, transistor characterization was limited at millimeter wave frequencies due to the absence of adequate impedance measurement techniques. Recently, some progress has been made in the development of millimeter wave extenders for conventional four-port microwave network analyzers; however, the hardware required for such systems to down-convert the test and reference signals to low-frequency magnitude and phase detection circuits is complex and expensive. The millimeter wave six-port junction network analyzer provides a method of obtaining phasor reflection and transmission information from power measurements alone.⁴ The six-port is especially attractive since it can be constructed from commercially available discrete waveguide components and can be controlled with a desk-top computer.

This paper presents a new use for the W-band six-port

network analyzer for the direct two-port S -parameter measurement of active three terminal devices. The versatility of this six-port was extended from earlier reported millimeter wave six-port reflectometers^{5–7} to include transmission, as well as reflection measurement capability over the full WR-10 waveguide band while maintaining the system performance obtained in the earlier studies. Also presented is a direct comparison between the six-port and a W-band frequency extender for a conventional microwave network analyzer. Finally, the application of the six-port to characterize 0.1- μm gate length HEMTs is outlined and some representative results are given.

I. THE SIX-PORT JUNCTION FOR REFLECTION AND TRANSMISSION MEASUREMENTS

In this section, the theory of the six-port junction is reviewed⁴ to clarify the condition for the measurement of both reflection and transmission coefficients. The derivation of the six-port equations is aided by Fig. 1(a), which shows an arbitrary six-port junction where power detectors P_3 , P_4 , P_5 , and P_6 are attached to ports 3, 4, 5, and 6 respectively. The device under test is attached to port 2, and the signal source is connected to port 1. The only constraint imposed upon the junction is that the power levels detected at each port be linearly independent with respect to an arbitrary load at port 2. Then the waves leaving each port, b_i , can be related to the waves incident to each port, a_i , by a 6×6 S -parameter matrix such that

$$b_i = \sum_{j=1}^6 S_{ij} a_j, \quad i = 1, \dots, 6. \quad (1)$$

In addition, the waves at each port with an attached power detector are related by

$$b_i = \Gamma_{di} a_i, \quad i = 3, 4, 5, 6, \quad (2)$$

where Γ_{di} is the reflection coefficient of the power detector

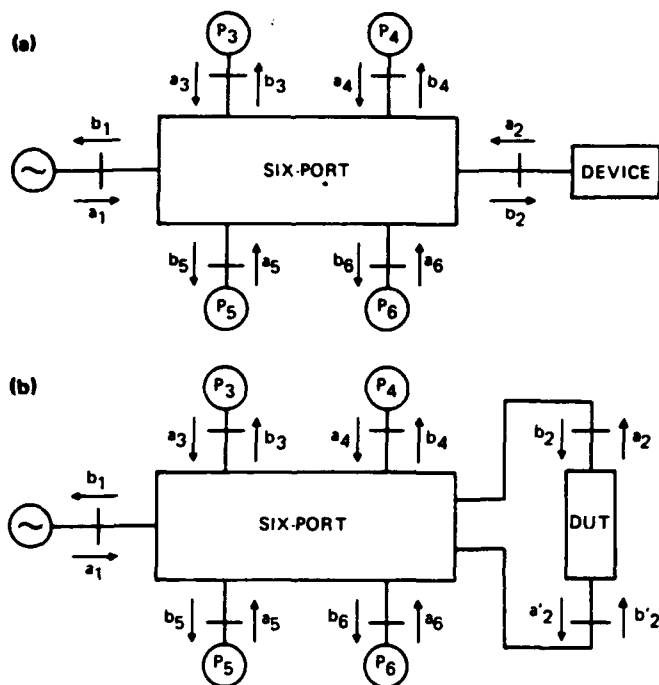


FIG. 1. (a) An arbitrary linear six-port junction for measuring reflection coefficients. Power detectors are labeled P_3 – P_6 and the device to be tested is placed at port 2. (b) An arbitrary linear six-port junction for measuring transmission coefficients. Port 2 has been split into two subports, but in practical situations b'_2 is small and a_2 does not re-enter the six-port so that the device transmission coefficient can be determined using the six-port equations.

at port i , which is assumed to be known. Therefore, a system of ten equations can be written for 12 variables (the a_i and b_i), so that, if a_2 and b_2 are chosen as the independent variables for this system, then each of the ten remaining variables can be written as linear functions of a_2 and b_2 . The power P_i flowing into a detector at port i is directly proportional to $|b_i|^2$ which may be written as

$$P_i = |A_i a_2 + B_i b_2|^2, \quad i = 3, 4, 5, 6, \quad (3)$$

where A_i and B_i are functions of the 36 S parameters and the four-power detector reflection coefficients.

A simplification of the six-port theory results by setting $A_3 = 0$, a restriction that is nearly met by many six-port network analyzers, but is not necessary for six-port operation. Then Eq. (3) can be written as⁴

$$|\Gamma_L - C_i|^2 = (|B_i|^2 P_i) / (|B_3|^2 P_3), \quad i = 4, 5, 6, \quad (4)$$

where $C_i = -A_i/B_i$, and $\Gamma_L = -a_2/b_2$ is the device's reflection coefficient. These equations represent three circles in the complex Γ_L plane. The centers of each circle are given by C_i and the radius by

$$(|B_i|/\sqrt{P_i}) / (|B_3|/\sqrt{P_3}).$$

Since the load is tangible, the loci of points satisfying these equations must intersect at the unique solution Γ_L .

The above equations are valid only for the determination of reflection coefficients. However, an extension of this theory allows for the determination of transmission coefficients. Figure 1(b) shows the general six-port configuration for transmission measurements, where now port 2 has been

split into two subports. The waves at the test ports can be related through the device transmission and reflection coefficients so that, referring to Fig. 1(b), one finds that

$$a'_2 = T_F b_2 + \Gamma_B b'_2,$$

where T_F is the forward transmission coefficient of the device with a matched load on the primed port ($b'_2 = 0$) and Γ_B is the reverse reflection coefficient with $b_2 = 0$. The total forward transmission coefficient can be written as

$$T_L = a'_2/b_2 = T_F + \Gamma_B (b'_2/b_2). \quad (5)$$

For the six-port equations to be applicable to transmission measurements the condition

$$|T_F| \gg |\Gamma_B| (|b'_2|/|b_2|) \quad (6)$$

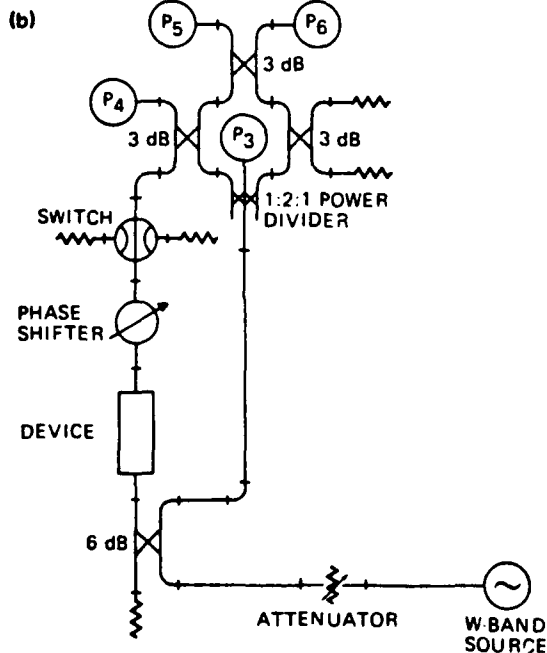
must be met, therefore, the network analyzer should be designed to make b'_2 small. The above analysis also assumes that the wave a'_2 reflected from the device does not re-enter the six-port. When condition (6) is satisfied, then a'_2 may be substituted for a_2 in Eq. (3), and the six-port transmission equations are identical to Eq. (4) except that they are now in terms of T_L instead of Γ_L .

In practice, the 36 S parameters of Eq. (1) are unknown. Therefore, the electrical characteristics of the six-port junction and power detectors, as seen from the device test port are determined through the process of calibration, whereby a number of standard loads are measured to find the system constants.^{8,9} The calibration procedure that was used for the W-band six-port was developed by Li and Bosio¹⁰ and required four ideal short and offset short circuits plus a matched load for reflection calibration, and four ideal phase delays and an infinite attenuation for the transmission calibration.

II. THE W-BAND SIX-PORT NETWORK ANALYZER

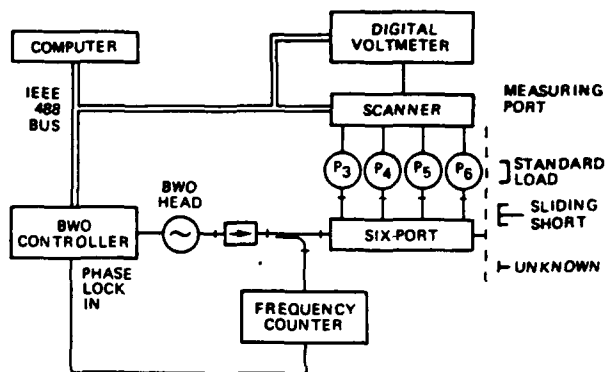
The above theory provided the foundation for the development of the W-band six-port network analyzer. This section describes the construction of the six-port from discrete waveguide components and the control with a microcomputer. In addition, sample measurement results of precision standards which were used for the system evaluated are presented.

Schematic drawings of the W-band six-port network analyzer in the reflection and transmission measurement modes are shown in Figs. 2(a) and 2(b). As can be seen from the figures, the core of the six-port consisted of a sum and difference network comprised of 3-dB bidirectional couplers and a 1:2:1 power divider. W-band thermistors (Hughes Aircraft Co. model No. 45776H), labeled P_3 , P_4 , P_5 , and P_6 in the figure, were used as power detectors; each thermistor had a linear range from -20 to 10 dBm. The input power was split into a test and reference channel by a 6-dB bidirectional coupler. The system was powered by a backward wave oscillator (Micro-Now model No. 728) that provided 10 to 20 mW of power from 75 to 110 GHz, and was frequency locked by a frequency counter (EIP model No. 578). The power detected by each thermistor was read by an analog power meter (Hewlett-Packard model No. 432A). Each meter's output was directed to a digital voltmeter (Hewlett-



Packard model No. 3488A). Both scanner and voltmeter were controlled by a microcomputer (Hewlett-Packard model No. 236).

435 Rev. Sci. Instrum., Vol. 60, No. 3, March 1989



bration standards consisted of a tunable sliding short circuit (Hughes Aircraft Co. model No. 45676H) which was tuned for relative phase delays of 0° , 90° , 180° , and 270° at each discrete frequency. The transmission calibration was performed with a direct reading precision phase shifter (Hughes Aircraft Co. model No. 45756H) to provide transmission phase lags of 0° , 90° , 180° , and 270° at each frequency. The determination of the correct roots of the calibration equations were accomplished with a waveguide matched load for the reflection calibration and with a total transmission absorber (a switch into a waveguide matched load) for transmission calibration.

A line graph showing the magnitude of a signal as a function of the electrical delay of a shorting plane. The x-axis is labeled 'ELECTRICAL DELAY OF SHORTING PLANE (DEGREES)' and ranges from 0 to 400. The y-axis is labeled 'MAGNITUDE' and ranges from 0.96 to 1.04. A dashed horizontal line is drawn at a magnitude of 1.00. The solid line starts at 1.00 at 0 degrees, rises to a peak of approximately 1.012 at 50 degrees, then drops to about 1.002 at 100 degrees. It remains near 1.00 until 175 degrees, where it dips slightly to 0.998. It then rises to 1.00 at 200 degrees, drops to a minimum of approximately 0.992 at 250 degrees, and finally rises to about 1.008 at 350 degrees.

Electrical Delay (Degrees)	Magnitude
0	1.000
25	1.005
50	1.012
75	1.011
100	1.002
125	1.000
150	0.999
175	0.998
200	1.000
225	0.995
250	0.992
275	0.992
300	0.992
325	1.000
350	1.008

Millimeter wave transistors

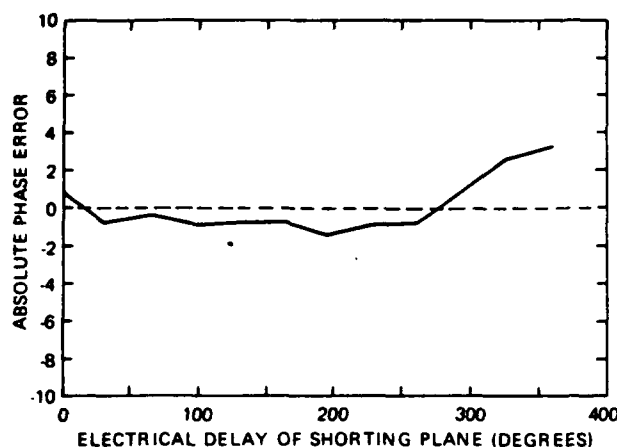


FIG. 5. Absolute phase error of the reflection coefficient of a tunable short circuit as the shorting plane is varied over 360° . The absolute phase error is the difference between the calculated reflection phase and the reflection phase measured by the six-port.

fied accuracy of $\pm 1^\circ$). Over the entire band, it was found that the transmission coefficient of the phase shifter varied in magnitude by less than 0.035 from unity and the absolute phase error was less than 4° as the phase lag was varied over 360° .

In order to check the system response for large return or insertion losses, a variable attenuator was placed in the test port. Figure 6 shows an example of an insertion loss measurement at 94 GHz where the measured attenuation is plotted against the attenuator setting. It can be seen that the measured insertion loss is 12% less than the attenuator setting at 20 dB (2% of this can be attributed to the accuracy of the attenuator).

As a comparison of different measurement technologies, the measurements of the tunable short circuit were repeated using a down-converter-type frequency extender (Honeywell model No. CAW-8S) used with a microwave network analyzer (Hewlett-Packard model No. 8410B).

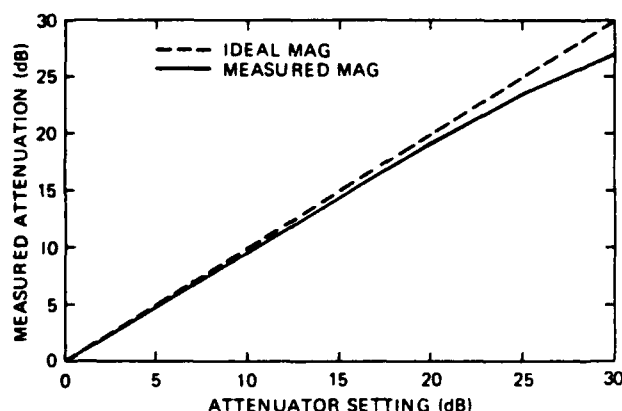


FIG. 6. Insertion loss of a variable attenuator measured by the six-port as the attenuator setting was varied. The solid curve was the measured magnitude (in dB) of the transmission coefficient, and the dashed curve is the transmission coefficient that would be obtained from an ideal measurement system.

The network analyzer frequency extender consisted of millimeter wave waveguide reference and test signal inputs, a free-running 89 GHz Gunn diode local oscillator, and matched mixers on both the reference and test arms. The mixer outputs are connected to the reference and test signal inputs of the microwave network analyzer. Figure 7 shows the frequency extender configured to measure reflection coefficients. The frequency extender/network analyzer combination was calibrated by setting the sliding short circuit to the same offset used as 0° for the six-port and then adjusting the network analyzer to read 0° and 0 dB.

Using the frequency extender, the measured magnitudes of the tunable short circuit were 1.00 ± 0.18 , 1.00 ± 0.05 , and 1.00 ± 0.09 at 75, 90, and 100 GHz, respectively, indicating that the measurement performance degraded as the source frequency moved away from the 89 GHz LO frequency. The worst case difference between measured and calculated phase was found to be on the order of 10° . For large return loss measurements, a waveguide termination with a specified reflection coefficient magnitude of 0.029 was measured by the frequency extender as having a magnitude of 0.14; the six-port measured this termination as having a magnitude of 0.033. Thus, from these W-band measurements, it may be concluded that the six-port network analyzer is more accurate than the frequency extender.

III. W-BAND CHARACTERIZATION OF SUBMICRON GATE LENGTH HEMTs

As an example of the application of the six-port to W-band transistor measurements, the characterization of submicron HEMTs is presented. The determination of the complete set of two-port device S parameters from a single six-port required that, in addition to reconfiguring the system between reflection and transmission measurements, the transistor test fixture had to be physically rotated 180° between forward and reverse parameter measurements.

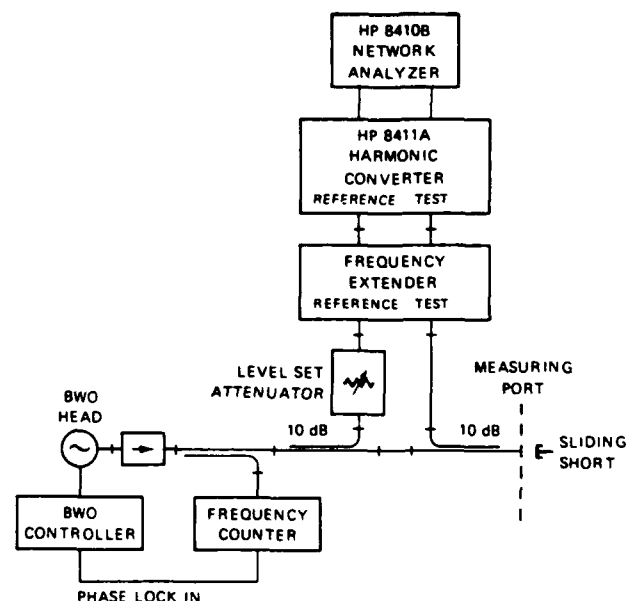


FIG. 7. W-band frequency extender/network analyzer combination configured for reflection measurements. A tunable short circuit was used to compare the performance of the six-port network analyzer to this system.

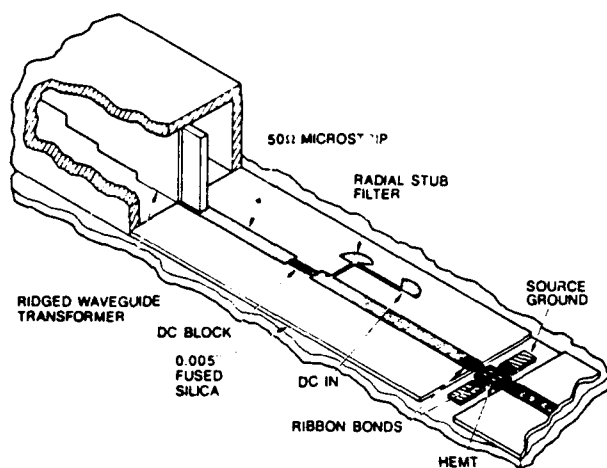


FIG. 8. Attachment of the HEMT to the 50- Ω microstrip transmission line test fixture. A five-section ridged waveguide transformer coupled the microstrip line to the waveguide of the six-port. Printed circuit bias tees provided a reliable method of dc biasing the transistor.

Also, the transistor's S parameters had to be de-embedded from the test fixture.

A test fixture, shown in Fig. 8, consisted of a transistor connected from the gate and drain pads to 50- Ω microstrip lines that were fabricated on 0.005-in. fused silica substrates, and the source was grounded to the test fixture. Gold bond ribbons were used for the electrical interconnections in order to reduce the parasitic inductance. Printed circuit bias tees were fabricated as part of the microstrip line to provide bias current to the device and dc isolation from the test fixture. The dc block was made from quarter-wavelength coupled lines,¹¹ and the bias current was fed through low-pass radial stub filters¹² that provided a broadband open circuit to the W-band signals. In order to couple the waveguide of the six-port to 50- Ω microstrip line, five-section Chebyshev ridged waveguide transformers were incorporated into the test fixture. The efficiency of the waveguide-to-microstrip transitions was measured with a test fixture that was comprised of back-to-back transformer/bias tee sections. The measured

insertion loss of this fixture ranged from 1.5 dB at 75 GHz to 4 dB at 95 GHz, with an average value of 2.3 dB from 75 to 105 GHz. The return loss of a single transformer/bias tee section was found to vary from 8 dB at 95 GHz to 15 dB at 105 GHz, with an average return loss of 11 dB from 75 to 105 GHz.

Since the six-port network analyzer was calibrated with waveguide standards, a de-embedding procedure had to be employed to remove the transistor's S parameters from the measured S parameters of the test fixture. This was accomplished by considering the test fixture as a symmetric cascade of two-port networks consisting of the device and the two transitions. The first step in the de-embedding process was to find the two-port S parameters of the waveguide-to-microstrip transitions up to the ribbon bonds at the end of the microstrip line. This was done with a special de-embedding fixture made of back-to-back transitions with a through length of microstrip line that duplicated a test fixture without the transistor. Measurements of (1) the reflection coefficient of a single transition with a matched microstrip termination, (2) the reflection coefficient of the entire de-embedding fixture with a waveguide termination, and (3) the transmission coefficient of the de-embedding fixture allowed the two-port S parameters of the waveguide-to-microstrip transitions to be determined.¹³ The next step was to measure the forward and reverse reflection and transmission coefficients of the transistor test fixture. This information, along with the characterization of the de-embedding fixture and the assumption of a symmetrical test fixture, enabled the S parameters to be de-embedded.¹⁴

A number of HEMTs, with gate lengths ranging from 0.1 to 0.5 μm , were measured on the six-port, but only the 0.1- μm gate length HEMTs had gain at W-band.¹⁵ The S parameters of two of the best devices measured to date are presented in Table I. The transistors were characterized from 75 to 105 GHz in 5-GHz increments. It is apparent from Table I that the S parameters of these devices showed a complicated frequency dependence. Repeated measurements of the transistor and de-embedding test fixtures indicated that this frequency behavior was primarily due to the

TABLE I. S parameters of two 0.1- μm gate length HEMTs from 75 to 105 GHz in 5-GHz increments. The de-embedded S parameters include the bond ribbon interconnections between the device and the microstrip line. Note that device No. 1 had gain ($S_{21} > 1$) in a 50- Ω system.

Freq. (GHz)	Device No.	S_{11}		S_{12}		S_{21}		S_{22}	
		MAG	PHA	MAG	PHA	MAG	PHA	MAG	PHA
75	1	0.599	14.4	0.105	-37.6	0.632	-74.2	0.357	67.6
	2	0.342	51.6	0.101	-56.9	0.439	-70.9	0.403	31.3
80	1	0.413	-22.2	0.385	-53.9	1.126	-98.4	0.695	57.9
	2	0.610	50.3	0.492	-44.7	0.886	-92.5	0.283	-5.6
85	1	0.635	-13.9	0.327	-48.3	0.578	-93.4	0.533	35.4
	2	0.281	21.0	0.587	-45.1	0.657	-63.6	0.414	-42.7
90	1	0.378	-44.4	0.604	-98.7	0.852	-122.2	0.735	20.2
	2	0.522	23.3	0.678	-95.7	0.832	-98.0	0.263	-112.9
95	1	0.655	-36.9	0.440	-86.3	0.542	-88.4	0.453	-10.4
	2	0.401	5.6	0.749	-101.9	0.906	-91.7	0.328	-57.7
100	1	0.281	-33.3	0.605	-124.0	0.843	-117.3	0.192	0.4
	2	0.324	23.4	0.591	-132.9	0.820	-115.4	0.089	142.7
105	1	0.219	4.1	0.608	-155.3	0.915	-140.9	0.233	44.4
	2	0.316	56.2	0.548	-138.5	0.703	-125.2	0.278	90.0

distributed nature of the transistors and their bond ribbons as they became a significant fraction of a wavelength, rather than the de-embedding errors caused by the slight asymmetry in the test fixture. More important was the maximum available gain (MAG) of these devices that was calculated from the measured S parameters. It was found that device 1 had gain peaks of 5.5 dB at 77 and 79 GHz, and peaks of 1.5 and 0.6 dB at 90 and 105 GHz, respectively. Device 2 had MAG peaks at 80, 90, and 95 GHz of 2.3, 1.8, and 1.6 dB, respectively.

The successful characterization of the HEMTs at W-band implies that active circuits with operational frequencies near 100 GHz can now be designed and fabricated. It is true that a paper design of a W-band oscillator or amplifier can be completed with the S parameters of Table I, however, the fabrication technology for 0.1- μ m HEMTs is still in the experimental stage and widespread performance variations exist among transistors, even if they are from the same wafer. At this point, many more devices need to be characterized to obtain the statistical information that would allow a practical design of a W-band HEMT circuit.

This work demonstrated the capability of the six-port to characterize active devices at W-band. The hardware simplicity, and thus the system reliability, of the six-port junction makes it an attractive millimeter wave network analyzer alternative to the conventional network analyzer. For example, if a component such as a thermistor fails, then replacement of the bad element can be accomplished quickly and the system can be made operational without the need for critical tuning adjustments, as would be necessary with a conventional network analyzer. While advances can be expected in millimeter wave frequency extenders that would improve their performance, these systems will still require the measured signals to be downconverted to complex and

expensive low-frequency magnitude and phase detection circuits.

ACKNOWLEDGMENTS

The authors would like to thank P. MacDonald at UCLA and R. E. Johnson at Hughes Aircraft Co., Missile Systems Group for their help in the construction of the six-port network analyzer. This work was supported in part by the Air Force Office of Scientific Research.

^{a1} Now with NASA Langley Research Center, Hampton, VA.

^{b1} Now with Hughes Aircraft Company Research Laboratory, Malibu, CA.

¹H. Q. Tserng and B. Kim, *Electron. Lett.* **21**, 178 (1985).

²P. M. Smith, P. C. Chao, K. H. G. Duh, L. F. Lester, and B. R. Lee, *Electron. Lett.* **22**, 780 (1986).

³L. Deardon, G. Miner, and M. Sayed, *IEEE Int. Symp. Dig.* 385 (1986).

⁴G. F. Engen, *IEEE Trans. Microwave Theory Tech.* **MTT-25**, 1075 (1977).

⁵H. M. Cronson and R. A. Fong-Tom, *IEEE Trans. Microwave Theory Tech.* **MTT-30**, 1260 (1982).

⁶M. P. Weidman, *WR-10 Single Six-Port Measurement System* NBSIR 81-1650 (National Bureau of Standards, Washington, DC, 1981).

⁷M. P. Weidman, *IEEE Trans. Microwave Theory Tech.* **MTT-25**, 1083 (1977).

⁸G. F. Engen, *IEEE Trans. Microwave Theory Tech.* **MTT-25**, 1086 (1977).

⁹D. Woods, *Proc. Inst. Electro. Eng.* **126**, 221 (1979).

¹⁰S. Li and R. G. Bosisio, *IEEE Trans. Microwave Theory Tech.* **MTT-30**, 1085 (1982).

¹¹D. Lacombe and J. Cohn, *IEEE Trans. Microwave Theory Tech.* **MTT-28**, 925 (1980).

¹²B. A. Syrett, *IEEE Trans. Microwave Theory Tech.* **MTT-28**, 925 (1980).

¹³E. R. Ehler, *IEEE MTT-S Int. Microwave Symp. Dig.* 275 (1986).

¹⁴W. Kuppa and K. F. Sodomsky, *IEEE Trans. Microwave Theory Tech.* **MTT-19**, 122 (1971).

¹⁵J. H. Schaffner, F. K. Oshita, H. R. Fetterman, J. J. Berenz, K. Nakano, and H. C. Yen, *IEEE MTT-S Int. Microwave Symp. Dig.* 233 (1988).

J.H. Schaffner, Student Member, IEEE
F.K. Oshita, Student Member, IEEE
H.R. Fetterman, Senior Member, IEEE
School of Engineering and Applied Science,
University of California, Los Angeles, CA

J.J. Berenz, Senior Member, IEEE
K. Nakano, Member, IEEE
H.C. Yen, Member, IEEE
Electronics Systems Group, TRW
Redondo Beach, CA

Abstract -- The scattering parameters of 0.1 μm high electron mobility transistors were measured from 75 GHz to 105 GHz utilizing a specially constructed six-port network analyzer. Testing a representative device biased to have a DC transconductance of 413 mS/mm, the maximum available gain was found to be as high as 5.5 dB at 77 GHz and 79 GHz, 1.5 dB at 90 GHz, and 0.6 dB at 105 GHz. Comparison with a similar transistor that was characterized at microwave frequencies and extrapolated up to W-Band (75 GHz to 105 GHz) shows qualitative agreement with the millimeter wave measurements. This is the first reported scattering parameter measurements on a transistor with gain at these frequencies.

Recent advances in heterojunction material growth and device fabrication have led to high electron mobility transistors (HEMTs) with superior high frequency performance [1], which has resulted in their increasing use in millimeter wave active circuits [2], [3]. Typically, the design of these circuits is preceded by scattering parameter measurements of the HEMT at microwave frequencies, from which a small signal model is derived. The model is then extrapolated to the desired frequency of operation for circuit synthesis, but extensive tuning and substitution of devices is usually required to obtain an operating circuit. A more systematic approach to millimeter wave circuit design is to characterize the active device at the expected circuit frequency of operation by collecting two-port scattering parameters. This paper presents the first reported direct W-band (75-110 GHz) characterization of a three-terminal active device,

† This work was supported in part by the Air Force Office of Scientific Research.

in this case a 0.1 μm HEMT [4].

The HEMT scattering parameters were acquired with a W-Band six-port network analyzer which was constructed using discrete commercially available waveguide components and W-band thermistors [5]. The six-port junction allowed the complete determination of the device reflection or transmission coefficient by power measurements at four ports [6]. The test fixture was comprised of a grounded source HEMT which was centered between two 50 Ω microstrip lines, and two five-section Chebyshev ridged waveguide transformers that coupled the microstrip line to the six-port [7].

The transistor was DC biased through input and output printed circuit bias tees which had quarter-wavelength coupled lines for DC blocks and radial stub low pass filters for the bias current. A detailed drawing of the bias tee and the HEMT connected by ribbon bonds is presented in Figure 1. The average insertion loss of two back-to-back transistors varied from 1.46 dB (75 GHz) to 3.96 dB (95 GHz) with an average of 2.3 dB from 75-105 GHz.

The transistor's scattering parameters were determined from the six-port data by a two-tier de-embedding process [8], that assumed a symmetrical test fixture [9]. First, the scattering parameters of the test fixture up to the transistor were determined from a calibration fixture which was composed of back-to-back transitions with a through length of microstrip line that duplicated a test fixture without the HEMT. Next, the forward and reverse reflection and transmission coefficients of the test fixture with the HEMT were obtained. Finally, the calibration fixture characterization was used to de-embed the scattering parameters of the transistor, including bond ribbons, from the test fixture measurements.

The 0.1 μm HEMT was initially characterized from 75-105 GHz in increments of 5 GHz, and its de-embedded scattering parameters, which include the bond ribbons, are presented in Table 1. The bias condition on the HEMT was 2.0 volts on the drain and 0.2 volts on the gate, at which point the DC transconductance reached its maximum value of 413 mS/mm at a drain current of 8.82 mA. The input power

was held below 150 μ W to guarantee small-signal operation.

For a higher resolution of the HEMT behavior, Figures 2 and 3 display polar plots of S_{11} and S_{21} from 75-85 GHz in increments of 1 GHz. These curves reveal that the maximum magnitude of S_{21} occurred at 79 GHz with a value of 1.31, and also that the scattering parameters contained a lot of frequency dependent fine structure. Repeated measurements of the test and calibration fixtures, which included reassembly of the transitions, have reproduced these resonances. Thus, the observed frequency dependence appears to be due to the distributed nature of the transistor when the millimeter wavelengths approach the device dimensions and the high frequency parasitic effects of the bond ribbons and fringing capacitances. Further research is being conducted to separate the transistor response from its parasitics. For qualitative comparison, the 2 - 26 GHz scattering parameters of a 0.1 μ m HEMT with the same geometry and similar DC characteristics are added to Figures 2 and 3.

The maximum available gain of the HEMT, which was calculated from the measured scattering parameters, is plotted in Figure 4. The gain reaches peaks at 5.5 dB at 77 GHz and 79 GHz, 1.5 dB at 90 GHz, and 0.6 dB at 105 GHz. The calculated gain shows a substantial amount of ripple due to parasitics and resonances. Also shown is the maximum available gain that was extrapolated from a microwave circuit model of the HEMT. The model predicted a gain of 3.9 dB at 80 GHz and a maximum frequency of oscillation near 140 GHz. Even though the extrapolated curve contains no parasitic resonances, it does support the observed gain at W-band. However, more devices need to be tested before any general assertions can be made between the measured and extrapolated performance of the HEMT.

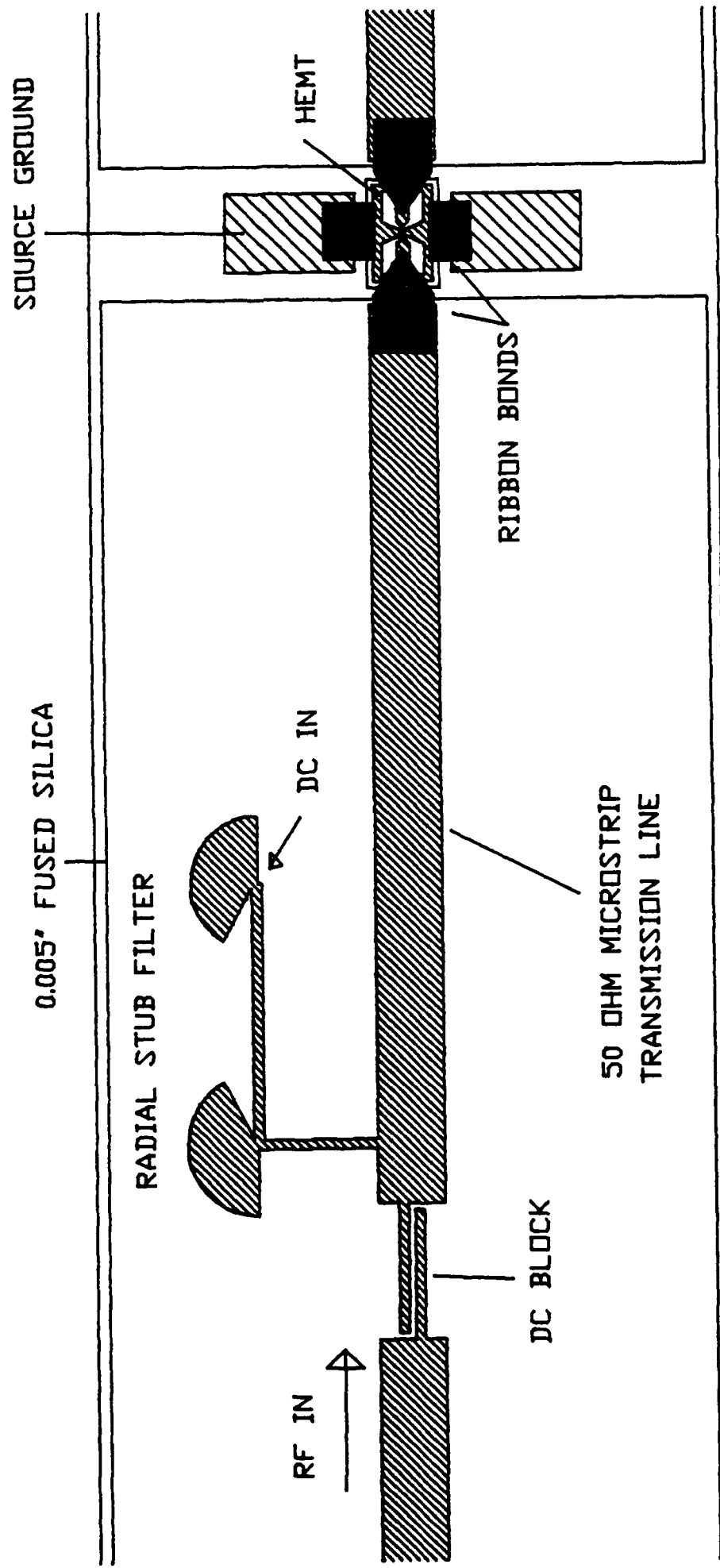
In conclusion, direct experimental characterization of a 0.1 μ m gate length HEMT at W-band has indicated the maximum gain that the device was capable of achieving at these frequencies in its parasitic environment. The results were qualitatively consistent with the extrapolated microwave transistor model. Although this ability to obtain W-band scattering parameters is certainly required by the millimeter wave

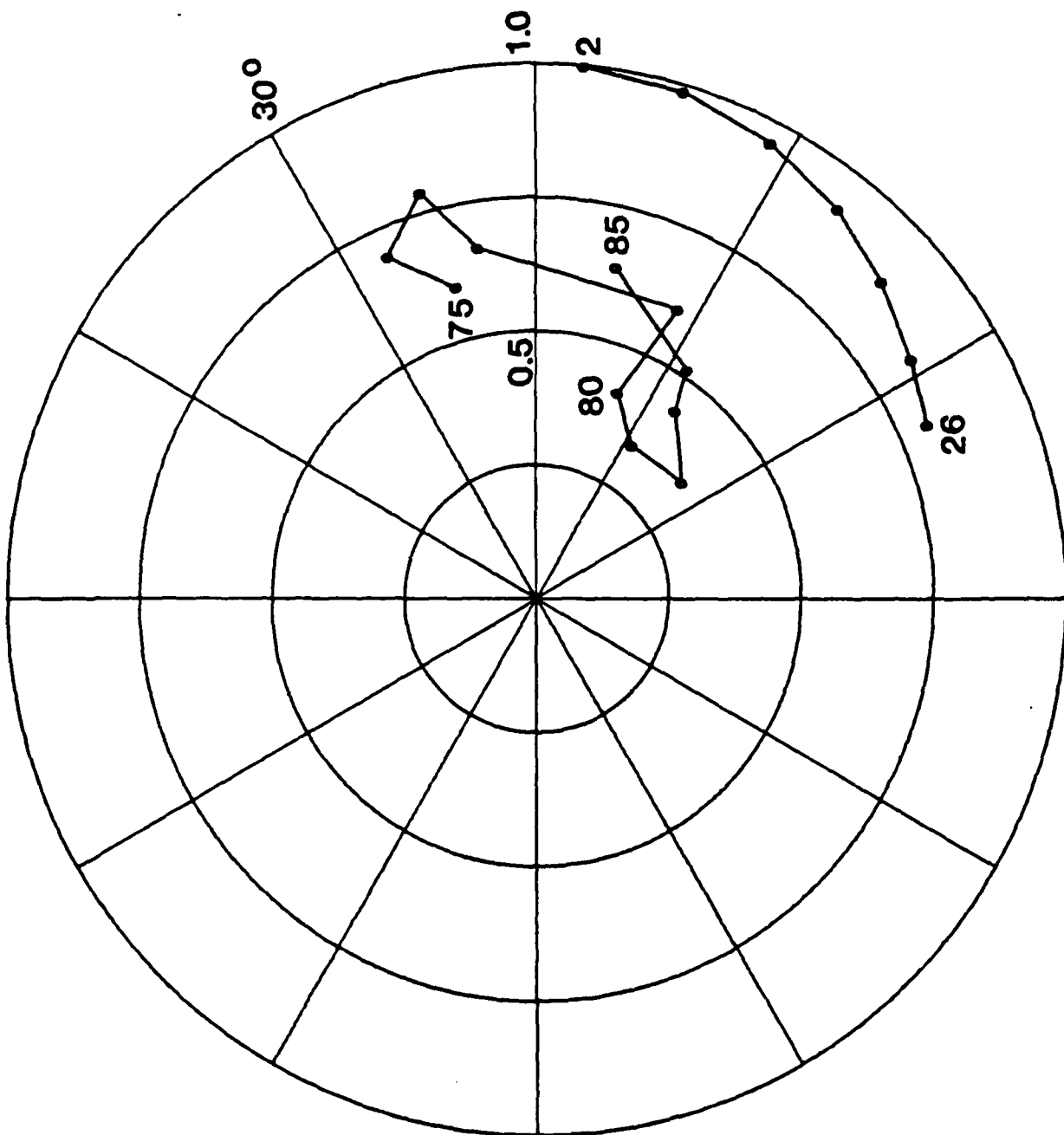
active circuit designer, the millimeter wave device data can also be used to determine which elements of high frequency device fabrication are most critical. This first measurement of transistor W-band scattering parameters permits the extension of sophisticated computer aided design techniques to the advanced development of millimeter wave devices and circuits.

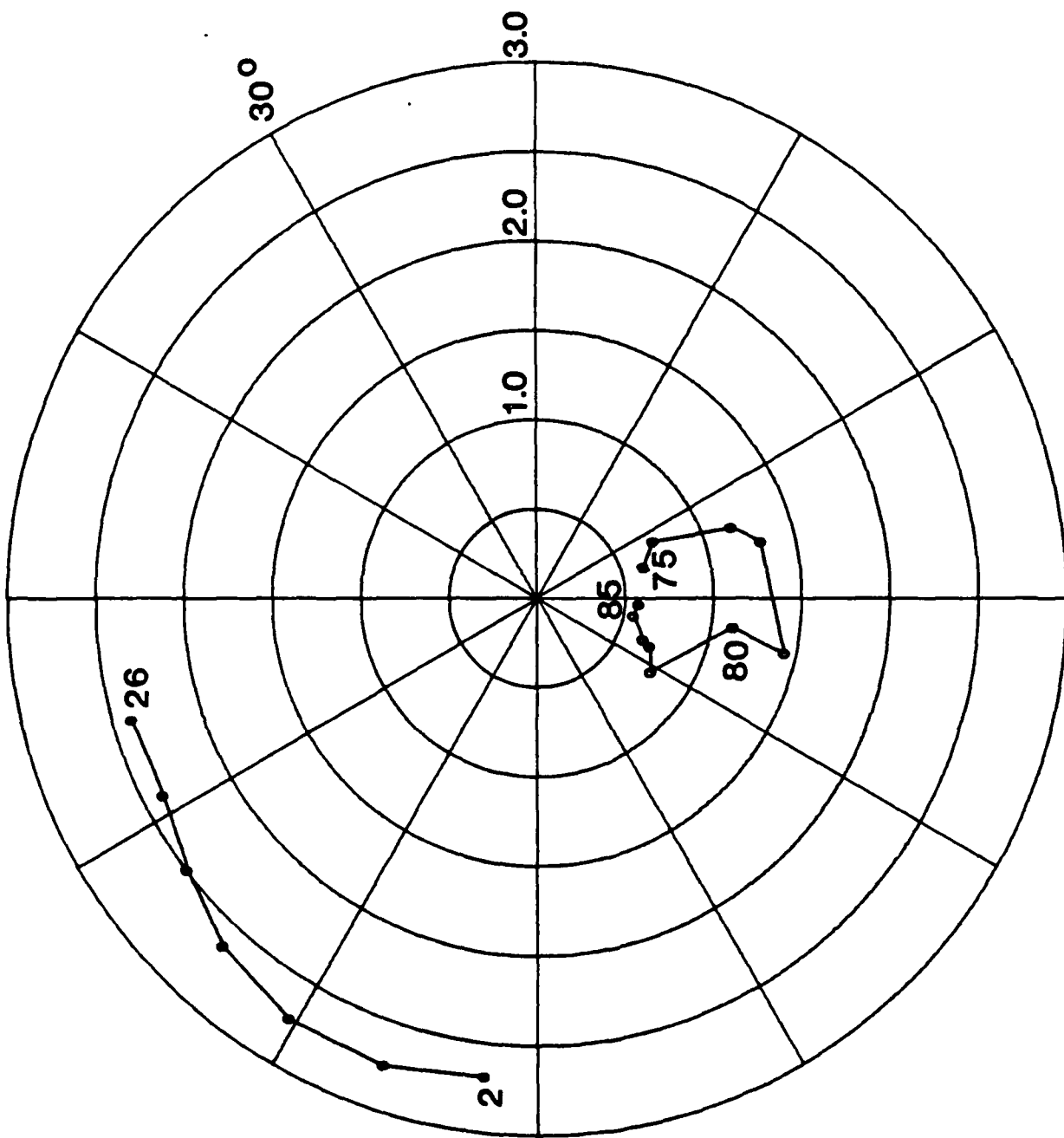
References

- [1] P.C. Chao, S.C. Palmateer, P.M. Smith, U.K. Mishra, K.H.G. Duh, and J.C.M. Hwang, "Millimeter-Wave Low-Noise High Electron Mobility Transistors", *IEEE Electron Device Lett.*, vol. EDL-6, no. 10, pp. 531-533, October 1985.
- [2] M. Sholley and A. Nichols, "60 and 70 GHz (HEMT) Amplifiers", in *IEEE MTT-S Dig.*, pp. 435-436, June 1986.
- [3] P.M. Smith, P.C. Chao, K.H. Duh, L.F. Lester, and B.R. Lee, "94 GHz Transistor Amplification Using an HEMT", *Electronics Letters*, vol. 22, no. 15, pp. 780-781, July 17, 1986.
- [4] K. Nakano, To be published.
- [5] K.J. Moeller, *Development and Evaluation of a Millimeter-Wave Six-Port Network Analyzer*, Masters Thesis, University of California, Los Angeles, 1986. Submitted for Publication: Review of Scientific Instruments.
- [6] G.F. Engen, "The six-port reflectometer: an alternative network analyzer," *IEEE Trans. Microwave Theory Tech.*, vol. MTT-25, pp. 1075-1080, Dec. 1977.
- [7] J.H. Schaffner, Doctoral Dissertation, University of California, Los Angeles, 1988.
- [8] R. Vaitkus and D. Scheitlin, "A two-tier deembedding technique for packaged transistors", in *IEEE MTT-S Dig.*, pp. 382-330, June 1982.
- [9] E.R. Ehlers, "Symmetric test fixture calibration", in *IEEE MTT-S Dig.*, pp. 275-278, June 1986.

- Fig. 1. Attachment of the HEMT to 50 Ω microstrip line and printed circuit bias tee.
- Fig. 2. S_{11} of a 0.1 μm gate length HEMT measured from 75 to 85 GHz on the six-port, and from 2 to 26 GHz on an automatic network analyzer with a coplanar line probe.
- Fig. 3. S_{21} of a 0.1 μm gate length HEMT measured from 75 to 85 GHz on the six-port, and from 2 to 26 GHz on an automatic network analyzer with a coplanar line probe.
- Fig. 4. Maximum available gain of the 0.1 μm gate length HEMT calculated from measured S-parameters.
- Table 1. Scattering Parameters of a 0.1 μm HEMT gate length HEMT measured with a six-port network analyzer.

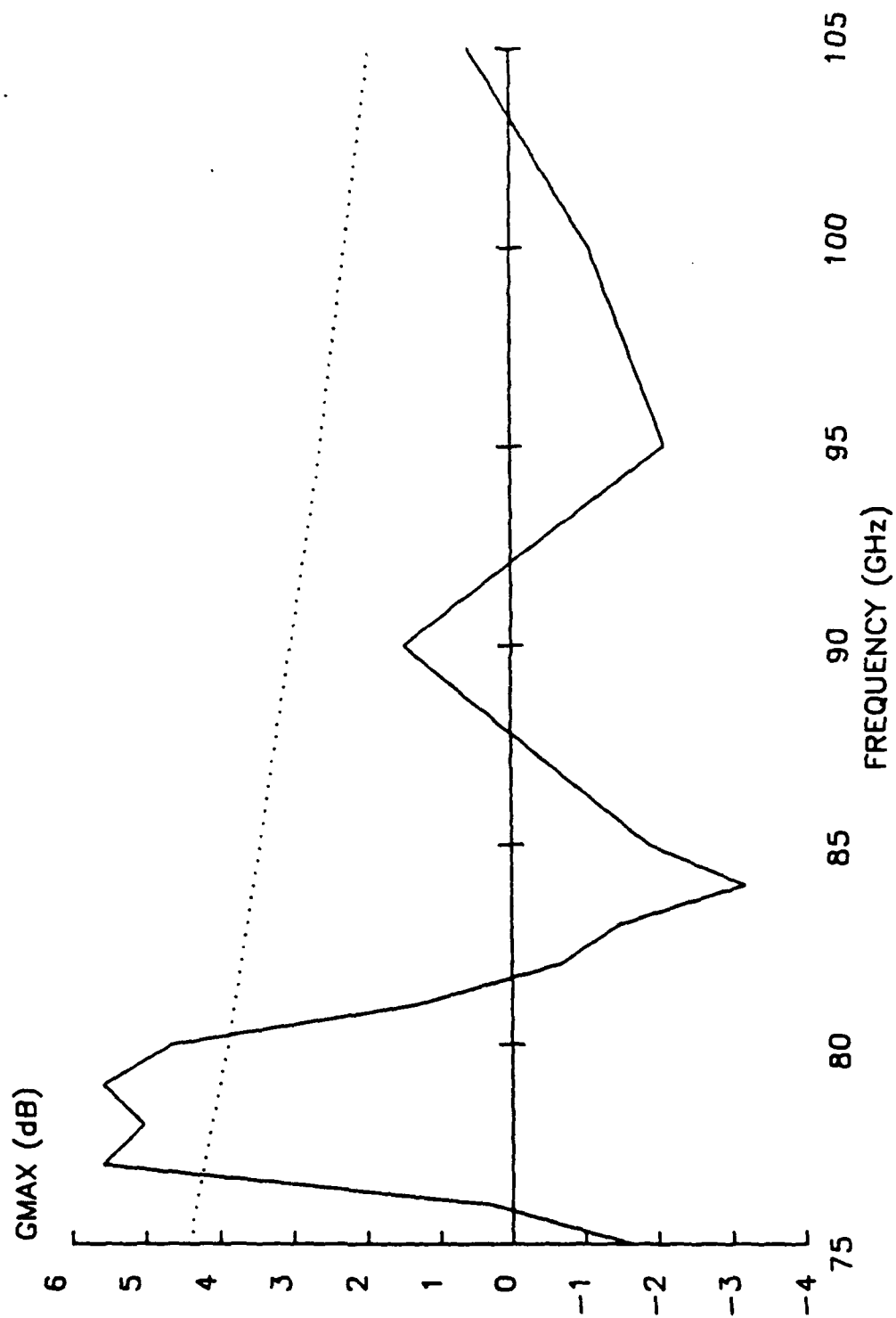






MEASURED
S-PARAMETERS

EXTRAPOLATED
S-PARAMETERS



Frequency (GHz)	S ₁₁		S ₂₁		S ₁₂		S ₂₂	
	Mag	Phase	Mag	Phase	Mag	Phase	Mag	Phase
75.0	0.599	14.4	0.632	-74.2	0.105	-37.6	0.357	67.6
80.0	0.413	-22.2	1.126	-98.4	0.385	-53.9	0.695	57.9
85.0	0.635	-13.9	0.578	-93.4	0.327	-48.3	0.533	35.4
90.0	0.378	-44.4	0.852	-122.2	0.604	-98.7	0.735	20.2
95.0	0.655	-36.9	0.542	-88.4	0.440	-86.3	0.453	-10.4
100.0	0.281	-33.3	0.843	-117.3	0.605	-124.0	0.192	0.4
105.0	0.219	4.1	0.915	-140.9	0.608	-155.3	0.233	44.4